

Continuous Pulsation Dynamics
in the High-Latitude
Magnetosphere-Ionosphere System

Thesis submitted for the degree of
Doctor of Philosophy
at the University of Leicester

by

S. Carlos Gane

Radio and Space Plasma Physics Group
University of Leicester

December 2010

Declaration

I, S. Carlos Gane, confirm that the work presented in this thesis is my own. Information derived from other sources has been suitably referenced.

Abstract

Continuous Pulsation Dynamics in the High-Latitude Magnetosphere-Ionosphere System

S. Carlos Gane

The thesis investigates Ultra Low Frequency waves in the band 0.1 Hz to 5 Hz in the terrestrial magnetosphere-ionosphere system. Utilising mid-high latitude ground-based induction coil magnetometers, continuous (Pc1-2) and irregular (Pi1-c) pulsations are explored through the application of digital spectral analysis.

An assessment of two spectral analysis techniques is conducted. From which it is concluded that, for routine ground-based analysis of Pc1-2 pulsations, treating the horizontal components of magnetic field variation as a single complex signal is computationally beneficial with minimal loss of useful information. Polarisation parameters and values of cross spectral phase are derived using a weighted histogram technique and are subsequently used to distinguish discrete pulsations and infer their location through simple triangulation.

The results of a statistical study of ~1200 discrete Pc1-2 events over the full year of 2007, during the declining phase of solar cycle 23, are presented. This study, for the first time, reports the ground-based polarisation properties of Pc1-2 waves as a function of latitude. The derived diurnal frequency behaviour supports the suggestion that the Ionospheric Alfvén Resonator may play a part in the filtration of ground-based Pc1 observations. Pc1-2 behaviour over the course of 26 geomagnetic storms is also presented, with support being found for the association of pulsation enhancement with plasmaspheric plume formation in the recovery phase.

A case study, combining coherent and incoherent radar, in situ particle measurements and ground based magnetometry, has focused on high latitude Pi-c activity during a period of enhanced dayside reconnection. This study has provided support for the association of Electromagnetic Ion cyclotron waves with the SuperDARN spectral width enhancements observed in the flanks of the ionospheric cusp.

Acknowledgements

I would like to thank my Parents for their unwavering support and encouragement.

I thank the Science and Technology Facilities Council (STFC) for their financial support of my studies.

I acknowledge the support of the European Community - Research Infrastructure Action under the FP6 "Structuring the European Research Area" Programme, LAPBIAT (RITA-CT-2006-025969). I would also like to extend my gratitude to the members of the SGO who were outstanding hosts during my visits to the observatory. The gigabytes of data, insight and hospitality provided by Tero Raita made this thesis possible.

I would like to thank the members of the Radio and Space Plasma Physics Group who have made a significant difference to my journey through this PhD. Dr Steve Milan and Professors Terry Robinson and Tim Yeoman receive my thanks for helpful discussion and direction in the course of my studies as does my supervisor Dr Darren Wright who has enriched my life more than words can express.

I am grateful to Stuart, Mick and Richard, who were always there to indulge my often not so technical whims.

My thanks go to Colin Forsyth and Sarah Grocott for various sporting misadventure and to Adrian Grocott for the tantalising promise of diving.

My various office mates over the years deserve my thanks for enduring my numerous odd habits. In particular, I thank Ingrid for an endless supply of pens and Gabby for absolutely everything.

I would like to thank Alex for lending a discerning ear and providing avian and murine sustenance in times of need.

My final and greatest thanks of all go to Lilla.

Contents

1	Introduction	1
1.1	Introduction	1
1.2	The Solar and interplanetary environment	1
1.2.1	The Sun	1
1.2.2	The Solar Wind and Interplanetary Magnetic Field	6
1.3	The Near-Earth environment	12
1.3.1	The Neutral Atmosphere	12
1.3.2	The Ionosphere	13
1.3.3	The Magnetosphere and associated current systems	20
1.4	Summary	26
2	Plasma Motion and Waves	28
2.1	Basic plasma dynamics	28
2.1.1	Charged particle motion in a static electromagnetic field	28
2.1.2	Charged particle motion in magnetic a magnetic field	30
2.1.3	Adiabatic processes	36
2.1.4	Ideal behaviour	39
2.1.5	A Fluid Approach	41
2.2	Magnetohydrodynamic waves	47
2.2.1	MHD dispersion relation	48
2.2.2	Geomagnetic pulsations	50
2.2.3	Electromagnetic Ion Cyclotron Waves	52
2.3	Summary	53
3	Review of Pc1-2 studies	55
3.1	Morphology and occurrence	55
3.2	Solar activity dependence	62
3.3	Geomagnetic storms and currents	65

3.4	Particle precipitation	67
3.5	Pearl repetition period and growth modulation	68
3.6	Polarisation and propagation	72
3.7	Unorthodox geophysical correlations with Pc1-2 pulsations	75
3.8	High latitude studies	75
3.9	Summary and outstanding issues	76
4	Instrumentation and Data Analysis Techniques	77
4.1	Ground based instrumentation	77
4.1.1	Finish Pulsation Magnetometer Chain	77
4.1.2	International Monitor for Auroral Geomagnetic Effects (IMAGE)	78
4.1.3	Geomagnetic indices	80
4.1.4	Coherent Scatter Radar (CSR)	81
4.1.5	Incoherent Scatter Radar (ISR)	84
4.2	Space based instrumentation	88
4.2.1	The OMNI dataset	88
4.2.2	Los Alamos National Laboratory (LANL) geosynchronous satellites	90
4.2.3	Defence Meteorological Satellite Program	91
5	Pulsation Analysis Techniques	93
5.1	Introduction	93
5.2	Spectral analysis techniques	94
5.2.1	Fourier analysis	94
5.2.2	Spectral Matrix Analysis	96
5.2.3	Complex Input Spectral Analysis	97
5.2.4	Complex input versus spectral matrix analysis	100
5.2.5	Correlation analysis	102
5.3	Pulsation processing	106
5.3.1	Pre-processing and background extraction	106
5.3.2	Discrete event parameter characterisation	108
5.3.3	Determination of the degree of structuring within pulsation	110
5.3.4	Spectral parameter continuity as an event discriminator	115

5.4	Inter-station time delay determination	115
5.5	Source triangulation	116
5.6	Discussion	119
5.6.1	Analysis techniques and processing	122
5.6.2	Inter-station time delay and source triangulation	123
5.7	Summary	125
6	Characteristics of Pc1-2 Pulsations from Multi-station Data	126
6.1	Introduction	126
6.2	Event Identification and Processing	128
6.2.1	Pre-processing and background extraction	129
6.2.2	Manual frequency boundary selection	129
6.2.3	Statistical parameter determination	135
6.2.4	Event categorisation and degree of structuring	135
6.2.5	Identification of geomagnetic storm activity and determination of solar wind driving structures.	138
6.2.6	Magnetopause and plasmopause positions	139
6.3	Statistical Results	139
6.3.1	Pc1-2 dataset statistics	139
6.3.2	Geomagnetic storm statistics	158
6.3.3	Storm-time pulsation occurrence	158
6.4	Discussion	173
6.4.1	Analysis Technique	173
6.4.2	Pulsation dataset	175
6.4.3	Storm characteristics	179
6.4.4	Storm related pulsations	179
6.5	Summary	181
7	Coordinated Observations of the Cusp Region	183
7.1	Introduction	183
7.2	Instrumentation and data acquisition	184
7.2.1	Interplanetary and Geomagnetic data	184

7.2.2	Coherent scatter radar	185
7.2.3	The Finnish Pulsation Magnetometer Chain (FPMC)	187
7.2.4	The EISCAT Svalbard Radar (ESR)	187
7.2.5	In situ particle data	188
7.3	Observations	188
7.3.1	Interplanetary and geomagnetic conditions	188
7.3.2	Ground based radar and pulsation magnetometer observations	190
7.3.3	In situ particle observations	206
7.4	Discussion	209
7.4.1	Morphology and Motion of the Cusp	209
7.4.2	Correspondence of irregular pulsations to radar measurements	211
7.5	Summary	215
8	Summary and Further Work	216
8.1	Summary	216
8.2	Further work	218
A	Vector identities	221
B	IMAGE Magnetometer Locations	222
	References	223

Chapter 1. Introduction

1.1 Introduction

Understanding the near-space environment is paramount to countless areas of scientific research. From the determination of the Sun's influence on the earth's climate to precise navigation and communication systems, the ionised regions that envelope the neutral atmosphere have a profound effect on the energy that flows through them. This thesis investigates the flow of electromagnetic energy through those regions in the form of Ultra Low Frequency (ULF) waves.

The form and function of the sun are fundamental to the understanding of terrestrial ULF wave behaviour, as are the near-earth regions through which they propagate. Henceforth, this chapter will introduce the solar and terrestrial spheres and outline the dynamic processes that occur within and between them.

1.2 The Solar and interplanetary environment

The following section will outline the main features of the sun and interplanetary medium, concentrating on the concepts that are of most relevance to this work.

1.2.1 The Sun

The sun, our closest star and provider of the energy to sustain life on earth is rather astronomically unremarkable. It is a yellow-orange, variable star of modest size, which classifies it as a G2 V in the main sequence of its life cycle. Composed of predominantly hydrogen (~92.1%), helium (~7.8%) and a multitude of trace elements in the hot dissociated state of plasma, the sun has been undergoing nuclear fusion for approximately 4.3 of its estimated 11 billion year productive lifespan. Figure 1.1 is a composite image depicting an artist's impression of the inner structure of the sun, superimposed on which are satellite observations of solar surface features.

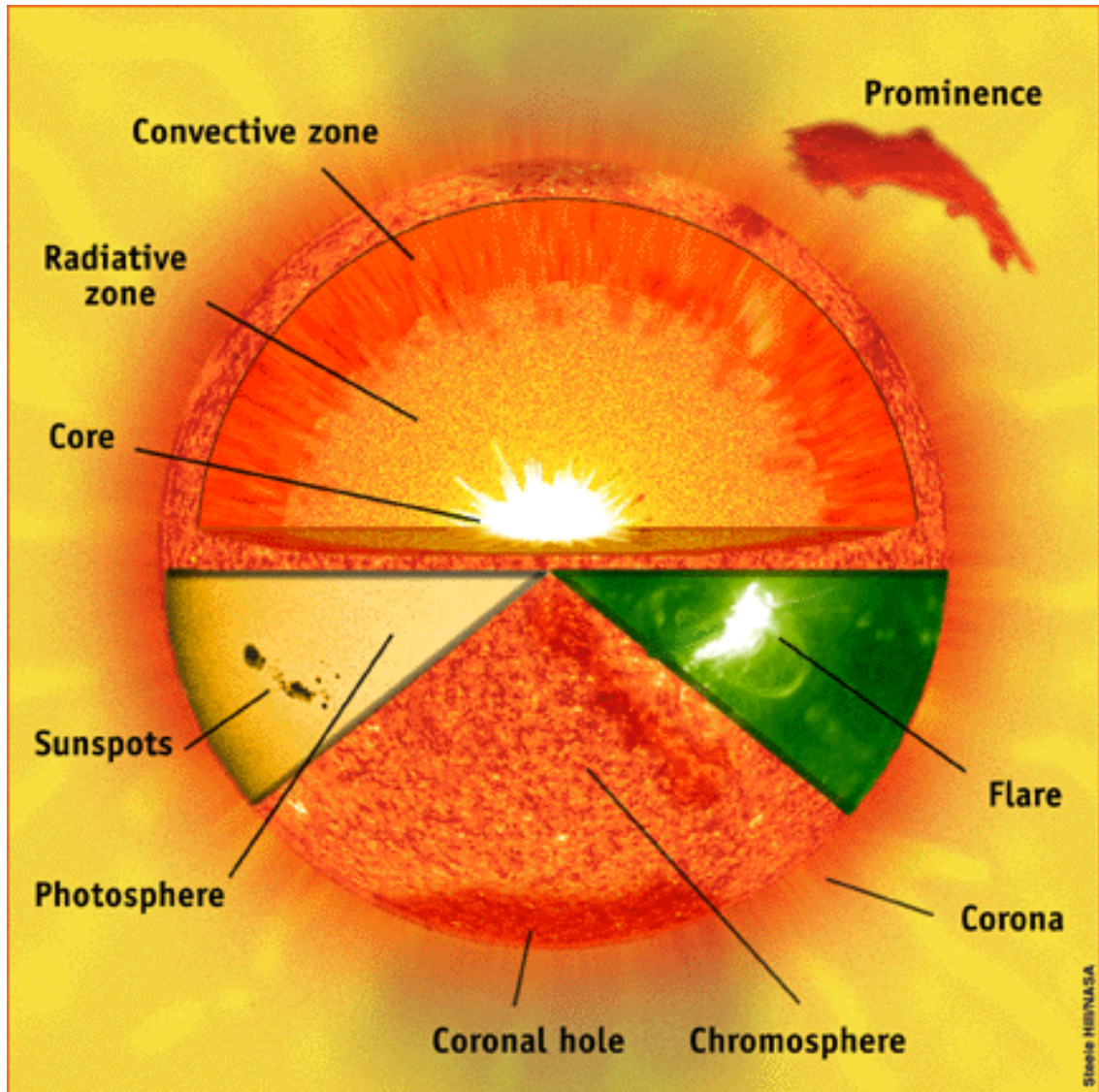


Figure 1.1: Composite diagram of an artist's impression of the solar interior overlaid with SOHO images.
<http://www2.warwick.ac.uk/fac/sci/physics/research/cfsa/people/inglisa/research/basics/>, image credit: SOHO (ESA & NASA).

At the base of the solar atmosphere resides the photosphere, beneath which optical opacity becomes so great that direct observation is no longer possible, hence, what is known about the internal dynamics of the sun is derived predominantly from indirect observation or theoretical models constrained by observable parameters.

The Sun has an effective temperature of ~ 5800 K and a synodic rotational period of approximately 27 days at the equator and 31 near its poles. Spectroscopic techniques have since shown that photospheric rotation is not fixed in time or latitude but fluctuates according to solar activity; this remains a subject of active research (Schwenn, 2006). Variation in the number of sunspots was first characterised by Heinrich Schwabe, who recognised an approximate 11 year cycle of occurrence (Humboldt, 1850). The number of sunspots varies from cycle to cycle, as shown in figure 1.2, which is a plot of total annual sunspot numbers for the past 400 years. Sunspot number has a close association with total solar irradiance, yet correspondence is most evident in the high energy/short wavelength part of the spectrum (Willson and Hudson, 1988). A feature of great interest is the period from the mid seventeenth to early eighteenth centuries, known as the Maunder minimum. During this period of reduced solar activity European climate exhibited a significant fall in temperature. This period enabled the winter pastime of skating on the Thames and saw the shortening of the Italian tree-growing season, such that the wood used in the crafting of Stradivari's violins was of a homogeneity that may never be seen again, accounting for their unsurpassed excellence (Burckle and Grissino-Mayer, 2003).

Zeeman splitting of spectral lines, and subsequent polarisation analysis of spectroheliographic observations, led George E. Hale to postulate the presence of magnetic fields on the surface of the sun (Hale, 1908). Hale further showed that the polarity of the sun's magnetic field reversed at each solar maximum, lengthening the true solar cycle from 11 to 22 years. Figure 1.3 shows a magnetogram of the radial component of the Sun's magnetic field. The characteristic equatorward track of sunspots throughout each cycle may be seen, as well as the polar magnetic field, which clearly reverses at sunspot maximum. Sunspots owe their dark appearance to the magnetic fields evident in figure 1.3, which inhibit normal surface convection by trapping charged particles, creating localised regions of relatively cool plasma. To a first order approximation, the solar magnetic field is dipolar; however, as figure 1.3

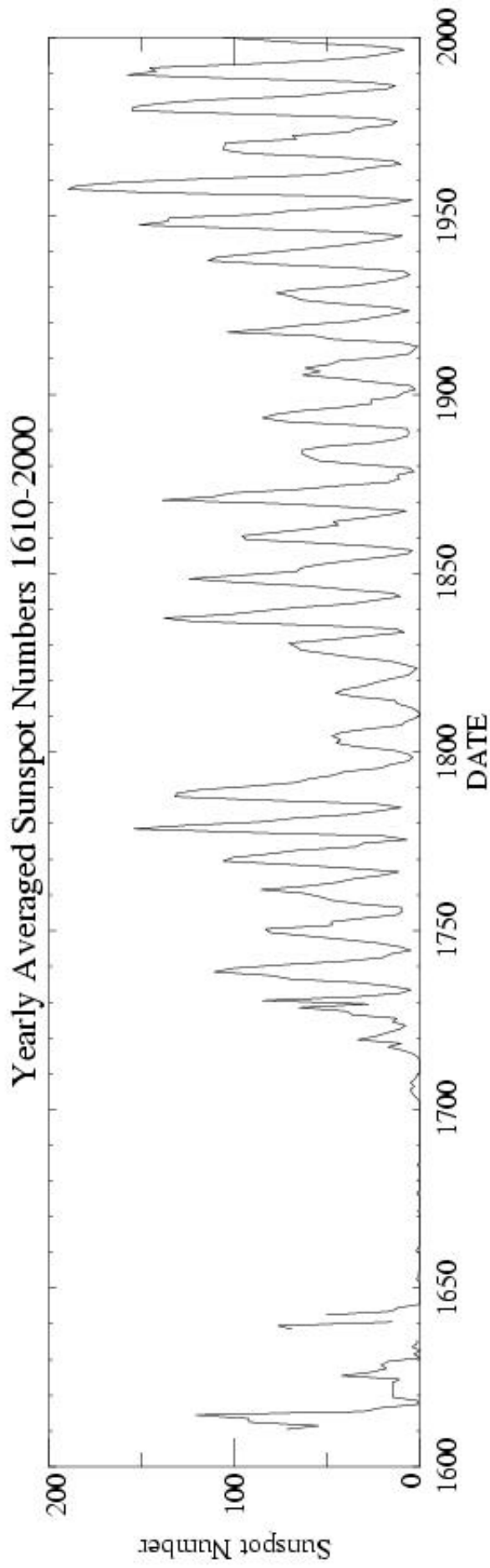
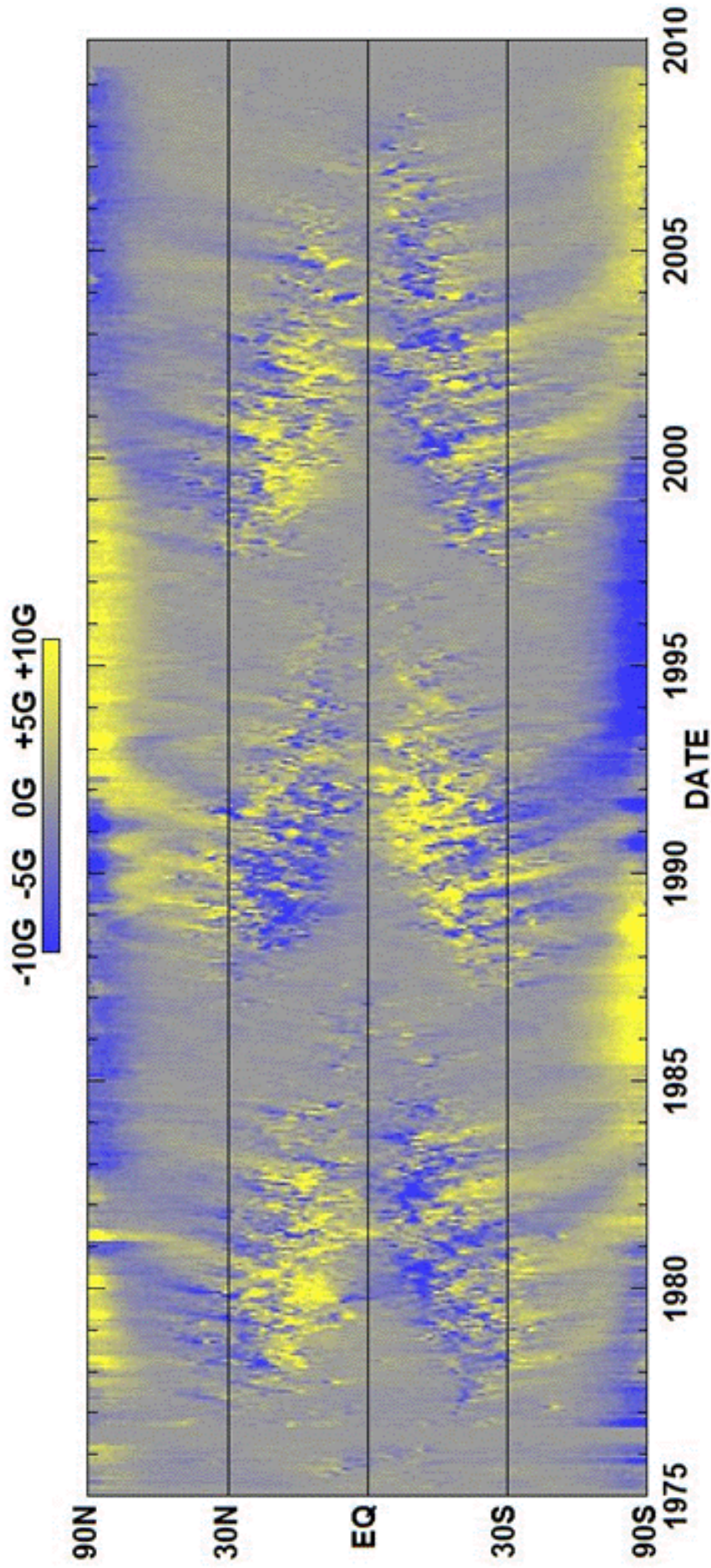


Figure 1.2: Average yearly sunspot number, displaying variation between cycles. The period of low sunspot number between the mid 1600s and early 1700s is known as the Maunder minimum and has been associated with the mini ice age phenomenon of the same period.
<http://spacescience.spaceref.com/ss/pad/solar/sunspots.htm>, image credit: NASA/MSFC



Hathaway/NASA/MSFC 2009/07

Figure 1.3: Solar magnetogram, showing the magnetic field strength of the Sun's surface. Solar field reversals can be seen at the time of sunspot maximum as well as the magnetic signature of sunspot pairs as they migrate toward the equator throughout the cycle.

<http://solarscience.msfc.nasa.gov/images/magbfly.jpg>, image credit: D.Hathaway, NASA/MSFC

shows, its complexity far exceeds that approximation. The myriad of dynamic magnetic events cause a field line guidance of plasma that may extend well into the interplanetary medium as they are carried by the solar wind.

1.2.2 The Solar Wind and Interplanetary Magnetic Field

The solar atmosphere, unlike that of the Earth, is not in hydrostatic equilibrium but continuously streams outward in to interplanetary space (Parker, 1958). The corona forms the uppermost region of the solar atmosphere and is the source of the solar wind. Density in the corona falls rapidly with altitude yet, paradoxically, its temperature rises from 6×10^3 K at its base to approximately 10^6 K at an altitude of 10^4 km. The immense volume of the solar atmosphere means that the Sun's gravitational attraction may not be considered as constant throughout, as is the hydrostatic case of the Earth, but must be treated fully according to its inverse square field decay. The kinetic pressure of the high temperature upper atmosphere subsequently overcomes the Sun's gravity and flows radially outward at a modal speed of some 400 km s^{-1} , forming the solar wind.

The speed at which purely compressional perturbations may propagate through a medium, its sound velocity, is given by the square root of the ratio of thermal pressure to mass density, C_s :

$$C_s^2 = \frac{\gamma k_b T}{m_i}. \quad (1.1)$$

where γ is ratio of specific heats, k_b is the Boltzmann constant, T is temperature and m_i is particle mass. Furthermore, the ratio of flow speed, v , to sound speed, the sonic Mach number, M_s , is given by

$$M_s = \frac{v}{C_s}, \quad (1.2)$$

which, when evaluated at the upper boundary of the solar atmosphere, shows that if adiabatic heat transfer is assumed, i.e. $\gamma = 5/3$, the solar wind is highly supersonic with a Mach number of ~ 3 . The supersonic nature of the solar wind is of great importance to its interaction with the magnetosphere as shall be seen in section 1.3. Given its low density and high temperature, the collision frequency in the solar atmosphere is low. Consequently, conductivity is high as is plasma velocity, which when coupled with a

large scale size leads to a high ratio of diffusive to convective contribution to plasma motion, known as the magnetic Reynolds number (Ch.2, Eqn. 2.42). Plasma configuration is determined by the dominance of either magnetic or kinetic energy density. Equating those two quantities and rearranging to form the following inequality shows that flow domination occurs when

$$v > \frac{B}{(\rho_m \mu_0)^{\frac{1}{2}}}, \quad (1.3)$$

Where B is magnetic field strength, ρ_m , is mass density and μ_0 is the permittivity of free space. The quantity on the right hand side is the Alfvén speed, V_A , which shall be considered in greater detail in chapter 2. At very low altitudes, the intense solar magnetic field binds plasma motion to the surface region. With increasing altitude, coronal kinetic energy density dominates allowing plasma flow to dictate magnetic configuration. These conditions allow Alfvén’s theorem (Ch. 2.1.5) to hold and the Sun’s magnetic field to be frozen in to the out-flowing solar wind.

Solar plasma drags with it the solar magnetic field, which upon escaping the corona constitutes the Interplanetary Magnetic Field (IMF). As the solar wind rapidly expands, it distorts the IMF. This has the effect of elongating field lines, such that at large distances the direction of the field gains a radial component. The resultant field configuration is depicted in figure 1.4, which is the MHD model simulation of Pneuman and Kopp (1971) showing a rapidly expanding solar corona with a chromospheric dipolar magnetic field. Evident from figure 1.4 is that the radial direction of the IMF must reverse across the equatorial plane; hence, according to Ampere’s law, a thin current sheet must exist there. As predicted by Parker, the radially expanding solar wind and the corotating solar magnetic field, generate an IMF curvature, depicted in figure 1.5. The figure shows that as the footprint of a field line rotates with the photosphere, the coronal plasma into which it is frozen follows a radial path, “winding up” the IMF as it flows away. This mechanism creates the Parker spiralling magnetic field, shown in figure 1.6, which shows that the direction of the IMF in the ecliptic plane at the radius of Earth’s orbit is close to 45° to the Sun-Earth line. The undisturbed IMF configuration is further complicated by the Sun’s tilted axis of rotation, which is oriented at 7.25° to the normal of the ecliptic plane (Labonte, 1981). The culmination of tilt and spiral is the wave-like Heliospheric Current Sheet (HCS) seen in figure 1.7. The figure displays the

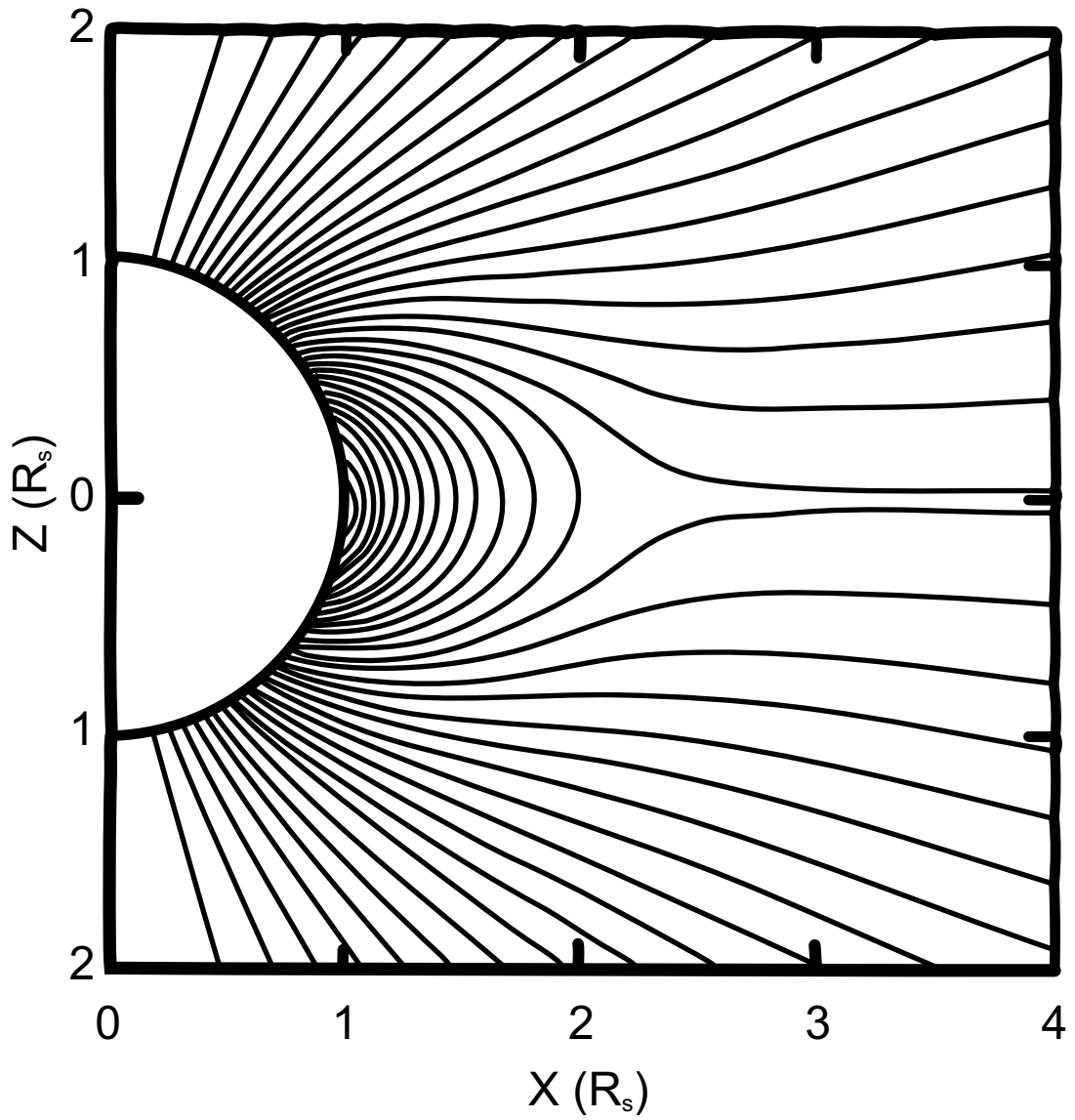


Figure 1.4: Heliocentric Magnetic Equatorial reference frame plot of “frozen in” solar magnetic field lines as they propagate with the outflowing solar wind. Adapted from Pneumann and Kopp (1971).

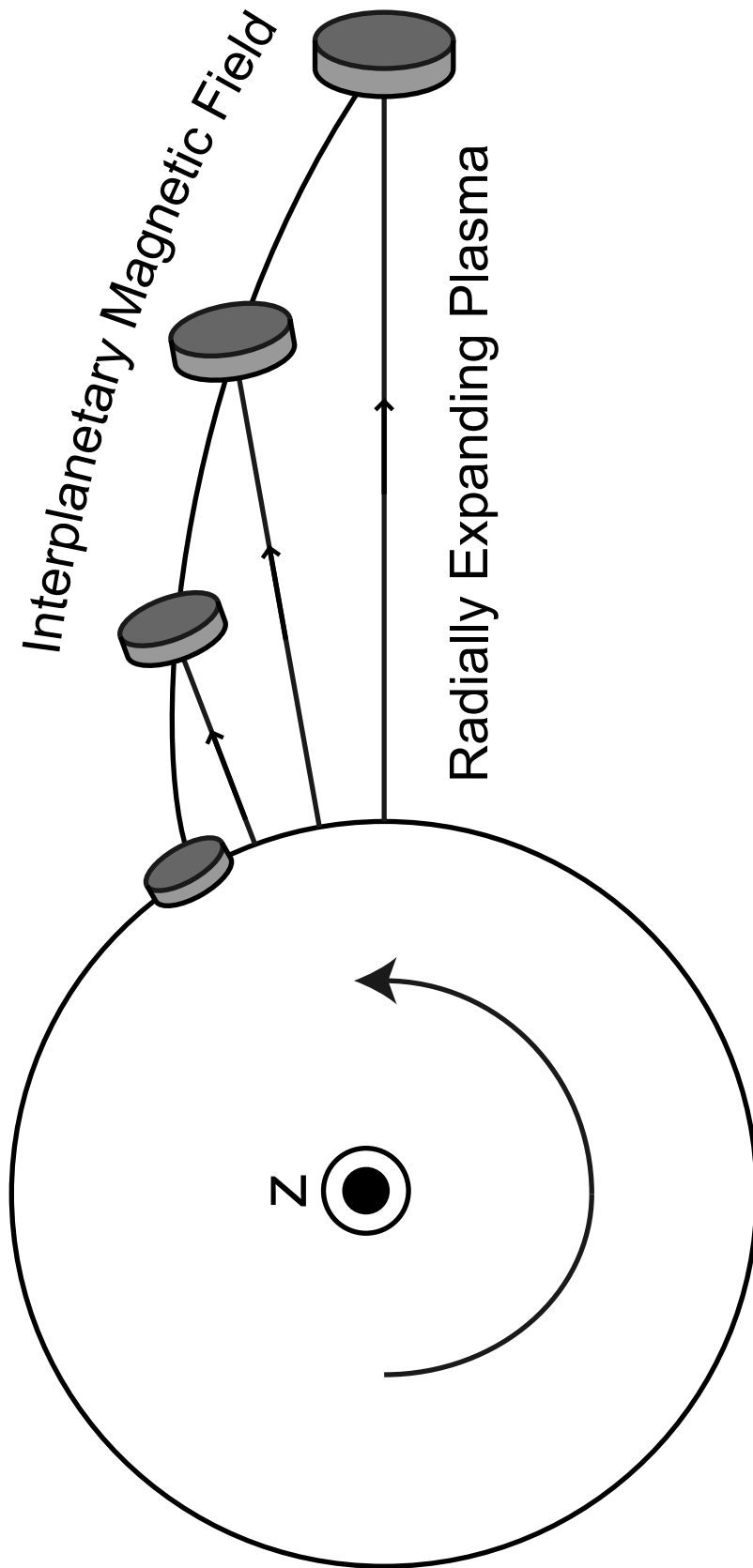


Figure 1.5: Archimedean spiraling solar magnetic field, viewed looking down on to the rotational plane of the sun.

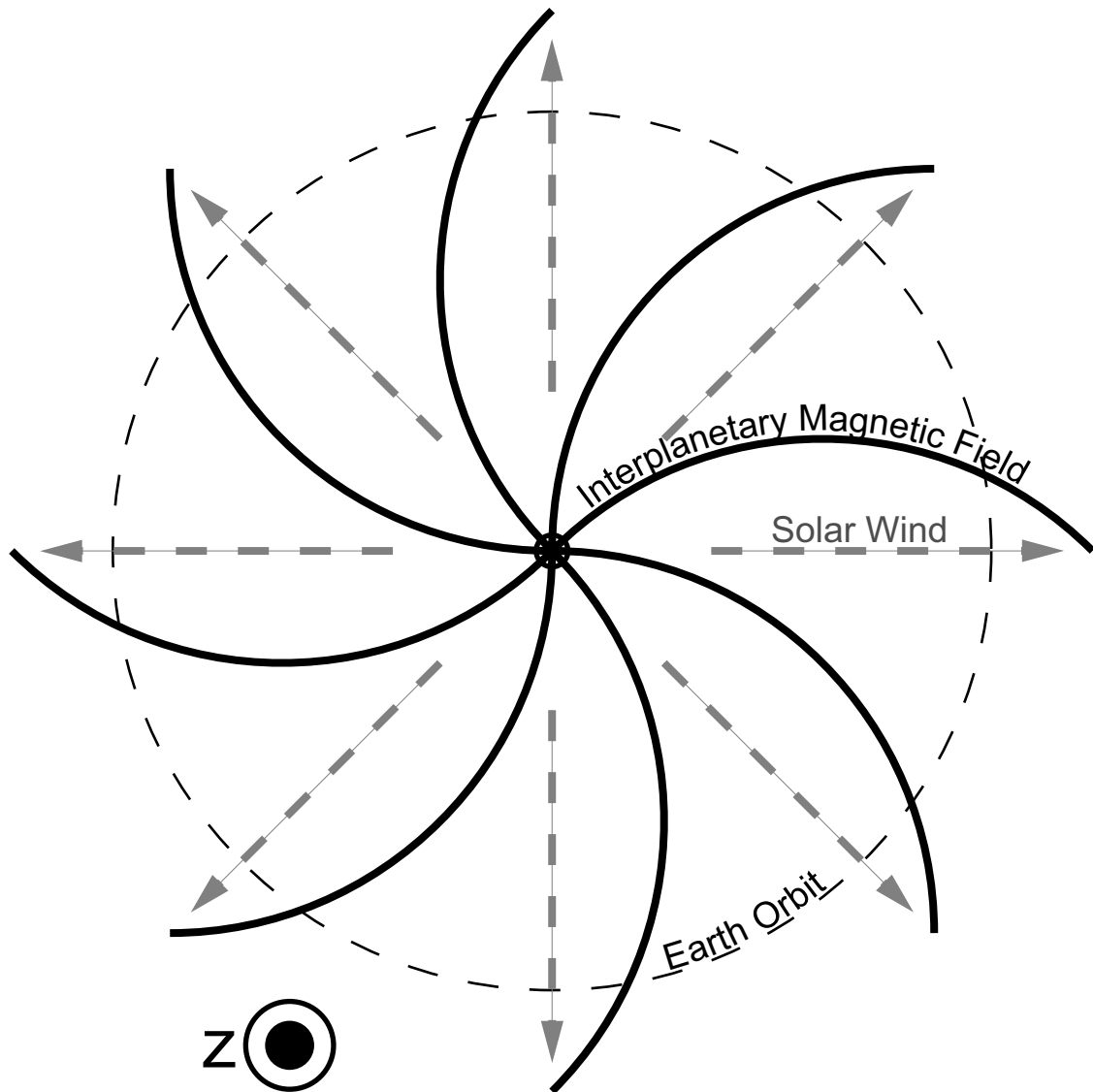


Figure 1.6: The Parker Spiral, showing the configuration of the Interplanetary Magnetic Field as it is swept out by the solar wind. Looking down on to the Sun's plane of rotation, adapted from Parker (1958).

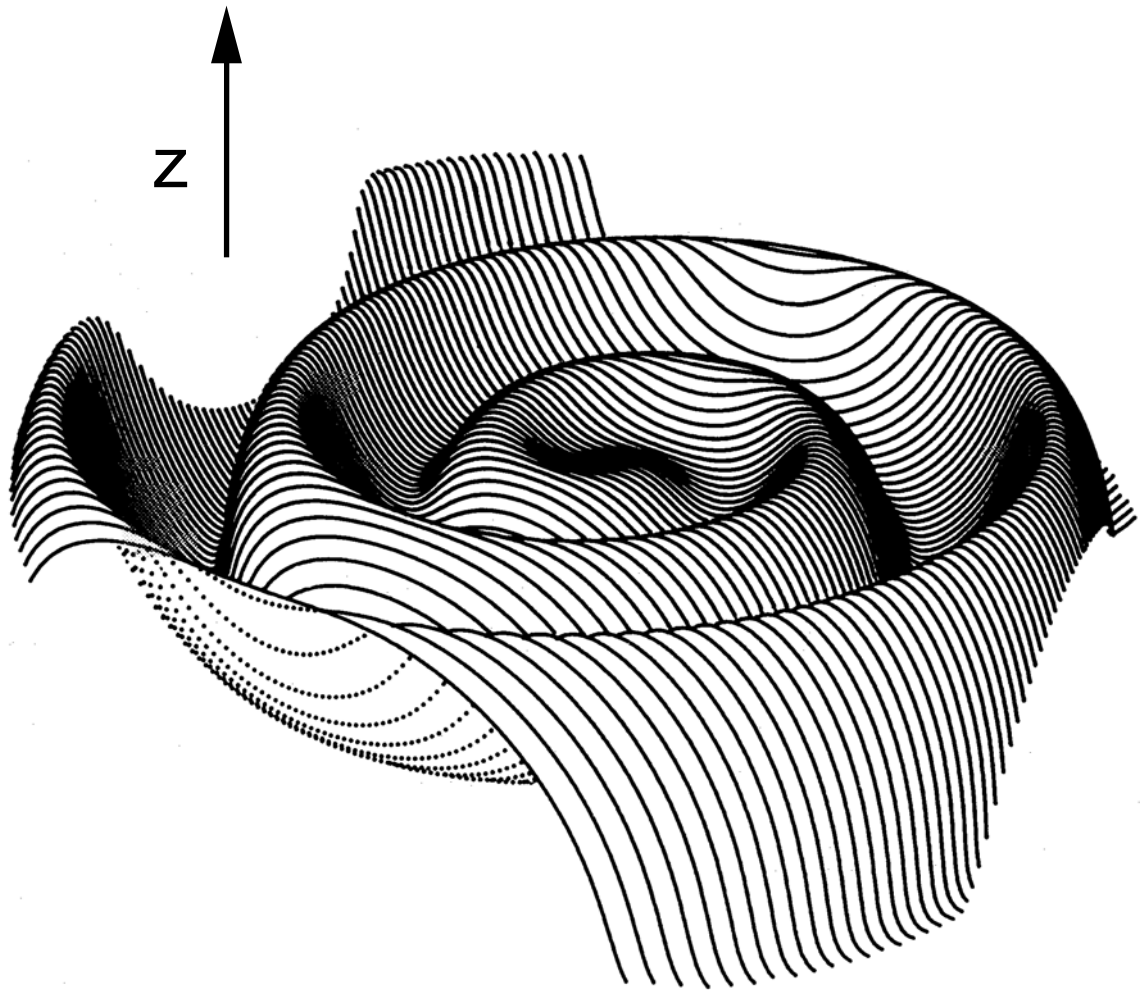


Figure 1.7: Heliocentric Solar Ecliptic reference frame view of the wavy Heliospheric Current Sheet. Adapted from Jokipii and Thomas (1981).

Jokipii and Thomas (1981) model representation of the HCS viewed from 30° above the ecliptic at 75AU and clearly shows how the undulating nature of the IMF extends far into the solar system.

The regions, processes and periodicities outlined in this section are a mere first order approximation of the driving force behind the solar-terrestrial environment. The solar interior, surface and atmosphere are orders of magnitude more complex than these brief descriptions suggest, yet the fundamental properties of the Sun and solar wind will be shown to have a profound affect on the occurrence and behaviour of the geomagnetic pulsations that are the focus of this thesis.

1.3 The Near-Earth environment

Magnetically shielded from the supersonic solar wind, the near earth environment is comprised of a mixture of particle species of both solar and terrestrial origin. The dynamics of this region are dependent on chemical composition and relative energy density, which, as shall be seen, are influenced by the Sun. The Earth's intrinsic magnetic field owes its structure to the subterranean rotating flow of molten iron, which generates its dipolar configuration. This magnetic field permeates the entire terrestrial environment yet its effects only really become important when the neutral atmosphere becomes rare, dissociated and ionised, which begins to occur at a height of somewhere between 60 and 100 km. This section seeks to introduce the terrestrial spheres and outline the dominant processes that dictate their behaviour and ultimately govern the ULF waves within.

1.3.1 The Neutral Atmosphere

In contrast to the Sun, the Earth's atmosphere is thin, constrained by gravity and in hydrostatic equilibrium. The Earth's low altitude atmosphere is a turbulent mixture of neutral gases. Neutral winds and tidal forces ensure that atmospheric composition is homogeneous up to the turbopause, where low density allows the gravitational striation of species according to mass. Heating of the atmosphere may occur through a number of kinetic and chemical processes but predominantly occurs by the absorption of solar

radiation. The atmosphere is categorised according to temperature gradient, each distinct gradient region comprising a “sphere”, each gradient reversal being termed a “pause”. Temperature and mass density profiles from the MSIS-E-90 atmospheric model (Hedin, 1991) can be seen in figure 1.8. The figure shows a temperature increase in the stratosphere owing to the absorption of solar ultraviolet radiation by ozone, which is photochemically destroyed at higher altitudes, accounting for subsequent cooling. Above the mesopause, photochemical reactions significantly change atmospheric composition; the main components of which can be seen in figure 1.9. Photo-ionisation also becomes important in this region, where the inhibition of vertical transport sways the balance between ionisation and recombination in favour of ion production, leading to the high altitude formation of the ionosphere. The ionosphere is of great importance to the propagation of ULF waves as it is not only responsible for the measurable perturbations that are registered on the ground but may also cause refraction, ducting and polarisation of the waves that are incident upon it. Discussion of these processes is reserved for Ch. 3; however, the following section describes the basic form and function of the ionosphere.

1.3.2 The Ionosphere

The existence of an electrically conducting atmospheric layer was almost simultaneously predicted by Arthur E. Kennelly (Kennelly, 1902) and Oliver Heaviside (Heaviside, 1902) and was experimentally verified by Sir Edward Appleton in 1925 (Appleton and Barnett, 1925). The nomenclature for the layers of the ionosphere has its basis in the naming of this Electrically conducting “E” layer. Figure 1.8 also shows electron density profiles derived from the IRI-2007 (Bilitza and Reinisch, 2008) ionospheric model for the sub-auroral, summer, day- and night-time ionospheres. The daytime electron density profile exhibits four discernable regions, distinguishable by their density peak or gradient. In this particular profile, the aforementioned E-region peak resides at approximately 100 km, below which is the D-region and above is the F-region, which under heightened conditions is further divided into to the F1- and F2-regions. The local relative concentration of charged species, which under the assumption of charge neutrality translates in to electron density, is determined by the rate of charge creation/annihilation and the transport of its products in to and out of the

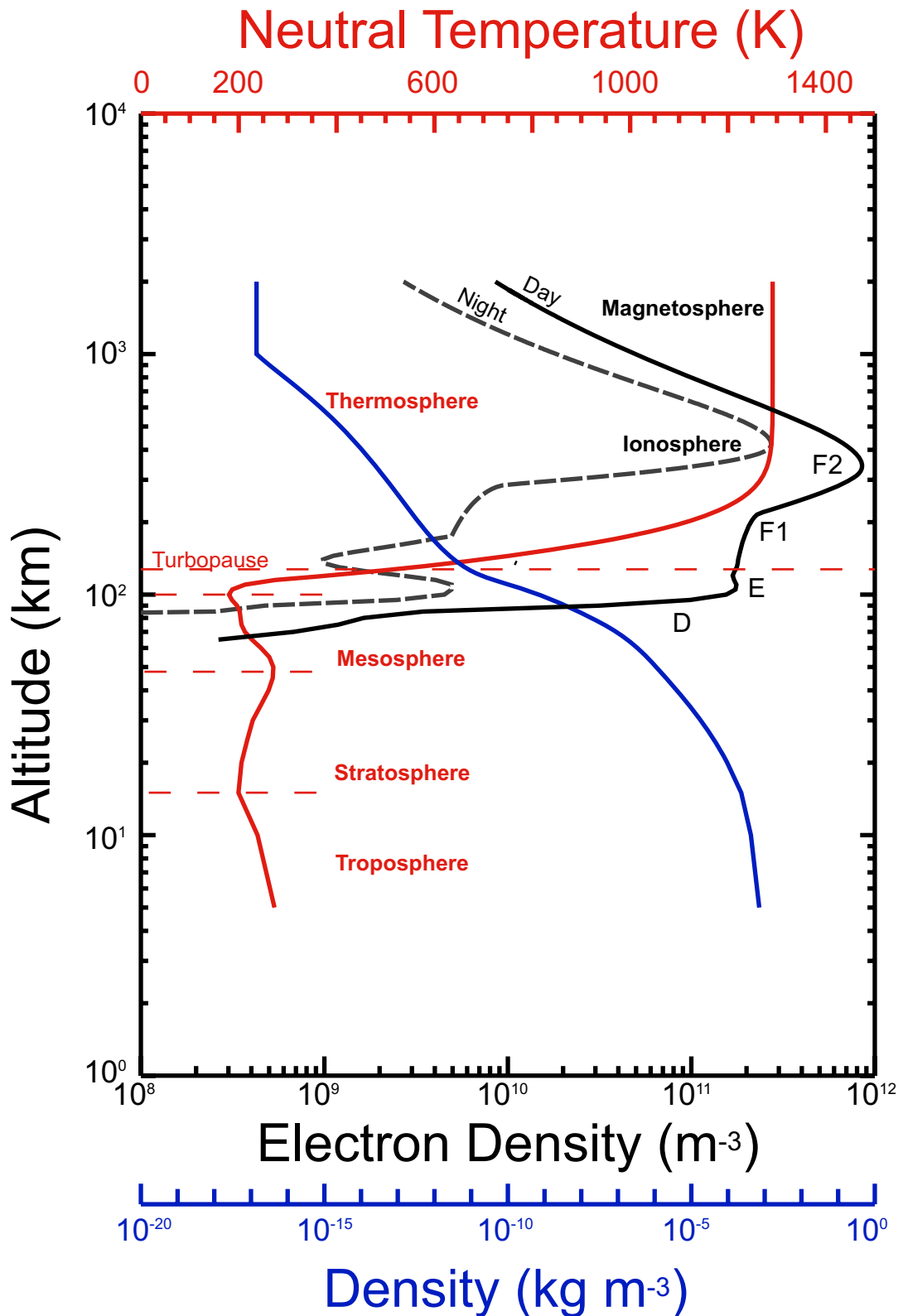


Figure 1.8: Vertical distribution of electron density, neutral temperature and mass density. The boundary of each neutral atmospheric layer is denoted with a red dashed line. The IRI 2007 and the MSIS-E-90 models were used, assuming high solar activity

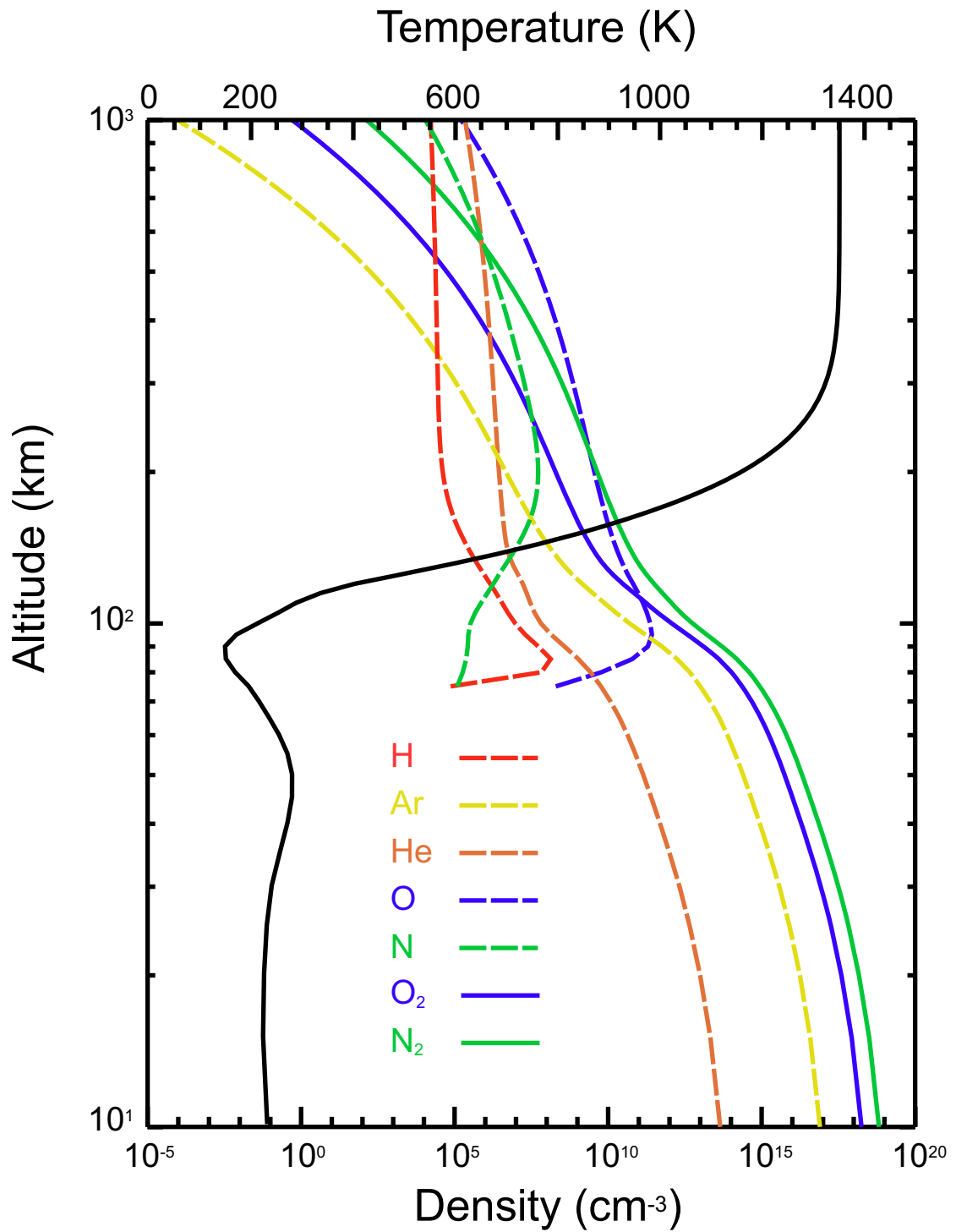


Figure 1.9: MSIS-E-90 atmospheric model neutral temperature (black line) and major atmospheric components. Profiles were obtained from the VITMO online interface, for July 2007 at midday.

region. The contribution of each mechanism varies according to altitude, latitude, local time and level of solar activity.

In the intensely sunlit regions of the upper atmosphere, ionisation predominately occurs via solar Extreme Ultra-Violet (EUV) photon absorption. The rate of photo-ionisation is dependent on the intensity of solar EUV and the concentration of neutral particles. As seen in figure 1.9, neutral particle densities fall rapidly with altitude and as solar radiation incident on the upper atmosphere is absorbed its intensity falls with decreasing altitude. Hence, for each atmospheric species a peak photo-ionisation rate is reached at the height where its neutral density and the solar radiative flux of sufficient energy are optimised.

Figure 1.10 illustrates the altitude at which vertically incident solar radiation in the EUV-UV range is attenuated by e^{-1} (its optical depth). EUV attenuation is due to both photo-ionisation and photo-dissociation. In the upper portion of the figure can be seen the absorption bands of the species important to ionospheric formation. The critical ionisation energies of relevant species are also arrowed beneath the curve. EUV of wavelengths $\lambda > 175$ nm can be seen to penetrate deep in to the atmosphere, where they are involved in the photochemical reactions that shape the aforementioned thermal atmospheric structure (1.3.1). EUV capable of ionising O_2 and NO ($\lambda < 121$ nm) reaches its optical depth at ~ 80 km altitude, where it is responsible for the formation of the D- and E-regions of the ionosphere. Towards the upper boundary of the E-region, photons in the wavelength band $130 \text{ nm} < \lambda < 175 \text{ nm}$ are responsible for the dissociation of O_2 ; atomic oxygen may then be ionised by EUV of $\lambda < 91$ nm, which forms the main constituent of the ionospheric F-region. The relative composition of the ionosphere is presented in figure 1.11, in which can be seen the dominance of molecular NO^+ and O_2^+ ions in the D- and E-regions and atomic O^+ in the F-region. The boundary between the E- and F- regions also marks the transition from a predominantly photochemically driven plasma distribution to one that is governed largely by dynamic processes.

Ionospheric plasma concentration is reduced primarily via two mechanisms; recombination, through a number of reaction paths, and diffusion. Radiative

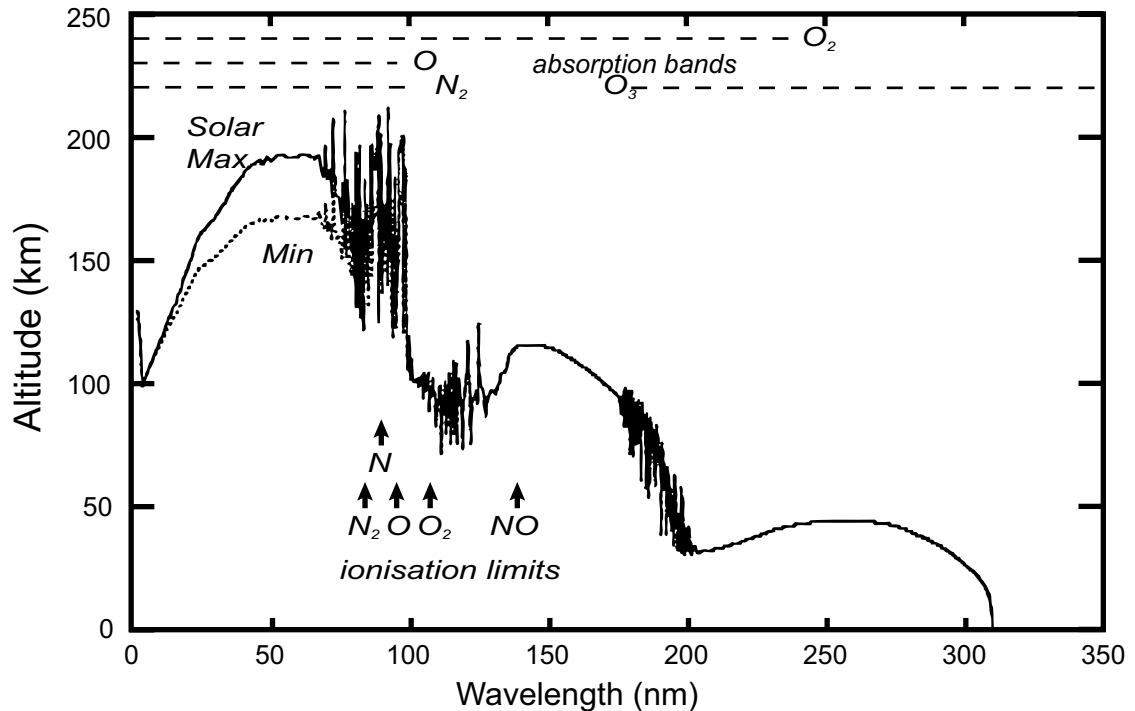


Figure 1.10: Vertical incident solar UV optical depth. The above profile shows the altitude at which UV radiation in the range 0-350 nm is attenuated by e^{-1} . Ionisation thresholds for the major species are indicated with arrows and significant absorption bands are shown with dashed line. After Meier (1991).

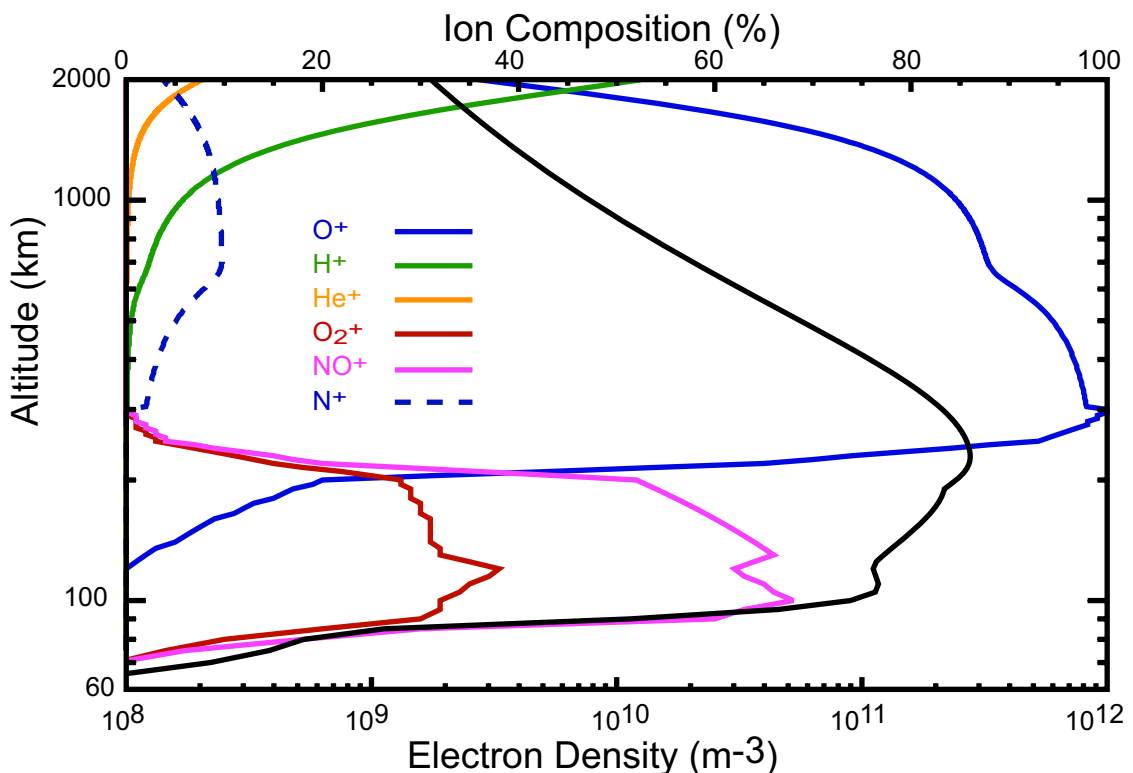


Figure 1.11: IRI-2007 model ion species percentage composition for midday 01/07/2007 at 60° lat, 0° lon (geographic). The profiles highlight the abundance of NO and O₂ ions in the E region and the dominance of O ions in the F-region. The model electron density is also included (black line) to allow ionospheric regions to be identified.

recombination involves an ion directly accepting a free electron, with the resultant surplus energy being emitted in the form of a photon, however, the reaction rate of this process is extremely low and it can be ignored for most of the ionosphere. Dissociative recombination may occur directly, with a molecular ion accepting an electron resulting in two neutral atoms or via a charge exchange in a two-step process that involves the interaction of a positive atomic ion and a neutral to form a molecular ion, which is then dissociated, by the acceptance of a free electron, in to two neutrals.

As seen in figure 1.11 the D- and E-regions are populated with molecular ions that may directly recombine and dissociate, hence, their daytime distributions mirror their ionisation profiles. The relatively large reaction rate of direct dissociative recombination, which is not dependent on neutral concentration, accounts for the practical disappearance of the D- and E-regions during the night. Figure 1.12 is a geographic longitude-latitude contour plot of IRI-2007 model E-region electron density during the boreal summer, which illustrates its global spatial variation. The F-region is characterised by its atomic ion population, however, during periods of heightened solar activity, molecular ions may also be present at its base and the subsequent increase in plasma concentration forms the F1-region, which is subject to the same recombination process that occur at lower altitude. The presence of O^+ ions requires charge exchange for effective dissociative recombination to occur, hence, its recombination rate becomes dependent on the neutral concentration, which decreases with altitude. The formation of the F1-region ultimately depends on the height at which charge exchange recombination dominates direct recombination. The F2-region is composed mainly of O^+ , hence, has a recombination rate that is dependent on neutral concentration, which at such altitudes is rather low. Subsequently, the plasma concentration of the F2-region is relatively stable in the absence of sunlight.

In the high latitude ionosphere, where solar EUV flux is low and geomagnetic field lines are highly inclined, energetic particle precipitation becomes an important source of ionisation. As charged particles spiral along lines of magnetic field (Ch. 2.1.4), they may be guided to ionospheric altitudes, where neutral particle densities and collision frequencies are high. Subsequent collisions may ionise neutral particles through a range of mechanisms, provided that the precipitating particles are of sufficient energy. These collisions are also the origin of the aurorae, as surplus energy in any

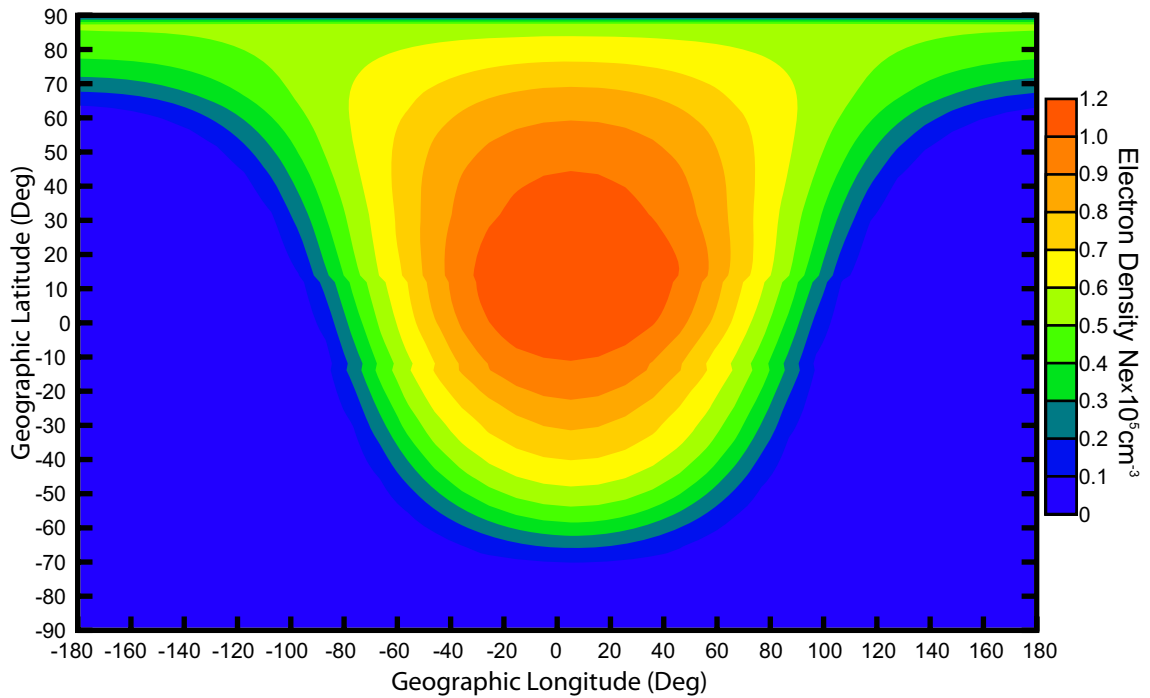


Figure 1.12: Contour plot of the IRI-2007 model global E-region electron density computed for 01/07/2007 at midday and 100 km altitude. The model illustrates the longitude/latitude variation of the E-region density, which is an important factor in the formation the ionospheric duct and the transmission ULF waves to the ground.



Figure 1.13: Auroral display over Spitzbergen. Image taken by S.C.Gane on experimental campaign, 10/03/2007.

collisional process is emitted in the form of a photon. Aurorae serve as a useful diagnostic tool for magnetosphere-ionosphere dynamics as their emitted photons are indicative of the emitting species and their spatial and temporal structure elucidate the dynamics of the regions that geomagnetically map to their location. An example of a structured auroral display may be seen in figure 1.13. The image of green-line, low altitude atomic oxygen aurorae, caused by electron precipitation, was taken at 75.4° north on the Island of Spitzbergen during an experimental campaign in march 2007.

In the topside ionosphere where the aforementioned processes have ionised a significant fraction of the particle population, rapidly decreasing density allows the stratification of species according to mass. As electrons are of significantly lower mass than their surrounding ions they rise to greater altitudes creating a net negative electric charge above a region now filled predominantly with positive ions. The resultant electric field accelerates ions upward and out of the ionosphere. The out-flowing plasma populates the region above the ionosphere where the collision is frequency low enough for geomagnetic dynamics to dominate particle motion; this region is known as the magnetosphere.

1.3.3 The Magnetosphere and associated current systems

As with the solar wind and IMF, the approximately collisionless, perfectly conducting nature of the magnetosphere causes magnetospheric plasma to be “frozen in” to the geomagnetic field. Subsequently, plasma is confined to flow along lines of magnetic field that have their footprints embedded in the partially ionised and collisional ionosphere which rotates with the Earth. Alfvén’s theorem dictates that regions of perfectly conducting plasma, frozen in to distinct and significantly differing magnetic fields may not mix. Consequently, the solar wind is impeded when it reaches the Earth’s magnetosphere, which effectively forms a cavity around which it must flow.

The magnetospheric cavity generates a bow shock upstream in the supersonic solar wind. As solar wind plasma crosses the bow shock it is thermalised, entering the turbulent region known as the magnetosheath. The boundary between the shocked solar wind and the magnetosphere is termed the magnetopause, along which is generated a thin current sheet in response to the regions of differing magnetic field direction and

intensity (Chapman and Ferraro, 1930). Figure 1.14 schematically depicts the principal regions and currents of the near-Earth environment. The bow shock and magnetopause are represented by dark and light blue surfaces respectively. With the sun off to the left, the nearest quarter of the schematic has been removed to reveal the internal structure of magnetosphere, which requires some phenomenological discussion before further description may be given. In an undisturbed terrestrial system, closed to external influences, the high altitude collisionless plasma of the magnetosphere would corotate with the Earth. However, the flow of the solar wind around the Earth introduces convective flows within the magnetosphere.

The dipolar configuration of the terrestrial magnetic field, said to be “closed” as it is isolated from the IMF, becomes distorted under the influence of the solar wind. The dayside magnetopause becomes compressed as its standoff position is dependent on the balance between the dynamic pressure of the solar wind and the magnetic pressure within the magnetosphere. However, where the conditions for frozen in flow are violated, the magnetic fields of the two regimes may merge through the process of magnetic reconnection, in which field lines that are sufficiently forced together and opposed in direction may reconfigure to allow the exchange of plasma between the regions. This situation commonly occurs on the dayside magnetopause, where the scale size of the magnetic field variation across the boundary becomes comparable with the plasma population’s radius of gyration (Ch. 2.1.1). Reconnection allows the IMF to become directly coupled to the geomagnetic field in the region of the cusp, dragging it antisunward over the terrestrial polar caps with the flow of the solar wind and in to the plasma mantle region. This effect, combined with the dynamic pressure of the solar wind, sweeps the nightside geomagnetic field out in to a tail-like configuration. As these lines of geomagnetic field, now “open” to the IMF, travel antisunward they may be closed by reconnection in the equatorial plane of the far magnetotail. Once closed, geomagnetic field lines convect back around to the dayside magnetosphere at lower latitudes completing the cycle first proposed by J. W. Dungey in the early 1960s, which now bears his name.

The Dungey cycle (Dungey, 1961) is depicted in figure 1.15, in which the upper diagram shows lines of interplanetary- and geo-magnetic field as they are reconnected at point 2, dragged over the polar cap in points 3-6 and reconnected in the far

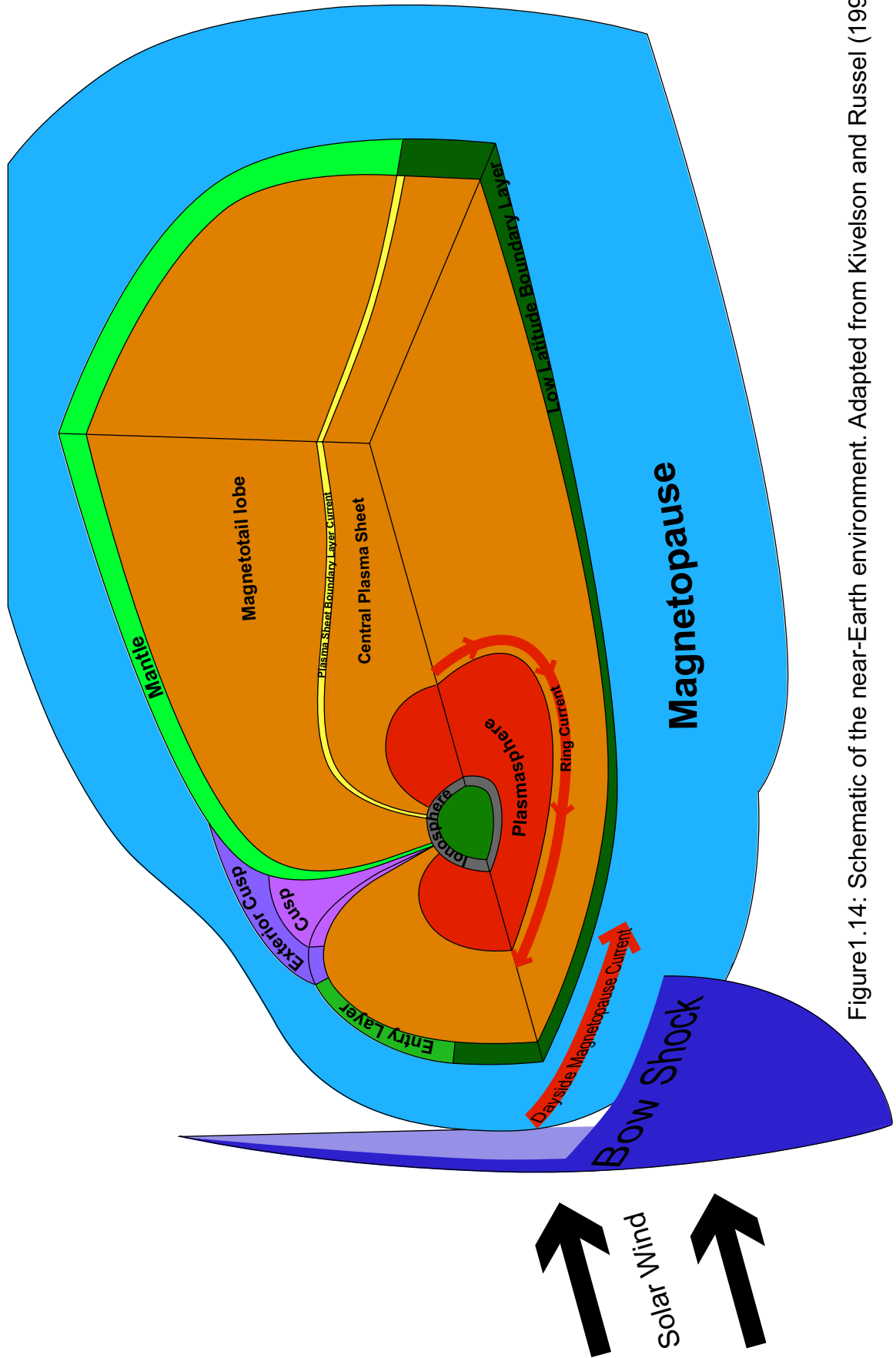


Figure 1.14: Schematic of the near-Earth environment. Adapted from Kivelson and Russel (1995)

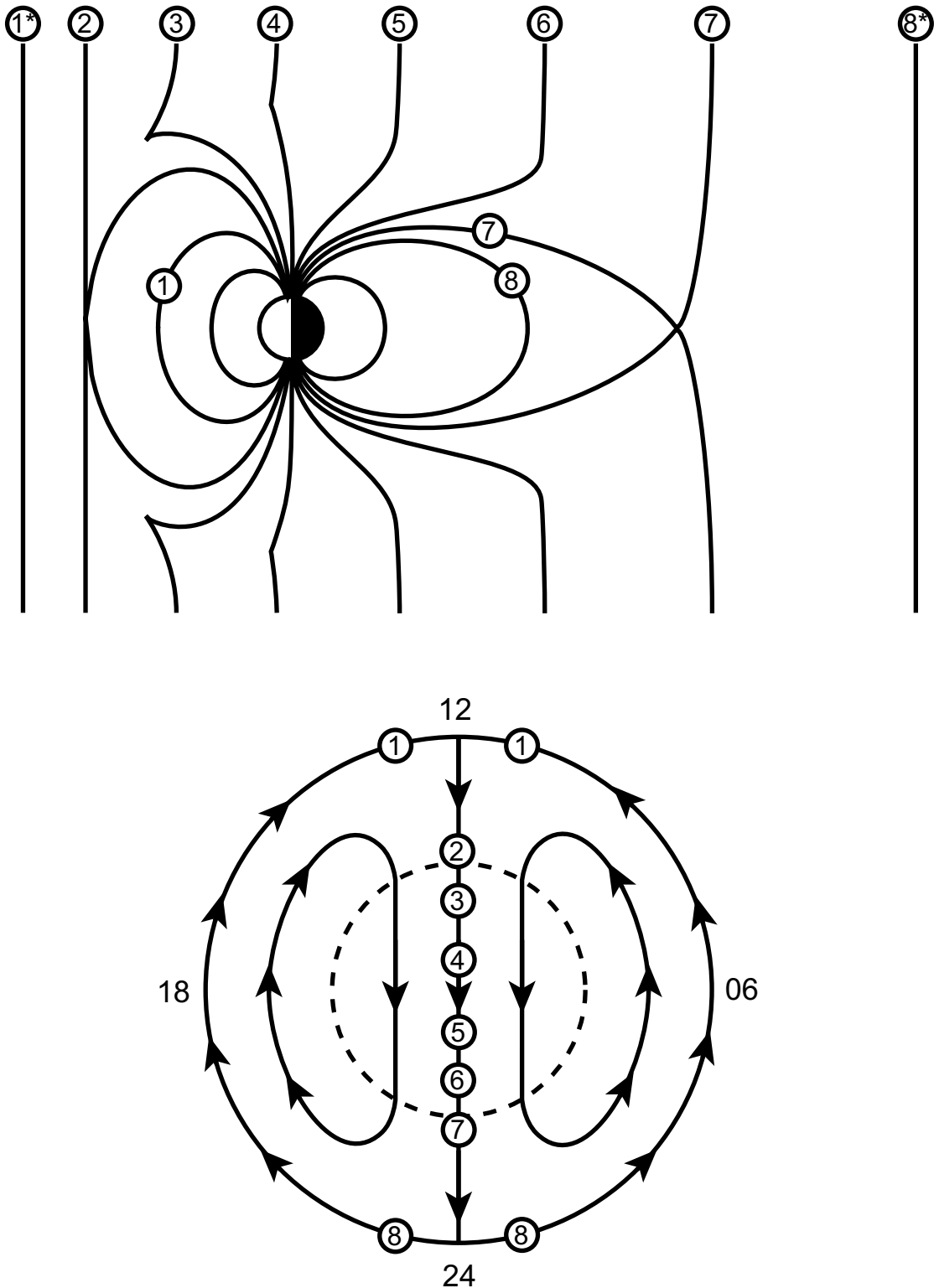


Figure 1.15: Schematic of the Dungey cycle convection pattern, adapted from Baumjohann (1997). The upper diagram depicts field line motion as the IMF reconnects with the geomagnetic field at the dayside magnetopause (2) and drags it anti-sunward (3-6), reconnecting again at the nightside (7). The lower diagram illustrates the ionospheric footprint of the above field lines as they convected anti-sunward over the polar cap then return to the dayside at lower latitudes. The dotted circle denotes the open/closed field line boundary.

magnetotail at point 7. The lower diagram depicts the ionospheric footprints of geomagnetic field lines throughout the Dungey cycle and highlights their lower latitude return to the dayside from point 8, immediately after becoming closed in the magnetotail, to point 1 prior to dayside reconnection, completing a characteristic twin-celled convection pattern. Acceleration of plasma during the reconnection process provides sufficient energy for enhanced particle precipitation to occur. Subsequently, the ionospheric footprints of the return-flow convecting plasma experience increased precipitation leading to enhanced ionisation and auroral generation. These field lines trace out an ionospheric region known as the auroral oval.

The contribution of convection and corotation to magnetospheric plasma flow in the equatorial plane is depicted in figure 1.16, which retains the colour scheme of figure 1.14. The inner region that approximately corotates with the Earth is known as the plasmasphere (coloured red in both figures), in which cold plasma of ionospheric origin becomes trapped (Ch. 2.1.3). Outside this region, Dungey cycle convection strips plasma from the inner magnetosphere and transports it sunward until it reaches the magnetopause where it may be lost to the magnetosheath. This process creates a sharp density gradient at the boundary between the corotating and convecting plasma populations, known as the plasmapause. The location of the plasmapause is dependent on local time and the level of geomagnetic activity as shall be seen in subsequent chapters. In the dusk sector, oppositely directed plasma streams create a region of flow stagnation, known as the plasmaspheric bulge, which causes a local outward migration of the plasmapause. The plasmasphere is of particular interest to this thesis as its trapped ion population plays a vital role in the generation and guidance of the ULF waves studied in subsequent chapters.

Motional plasma induces an electric field perpendicular to its bulk velocity and the magnetic field that permeates it (Ch. 2.1.5). Both convection and corotation induce electric fields, which are represented as blue arrows in figure 1.16. In the corotating plasmasphere the induced electric field is directed earthward, whereas the convective return flows associated with the Dungey cycle induce an electric field that is predominantly directed from dawn to dusk. Similarly, electric fields are induced in the high latitude regions of the magnetosphere and in the ionosphere to which they geomagnetically map.

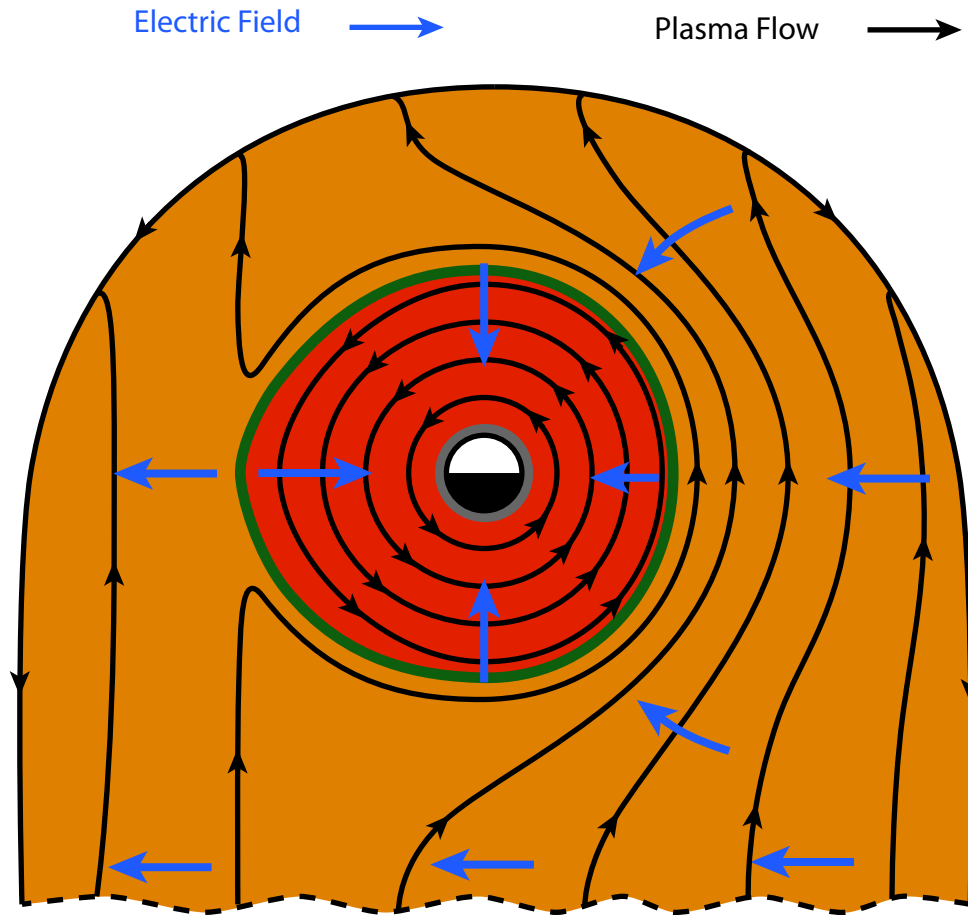


Figure 1.16: Schematic of central plasma sheet convection and electric field, adapted from Kelly (1991) and Baumjohann (1997). The colour scheme is retained from figure 1.14 with the addition of the plasmopause, which is coloured green. The direction of the electric fields associated with corotation inside the plasmopause and convection outside are represented by blue arrows that are not scaled according magnitude.

The ionospheric footprints of the northern-hemisphere high-latitude magnetospheric convection pattern associated with the Dungey cycle are shown again in figure 1.17. The convection-associated electric fields are again represented by blue arrows. The antisunward flow over the pole induces a polar cap electric potential from dawn to dusk, whereas return flows induce electric fields across the auroral oval directed poleward on the dusk side and equatorward on the dawn side.

As the plasma, frozen in to convecting field lines, is dragged through the ionosphere the increase in neutral density with decreasing height drives current systems in the polar cap and auroral zone. Ion/electron drift velocities are dependent on the ratio of gyrofrequency to collision frequency, which in turn are functions of neutral density. The difference in this ratio for electrons and ions leads to a flow of current dependent on their relative mobility (Ch. 2.1.4). These ionospheric currents form loops that are closed through the magnetosphere and are connected via field aligned currents (FAC). Figure 1.17 displays these FAC as circled dots flowing out of the diagram and circled crosses in to the diagram. The region 2 FAC (shaded in green) connects currents flowing across the auroral zone to those in the outer ring current and inner plasma sheet regions. FACs that encircle the open closed field line boundary connect ionospheric currents associated with polar cap convection to tail lobe magnetopause currents and are know as region 1 currents (shaded orange). Together these current flows form the auroral zone current circuit.

1.4 Summary

This chapter has introduced the principal regions of the solar-terrestrial system and outlined the basic processes that drive their behaviour. A description of some of the fundamental plasma dynamics that are important to the rest of this work is given in chapter two. Chapter three will review some of the previous works, upon which the studies that follow are built. Chapter four outlines the instrumentation and acquired data used in chapters five through seven, which contain studies of mid-high latitude ULF pulsations.

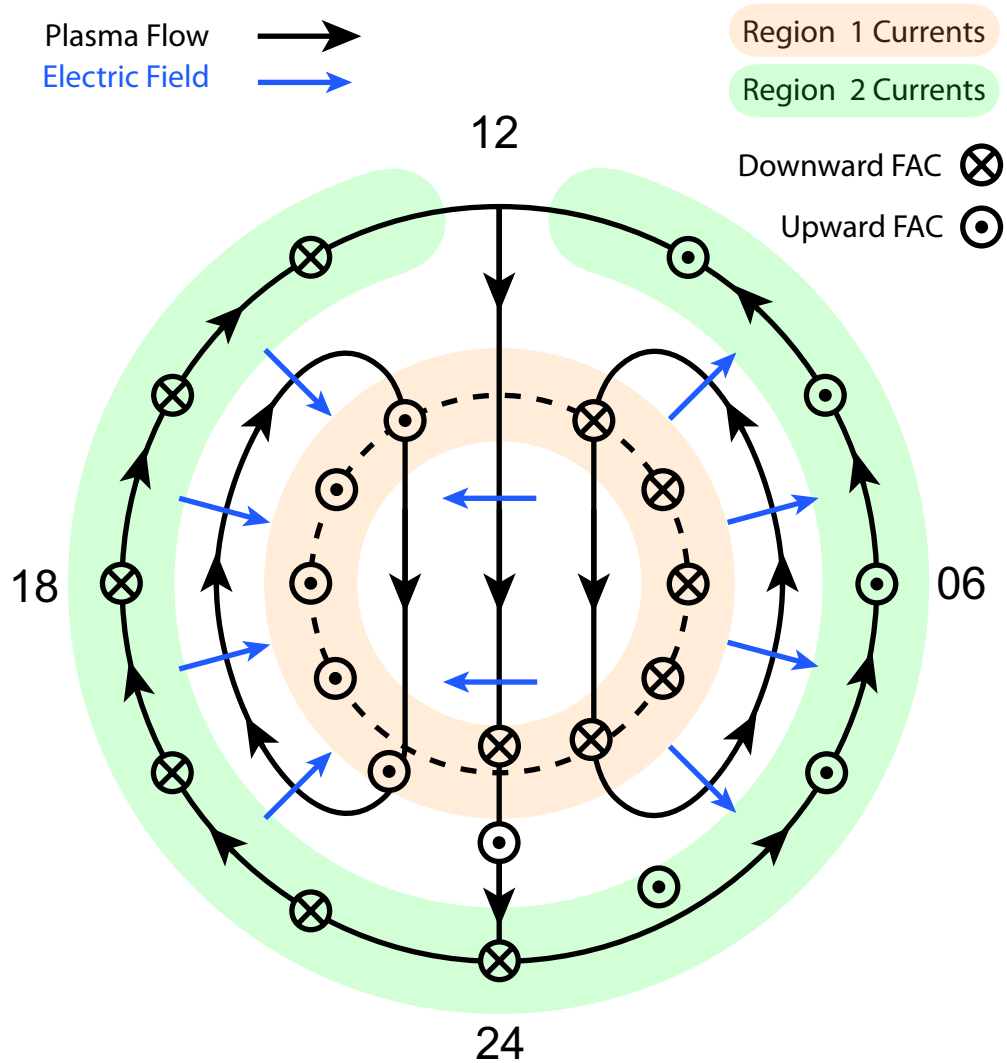


Figure 1.17: Ionospheric flow map of the Dungey cycle convection pattern. Plasma streamlines are indicated by black arrowed lines, electric field direction is given by blue arrows and the open/closed field line boundary is shown as a dotted line. Upward field aligned currents (FAC) are indicated by circled dots, downward by circled crosses. Region 1 and 2 FACs are shaded in orange and green respectively. Adapted from Cowley (2000) and Iijima (2000).

Chapter 2. Plasma Motion and Waves

2.1 Basic plasma dynamics

The plasma populations encountered in the solar-terrestrial environment are highly varied in their density, composition, energy and degree of ionisation. For the case of a tenuous population, such as that of the constant outflow of charged particles from the sun, known as the solar wind, in which collisional frequency is negligible, it is possible to consider the individual motion of each particle when describing the behaviour of that plasma. However, this single particle approach is less useful when considering the macroscopic behaviour of a population in which collective particulate effects become significant and the field generated by the motion of the plasma itself becomes important. This is the case for much of the geophysical plasma encountered in this work for which it is more instructive to treat the plasma as a conducting fluid, considering only bulk properties and collective interactions.

The following section will begin by applying the fundamental laws of particulate motion and the equations of electromagnetism, set out by Maxwell (1865) to the simplest case of a tenuous, uniform, homogenous, quasi-neutral, fully ionised plasma immersed in an electromagnetic field. The illuminating concepts of guiding centre drift and frozen in flux conceived by Alfvén (1942) will be introduced. The principal particle periods and drifts induced by appropriately direct or spatially inhomogeneous fields will be considered and their importance to the following work briefly discussed. Finally, the inclusion of collisions and collective particle behaviour will allow an introduction to the fluid approach of Magnetohydrodynamics (MHD) and the basic wave modes that can arise in a magnetised plasma, providing a basis for that which will follow in subsequent sections.

2.1.1 Charged particle motion in a static electromagnetic field

Introducing the electromagnetic field equations of Coulomb and Lorentz, which govern the forces of a static and motional charge respectively, Newton's second law may be applied to solve for the motion of a charged particle in an electromagnetic field.

The Coulomb force,

$$\mathbf{F}_C = q_s \mathbf{E}, \quad (2.1)$$

experienced by a particle of species s and of charge q_s in an electric field \mathbf{E} and the Lorentz force,

$$\mathbf{F}_{Lm} = q_s (\mathbf{v}_s \times \mathbf{B}), \quad (2.2)$$

felt if that particle is moving in a magnetic field \mathbf{B} , may be combined to form the total Lorentz force law:

$$\mathbf{F}_L = q_s (\mathbf{E} + \mathbf{v}_s \times \mathbf{B}). \quad (2.3)$$

Inserting the Lorentz force in to Newton's second law gives

$$m_s \dot{\mathbf{v}}_s = q_s (\mathbf{E} + \mathbf{v}_s \times \mathbf{B}) + \mathbf{F}_{ex}, \quad (2.4)$$

where \mathbf{F}_{ex} represents the sum of external forces, such as gravitational and centripetal, m_s is the particle's mass and $\dot{\mathbf{v}}_s$ is the time derivative of the particle's velocity. Considering the case of a particle in an x,y,z Cartesian coordinate system, where external forces are negligible ($\mathbf{F}_{ex} = 0$) and the external electric field is everywhere zero ($\mathbf{E} = 0$), equation 2.4 may be rewritten as

$$m_s \dot{\mathbf{v}}_s = q_s (\mathbf{v}_s \times \mathbf{B}). \quad (2.5)$$

Taking the scalar product with \mathbf{v} of both sides:

$$m_s \mathbf{v}_s \cdot \dot{\mathbf{v}}_s = \frac{d}{dt} \left(\frac{1}{2} m_s v_s^2 \right) = q \mathbf{v}_s \cdot (\mathbf{v}_s \times \mathbf{B}) = 0, \quad (2.6)$$

shows that the kinetic energy of the particle is constant. This is physically consistent as no force is being exerted in the direction of motion, thus, no work is being done on the particle. If the external magnetic field is constant and is directed along the z axis ($\mathbf{B} = B\hat{z}$), the components of equation 2.5 may be written as

$$\begin{aligned} m \dot{v}_{ys} &= -qBv_{xs} \\ m \dot{v}_{xs} &= qBv_{ys} \\ m \dot{v}_{zs} &= 0 \end{aligned} \quad (2.7)$$

Taking the second derivative of equations (2.7) yields:

$$\begin{aligned} \ddot{v}_{ys} &= -\left(\frac{q_s B}{m_s} \right)^2 v_{ys} \\ \ddot{v}_{xs} &= -\left(\frac{q_s B}{m_s} \right)^2 v_{xs} \end{aligned}, \quad (2.8)$$

which are equations for the simple harmonic motion of v_{xs} and v_{ys} with angular frequency, Ω_{cs} :

$$\Omega_{cs} = \frac{q_s B}{m_s}, \quad (2.9)$$

It can be seen that Ω_{cs} , the principal gyrofrequency or cyclotron frequency, is independent of particle velocity and is a function of the particle's mass, charge and the applied magnetic field only. It is also apparent that the sign of the cyclotron frequency is dependent on the charge of the particle, implying that oppositely charged particles gyrate in opposite directions when immersed in the same magnetic field. The period of gyration, T_c , given by

$$T_{cs} = \frac{2\pi}{\Omega_{cs}}, \quad (2.10)$$

is the first of three fundamental periods of importance to the understanding of the behaviour of charged particles in a magnetic field. Gyration about the focal point, known as the guiding centre occurs with radius r_c , dictated by the particle's gyrofrequency and velocity perpendicular to the ambient magnetic field v_{\perp} :

$$r_{cs} = \frac{v_{\perp s}}{\Omega_{cs}}. \quad (2.11)$$

This is displayed in figure 2.1 for the case of an electron and a proton, each of energy 10 keV in a magnetic field of strength of 500 nT, similar to that of the inner regions of the magnetosphere.

Having described basic gyromotion in a plane perpendicular to the ambient magnetic field, it is now possible to consider the behaviour of a charged particle when its parallel velocity is non-zero and the fields present result in quasi-consistent accelerations that may modify both micro- and macro-scopic behaviours.

2.1.2 Charged particle motion in a magnetic field

The electric and magnetic fields that permeate the terrestrial environment induce a variety of motions, or drifts, in the particle populations that flow through them. These so-called drifts are responsible for much of the morphology and behaviour of the

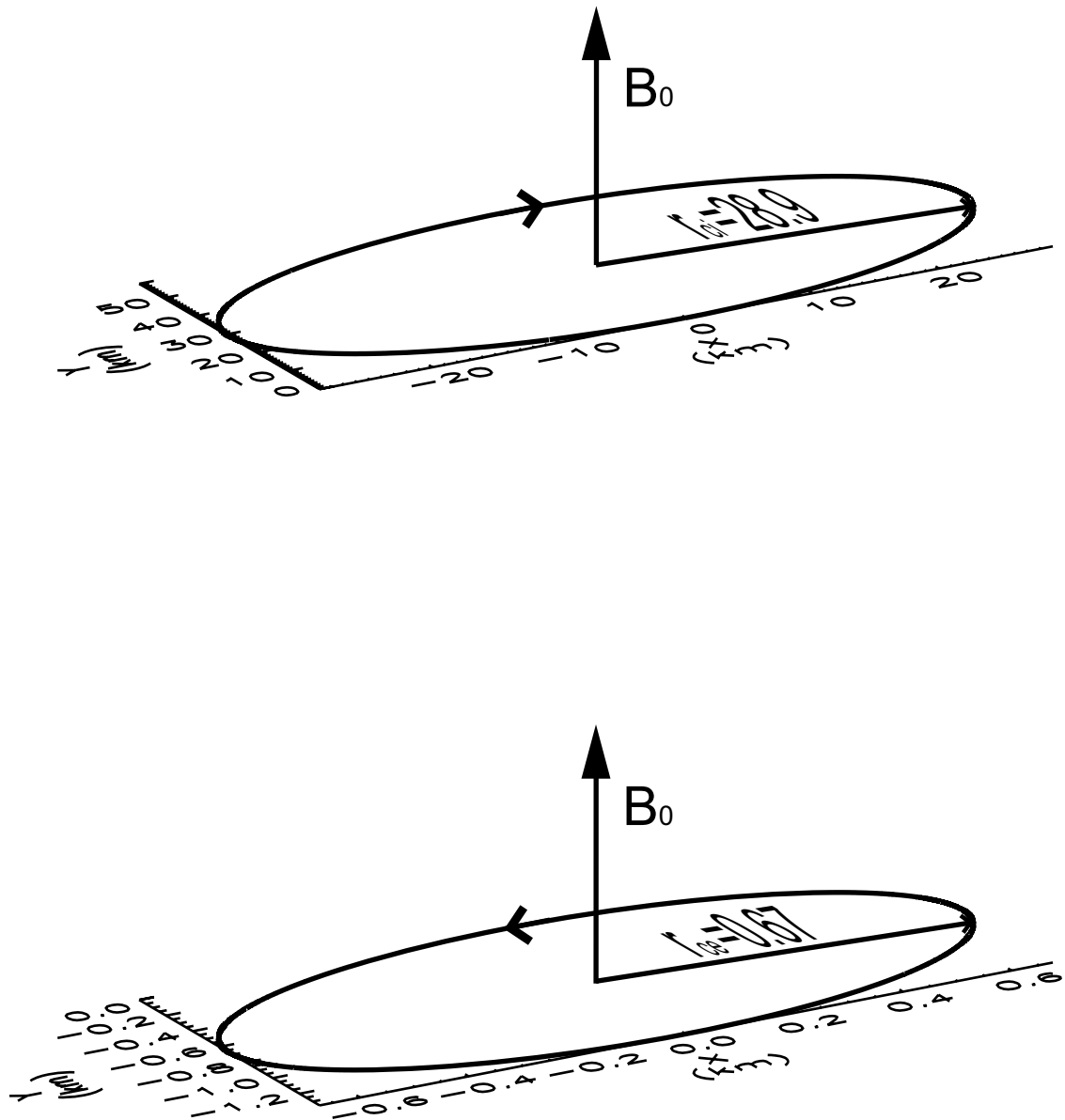


Figure 2.1: Charged particle gyration in a magnetic field. A 10 keV proton (upper panel) and electron (lower panel) are immersed in a 500 nT magnetic field. Arrows indicate the direction of gyration, which is opposite for each species.

ionosphere-magnetosphere system; this section will outline the induced motions of most importance to this thesis.

When an electric field, \mathbf{E} , is present, each particle experiences a coulomb acceleration as described by equation 2.1. As has been shown, particle motion parallel to a static, homogeneous magnetic field is independent of that field. Hence, when an electric field is directed parallel or antiparallel to the ambient magnetic field, particle acceleration may occur in an unrestricted manner. As mobility along \mathbf{B} is unhampered, ions and electrons are rapidly accelerated in opposite directions, creating a charge separated potential field that equally opposes the electric field inducing it. The geophysical consequence of this mechanism is that: it may be assumed that if the parallel component of any electric field, E_{\parallel} , is sustained for long enough to invoke a full response from the charges within, it will quickly vanish. However, if \mathbf{E} has a component perpendicular to \mathbf{B} , E_{\perp} , then the acceleration experienced by a particle will affect its perpendicular velocity and subsequently its gyroradius. Extending the scenario of section 2.1.1 to include a non-zero perpendicular electric field, the equations of harmonic motion given in equations 2.7 must now include a coulomb term as per the total Lorentz force law, equation.2.3, the components of which are

$$\begin{aligned} m_s \dot{v}_{xs} &= q_s B v_{ys} + q_s E_x \\ m_s \dot{v}_{ys} &= -q_s B v_{xs} + q_s E_y . \\ m \dot{v}_z &= q_s E_z \end{aligned} \quad (2.12)$$

For an electric field directed entirely along x ($\mathbf{E} = E_x$) it can be seen from the first of equations 2.12 that the influence of the coulomb term will be to accelerate for half a harmonic cycle and decelerate for the other half. Subsequently, the particle's resultant perpendicular velocity and gyroradius will increase for half a cycle, then decrease for the remaining half. This periodic modification of gyroradius leads to a guiding centre drift in the y direction, perpendicular to both the magnetic and electric fields and is commonly termed the E cross B drift which has the general form

$$\mathbf{V}_E = \frac{\mathbf{E} \wedge \mathbf{B}}{B^2} . \quad (2.13)$$

Apparent from equation 2.13, the $\mathbf{E} \wedge \mathbf{B}$ drift is independent of particle charge and mass; hence, the presence of a static, homogenous, perpendicular electric field does not induce a current in a collisionless plasma. This is displayed in figure 2.2, which adopts

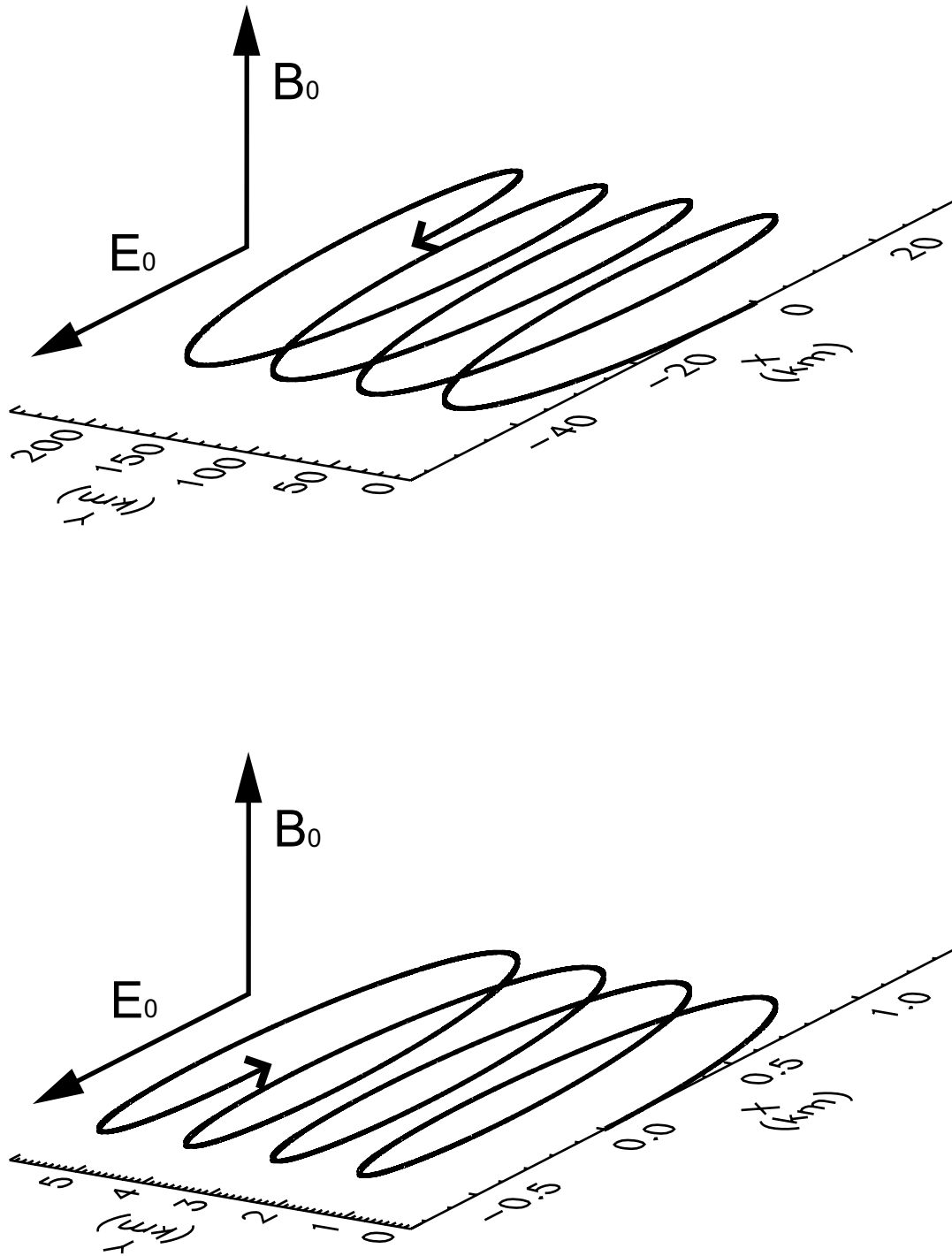


Figure 2.2: Charged particle motion subject to static magnetic and electric fields. Both proton (upper panel) and electron (lower panel) drift in the same direction, orthogonal to E and B , at the same velocity. A magnetic field of 500 nT and electric fields of 0.2 Vm^{-1} and 9.0 Vm^{-1} were used respectively.

the same parameters as figure 2.1 with the addition of a non-zero perpendicular electric field.

Inhomogeneity in the ambient magnetic field may also produce a drift that, as with the electric drift, \mathbf{V}_E , is perpendicular to both field and the direction of the imposing force. Considering again the case of 2.1.1, this time with a magnetic field that increases in strength in the positive x direction, it can be seen from equation 2.9 and 2.11 that as the particle oscillates in the x direction its gyroradius sinusoidally increases and decreases. This periodic modification of gyroradius again causes a drift in the y direction. This resultant drift, \mathbf{V}_g , may be generalised as

$$\mathbf{V}_{gs} = \left(\frac{1}{2} m_s v_{\perp s}^2 \right) \frac{\mathbf{B} \wedge \nabla B}{q_s B^3}. \quad (2.14)$$

where the ∇ operator denotes field gradient. This scenario is displayed in figure 2.3, which again retains the parameters of figure 2.1, with the addition of a magnetic field gradient in the positive x direction. Equation 2.14 shows that this, so called, gradient drift, which is the first of the magnetic drifts that shall be considered, is dependent on particle charge and thus does induce a current flow. It should be noted here that the bracketed term in equation 2.14 is the particle's perpendicular thermal kinetic energy.

The second magnetically induced motion of consequence to geophysical plasmas arises from the parallel velocity of a particle's trajectory in a curved field, which is of great importance when considering motion in the earth's approximate dipolar field geometry. If a particle's guiding centre follows a curved path then it will be subject to a centrifugal force directed away from the instantaneous focus of its curvature. The contribution of this force to the equation of particle gyromotion will cause an increase in gyroradii in the half cycle furthest from the centre of curvature and, conversely, a decrease in the closest half cycle; again causing a drift in the direction perpendicular to both field and curvature radius, \mathbf{R}_c . This centrifugal force may be represented as

$$\mathbf{F}_{cs} = m_s v_{\parallel s}^2 \frac{\mathbf{R}_c}{R_c^2}, \quad (2.15)$$

which, through Coulomb's law, may be substituted for \mathbf{E} in equation 2.13 yielding:

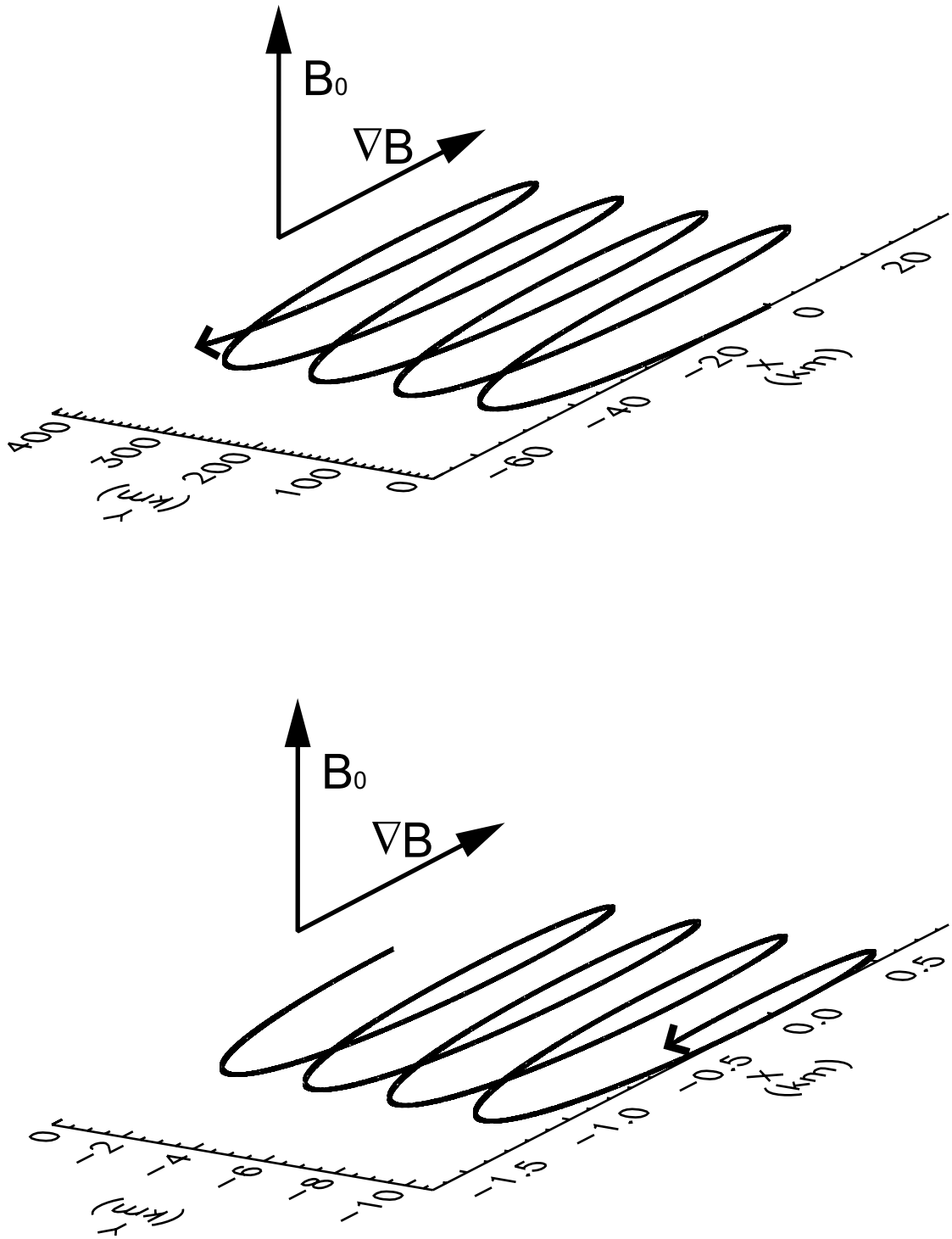


Figure 2.3: Charged particle motion in a magnetic field gradient directed in the positive x direction. Particle drift is opposite for a proton (upper panel) and an electron (lower panel), hence a current flow is induced.

$$\mathbf{V}_{cs} = \frac{2}{q_s} \left(\frac{1}{2} m_s v_{\parallel s}^2 \right) \frac{\mathbf{R}_c \wedge \mathbf{B}}{R_c^2 B^2}. \quad (2.16)$$

This curvature drift, \mathbf{V}_c , much like \mathbf{V}_g , is dependent on particle charge and again contributes to an induced current flow; however, it is parallel thermal energy in this case that governs its magnitude. In the case of the earth's inner, equatorial magnetosphere, it is reasonable to assume cylindrical field symmetry, in which case:

$$-\nabla B = \frac{B}{R_c^2} \mathbf{R}_c. \quad (2.17)$$

This assumption and subsequent substitution of equations 2.17 into 2.16, allows a total magnetic drift velocity to be expressed as the sum of the two aforementioned drifts:

$$\mathbf{V}_{Bs} = \mathbf{V}_{gs} + \mathbf{V}_{cs} = \left(v_{\parallel s}^2 + \frac{1}{2} v_{\perp s}^2 \right) \frac{\mathbf{B} \wedge \nabla B}{\Omega_{cs} B^2}. \quad (2.18)$$

This total magnetic drift, which is, ultimately, dependent on total particle energy is the origin of the magnetospheric ring current.

2.1.3 Adiabatic processes

The motions described so far have taken place in static fields in which energy and momentum have remained constant or have varied according to generalised force laws. In physically reasonable plasmas, it is also possible for certain parameters, known as adiabatic invariants, to remain constant in a varying field, provided that the characteristic time and length scales of their variation are longer than those for the mode of motion concerned. There is an adiabatic invariant associated with each of the principal magnetospheric particle motions; however, only the first and second invariants are of significant importance to this work. Consequently, the discerning reader is directed to such texts as (Baumjohann *et al.*, 1997, Kivelson and Russell, 1995) for details of the third invariant.

Defining the first invariant, μ , the magnetic moment of gyration, as perpendicular kinetic energy over magnetic field magnitude:

$$\mu_s = \frac{\frac{1}{2} m_s v_{\perp s}^2}{B} = \text{CONSTANT}, \quad (2.19)$$

it follows that the magnetic flux through the surface bound by one complete gyration is also constant under the adiabatic condition. Given magnetic flux, ϕ , as

$$\phi_s = \oint B \cdot \hat{n} dA = B \pi r_{cs}^2 \quad (2.20)$$

and inserting equations 2.9, 2.11 and 2.19 yields

$$\phi_s = \frac{2\pi m_s}{q_s^2} \mu_s = \text{CONSTANT} . \quad (2.21)$$

Equations 2.20 and 2.21 suggest that as the ambient magnetic field strength increases, the square of the gyroradius must decrease accordingly. The implications of this invariance are vast and are applicable to most of the regions dealt with in this work. Equation 2.19 implies that, if no field induced acceleration occurs and total kinetic energy is conserved, a particle moving in to a region of increasing field strength will experience an increase in perpendicular velocity and subsequent decrease in parallel velocity. This may continue until all kinetic energy is contained within the perpendicular component, rendering parallel velocity zero, at which point, the mirror point, the particle's parallel trajectory is reversed and it is said to be mirrored. This is depicted in figure 2.4, where magnetic field lines (coloured blue) converge towards the top of the figure. The particle's parallel velocity and gyroradius can be seen to decrease as the mirror point is reached. Magnetic mirroring is responsible for the trapping of the magnetospheric particles, which "bounce" between conjugate reflection points in opposite hemispheres as they flow along magnetospheric field lines that converge in the polar regions. This process is effective wherever the increase in field strength is great enough to balance a particle's parallel velocity, significant temporal variations occur much slower than particle gyration and spatial variations occur over a length scale that is much greater than particle gyroradius.

Assuming a magnetospheric field topology that is reasonably symmetrical, particles will bounce periodically between hemispheres with a frequency determined by their parallel velocity and the length of field line between conjugate mirror points. The second adiabatic invariant, J , is conserved along the particle's closed bounce trajectory:

$$J = \oint m v_{\parallel} ds = 2lm \langle v_{\parallel} \rangle . \quad (2.22)$$

Hence, a change in the length of the field-line to which a particle is bound evokes a change in average parallel velocity.

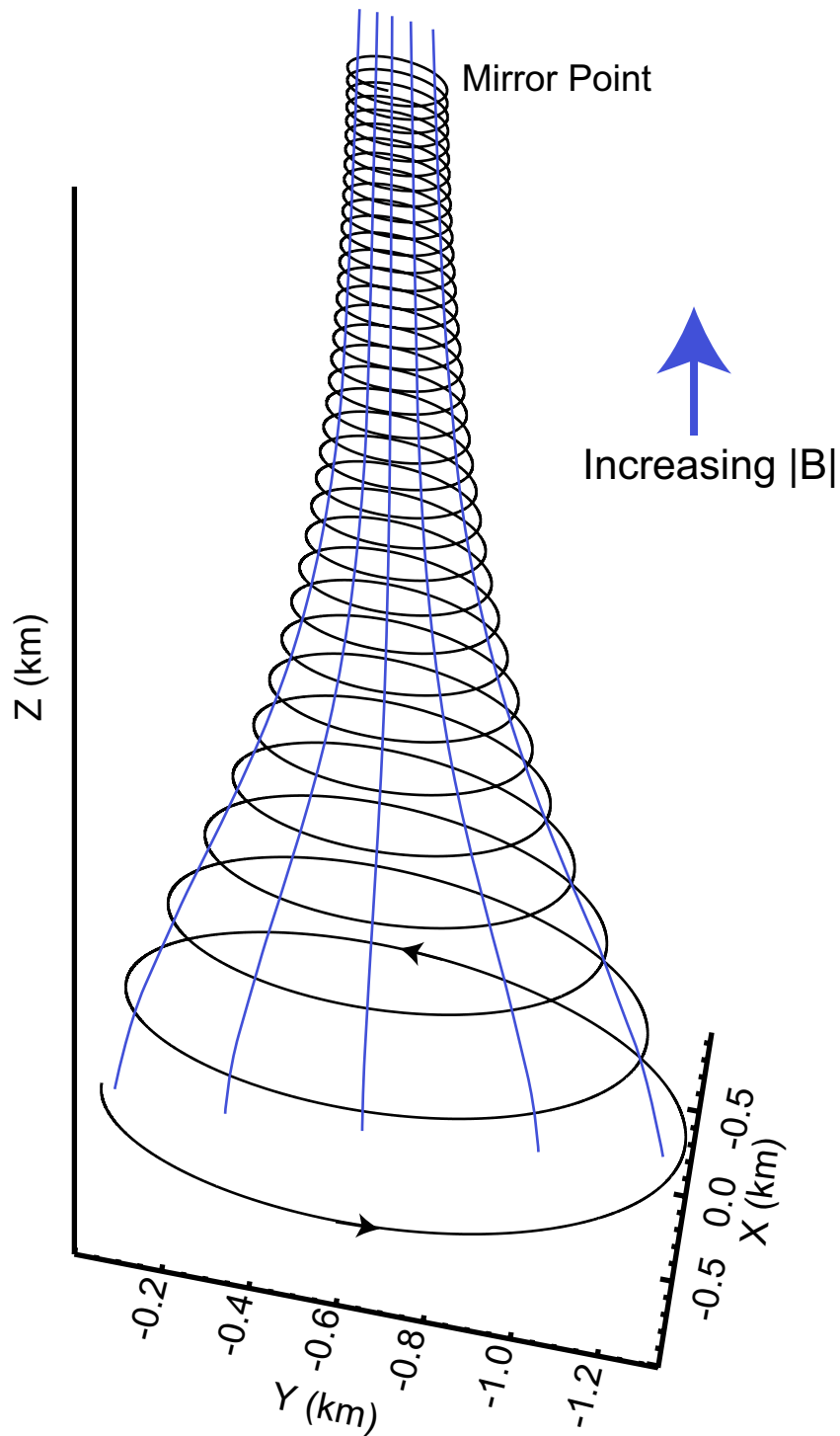


Figure 2.4: Charged particle motion in a static electric and converging magnetic field. Field lines are shown in blue and particle trajectory is in black, arrows indicate the direction of travel and increase in field strength. As the particle enters a region of higher field strength its gyroradius and parallel velocity are reduced up to the mirror point where it is reflected.

2.1.4 Ideal behaviour

For an ionised gas to behave as an idealised plasma its components must act freely and it must appear externally quasi-neutral. For this to occur, a balance must be maintained between the thermal motions of the particle population and the electrostatic potentials felt by each particle's nearest neighbour. The characteristic length over which this is true is the Debye length, λ_D , which is the distance from a given charge that its electrostatic potential is shielded by the collective potentials of its surrounding particles. Assuming that ion and electron temperatures are approximately equal, $T_i = T_e$, as is assumed of charge carrier densities, $n_i = n_e$, for a singly ionised gas such as a proton-electron plasma the Debye length is given by

$$\lambda_D = \left(\frac{\epsilon_0 k_B T_e}{n_e e^2} \right)^{\frac{1}{2}}, \quad (2.23)$$

where ϵ_0 , is the permittivity of free space and k_B is the Boltzmann constant. For the quasi-neutral approximation to hold in a real plasma the physical dimensions of the regime must be much larger than the Debye length and the number of charges in the spherical volume of radius λ_D , the Debye sphere, must be large enough for collective screening to occur. This is true for the majority of the solar terrestrial environment, however, as the boundaries that separate plasma regions are approached these conditions are violated and the approximation breaks down. If these conditions are met, each element of the plasma will respond to an externally driven perturbation by oscillating about its equilibrium position with a natural frequency, the plasma frequency, given for each species by

$$\omega_{ps} = \frac{n_s q_s^2}{\epsilon_0 m_s}. \quad (2.24)$$

This plasma frequency is of integral importance to the propagation of waves through a plasma; it also has a profound effect on the behaviour of a plasma when collisions are considered. The freely acting particle condition for treatment as an idealised plasma may still be satisfied in a collisional regime, provided that the collision frequency, ν_c , of its components is much smaller than its plasma frequency. Consideration of collision frequency also allows the introduction of a plasma conductivity, σ_0 , as

$$\sigma_0 = \frac{n_e e^2}{m_e \nu_c}. \quad (2.25)$$

This assumes a flow of mobile electrons in a wash of torpid ions and can be seen to tend to infinity as collision frequency tends to zero, implying that a collisionless plasma has infinite conductivity.

Whether a plasma is partially or fully ionised, the inclusion of collisions alters the equation of motion, which must subsequently include a collisional, or frictional, term. The external force term in equation 2.4 consequently takes the form

$$\mathbf{F}_{ex} = -m_e \nu_c \mathbf{v}_e, \quad (2.26)$$

the Langevin force, which makes no distinction between the coulomb collisions of a fully ionised plasma and the neutral collision of a partially ionised plasma, hence, holds true for any degree of ionisation provided that the appropriate collision frequency is used. Consequently, in a magnetised plasma, the inclusion of collisions introduces anisotropy to current flow, which again is assumed to be carried entirely by the relatively mobile electrons and is described by

$$\mathbf{j} = -en_e \mathbf{v}_e. \quad (2.27)$$

However, in a magnetised plasma Ohm's law takes the form:

$$\mathbf{j} = \sigma_0 (\mathbf{E} + \mathbf{v}_e \wedge \mathbf{B}). \quad (2.28)$$

Thus combining equations 2.25 - 2.27 yields

$$\mathbf{j} = \sigma_0 \mathbf{E} - \frac{\sigma_0}{n_e e} \mathbf{j} \wedge \mathbf{B}, \quad (2.29)$$

which, in a system where the ambient magnetic field is directed along the z axis, may be represented simply as Ohm's law:

$$\mathbf{j} = \sigma \cdot \mathbf{E}, \quad (2.30)$$

where σ is the conductivity tensor given by

$$\sigma = \begin{pmatrix} \sigma_P & -\sigma_H & 0 \\ \sigma_H & \sigma_P & 0 \\ 0 & 0 & \sigma_{||} \end{pmatrix}, \quad (2.31)$$

with elements:

$$\begin{aligned}
\sigma_P &= \frac{v_c^2}{v_c^2 + \Omega_{ce}^2} \sigma_0 \\
\sigma_H &= -\frac{\Omega_{ce} v_c}{v_c^2 + \Omega_{ce}^2} \sigma_0 \cdot \\
\sigma_{\parallel} &= \sigma_0
\end{aligned} \tag{2.32}$$

Each tensor element governs current flow in one of three directions relative to the electric and magnetic fields. σ_P is the Pedersen conductivity that controls the current flow in the direction of that component of the electric field, E_{\perp} , that is perpendicular to the magnetic field. σ_H is the Hall conductivity and controls current flow orthogonal to both the electric and magnetic fields and σ_{\parallel} is the parallel conductivity that governs the field aligned current induced by the parallel electric field, E_{\parallel} . In an arbitrary coordinate system, equations 2.30 - 2.32 may be written as

$$\mathbf{j} = \sigma_{\parallel} \mathbf{E}_{\parallel} + \sigma_P \mathbf{E}_{\perp} - \sigma_H \frac{(\mathbf{E}_{\perp} \wedge \mathbf{B})}{B}. \tag{2.33}$$

The dependence of the Pederson, Hall and parallel current on the ratio of gyro to collision frequency, displayed in figure 2.5 using an electron density value typical of the terrestrial ionosphere, shows that in a predominantly collisional regime conductivity becomes isotropic. As collisions decrease, conductive anisotropy is introduced as electrons are increasingly permitted to $\mathbf{E} \wedge \mathbf{B}$ drift before each collision. This anisotropy is maximised when the collision and gyro frequencies are matched, as electrons impact once per gyration and drifts in both the \mathbf{E}_{\perp} and the $(\mathbf{E}_{\perp} \wedge \mathbf{B})$ directions resulting in drift motion 45° to both. As collision frequency decreases further, both Pedersen and Hall conductivities fall and thus only parallel conductivity remains. This implies that in a collisionless regime current flow is solely field aligned and charge carrying particles therefore travel exclusively parallel to the magnetic field line about which they gyrate.

2.1.5 A Fluid approach

Having touched briefly on the bulk behaviour of a collection of charged particles in the presence of an electromagnetic field, a further step may now be taken towards the MHD description by treating the plasma as a conducting fluid. It is also assumed that

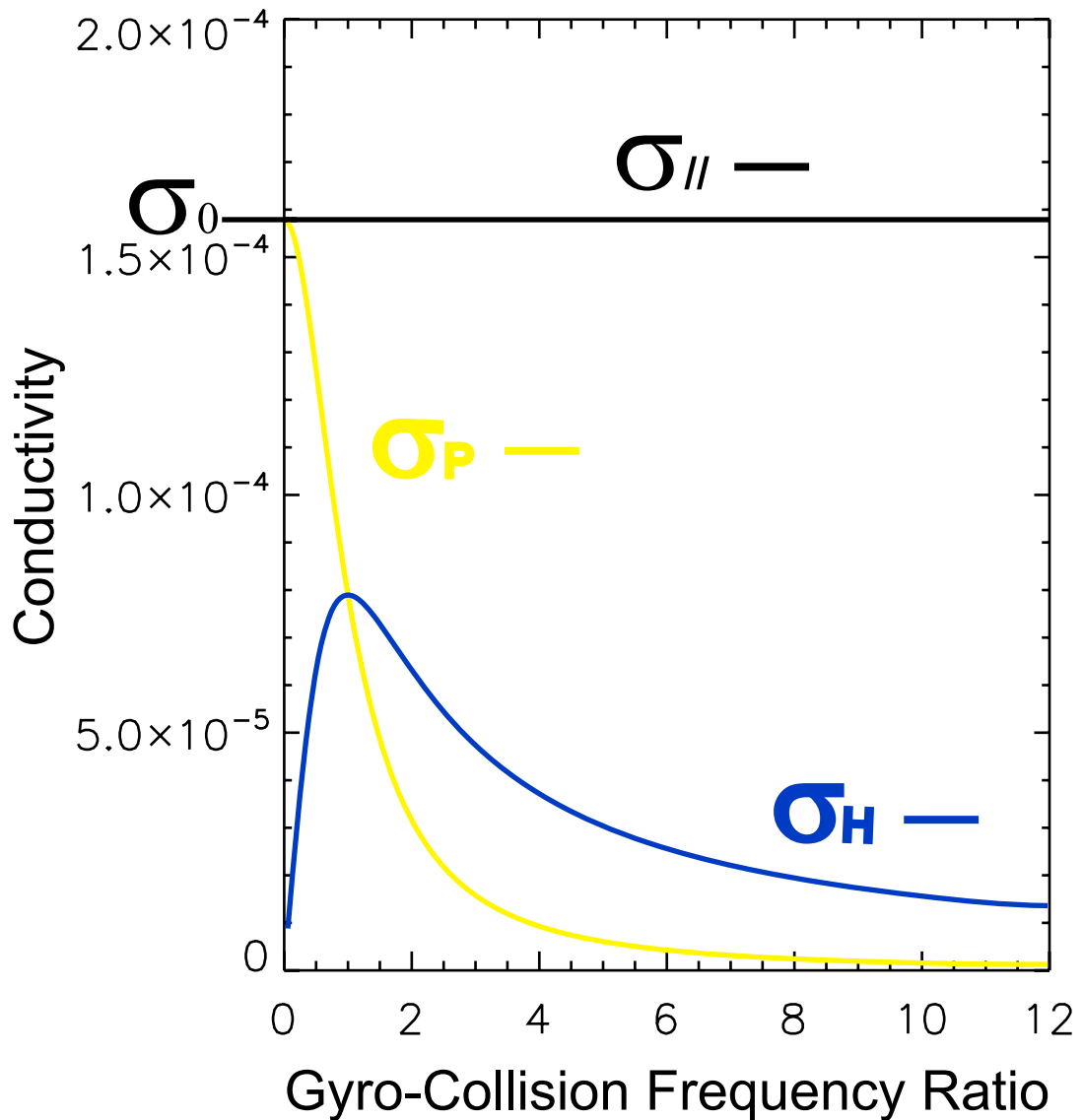


Figure 2.5: Dependency of the Parallel, Hall and Pederson conductivities on the gyro-collision frequency ratio. Each curve was generated using a typical ionospheric electron density value of $n_e = 10^5 \text{cm}^{-3}$.

electromagnetic variations are slow compared to particle gyrofrequencies, the low frequency limit approximation, and that less important spatial derivatives may be replaced with characteristic scale lengths. These approximations allow the electromagnetic laws of Maxwell and Ohm to be used in harmony with the equations of fluid mechanics that govern the continuous flow of a medium without the need for full knowledge of particle distribution functions.

The notion of field line guided motion may be further extended by introducing the concepts of magnetic diffusion and frozen in flux. As has been discussed, in the absence of strong field gradients and curvature, collisions and external forces, a particle is bound to gyrate about the magnetic field line on which it resides, with net motion only permitted in the parallel direction. Consequently, if a magnetic field is externally forced to reconfigure, its plasma population will remain “frozen” to their field lines and reconfigure with it. The converse may also be true; when a plasma population is externally forced, it may drag the magnetic field with it. The motion of a “frozen in” (Alfven, 1942) plasma is, therefore, dictated by the balance between the magnetic and kinetic energies of its field and particles. The degree to which the frozen in flow approximation holds is very much dependent on the length scale over which variation in the magnetic field occurs and the characteristic conductivity and relative perpendicular plasma velocity. To illustrate this point, three of Maxwell’s equations must be introduced, in their differential form. Firstly, Faraday’s Law of electromagnetic induction:

$$\nabla \wedge \mathbf{E} = -\frac{\partial \mathbf{B}}{\partial t}, \quad (2.34)$$

which relates the rate of change of magnetic field on a given surface to the circulation, or curl, of the electric field around the closed loop that encircles it. Secondly, the Ampere-Maxwell Law:

$$\nabla \wedge \mathbf{B} = \mu_0 \mathbf{j} + \varepsilon_0 \mu_0 \frac{\partial \mathbf{E}}{\partial t}, \quad (2.35)$$

where ε_0 and μ_0 are the permittivity and permeability of free space, relates the flow of conduction and displacement currents through a surface to the curl of the magnetic field around its bounding curve. Thirdly, Gauss’s law for magnetism:

$$\nabla \cdot \mathbf{B} = 0, \quad (2.36)$$

which states that the net flux, or divergence, of magnetic field through a closed surface must be zero. Ultimately, this means that no magnetic sources or sinks may exist and that all magnetic field lines must be closed loops. Solving the generalised form of Ohm's law, equation 2.29, for the electric field and the Ampere-Maxwell law, equation 2.35, for current, neglecting the displacement term in the low frequency limit, allows the restatement of Faraday's law as

$$\frac{\partial \mathbf{B}}{\partial t} = \nabla \wedge (\mathbf{v} \wedge \mathbf{B}) + \frac{\nabla^2 \mathbf{B}}{\mu_0 \sigma_0}, \quad (2.37)$$

where \mathbf{v} is the bulk plasma velocity and the vector identity A.1 and Gauss's law for magnetism have also been used. This general induction equation for a magnetised plasma describes the relationship between the rate of change of magnetic field, the motion of the plasma within and the spatial diffusion of that field. It can be seen that for a stationary plasma of finite conductivity this expression of generalised induction simply becomes a diffusion equation:

$$\frac{\partial \mathbf{B}}{\partial t} = \frac{\nabla^2 \mathbf{B}}{\mu_0 \sigma_0}, \quad (2.38)$$

describing the tendency of the magnetic field to homogenise throughout the plasma. Conversely, for a collisionless plasma of infinite conductivity, the induction equation becomes

$$\frac{\partial \mathbf{B}}{\partial t} = \nabla \wedge (\mathbf{v} \wedge \mathbf{B}), \quad (2.39)$$

which, implies that any change in magnetic field will be met with a change in plasma motion. In this frozen in limit, the divergenceless flux condition, set by Gauss's law for magnetism, not only applies to the magnetic field but to the motion of the particles that are bound to it. This gives rise to the concept of flux tubes along which plasma may flow freely, provided that the surface they intersect obeys the conservation of magnetic flux. It is possible here to demonstrate equivalence between the single particle approach of sections 2.1.1 – 2.1.3 and the present bulk representation by substituting Faraday's law back in to equation 2.39 to yield

$$\mathbf{E} = -\mathbf{v} \wedge \mathbf{B}. \quad (2.40)$$

This relation shows that an electric field is generated in response to a movement of plasma, generally known as the convection electric field, and conversely that when an electric field is present a velocity is induced. However, this also shows that, in the

absence of collisions, no parallel electric field may exist, as the cross product result of plasma flow parallel to the magnetic field is zero.

A useful metric for how a plasma might be expected to behave is the magnetic Reynolds number, which is the ratio of the convective to diffusive components of a plasma. The general induction equation (2.37) may be restated in dimensional form as

$$\frac{B}{\tau} = \frac{VB}{L_B} + \frac{B}{\mu_0 \sigma_0 L_B^2}, \quad (2.41)$$

where B is the mean magnetic field strength, τ and L_B are the characteristic time and length scales over which field variations occur and V is the average plasma velocity perpendicular to the field. From this, the Magnetic Reynolds number may be taken as

$$R_m = \mu_0 \sigma_0 L_B V. \quad (2.42)$$

Given that plasma flow speeds in the solar-terrestrial environment are usually limited to $\sim 10^6 \text{ m s}^{-1}$ (Baumjohann *et al.*, 1997, Cliver *et al.*, 1990) and are generally much smaller, the magnitude of the magnetic Reynolds number is predominately controlled by the values of conductivity and scale length. When $R_m \gg 1$, a plasma is flow dominated and the frozen in flux approximation holds well. However, as R_m nears unity, magnetic field diffusion becomes important and may begin to dominate plasma behaviour. Typically, R_m is large for regions such as the solar wind and terrestrial magnetosphere, where scale sizes and conductivities are great. However, in regimes of high collision frequency, low velocity and small scale size such as the terrestrial ionosphere and plasma boundary regions R_m frequently becomes less than 1 and the frozen in approximation breaks down.

The simplicity of the fluid approach is that it allows the determination of the bulk parameters of interest, namely density, velocity, temperature and pressure, without the need to evaluate the full kinetic equation of motion over all space. It does, however, require a number of simplifying assumptions that render its application inappropriate to all but the most accommodating of regimes, fortunately a number of regions of interest to the present study are indeed relatively accommodating. In its simplest form, MHD assumes that a plasma consists of a single-species, conducting, quasi-neutral fluid, where mass, momentum and energy are conserved. In order for this to occur the fluid

variables for each species of the real proton-electron plasma being considered must be combined as follows. Fluid number density, n , becomes

$$n = \frac{m_e n_e + m_i n_i}{m_e + m_i}, \quad (2.43)$$

fluid mass, m :

$$m = m_i \left(1 + \frac{m_e}{m_i} \right), \quad (2.44)$$

fluid velocity, \mathbf{v} :

$$\mathbf{v} = \frac{m_e n_e \mathbf{v}_e + m_i n_i \mathbf{v}_i}{m_e n_e + m_i n_i}, \quad (2.45)$$

and fluid pressure, p :

$$p = n_e k T_e + n_i k T_i. \quad (2.46)$$

Similarly, the macroscopic charge and current become

$$\rho_c = e(n_e - n_i), \quad (2.47)$$

$$\mathbf{j} = e(n_e \mathbf{v}_e - n_i \mathbf{v}_i). \quad (2.48)$$

Given the further assumption that the plasma is devoid of creation or annihilation mechanisms, which is not necessarily the case as noted in the heliospheric and ionospheric discussions, the fluid continuity equation may be stated as

$$\frac{\partial n}{\partial t} + \nabla \cdot (n \mathbf{v}) = 0, \quad (2.49)$$

which relates the rate of change of number density to net particle flux. The partial derivative is used here as only the temporal variation of n is of concern. The conservation of momentum may also be stated, following a similar argument, as

$$\frac{\partial \rho_m \mathbf{v}}{\partial t} + \nabla \cdot (\rho_m \mathbf{v} \mathbf{v}) = -\nabla P + \rho_c \mathbf{E} + \mathbf{j} \wedge \mathbf{B} + n \mathbf{F}_{ex}, \quad (2.50)$$

where $\rho_m = nm$. This MHD equation of motion balances the rate of change and net flux of fluid momentum to the sum of the forces acting upon it. These forces consist of a plasma fluid pressure, an electric, a magnetic and an external force term. Consideration of the magnetic, or Hall, term reveals two unique attributes of magnetised fluids, those of magnetic pressure and tension. As with the derivation of the generalised induction equation above, in the low frequency limit, the Ampere-Maxwell law may be used with the aid of vector identity A.2 to yield

$$\mathbf{j} \wedge \mathbf{B} = -\nabla \frac{B^2}{2\mu_0} + \frac{\nabla \cdot \mathbf{B}\mathbf{B}}{\mu_0}. \quad (2.51)$$

The first term on the RHS adds to the existing thermal pressure with a magnetic pressure, defined as

$$P_B = \frac{B^2}{2\mu_0}. \quad (2.52)$$

The second term is generally known as magnetic tension, which exerts a force antiparallel to the radius of curvature of a given field line; this ultimately has the affect of straightening field curvature. This term becomes extremely important when field lines are highly contorted and can be responsible for dramatically changing the energy distribution in a plasma population. Another useful metric in ascertaining the behaviour of a plasma is the ratio of thermal to magnetic pressures, β :

$$\beta = \frac{2\mu_0 P}{B^2}. \quad (2.53)$$

The value of the plasma beta parameter reveals if the assumption that the kinetic affects that complicate the equation of plasma motion may be ignored is valid. When $\beta \ll 1$ magnetic pressure dominates, as β approaches unity kinetic affects and associated currents become important.

To enable complete prescription of a plasma, knowledge of energy conservation must be obtained. To simplify this treatment, energy distribution assumptions are usually made. The isothermal or adiabatic assumptions may be applied, in which cases the equation of state, equation 2.46, allows the use of $p \propto \rho_m$ or $p \propto \rho_m^\gamma$ respectively, where γ is the ratio of specific heats.

2.2 Magnetohydrodynamic waves

ULF waves provide a significant mechanism for the transfer of energy throughout the solar-terrestrial environment. Determination of their properties allows inference on the nature of their driving mechanism and medium through which they propagate. Although much of the geospace environment consists of hot, inhomogeneous, multi-component plasma, some illumination is provided by considering the simplest case of wave

propagation through a cold uniform medium. The following section briefly outlines sufficient theory to allow meaningful discussion of the phenomenological studies in subsequent chapters. For thorough treatments of MHD waves, the interested reader is directed to such text as (Alperovich and Fedorov, 2007, Walker, 2005, Guglielmi and Pokhotelov, 1996, Stix, 1992).

2.2.1 MHD dispersion relation

Knowledge of the dispersion relationship between frequency and wavenumber allows the determination of allowed propagation modes and their properties. It is possible to derive the general MHD dispersion relation in the following manner. The MHD equation of motion may be simplified by assuming macroscopic charge neutrality, i.e. $\rho_c = 0$, and that external forces are in balance, i.e. $\mathbf{F}_{ex} = 0$. Subsequently, in the frame of the bulk plasma flow, equation 2.50 reduces to

$$\rho_m \frac{d\mathbf{v}}{dt} = \mathbf{j} \wedge \mathbf{B} - \nabla p. \quad (2.54)$$

The Ampere-Maxwell law in the low frequency limit can then be used to eliminate current, resulting in an equation containing the four parameters ρ_m , \mathbf{B} , p and \mathbf{v} :

$$\rho_m \frac{d\mathbf{v}}{dt} = -\nabla \left(p + \frac{B^2}{2\mu_0} \right) + \frac{(\mathbf{B} \cdot \nabla)}{\mu_0} \mathbf{B}. \quad (2.55)$$

The equation of continuity (2.49) may also be combined with the adiabatic assumption and rearranged to give

$$\frac{dp}{dt} = -\gamma p \nabla \cdot \mathbf{v}. \quad (2.56)$$

Similarly, Faraday's law (2.34) may be combined with the convection electric field equation (2.40) and vector identity A.3 to yield

$$\frac{\partial \mathbf{B}}{\partial t} = \mathbf{B} \cdot \nabla \mathbf{v} - \mathbf{B} \nabla \cdot \mathbf{v}. \quad (2.57)$$

By further assuming that wave amplitudes are small, equations 2.55 to 2.57 may be linearised by representing variations as perturbations about the equilibrium values of the four parameters above:

$$\begin{aligned}
\rho_m &\rightarrow \rho_{m0} + \rho_m \\
\mathbf{v} &\rightarrow \mathbf{v} \\
\mathbf{B} &\rightarrow \mathbf{B} + \mathbf{b} \\
p &\rightarrow P + p
\end{aligned}
, \quad (2.58)$$

and ignoring small second order terms, which yields

$$\rho_{m0} \frac{d\mathbf{v}}{dt} = -\nabla \left(P + \frac{\mathbf{B} \cdot \mathbf{b}}{\mu_0} \right) + \frac{(\mathbf{B} \cdot \nabla)}{\mu_0} \mathbf{b}, \quad (2.59)$$

$$\frac{dp}{dt} = -\gamma P \nabla \cdot \mathbf{v}, \quad (2.60)$$

$$\frac{\partial \mathbf{b}}{\partial t} = \mathbf{B} \cdot \nabla \mathbf{v} - \mathbf{B} \nabla \cdot \mathbf{v}. \quad (2.61)$$

By taking the time derivative of 2.59 and subsequently using 2.60 and 2.61 to eliminate ρ_m and p , a second order equation is formed:

$$\rho_{m0} \frac{\partial^2 \mathbf{v}}{\partial t^2} = \nabla \cdot \left\{ \left(\gamma P + \frac{B^2}{\mu_0} \right) \nabla \cdot \mathbf{v} - \left(\frac{\mathbf{B}}{\mu_0} \cdot (\mathbf{B} \cdot \nabla) \mathbf{v} \right) \right\} - \frac{1}{\mu_0} (\mathbf{B} \cdot \nabla) \{ \mathbf{B} \nabla \cdot \mathbf{v} - (\mathbf{B} \cdot \nabla \mathbf{v}) \}. \quad (2.62)$$

Assuming spatial uniformity and that all waves sinusoidally vary according to $e^{i(\mathbf{k} \cdot \mathbf{r} - \omega t)}$, where \mathbf{k} and \mathbf{r} are the wave and position vectors and $\mathbf{k} = k \hat{\mathbf{n}}$, with $\hat{\mathbf{n}}$ the direction of propagation, then equation (2.62) reduces to

$$\left\{ \omega^2 - (\mathbf{k} \cdot \mathbf{V}_A)^2 \right\} \mathbf{v} - \mathbf{k} (V_A^2 + C_s^2) \mathbf{k} \cdot \mathbf{v} + (\mathbf{k} \cdot \mathbf{V}_A) \{ \mathbf{k} (\mathbf{V}_A \cdot \mathbf{v}) + \mathbf{V}_A (\mathbf{k} \cdot \mathbf{v}) \} = 0, \quad (2.63)$$

where V_A and C_s are the Alfvén and sound velocities given in Ch. 1.2.2.

In wave normal coordinates, equation 2.63 can be expressed in matrix form as

$$\begin{pmatrix} \omega^2 - k^2 V_A^2 \cos^2 \theta & k^2 V_A^2 \cos^2 \theta \\ -k^2 V_A^2 \sin^2 \theta & \omega^2 - k^2 (V_A^2 \cos^2 \theta + C_s^2) \end{pmatrix} \begin{pmatrix} v_T \\ v_L \end{pmatrix} = 0, \quad (2.64)$$

$$(\omega^2 - k^2 V_A^2 \cos^2 \theta) v_y = 0, \quad (2.65)$$

where the background field is in the z direction, the wavevector is in the x-z plane, v_T and v_L are the transverse and longitudinal components of velocity and θ is the angle between the wavevector and background magnetic field.

These two decoupled dispersion relations may be written as

$$\omega^2 - k^2 V_A^2 \cos^2 \theta = 0, \quad (2.66)$$

which represents the transverse Alfvén mode and

$$\omega^4 - \omega^2 k^2 (C_{ms}^2) - k^4 V_A^2 C_s^2 \cos^2 \theta = 0, \quad (2.67)$$

the magnetosonic mode, where $C_{ms}^2 = V_A^2 + C_s^2$ is the magnetosonic speed. The phase velocity of these modes may then be found directly in case of the Alfvén mode as

$$\mathbf{V}_{ph,A} = V_A \cos \theta \quad (2.68)$$

and for the magnetosonic mode by solving the resultant quadratic as

$$\mathbf{V}_{ph,ms}^2 = \frac{1}{2} \left[(C_{ms}^2) \pm \left((C_{ms}^2)^2 - 4V_A^2 C_s^2 \cos^2 \theta \right)^{\frac{1}{2}} \right]. \quad (2.69)$$

From this result it can be seen that two possible phase velocities exist for the magnetosonic mode known as the slow and fast modes. The phase velocities of all three wave branches are shown diagrammatically in figure 2.6 for the case where the Alfvén speed is greater than the sound speed. The solid lines trace out the velocity of each wave mode as a function of the angle between their wavevector and the background magnetic field. The diagrams clearly show the quasi-isotropic nature of the fast magnetosonic mode and the restriction on the slow and Alfvén modes to propagate mainly in the direction of the background magnetic field. The phase velocity anisotropy introduced by the presence of the background field is of great importance when considering geomagnetic pulsations which may potentially propagate in any of the possible wave modes.

2.2.2 Geomagnetic pulsations

Geomagnetic pulsations have been recorded and actively studied for over two hundred years (Saito, 1969), yet there remains a great deal of information on the solar-terrestrial environment entangled in their behavior that is still to be revealed. ULF pulsations are those that have frequencies that are generally lower than the characteristic natural frequencies of the near-space environment. They may be categorised according to the IAGA classification system (IAGA, 1981), seen in table 2.1, in to irregular and continuous pulsations and then subcategorised according to their period of oscillation. ULF pulsations are generally indicative of their source region and generation mechanism and can be simplistically categorised in to those which are driven directly by mechanisms external to the magnetosphere and those that are driven internally;

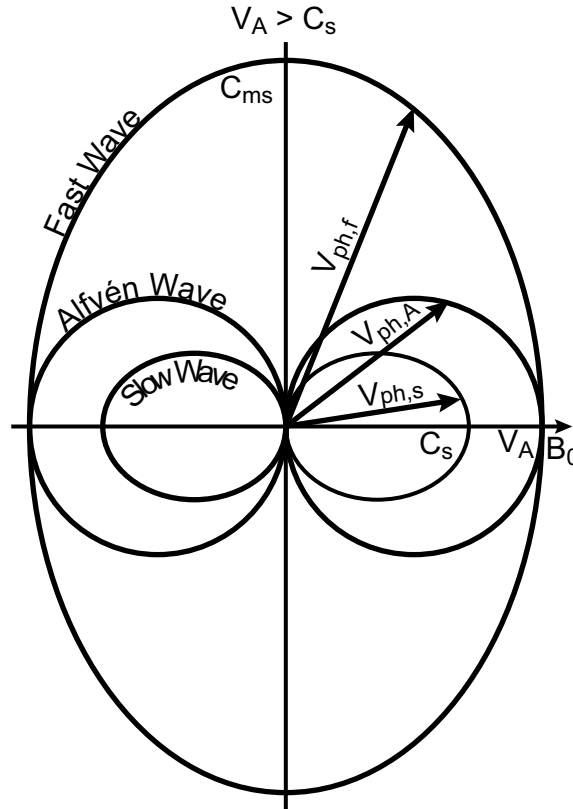


Figure 2.6: Phase velocity diagrams for the Alfvén, fast and slow MHD propagation modes as functions of their angle to the background magnetic field, B_0 . $V_{ph,A}$, $V_{ph,s}$ and $V_{ph,f}$ represent phase velocity vectors of the three modes and V_A , C_s and C_{ms} are the Alfvén, sound and magnetosonic speeds. The diagram represents the case where the Alfvén velocity of the medium is greater than its sound speed.

Continuous Pulsation (Pc)		Irregular Pulsations (Pi)	
Classification	Period (s)	Classification	Period (s)
Pc1	0.2 - 5	Pi1	< 1 - 40
Pc2	5 - 10	Pi2	40 - 150
Pc3	10 - 45	Pi3	150 +
Pc4	45 - 150		
Pc5	150 - 600		
Pc6	600+		

Table 2.1: The IAGA pulsation classification scheme. Pulsations are categorised according to their continuous or irregular nature and then by period of oscillation.

although, often more than one driving mechanism is responsible for pulsations within a given frequency band.

Compressional or “poloidal mode” Pc5 pulsations oscillate in a plane that intersects the magnetic poles (Orr, 1973). Such waves, with moderate azimuthal wave numbers (Where azimuthal wave number is defined as the number of degrees of change in phase per degree of longitude), may be induced by drift (drift-bounce) resonance interactions and are subsequently directly internally driven (Southwood, 1973). Toroidal mode Pc5 pulsations oscillate perpendicularly to the magnetic meridian and are considered to be fundamental mode Field Line Resonances (FLRs), driven by external coupling processes such as solar wind buffeting on the dayside magnetopause, Kelvin-Helmholtz instabilities on the magnetopause flanks and dayside magnetic reconfigurations (Orr, 1973).

Poloidal mode Pc4 pulsations are thought to be a consequence of drift-bounce resonance of freshly injected ions, possessing a non-Maxwellian distribution function, during substorm activity, which may occur at some harmonic of the fundamental FLR mode (Mann *et al.*, 1997).

Pc1-2 pulsations are generated by ion cyclotron resonance in a number of regions of the solar-terrestrial environment and are discussed in more detail in the following section.

2.2.3 Electromagnetic Ion Cyclotron Waves

So far, discussion has been made of wave propagation in magnetised plasmas without consideration of the kinetic effects of individual particles. To enable further discussion of the Pc1-2 pulsations in subsequent chapters, consideration must be made of the case where wave frequency approaches the local ion cyclotron frequency, enabling wave particle interaction and the transfer of energy between the regimes.

When an electromagnetic wave is incident on a charged particle gyrating about an ambient magnetic field, there may be a significant exchange of energy and momentum between the two. This exchange of energy becomes efficient if the

frequency of the wave matches the particle's gyrofrequency and their senses of rotation are the same. This resonance condition may be stated as

$$\omega - \mathbf{k} \cdot \mathbf{V}_{\text{ph}} = \Omega_c. \quad (2.70)$$

For the case of a positive ion, gyrating anti-clockwise about an ambient magnetic field, a left-hand circularly polarised wave of the appropriate frequency, Doppler shifted in to the frame of the ion, travelling in the opposite direction, appears to have a stationary electric field. Hence, the ion may be accelerated or decelerated, in the direction perpendicular to its guiding centre trajectory. Such waves are known as ElectroMagnetic Ion Cyclotron (EMIC) waves. Perpendicular acceleration of this nature causes a change in the particles pitch angle, α , which is defined as

$$\alpha = \tan^{-1} \left(\frac{V_{\perp}}{V_{\parallel}} \right). \quad (2.71)$$

This pitch angle scattering can have a significant effect on the distribution of ion velocities in populations such as those comprising the terrestrial ring current. A decrease in pitch angle may lead to a particle failing to mirror at the top of the ionosphere, subsequently penetrating to a depth where it may be collisionally lost.

Whether wave growth or damping occurs may be determined by considering the anisotropy of the ion population, which is defined as the ratio of perpendicular to parallel ion temperatures. When the value of anisotropy is high, typically greater than 1, instability can occur leading to wave growth. A classic example of this is in the recovery phase of a geomagnetic storm where EMIC wave interaction provides a mechanism for anisotropic ring current particles to be lost to the ionosphere.

2.3 Summary

This chapter has briefly introduced the basic principles that govern the near-space environment. By considering the fundamental equations of charged particle motion in a magnetic field it has been shown that when it is convenient to do so a magnetised plasma may be treated as fluid. It has also been shown that such a plasma may support wave modes that are capable of transporting energy both parallel and perpendicular to the ambient magnetic field. The simplifications to observational inference that a fluid

approach allows have been noted; however, the necessity for consideration of individual particle contribution to dynamical processes has been noted. It is hoped that the concepts discussed here will aid meaningful discussion of the studies within this thesis and the previous works on geomagnetic pulsations that are reviewed in the following chapter.

Chapter 3. Review of Pc1-2 Studies

Observations of the short period (0.1 Hz to 5 Hz) geomagnetic waves that are now known as Pc 1-2 pulsations were first published in the 1930s by Eyvind Sucksdorff (Sucksdorff, 1936) and Liev Harang (Harang, 1936). Sucksdorff made his discovery during his time as director of the Sodankylá Geophysical Observatory (Raita and Kultima, 2007), which remains to this day a world-leading institute for the gathering and dissemination of solar-terrestrial observations and is the primary data source for the work within this thesis. As MHD and plasma dynamic theory developed, the significance of Pc1-2 pulsations was recognised and it is now widely accepted that their study may aid in the understanding of fundamental aspects of the solar-terrestrial environment. Their generation is indicative of the plasma population from which they emerge, their propagation illuminates the media through which they travel and their interaction provides a transport mechanism, directly for energy and indirectly for material, throughout the magnetosphere-ionosphere system.

This chapter reviews relevant material from the abundance of theoretical and observational research that has focused on the nature and origin of terrestrial Pc1-2 waves and their interaction with the geospace environment since their discovery over 70 years ago.

3.1 Morphology and occurrence

Early observations of Pc1-2 activity consisted solely of magnetograms, which restricted their characterisation to parameters such as occurrence, duration and intensity. An example of such a magnetogram, presented by Sucksdorff (1936), is shown in figure 3.1, in which can be seen a periodic intensification in amplitude (W-E bottom trace). Sucksdorff likened these repeating wavepackets to a string of pearls and despite the loss of analogy in the modern method of dynamic spectral analysis (Ch.5) the term “pearl pulsation” persists today. Both of the original authors presented data that suggested regular diurnal and annual pulsation occurrence variations were present; however, the limitations of their La Cour quick-run magnetometers did not allow reliable conclusions to be drawn on the true occurrence distributions. Consequently, rigorous study of these

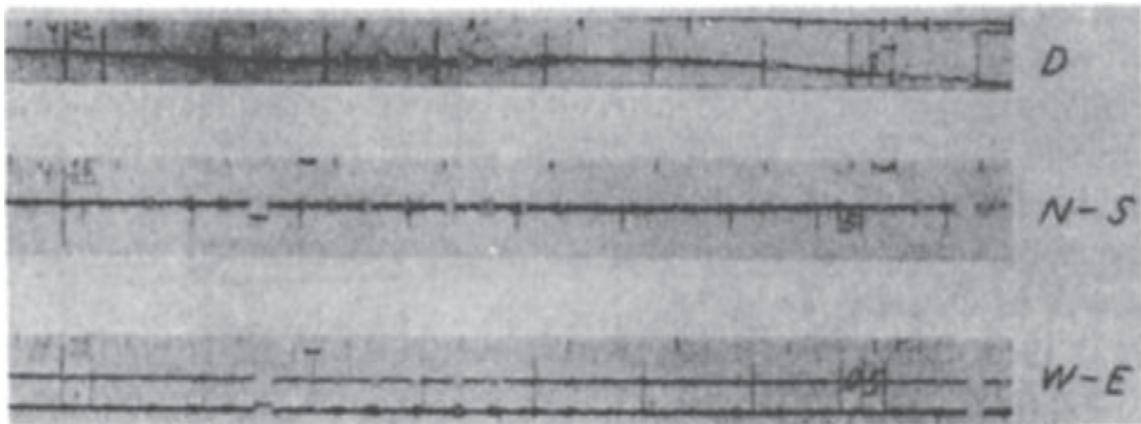


FIG. 1—RAPID MICROPULSATIONS RECORDED AT SODANKYLÄ, FEBRUARY 6, 1935, IN MAGNETIC DECLINATION AND IN NORTH-SOUTH AND EAST-WEST EARTH-CURRENT COMPONENTS

Figure 3.1: La Cour quick-run magnetograms, presented by Sucksdorff (1936), in which can be seen (most clearly in the W-E component) periodic amplitude intensification akin to a string of pearls.

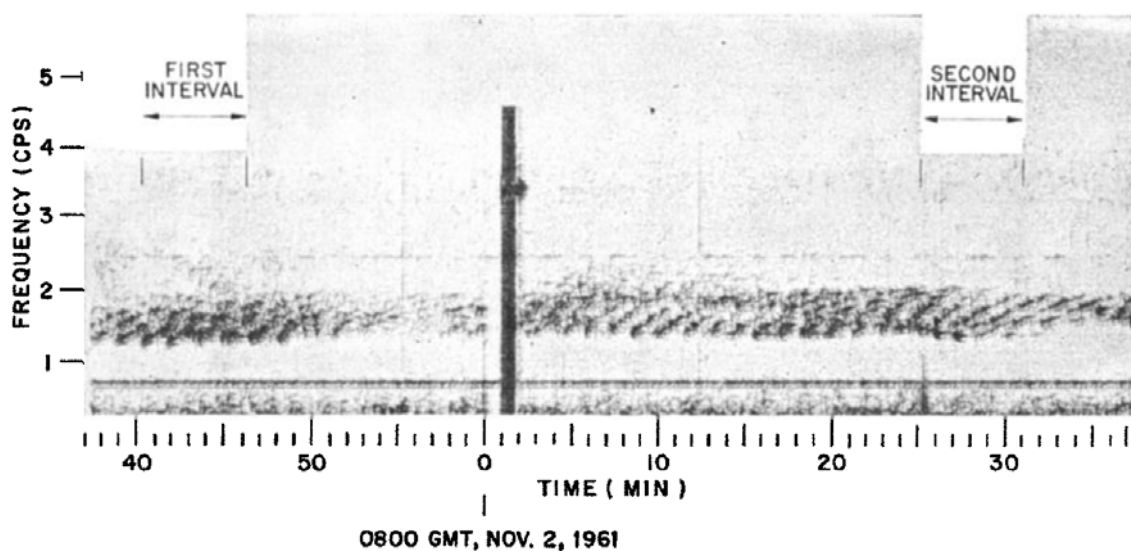


Figure 3.2: Induction coil sonogram of a structured (pearl) pulsation, presented by Tepley and Wentworth (1962). The rising tone structure of each wavepacket can be seen to elongate with time, a form that would later be misnomered as hydromagnetic whistler waves.

waves was not effectively undertaken until some 30 years later when instrumentation and signal processing techniques were developed that allowed spectral analysis to be conducted (Saito, 1969).

The frequency-time-amplitude sonogram representation of high temporal resolution induction coil magnetometer data, introduced in the 1960s (Tepley, 1961, Saito, 1960), allowed the dynamic nature of this branch of pulsations to be scrutinised. Figure 3.2 shows an early example of a sonogram (Tepley and Wentworth, 1962), which shows a sequence of repetitive intensifications in spectral power. These intensifications represent the wavepackets noted by Sucksdorff (1936). Displaying a reasonably stationary central frequency of 1.5 Hz and a stable bandwidth of approximately 0.8 Hz, each wavepacket is separated by a repetition period of the order 80 s and exhibits an increase in frequency from initiation to cessation or classic “rising tone dispersion”.

Morphological studies of pulsation dispersion behaviour have since revealed a quasi-continuum of spectral forms, ranging from simple narrow-band unstructured continuous emissions with no deviation in central frequency to structured pulsations that display intricate wavepacket dispersion and irregular shifts in central frequency and bandwidth. Nose emissions (Fraser, 1972) and chevron pulsations (Fraser-Smith, 1977) are among the more complicated observations and consist of combinations of falling and rising tones. The contribution of heavy ions to propagation from a single source region and multiple overlapping pulsations of independent source regions have been suggested as causes for these nontrivial dispersion characteristics; however, both explanations are yet to be conclusively proven or otherwise.

The vast range of frequency and amplitude modulations observed led to a series of pulsation nomenclatures (Kangas *et al.*, 1998, Fukunishi *et al.*, 1981, Saito, 1969, Troitskaya and Gul'Elmi, 1967), based entirely on their sonogram appearance. Of the multitude of classifications still in use, the number of terms used to describe pulsation events in this thesis is restricted to three: structure pulsations (pearls), unstructured pulsations and Intervals of Pulsations of Diminishing period (IPDP). As will be shown in the following chapters the correct application of even these few simple descriptive labels is not always clear.

As briefly discussed in section 2.2.3, pulsations of this category have been shown to be the result of the ElectroMagnetic Ion-Cyclotron (EMIC) instability (Cornwall, 1965). Generation occurs through normal ion cyclotron resonance, in which an energetic ion population with a non-Maxwellian ion distribution function (IDF), of typical energy $\sim 10\text{-}100$ keV, resonantly interacts with an anti-parallel, left-hand (L-mode) circularly polarized electromagnetic wave (Mauk and McPherron, 1980). The non-Maxwellian IDF exhibits a temperature anisotropy, such that the perpendicular temperature of the ion population is much larger than the parallel temperature (Roux *et al.*, 1982, Noerdlinger, 1964), which has been supported analytically (Gary and Winske, 1993) and by ground-based and in-situ measurements (Gary, 1991 and references therein). Resonant coupling may occur when the frequency of the incident wave, Doppler shifted into the parallel frame of the ion, matches a harmonic of the ion gyrofrequency, subject to the resonance condition (eqn. 2.70). When satisfied, this resonant relation allows the exchange of energy between the two regimes and ultimately wave growth or damping. The growth of the resulting EMIC wave is dependent not only on the governing parameters of both ions and wave, such as ambient magnetic field strength and ion density, but also on the relative direction and phase of the interacting systems.

As EMIC waves propagate in L-mode (Stix, 1992), they are strongly guided by the ambient magnetic field (Dowden, 1965). However, when they reach the dense, partially ionised ionosphere, mode conversion, via Hall currents, to fast-magnetosonic mode may take place, which then allows them to duct horizontally within the ionosphere (Tepley and Landshoff, 1966). Subsequently, the magnetospheric source region of pulsations observed on the ground may be estimated with knowledge of the wave's propagation characteristics and an appropriate geomagnetic field-line model.

Historically, the source region of Pc1s was linked with the equatorial plasmopause, where conditions such as reduced magnetic field strength and a large plasma density gradient are thought to favour wave growth (Fraser *et al.*, 1996, Thorne and Horne, 1992, Roth and Orr, 1975); with structured pulsations thought to be generated in a region bounded by the plasmopause. It has been shown empirically that these factors are not independently critical conditions for wave growth to occur and that

the plasmopause itself may not be the preferred site of Pc1 generation (Fraser and Nguyen, 2001). However, in situ Poynting vector analysis has suggested that wave growth is prominent at the equator in a region bound by $\pm 11^\circ$ magnetic latitude (Loto'aniu *et al.*, 2005).

Numerous statistical studies, over time periods ranging from a few days to four full solar cycles, have shown that Pc1-2 pulsations exhibit a dependence on, time of day and year, latitude, level of geomagnetic disturbance and solar activity. The ground based study of (Benioff, 1960) showed that low-latitude ($L < 2$) occurrence displays a somewhat dissimilar diurnal variation to the high-latitude case noted by Sucksdorff (1936). A similar low-latitude distribution was presented by Bortnik *et al.* (2007). All three diurnal distributions are shown in figure 3.3. Despite the vastly different observational techniques employed, the former authors using analogue signal processing and manual event selection, the latter authors using digital spectral matrix analysis and an automated event extraction algorithm, both low-latitude studies show that pulsation occurrence maximises during nighttime hours, unlike the daytime high-latitude case. Bortnik *et al.* (2007) suggest that this occurrence contradiction is owing to increased daytime ionospheric E-layer absorption yet fail to provide adequate explanation for their assertion.

Statistical satellite studies show that local-time EMIC wave occurrence is centred on a post-noon (Anderson *et al.*, 1992a, Anderson *et al.*, 1992b, Fraser, 1985) or early evening (Bossen *et al.*, 1976) peak, similar to that of the high-latitude distribution. The studies conducted by Anderson *et al.* (1992a, 1992b) are among the most comprehensive to date and include over 7500 hours of AMPTE satellite observation including ~ 350 hours of EMIC wave measurements, which unlike previous studies, were made over a range of altitudes and latitudes allowing spatial as well as local-time characterisation. A key finding of these studies, outlined in a subsequent publication (Anderson, 1996), was that the afternoon peak in occurrence extended in altitude to at least the upper boundary of AMPTE's orbit ($L \sim 9$), as this showed that EMIC generation may take place significantly further out than the average plasmopause position ($4 < L < 6$). This result can be seen in the local-time plot of Pc1-2 occurrence in figure 3.4.

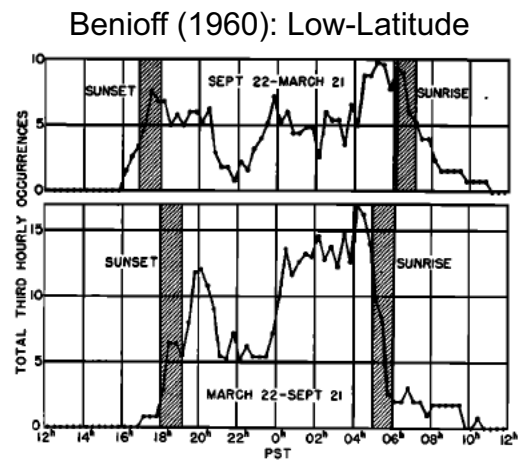
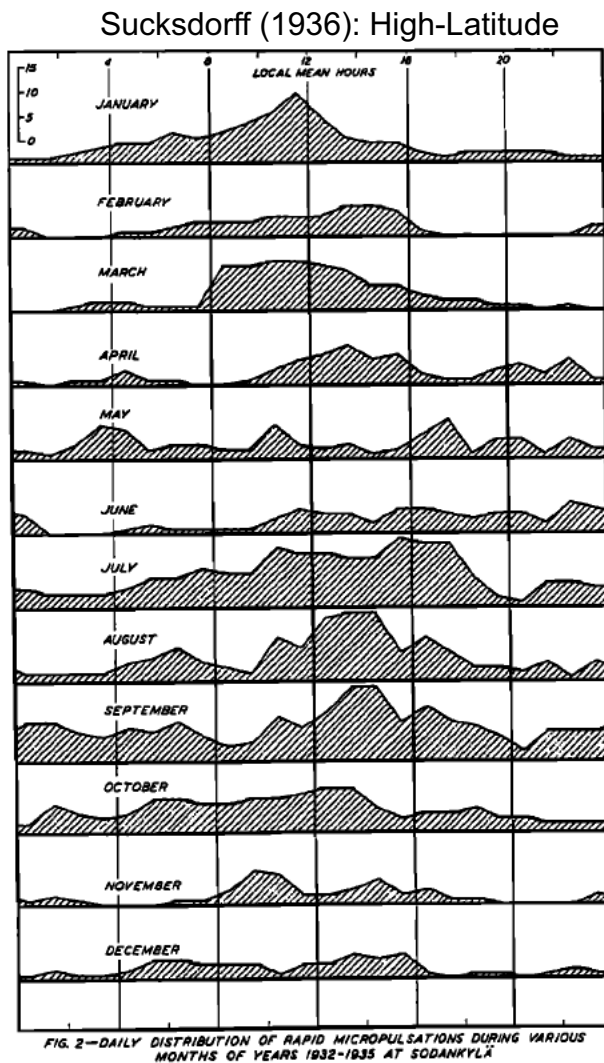


Fig. 8. Diurnal variations, type A oscillations, southern California, January 1955 to April 1959.

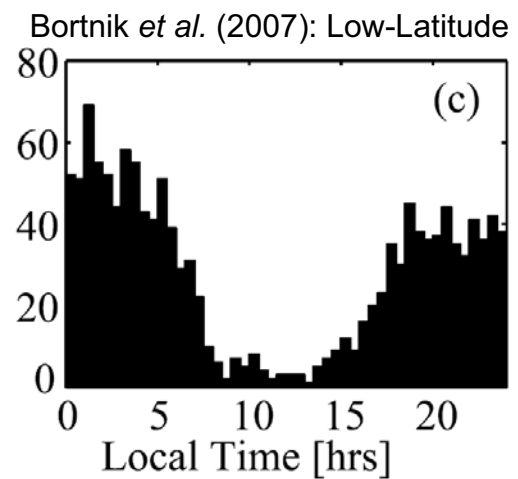


Figure 3.3: Diurnal distribution of Pc1-2 pulsations for high-latitude (left-hand panels) and low latitude (right-hand panels), taken from Sucksdorff (1936), Benioff (1960) and Bortnik *et al.* (2007). The distributions show that at high (low) latitude, activity is predominantly during the day (night) time. It should be noted that all three studies use different time conventions and that the low latitude plots are approximately 10 hours of local time behind the high latitude plots.

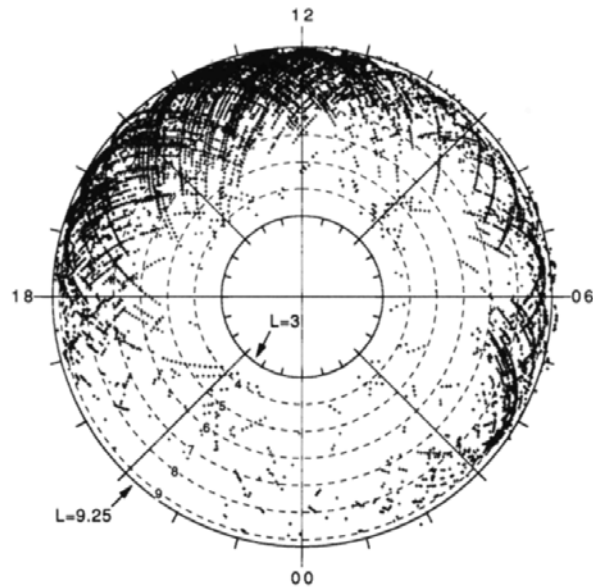


Figure 3.4: AMPTe satellite, local-time plot of Pc1-2 occurrence, presented by Anderson *et al.* (1992a), showing that a large number of events occur at a far greater radial distance than that of the average plasmapause.

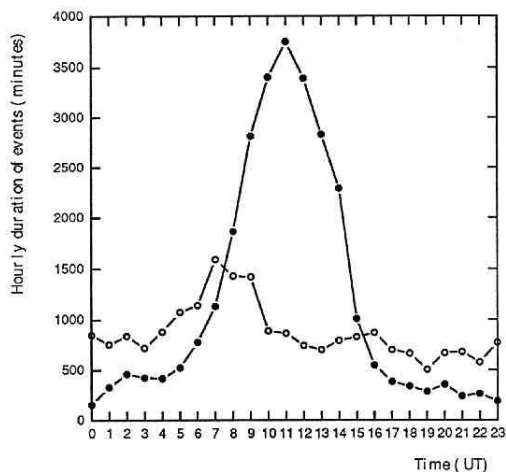


Figure 2. The diurnal distribution of the hourly duration of structured (open circles) and unstructured pulsation events (black circles) in minimum years.

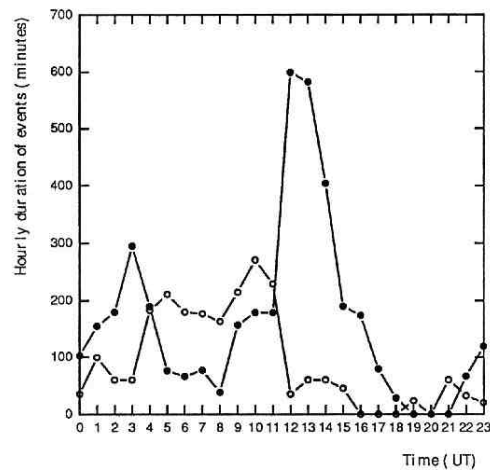


Figure 3. The diurnal distribution of the hourly duration of structured (open circles) and unstructured pulsation events (black circles) in maximum years.

Figure 3.5: Diurnal Pc1-2 occurrence distributions for solar minimum (left) and maximum (right), from Mursula *et al.* (1994). The local-time postnoon singular peak can be seen to consist mainly of structured pulsations at solar minimum, bifurcating into an early morning and early evening peak during solar maximum.

Given the transient nature of satellite observations, it is rather difficult to determine whether the observed pulsations are structured or otherwise; such a distinction is best made from ground-based observations. (Mursula *et al.*, 1994b) did just that when generating their diurnal distribution, shown in figure 3.5. The aim of their study was to determine the effect of the previously noted anti-correlation with the solar cycle (Fraser-Smith, 1970) on both structured and unstructured pulsations. They found that in the case of solar minimum, the aforementioned post-noon occurrence peak consisted mostly of structured pulsations, which bifurcated during solar maximum to reveal early morning and late afternoon peaks. This variation was initially explained in terms of the evolution of the ionospheric duct throughout the course of the solar cycle and the relative ducting propensity of each species of pulsation. However, this explanation was retracted in a subsequent paper (Mursula *et al.*, 1996) in favour of magnetospheric effects. As interesting as was the result of Mursula *et al.* (1994) it was based on a total of four months of data from a single high-latitude station, which, as highlighted by the authors, called in to question the validity of the finding.

3.2 Solar activity dependence

The inverse relationship between Pc1-2 pulsations and sunspot number (Fraser-Smith, 1970, Benioff, 1960), was further supported by almost four solar cycles of semi-continuous magnetometer observations (Mursula *et al.*, 1991). However, these authors used La Cour quick run magnetometers sensitive to the frequency range 0.3 Hz to 0.5 Hz; which, when compared to induction coil observations for common time periods, was found not to be precisely representative of the entire Pc1-2 band. Hence, it was the later study of Kangas *et al.* (1999) that confirmed the relationship. Using approximately two full solar cycles of continuous induction coil magnetometer data, Kangas *et al.* (1999) were able to separate out Pc and IPDP events in a fashion that was not possible with the La Cour magnetograms. Their derived Pc1-2 distribution is presented in figure 3.6, which shows a clear anticorrelation with the Zurich sunspot index (R_z).

The analytical work of (Trakhtengerts *et al.*, 2000) suggests that this relationship may be governed by the variation in the ionospheric electron density profile over the course of the solar cycle. This variation causes the reflection coefficient at the upper

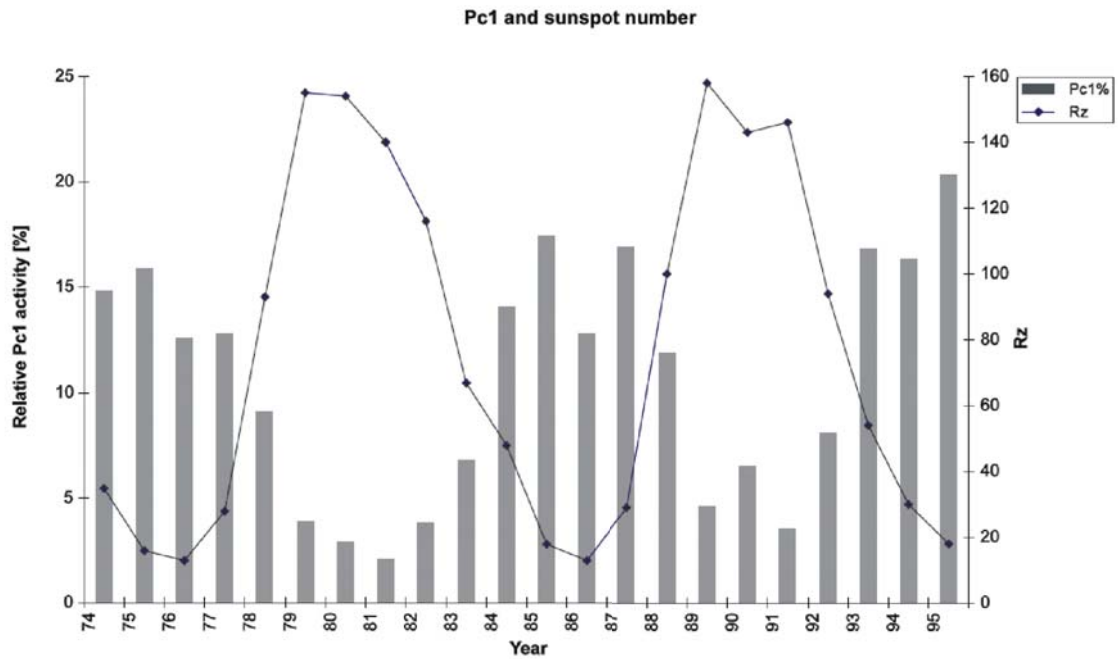


Figure 3.6: Annual percentage occurrence rate for high-latitude Pc1 pulsations and solar sunspot number (Rz, solid line), from Kangas *et al.* (1999). An inverse relationship between the two parameters is evident over the two solar cycles presented.

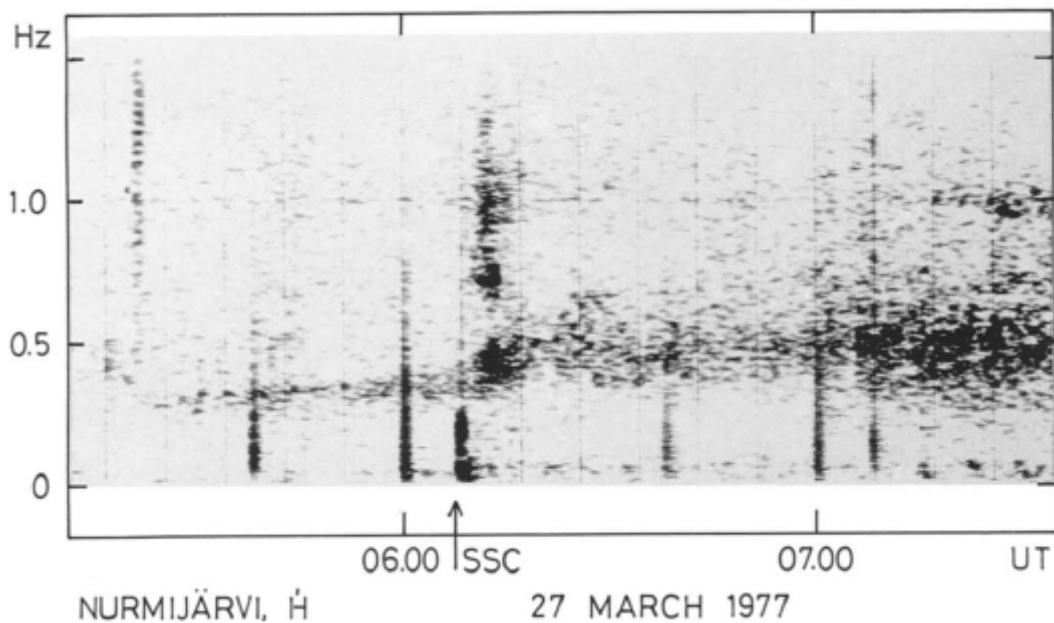


Figure 3.7: Pc1 dynamic spectrum, showing a step up in central frequency following a bursty SSC induced emission.

boundary of the ionosphere to vary inversely with sunspot number. However, this suggestion rests on the assertion that the generation of EMIC waves is dependent on efficacy of the magnetospheric cavity, which is far from proven.

Control of Pc1-2 generation and modification by solar wind parameters has been demonstrated by a number of authors, e.g. (Guglielmi and Kangas, 2007, Hirasawa, 1981, Heacock and Hessler, 1965). In the simplest case, a direct relationship between solar wind density and Pc1-2 occurrence has been reported (Guglielmi *et al.*, 2005). However, the derivation of this relationship did not consider the nature of the density enhancements or their subsequent effect on the state of the magnetosphere. It is likely that such a relationship is naturally explained by the well documented Pc1-2 response to interplanetary shock impact on the magnetopause, which causes a rapid compression of the dayside magnetosphere or “Sudden Impulse” (SI) (Kangas *et al.*, 1986, Olson and Lee, 1983, Hirasawa, 1981, Heacock and Hessler, 1965, Tepley and Wentworth, 1962). Upon studying a three-year interval of high latitude magnetometer records, Olson and Lee (1983) suggested that an SI was capable of adiabatically heating the dayside ion population, increasing its anisotropy and driving it in to EMIC instability. Support for this mechanism was provided by Anderson and Hamilton (1993), who showed, with in situ observations, that dayside magnetospheric EMIC waves are linked to SI. It was, however, Engebretson *et al.* (2002) who directly showed that even a modest compression may anisotropise the dayside outer magnetosphere. These authors also supported the suggestion that the state of magnetosphere at the time of compression was a determining factor in its behaviour (Kangas *et al.*, 1986); with quiet conditions immediately prior to SI leading to a greater probability of subsequent wave growth.

When SI is followed by a geomagnetic storm, it is termed a Storm Sudden Commencement (SSC), such events have a similar effect on the occurrence of Pc1-2 (Tepley and Wentworth, 1962, Troitskaya, 1961). Kangas (1986) demonstrated that SI or SSC can also modify the behaviour of an existing pulsation. Figure 3.7 displays a dynamic spectrum taken from Kangas (1986), which shows the central frequency of a Pc1 pulsation “step up” from ~ 0.3 Hz to ~ 0.4 Hz following an SSC induced bursty emission. Whether the pre- and post-SSC pulsations are directly related remains to be seen; however, the step up in central frequency, continuous or otherwise, appears to be a relatively common phenomenon. As common as SSC induced pulsations are, their

number is greatly exceeded by those occurring in the recovery phase of a geomagnetic storm (Wentworth, 1964) as energetic ring current ions provide sufficient anisotropy for EMIC instability.

3.3 Geomagnetic storms and currents

Wentworth (1964) analysed the low latitude Pc1 emissions surrounding 25 geomagnetic storms over a three-year period and determined that pulsations were more likely to occur in the seven days following storm initiation than in geomagnetically quiet times. Subsequent studies have been in general agreement with Wentworth's analysis (Bortnik *et al.*, 2008b, Kerttula *et al.*, 2001a, Kerttula *et al.*, 2001b, Heacock and Kivinen, 1972) and have gone on to show that the probability of Pc1-2 occurrence on the ground drastically reduces during storm main phase, gradually increasing up to a maximum during the recovery phase, some 4-7 days after initiation. Heacock and Hessler (1972) suggested that this pattern of occurrence may be explained by the gradual refilling of the plasmasphere and its intersection with cold, dense ring current plasma resulting in EMIC instability. This scheme would account for the prevalence of Pc 1-2 in the post noon sector, as refilling occurs preferentially there. However, Braysy *et al.* (1998) showed, with a single case study of a large storm, that magnetospheric EMIC wave intensity actually increased in the main phase, with the generation region moving to lower latitude and in to the late evening MLT sector by the beginning of the recovery phase.

The latitudinal behaviour of storm time pulsations was investigated in two companion papers by Kerttula (2001, 2001a), with a superposed epoch study of pulsations at two stations, one at high and one at mid latitude, over the course of 18 geomagnetic storms. These authors distinguished between structured and unstructured events and demonstrated that the occurrence of structured pulsations evolves during the course of a storm far more markedly than unstructured do. Figure 3.8 displays their derived occurrence probabilities as a function of time from SSC for weak (circles) and intense (squares) storms. The left-hand panels show that structured pulsation probability evolution is similar at both high and mid latitudes irrespective of storm intensity, maximising on day four. Conversely, high-latitude unstructured pulsations during

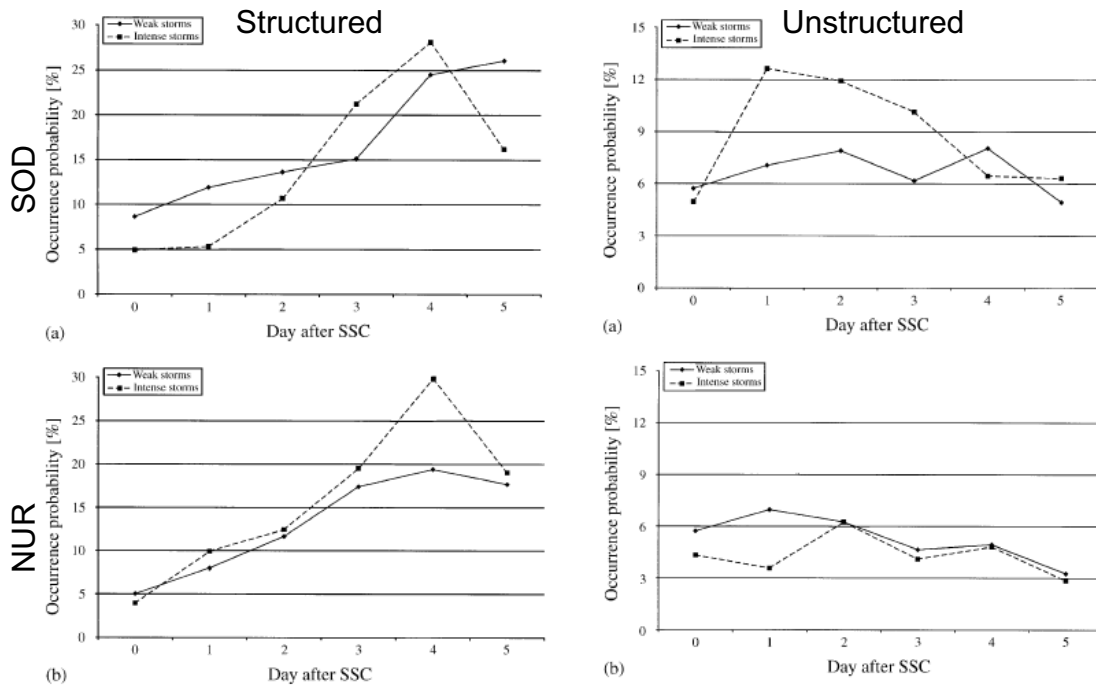


Figure 3.8: Daily Occurrence probability of structured (left) and unstructured (right) Pc 1-2 pulsations for high (top) and mid (bottom) latitude as a function of days after storm sudden commencement. The structured distribution appears to be more greatly affected at both latitudes increasing to a maximum probability on day 4. From Kertulla (2001)

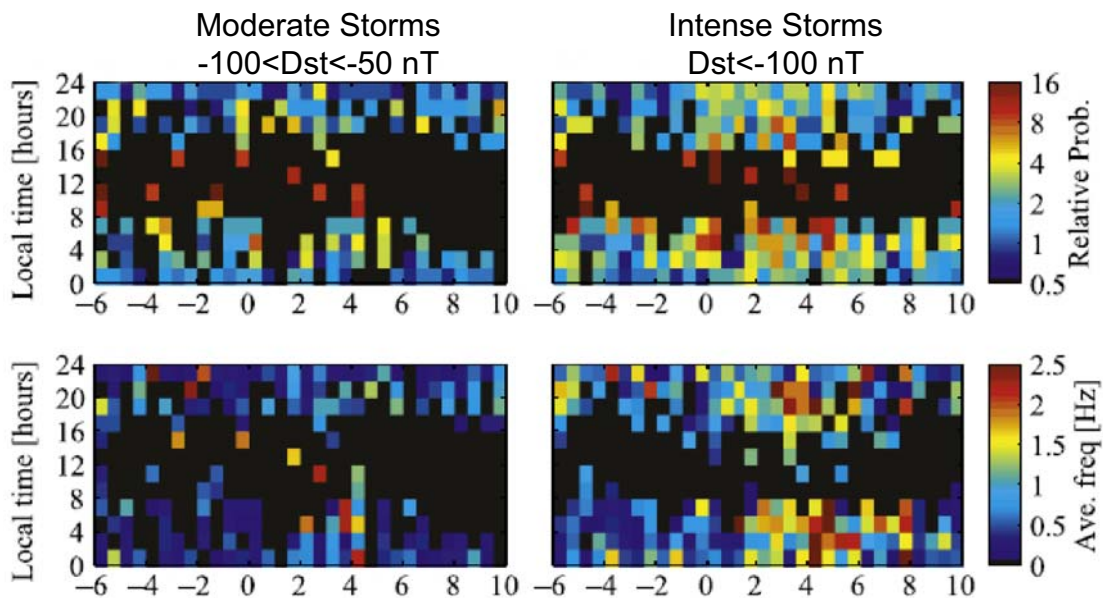


Figure 3.9: Low latitude superposed epoch analysis of Pc1 relative to moderate (left) and intense (right) geomagnetic storms (black represents missing data). Relative probability (top) and average frequency (bottom) are plotted as a function local time and day from SSC. A relative midday maximum on day 7 can be seen as well as a steady increase in average frequency. From Bortnik (2008).

intense storms significantly increase in the first day after SSC, gradually falling back to their undisturbed level over the following four days. No such enhancement was seen in the mid-latitude unstructured distribution. Bortnik *et al.* (2008) conducted a similar study at low-latitude, using automated storm and pulsation detection algorithms that identified 24 isolated storms and over 8000 individual Pc1 events from an 8-year interval. These authors derived a similar distribution, which can be seen in figure 3.9. However, they did not make the structured/unstructured distinction, which makes direct comparison of these two studies difficult. Both studies reported a gradual increase in frequency up to approximately day four; however, Kerttula *et al.* (2001) showed that this effect was only significant for structured pulsations. This increase in frequency contradicts the plasmaspheric expansion explanation of pulsation evolution. This contradiction led to the suggestion by Kerttula *et al.* (2001a) that the observed occurrence and frequency behaviour may be related to improved ionospheric propagation conditions. Furthermore, they suggested that the development of the Ionospheric Alfvén Resonator (IAR) over the course of a storm may dictate transmission to the ground. However, these claims are yet to be experimentally verified.

The relationship of Pc1-2 pulsations to the storm recovery phase is well established; however, the precise contribution of EMIC waves to the ring current relaxation process is still unknown (Daglis *et al.* (1999 and references therein)). However, it is clear that EMIC pitch angle scattering does provide a significant loss mechanism for energetic ring current ions.

3.4 Particle precipitation

The transfer of energy from anisotropic ring current ions to magnetospheric EMIC waves has been theoretically demonstrated, by consideration of their path-integrated amplification (Thorne and Horne, 1994). The result of this interaction is the pitch angle scattering of those ions into the loss-cone (Erlandson and Ukhorskiy, 2001), causing them to precipitate into the ionosphere. Localised particle precipitation has been experimentally linked with ground-based observations of Pc1-2s and IPDP (Yahnina *et al.*, 2000, Yahnina *et al.*, 2003), with in situ measurements confirming the presence of strong pitch angle diffusion.

High altitude observations, close to the EMIC generation region, have shown that instability may occur when energetic ring current ions intersect cold, dense plasma detached from the plasmasphere, resulting in local proton precipitation. These precipitating protons may then interact with the ionosphere and produce sub-auroral proton spots, which have been observed in the vicinity of Pc1-2s (Yahnin *et al.*, 2007). IMAGE-FUV observations also indicate that EMIC waves are generated at the intersection of subauroral proton arcs and the cold dense plasmaspheric plume formed in the wake of a geomagnetic storm (Spasojevic *et al.*, 2004).

3.5 Pearl repetition period and growth modulation

The origins of structured pulsations have yet to be conclusively proven. The classic rising tone pulsations so frequently seen on the ground have been observed in the magnetosphere (Mursula *et al.*, 1994a), although, the spatio-temporal ambiguity of such single point satellite observations does cast doubt on their interpretation. The Bouncing Wave Packet theory (BWP), proposed in the 1960s (Obayashi, 1965, Jacobs and Watanabe, 1964), was for a significant number of years the foremost theory on Pc1 pearl formation. However, several key incompatibilities with the BWP, in its original form, have meant that it is no longer able to account fully for observation without additional theoretical input. Originally based on the observation of pulsations that displayed approximate antiphase propagation observed by ground-based magnetometers in conjugate locations (Tepley, 1964), the BWP suggests the equatorial growth and partial reflection at the base of the ionosphere in conjugate hemispheres of a single, field line guided, wavepacket.

Loto'aniu *et al.* (2005) observed no wave energy directed toward the equator outside the aforementioned source region, suggesting an absence of wave reflection at the lower boundary of the ionosphere or that the reflected wave energy was below the detection threshold of the instrument used (Flux Gate Magnetometer and Electric field/Langmuir Probe aboard CRRES). It has, however, been shown that a realistic one hop growth rate could be responsible for such a reflected, upward travelling, wave packet with energy below the CRRES detection threshold at $\pm 11^\circ$ Mlat that would be

sufficiently amplified upon exit from the growth region to maintain a sustained pearl pulsation (Demekhov, 2007) and references therein. It has also been noted that any upward wave energy would be masked by the downward wave energy travelling through the same region, post amplification; hence, this observational fact alone does not invalidate the BWP.

Similarly the BWP predicts that the repetition period observed on the ground should be twice that of in situ observations, which have been shown to be the same (Mursula *et al.*, 2001, Erlandson and Anderson, 1996) this does, however, raise the same question concerning instrument detection threshold. Also, in this scheme the observed Pc1 periodicity, clearly, must be a function of field line length and hence latitude; accordingly, empirical relationships between central pulsation frequency, field line length and repetition period have indeed been formulated e.g. (Mursula *et al.*, 1999b). Contrary to this, in-situ observations have been made of events with wavepacket repetition periods too short to be explained by the BWP (Mursula *et al.*, 1997). A possible explanation for this may lie with the contribution of heavy ions to the resonant cavity in which the BWP operates. Reflection from regions of heavy ion content at some altitude significantly higher than the base of the ionosphere reduces the size of the BWP cavity, effectively shortening the path length of the wavepacket (Guglielmi *et al.*, 2001); hence, reducing the repetition period of the observed pearl pulsation.

This scheme also suggests that the path length of each successive wavepacket is increased by twice the field line guided separation of conjugate reflection points. Given the characteristic dispersion relation of classic pearls, which display rising tones such that lower (higher) frequency wave components have higher (lower) phase velocities that can remain constant, drift or fluctuate randomly (Fukunishi *et al.*, 1981), the BWP is inconsistent with observation. The increased path length of each wavepacket should cause greater dispersion between successive packets, where empirically this relationship is seen to be independent of pulsation history and is therefore incompatible with the BWP.

Equatorial Growth Modulation (EGM) theories have been shown to be capable of accounting for many of the observed features of pearl pulsations that the BWP, in its

simplest form, cannot (Mursula *et al.*, 1997). EGMs have been supported analytically (Gail, 1990) and empirically (Rasinkangas and Mursula, 1998, Plyasova-Bakounina *et al.*, 1996, Rasinkangas *et al.*, 1994) a number of times and describe a regime where wave growth, that as previously mentioned is believed to occur equatorially, is modulated by some mechanism external to the ion-cyclotron instability responsible for the growth.

EGMs of particular promise are those that describe equatorial modulation by long period ULF waves. These models describe a source region in a state of marginal stability that is forced in to instability by some time varying parameter. The time varying parameter may be an oscillating magnetic field (Gail, 1990), introduced by the presence of a long period ULF wave or by ion acceleration into and out of dissimilar neighbouring regions by the wave's electric field (Rasinkangas *et al.*, 1994). Consequently, in both schemes wave growth is modulated at the frequency of that ULF wave.

These models are rather attractive in that they remove the field line length dependence of the BWP and do not rely on ionospheric reflection. They also may account for the observed dispersion relation as the oscillating magnetic field could cause the generated wave frequency and phase speed to vary with time. They do not, however, in their simplest form account fully for observation. The anti-phase propagation in conjugate hemispheres is poorly described by such EGMs and, hence, further theory must be developed before they become wholly consistent with observation. Evidence in support of EGMs has been presented from ground based (Plyasova-Bakounina *et al.*, 1996) and ground-in situ studies (Mursula *et al.*, 2001, Mursula *et al.*, 1999a, Rasinkangas and Mursula, 1998, Rasinkangas *et al.*, 1994) . These studies have reported Pc1-2 modulated by Pc4-5 Field Line Resonances (FLRs), solar wind pressure pulse driven Pc5 FLRs and Pc3 pulsations directly injected from the upstream solar wind. For example, figure 3.10 displays data from the ground-satellite study of Mursula *et al* (2001). The upper two plates show that spectral power at a similar frequency is present in data from the Polar satellite and the Sodankylá pulsation magnetometer, when the two are approximately conjugate. The lower plate shows in situ spectral power at the repetition frequency of the structured pulsation observed on

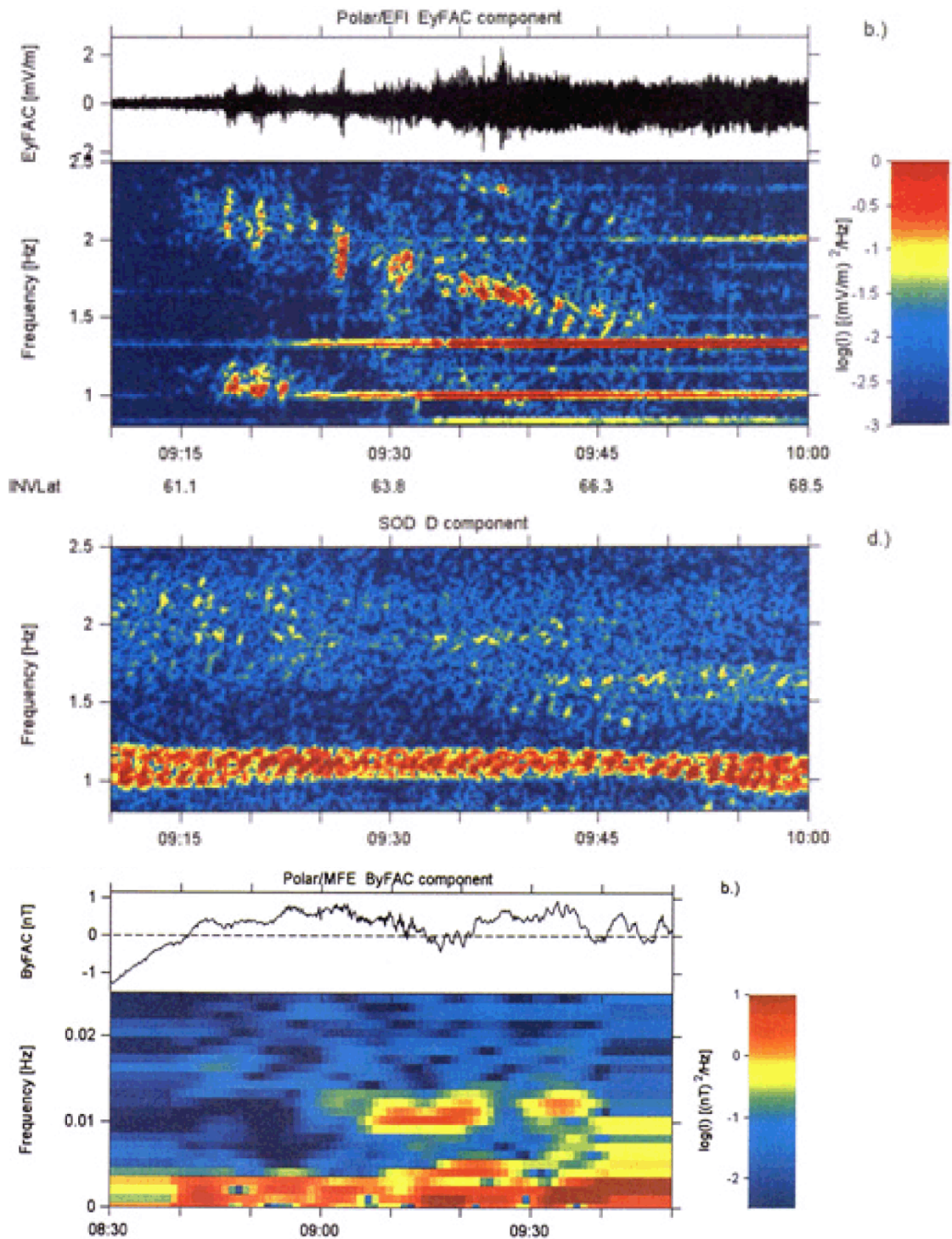


Figure 3.10: Plates from Mursula *et al.* (2001). Dynamic spectra of the Y component of the EFI instrument on board the Polar satellite and the D component of the Sodankylá pulsation magnetometer, during a period of approximate conjugacy, are displayed in the upper and middle panels. Spectral power at frequencies common to both instruments is present. The lower panel shows a dynamic spectrum of Polar MFE data for the same period, in which can be seen spectral power at a frequency similar to the repetition frequency of the observed structured pulsations. These data are interpreted by the authors as evidence of long period ULF wave modulation of EMIC wave growth.

the ground, interpreted by the authors as evidence of EMIC wave growth modulation by a long period ULF wave.

The inconsistency of the BWP with observation and the increasing number of reports on coincident Pc1-2-long period ULF waves, coupled with developing coherent theory that currently explains the interaction of the two wave regimes has led to similar EGMs now standing as prominent contenders in the search for a unified theory of Pc1 pearl generation.

A further magnetospheric pearl generation mechanism exists in the form of the Magnetospheric Cyclotron Maser, which is based on the Backward Wave Oscillator (BWO). Originally proposed as a mechanism to explain chorus emissions (Trakhtengerts *et al.*, 2004, Trakhtengerts, 1995), the BWO was put forward by Loto'aniu *et al.* (2005) as a possibility for their in situ observations. The BWO is a positive feedback mechanism, consisting of an equatorial magnetospheric cavity in which EMIC waves are partially trapped and interact with oppositely directed anisotropic ions. This cyclotron interaction causes phase bunching of the ion population. Wavepackets, reflected at the cavity boundaries, are then further enhanced by the previously phase bunched ions. This possibility has analytically been shown to be capable of producing the observations of Loto'aniu *et al.* (2005) by Trakhtengerts and Demekhov (2007). However, it was noted, by the latter authors, that direct observation must be made of the ion distribution function deformations necessary for the BWO to operate for this mechanism to stand as a viable candidate for pearl generation.

3.6 Polarisation and propagation

As discussed in sections 2.2.3 and 3.1 magnetospheric EMIC waves propagate with left-hand (LH) circular polarisation and are field-line guided. The observation of well-correlated pulsations at multiple widely spaced sites led to the suggestion that mode conversion to the isotropic fast-magnetosonic mode occurs in the lower ionosphere (Manchester, 1966, Tepley and Landshoff, 1966). Fast mode waves, which propagate with right-hand (RH) circular polarisation (Stix, 1992) may then be ducted along an ionospheric wave guide centred on the F2 electron density peak (Greifinger and

Greifinger, 1968), the signal registered on the ground then being the result of leakage across the E-region lower boundary. (Manchester, 1968). The scheme suggested by Tepley (1966) is reproduced in figures 3.11 and 3.12. The upper panel displays the ionospheric density, velocity and attenuation profiles derived by those authors and lower pane showing their schematic representation of propagation.

Following this suggestion, a number of multi-station techniques arose that attempted to locate the ionospheric mode conversion site at the footprint of the magnetospheric source field-line. The spatially inhomogeneous nature of the E-region precludes the use of wave power variation or attenuation as a method for locating the ionospheric source region as transmission through the lower duct boundary is dependent on density. Hence, transmitted wave power does not vary monotonically with distance from the source.

The polarisation of a transmitted wave should, however, be representative of the local dominant propagation mode. LH polarisation should indicate the ionospheric source, with RH polarisation gradually dominating with distance from the edge of that region, which has been shown to be as small as 60 km across (Erlandson *et al.*, 1996). Historically, three methods were employed to determine the polarisation characteristics of Pc1-2s: hodographic (Heacock and Hessler, 1967), goniometric (Fraser and Webster, 1979) and spectral matrix analysis (Rankin and Kurtz, 1970). Hodography involves tracing out the magnetic vector for a sufficient number of oscillations to determine the polarisation ellipse. Spectral matrix analysis, involves the construction of a time averaged spectral estimate of the analogue signal (Ch. 5). Goniometric analysis combines, in quadrature, the two horizontal component of the measured magnetic field (Ch. 5). Employing the hodographic technique (Summers and Fraser, 1972) demonstrated that the polarisation characteristics of a given pulsation event could be relatively stable and (Greifinger, 1972) analytically demonstrated that the orientation of the polarisation ellipse increasingly aligned with its direction of propagation with distance from its source. Subsequently, (Fraser, 1975) went on to show that multiple stations could be used to triangulate the source region. However, the success of this method was dependent upon the pulsation being sufficiently linearly polarised. i.e. the source region being at a great distance from all observation sites and there being no significant refractive effects (Webster and Fraser, 1985). Hence, this method is of

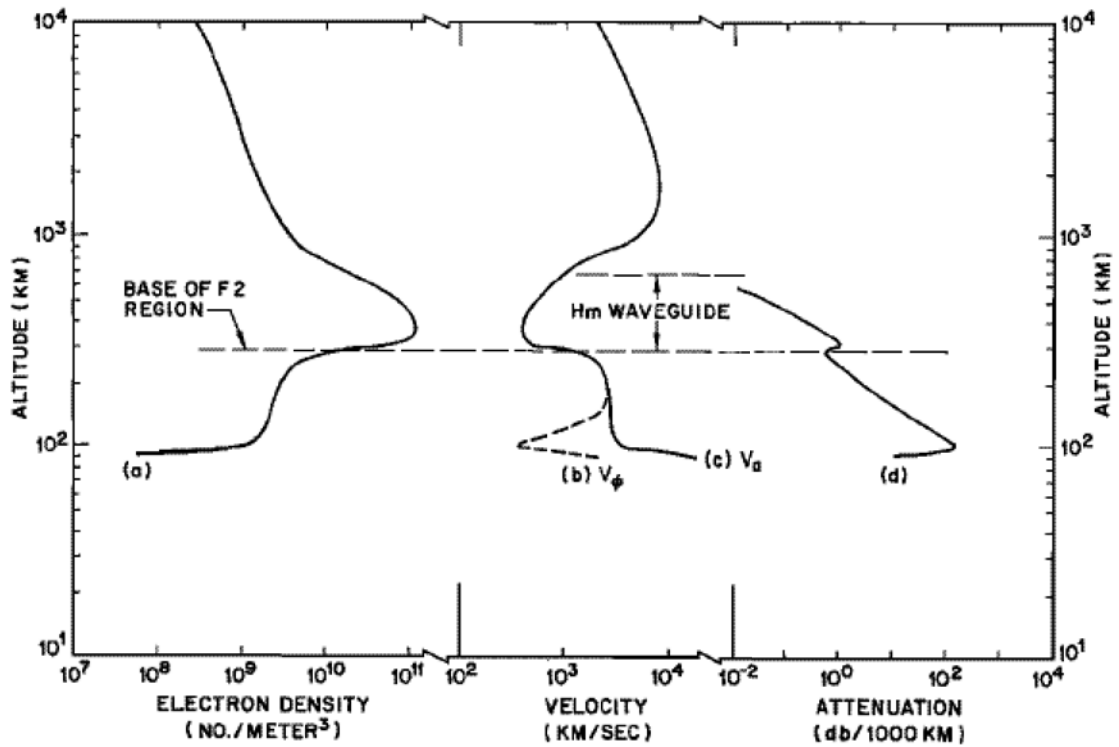


Figure 3.11: Ionospheric waveguide propagation characteristics for the fast-magnetosonic mode, from Tepley (1966)

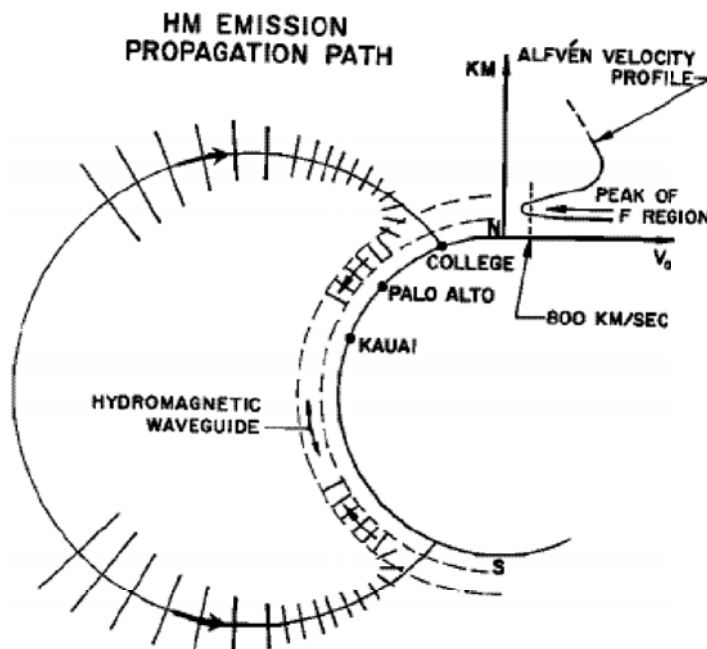


Figure 3.12: Propagation schematic for EMIC waves generated in the magnetosphere, from Tepley (1966). EMIC waves are guided along geomagnetic field-lines, converted to fast-magnetosonic mode in the lower ionosphere, then duct horizontally along in the hydromagnetic waveguide.

limited use in active regions where gradients in ionospheric density are likely, such as in the vicinity of the terminator.

Cross correlation to determine the time delay between multiple stations was used by a number of authors to determine the linear group velocity of ducted waves (Campbell and Thornberry, 1972), which was found to be between 300 km s^{-1} and 1000 km s^{-1} . Fraser (1975) went on to infer the source location through triangulation. Their method was based on plane wave propagation through a homogeneous planar medium. The planar assumption was estimated to introduce an error of $\sim 7\%$. However, the plane wave approximation, as with the polarisation technique, is only valid at large distances from the source region.

3.7 Unorthodox geophysical correlations with Pc1-2 pulsations

Pc1-2 pulsations have recently been linked to a number of seemingly unrelated phenomena with varying degrees of plausibility. The risk of Myocardial Infarction has shown a positive correlation with Pc1 occurrence (Kleimenova *et al.*, 2007). However, evidence other than a similar frequency range of Pc1 to the average heart rate is yet to be presented. Ionospheric modification owing to geo-seismic activity has been suggested, with an increased occurrence of Pc1-2 pulsation preceding significant earthquakes by several days (Bortnik *et al.*, 2008a). However, it has been stated that a great deal of further work is necessary before firm conclusion may be drawn on the exact nature of the geo-iono-seismic relationship.

3.8 High latitude studies

The distribution of Pc1-2 waves at high latitudes (above the auroral zone) is less well known than at mid-high latitudes as few comprehensive studies have been conducted. Using a single Antarctic station (-75° CGM), during a solar minimum interval, (Morris and Cole, 1991) showed that Pc1-2 pulsations at polar latitudes occur almost exclusively between the local times of 0600 and 1500. A result confirmed by Dyrud *et al.* (1997), who suggested mirroring energetic ions in the plasma mantle as the source of

EMIC instability. (Nykyri *et al.*, 2004, Nykyri *et al.*, 2003) used Cluster satellite observations in the high altitude cusp to link EMIC waves of mixed polarisation to sheared/stagnant plasma boundaries and filamentary flows.

The simultaneous ground-satellite (Polar, MFI/HYDRA) observations of Engebretson *et al.* (2005), led those authors to agree with the explanation of Dyrud (1997) that upward travelling mirroring ions convecting over the polar cap were the source of Pc1-2 pulsations observed on the poleward edge of the cusp. The former authors went on to associate similar pulsations with intense soft precipitation observed in optical data as Poleward Moving Auroral Forms. Safargaleev *et al.* (2004) presented a similar result linking unstructured Pc1 with enhanced dayside reconnection observed in SuperDARN radar data.

3.9 Summary and outstanding issues

The many decades of research on Pc1-2 pulsations and their magnetospheric counterparts EMIC waves has yielded a vast repository of information on their behaviour. It is known that they provide a mechanism for the transfer of energy throughout the geospace environment and are indicative of the state of the magnetosphere. However, an incalculable number of questions remain unanswered, a few of which are listed here. What is the origin of their occasionally structured appearance? Is it an ionospheric or magnetospheric effect? If it is magnetospheric, what contribution do heavy ions make to the process? Is it possible to derive information on the ionosphere from their propagation characteristics? What is their true contribution to the geomagnetic storm recovery process? Clearly, much work remains.

Chapter 4. Instrumentation

The work within this thesis is based upon data from a range of ground-based and space-based instrumentation. This chapter provides an overview of the primary instruments used and, in the case of pulsation magnetometry, the techniques used to analyse their data products.

4.1 Ground based instrumentation

4.1.1 Finnish Pulsation Magnetometer Chain

This thesis has predominantly been driven by the observation of Ultra Low Frequency (ULF) waves using the Finnish Pulsation Magnetometer Chain (FPMC). Built and maintained by the Sodankylä Geophysical Observatory (SGO) in conjunction with the Department of Physical Sciences, University of Oulu, the FPMC currently comprises of six operational search coil magnetometers. The six stations currently in operation span from Nurmijärvi (60.5° N, 24.7° E, geographic) at an L-shell value of L~3.4 to Kilpisjärvi (69.0° N, 20.8° E) at L~6.2. Built and deployed in a collaborative effort between the RSPP Group, Leicester, The Polar Geophysical Institute, Apatity and the SGO, a seventh instrument located in Barentsberg, in the Svalbard archipelago, operated between July-2005 and March-2007. During several periods of analysis in the chapters to come this seventh station was also used.

Each pulsation magnetometer consists of a tri-axial induction coil system, with a resolution of $\sim 1 \text{ pTs}^{-1}$ at 1 Hz, aligned due magnetic north, east and vertical at the time of installation. Each coil has a Fe-Ni μ -metal core and produces a voltage output according to Faraday's law,

$$V_i = -n \frac{d\phi_c}{dt}, \quad (4.1)$$

where V_i is the induced voltage, n is the number of turns in the coil and ϕ_c is the flux within the core. Given that the spectral analysis methods used throughout this work are based on Fourier theory, it is reasonable to consider the case of a sinusoidally varying magnetic field and, therefore, core flux of the form

$$\phi_c = \phi_{c\max} \cos(\omega t), \quad (4.2)$$

where $\phi_{c\max}$ is the magnitude of flux within the core and ω its angular frequency. Equation 4.1-1.1 then becomes

$$V_{\max} = n\omega\phi_{c\max} = n\omega\mu_r\mu_0H_iA_c, \quad (4.3)$$

where μ_r is the permeability of the core material, H_i is the internal magnetic field strength of the oscillating field and A_c is the area of the core. From this, a functional relationship between output voltage and magnetic perturbation can be constructed of the form,

$$V_{\max} \propto \omega H. \quad (4.4)$$

Hence, output voltage is dependent on the frequency of perturbation, which has a profound effect on its power spectral density. The inclusion of a μ -metal core increases the voltage output and sensitivity of the coil by a factor of the effective permeability of the core material but further complicates its frequency response (Göpel *et al.*, 1996). An analytical frequency response curve is not sought here; instead, a statistical method is employed that is described in Ch.5.

Output voltages are individually pre-amplified and cut-off filtered to 10 Hz, then digitised with a, GPS synchronised, sampling rate of 40 Hz. The geographic locations and coordinates of these stations can be found in table 4.1 and figure 4.1.

4.1.2 International Monitor for Auroral Geomagnetic Effects (IMAGE)

Currently the IMAGE network consists of 31 magnetometer stations in the European sector, spanning 21° of Corrected GeoMagnetic (CGM) latitude from Tartu, Estonia to NyÅlesund, Spitzbergen and 29° CGM longitude from Karmøy, adjacent to the west coast of Norway, to Hopen Island in the Barents Sea. Each station records three components (xyz, geographic) of absolute magnetic field strength. Although not identical in design, a common data format and operating parameters are adhered to by all stations. The dynamic range of each instrument is at least ± 2000 nT with a resolution of 1 nT or better (Lühr *et al.*, 1998). Irrespective of raw sampling rate, data is integrated up to 10 s at source and stored in IAGA (ASCII) format (IAGA, 1981). Station

Station	Code	Geographic		Geomagnetic		L-Shell
		Latitude	Longitude	Latitude	Longitude	
Barentsburg	BAR	78.09°N	14.12°E	75.4°N	110.3°E	16
Kilpisjärvi	KIL	69.02°N	20.86°E	66.1°N	103.3°E	6.2
Ivalo	IVA	68.55°N	27.28°E	65.3°N	108.1°E	5.8
Sodankylä	SOD	67.42°N	26.39°E	64.2°N	106.6°E	5.3
Rovaniemi	ROV	66.78°N	25.94°E	63.6°N	105.9°E	5.1
Oulu	OUL	65.08°N	25.90°E	61.8°N	104.9°E	4.6
Nurmijärvi	NUR	60.51°N	24.65°E	57.1°N	101.9°E	3.4

Table 4.1: Coordinates of the FPMC.

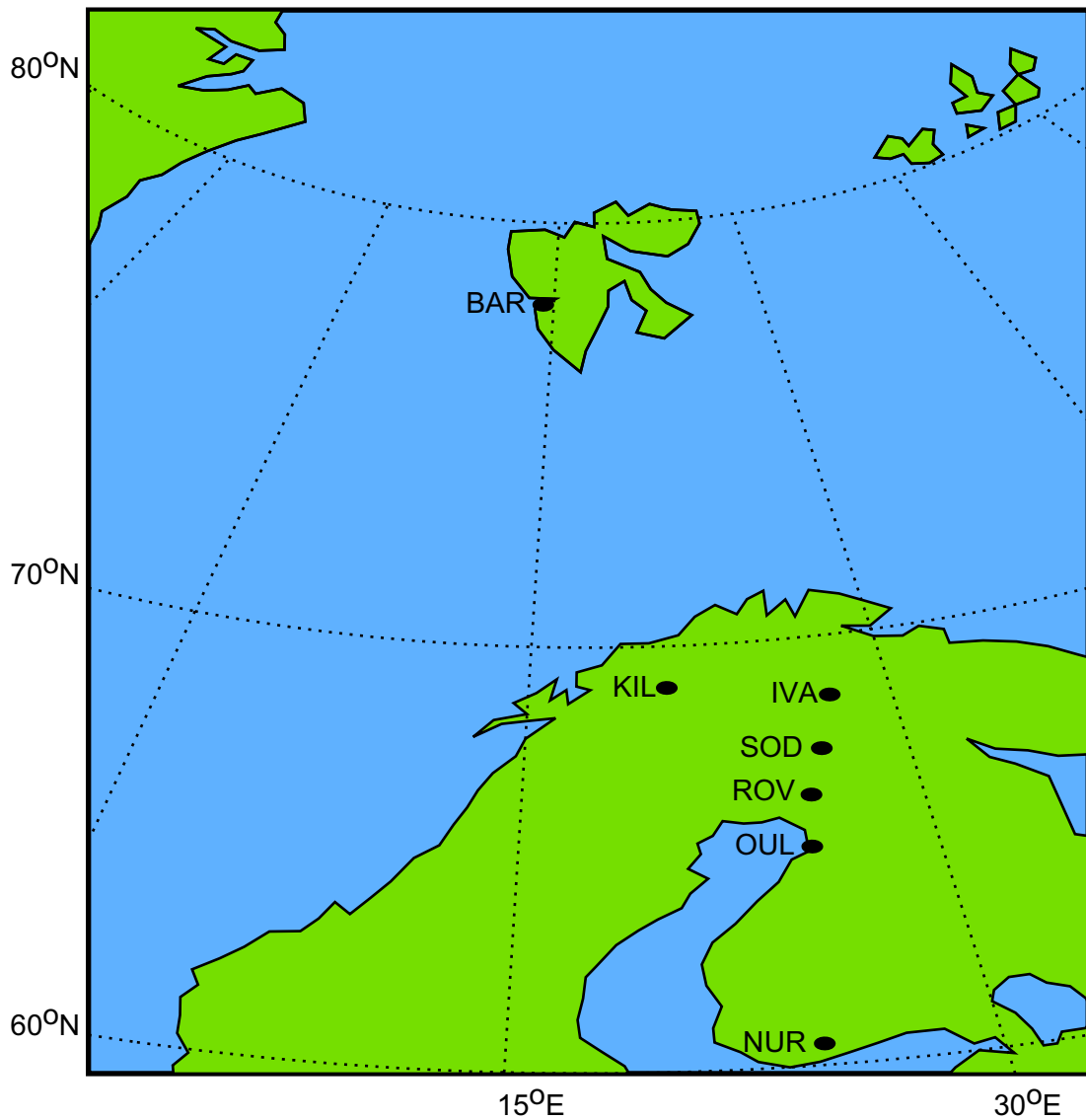


Figure 4.1: Geographic locations of the FPMC.

coordinates can be found in appendix B and a more comprehensive description of the network can be found in (Lühr, 1994).

4.1.3 Geomagnetic indices

Throughout this work, the Auroral Electrojet (AE) (Davis and Sugiura, 1966) and Horizontal Symmetric field disturbance (Sym-H) indices are used as indicators of substorm and storm activity, respectively. These one minute resolution data sets are provided by the World Data Centre for Geomagnetism, Kyoto.

The AE index is derived from excursions in the horizontal (dipole aligned) component of geomagnetic observations from between 10 and 13 stations, depending on the date considered, situated in the northern hemisphere auroral zone. Monthly normalisation is achieved by averaging data from all stations on the 5 internationally quietest days in each month then subtracting that baseline value from all measurements. The Auroral Upper (AU) and Auroral Lower (AL) indices are subsequently defined as the largest and smallest values of all data at that time, respectively. The AE and A0 indices are then derived as the difference and mean of the AU and AL values. Positive (negative) excursions in the H component of the auroral geomagnetic field are the consequence of an eastward (westward) electrojet, hence, the AE and A0 indices provide indications of the total electrojet activity and resultant auroral zonal current.

At small to moderate values of disturbance, which is the case for all intervals of study included in this work, the Sym-H index may be used as a de facto high-resolution Dst index (Wanliss and Showalter, 2006, Sugiura, 1964). The Sym-H index provides an indication of the magnetospheric ring current strength by measuring the excursion from the quiet-time mean of the horizontal component of the geomagnetic field at low-mid latitudes. Measurements are taken sufficiently poleward that the equatorial E-region electrojet does not obscure the magnetospheric component of magnetic perturbation. As with AE derivation, a monthly baseline value is computed from the 5 international quiet days in each month, however, only six of the available 11 stations currently used contributed to this mean. The location of contributing stations and a more exhaustive explanation of Sym-H derivation can be found at kugi.kyoto-u.ac.jp/aeasy/asy.pdf.

The Sym-H index is used cautiously throughout this work and consideration is in places made of the various contributions to its value. Adjustment, where appropriate, is made for the contribution of the dayside reconnection electric field (Burton *et al.*, 1975).

4.1.4 Coherent Scatter Radar (CSR)

CSR relies on the Bragg-like scattering of an emitted radio wave by small-scale irregularities to derive information on the large-scale motion of ionospheric plasma (Greenwald *et al.*, 1978, Bates and Albee, 1970). From the conservation of momentum, it can be seen that for an emitted wave, of wavevector k_r , incident on a volume of ionospheric irregularities, of wavevector k_i , the Bragg condition $k_i = \pm 2k_r$ must be satisfied in order for effective backscatter to occur (Fejer and Kelley, 1980). Ionospheric irregularities may be formed via a number of mechanisms, e.g. two-stream instability (E-region), and gradient drift and particle precipitation (F region), which are geomagnetic field aligned phenomena (Fejer and Kelley, 1980) and hence, have wavevectors that are orthogonal to the local magnetic field. For radars consisting of a single transmit/receive (Tx/Rx) station, this constrains observable ionospheric regions to those where the emitted wave is incident perpendicular to the local magnetic field.

Given that geomagnetic dip angle increases with latitude, for a ground based system, it becomes increasingly difficult to directly satisfy the orthogonality condition as the polar regions are approached. The CSRs of concern to this work use the refractive nature of the ionosphere, owing to its non-uniform density profile, to achieve orthogonality within regions of interest. Figure 4.2 (Milan *et al.*, 1997) shows a schematic diagram of some possible propagation paths and ionospheric backscatter regions for a poleward pointing High Frequency (HF) radar. The nomenclature used in the figure follows Davies (1967), in which can also be found further discussion of HF propagation modes. Ray A depicts low elevation launch and subsequent E-region backscatter. Ray C is emitted with a high elevation angle and is insufficiently refracted to achieve orthogonality and, hence, traverses the ionosphere and is lost. Ray B is the case of most interest as it allows “1^{1/2} hop” propagation, where significant refraction in the F region (1/2 hop) directs the ray earthward enabling a ground reflection (1 hop) and

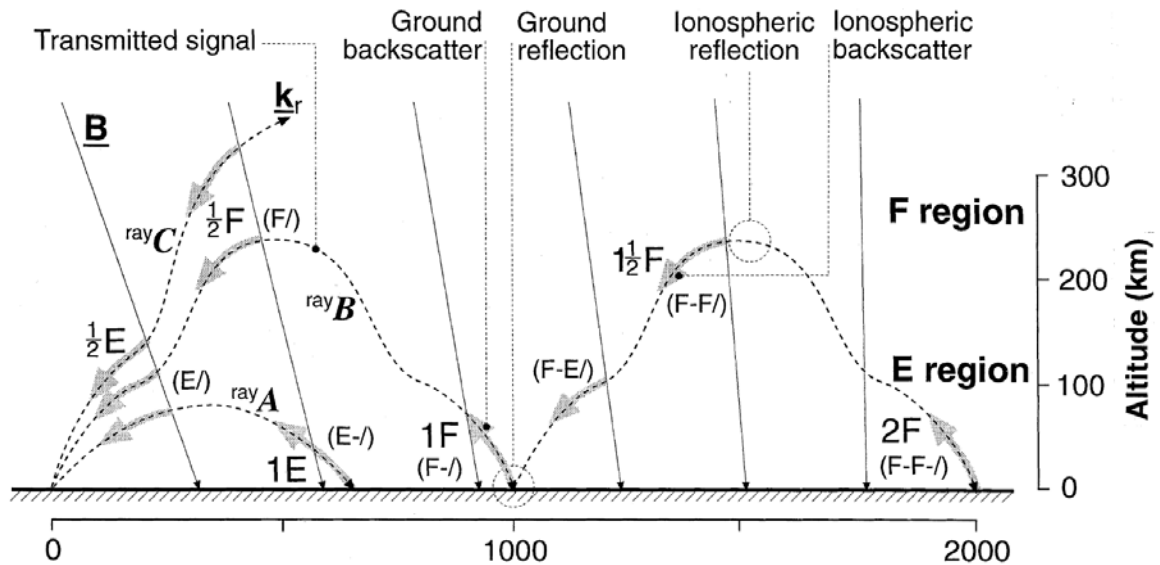


Figure 4.2. From Milan et al. (1997) A schematic diagram of some of the possible propagation modes and regions from which backscatter can occur. Mode nomenclature in parentheses follows Davies (1967). Ranges and altitudes are approximate and depend on ionospheric conditions. Three rays are illustrated: A, E region mode; B, F region mode producing far-range as well as near-range backscatter; C, a ray that penetrates the ionosphere.

a second ionospheric intersect ($1\frac{1}{2}$ hop). This scheme allows both E and F region backscatter for waves of appropriate frequency, drastically extending the range of an HF radar; albeit at the expense of interpretative ease of returns.

As of December 2010, the Super Dual Auroral Radar Network (SuperDARN; Greenwald *et al.*, 1995a, Chisham *et al.*, 2007) has 23 HF radars in operation across the globe, 16 in the northern and 7 in the southern hemisphere. Often but not exclusively deployed in pairs, to allow orthogonal, overlapping fields of view, the radars of SuperDARN are uniquely capable of mapping global ionospheric convection patterns by observing the irregularities that flow within them. Although slightly different in design, which reflects the hardware evolution that has taken place over the last decade and a half, common operating parameters and analysis techniques are employed across the entire network.

All radars are frequency agile and have programmable modes of operation. Each radar is capable of transmitting and receiving over most of the HF frequency band (8-20 MHz) and uses multi-pulse transmission from a phased array, which, typically, allows the formation of 16 independent look directions or “beams” within a Field-of-View (F-o-V) that exceeds 50° azimuth. An AutoCorrelation Function (ACF) of the received multi-pulse signal is constructed, from which an estimate of Line-of-Sight (L-o-S) Doppler velocity and spectral width may be made (Hanuise *et al.*, 1993). Transmitted pulse length dictates the range and spatial resolution along each beam. In common operation mode a $300\mu\text{s}$ pulse allows 45 km L-o-S resolution (each datum representing a range “gate”) over a range of ~ 180 km – 3500 km (75 gates). A dwell time of 3 or 7 s on each of the 16 beams creates a full F-o-V scan every 1 or 2 complete minutes, necessarily so to allow synchronisation between radars.

Overlapping fields of view allow vector merging of L-o-S measured velocities (Cerisier and Senior, 1994), from which true ionospheric flow vectors may be derived (Greenwald *et al.*, 1995a). However, to find a truly global representation of ionospheric flows, given that the entire earth cannot be covered with bi-static F-o-Vs, a best fit of all available L-o-S velocities to a model distribution of ionospheric electrostatic potential may be made. The Map Potential routine (Ruohoniemi and Baker, 1998) achieves this fit through the spherical harmonic series expansion of electrostatic potential

distribution, constrained by statistical models (Ruohoniemi and Greenwald, 2005, Ruohoniemi and Baker, 1998) that depend on the current IMF conditions. The global convection maps created by the Map Potential routine have proved to be powerful tools in diagnosing the large-scale morphology of the ionosphere and the physical processes that drive them e.g. (Chisham *et al.*, 2007) as is evidenced in the current work.

Two of the SuperDARN radars are of particular interest to the studies that follow, those of Hanksalmi (HAN) and Pykkvibær (PYK), which form the Co-operative UK Twin Located Auroral Sounding System (CUTLASS) (Milan *et al.*, 1997). The CUTLASS radars are identical in design and capability. They each consist of a main array of 16 polarised log periodic Tx/Rx antennas and a back interferometer array of 4 Rx only antennas, which allows the determination of elevation angle of arrival via cross-correlation of the main and back array received signals. The F-o-Vs of both radars encompass the EISCAT Svalbard Radar (4.1.5) and the upper section of the FPMC (4.1.1) which enables coordinated studies of small and large scale wave and plasma phenomena to be made. A key capability of CUTLASS that is shared by all type-3 Super DARN radars is their Stereo mode of operation (Lester *et al.*, 2004). Stereo mode utilises spare segments of the standard duty cycle to interleave a second Tx/Rx sequence in to normal operation, effectively creating two independent radar channels that may operate simultaneously. This enables a standard scan pattern to be maintained concurrently with a high temporal or spatial resolution scan that may focus on a region of interest, as shall be seen in chapter 7.

4.1.5 Incoherent Scatter Radar (ISR)

The primary backscatter mechanism for the emitted beam of an ISR is Thomson scattering from individual electrons in the target volume. The random motion and orientation of the electron population produces the so-called incoherent scatter spectrum. However, there is a contribution of Bragg-like backscatter also. Unlike the case of CSRs however, the origins of the ionospheric density structures from which waves are scattered are not field aligned irregularities but a Fourier spectrum of thermal fluctuations, which must satisfy some plasma wave dispersion relation. In further contrast to CSR the thermally associated density gradients are weak, have short correlation times and have small spatial scales; hence, the backscatter power generated

by them is considerably lower. Consequently, the transmitted frequency must be considerably higher than the HF used for coherent scatter experiments, as must transmitted power. Typical, although not exclusively, ISR operating frequencies are in the UHF (0.3 – 3 GHz) range; with average transmit powers ranging from 100 kW – 1 MW, ~ 3 orders of magnitude larger than the SuperDARN radars. Given the nature of these density structures, there is no need for orthogonality to a geomagnetic field line to ensure effective backscatter.

The predominant plasma wave modes that allow information on the scattering target to be derived are the ion acoustic and Langmuir modes. Each of these wave modes induce a Doppler shift in the returned signal that corresponds to their wave front propagation velocity both toward and away from the radar resulting in upward and downward shifted “ion” and “plasma” lines. This can be seen in figure 4.3, which is a cartoon of a received ISR signal. Ion lines are broadened and merged, by Landau and collisional damping, to form a single line, the shape of which is dictated by ion and electron temperatures and the ion-neutral collision frequency.

The central spectral shift from the transmitted frequency relates to the L-o-S plasma velocity. From the returned spectrum, it is also possible, with a few assumptions, to derive directly electron concentration, from plasma lines, and ion and electron temperatures, from the separation and height of the ion line peaks. Additional assumptions and model constraints must be employed to derive a host of further parameters, which shall not be considered here.

The European Incoherent SCATter (EISCAT) Scientific Association operates a number of ISR facilities throughout the fennoscandian sector. Data from the highest latitude of these ISRs is used to elucidate ionospheric dynamics in chapter seven of this thesis. The EISCAT Svalbard Radar (ESR) (Wannberg *et al.*, 1997) facility sits atop the Breinosa Mountain on the edge of the Advent Valley on the island of Spitzbergen at 78.09° N 16.02° E, which is often engulfed by the polar cap region and occasionally at the geomagnetic footprint of the magnetospheric cusp. In operation since 1996, the ESR is a twin incoherent scatter radar system, with static, geomagnetic field aligned (81.6° elevation, 182° azimuth) 42 m and fully steerable 32 m parabolic dishes. Figure 4.4 is a photograph of the ESR taken during an experimental campaign in 2007. With an

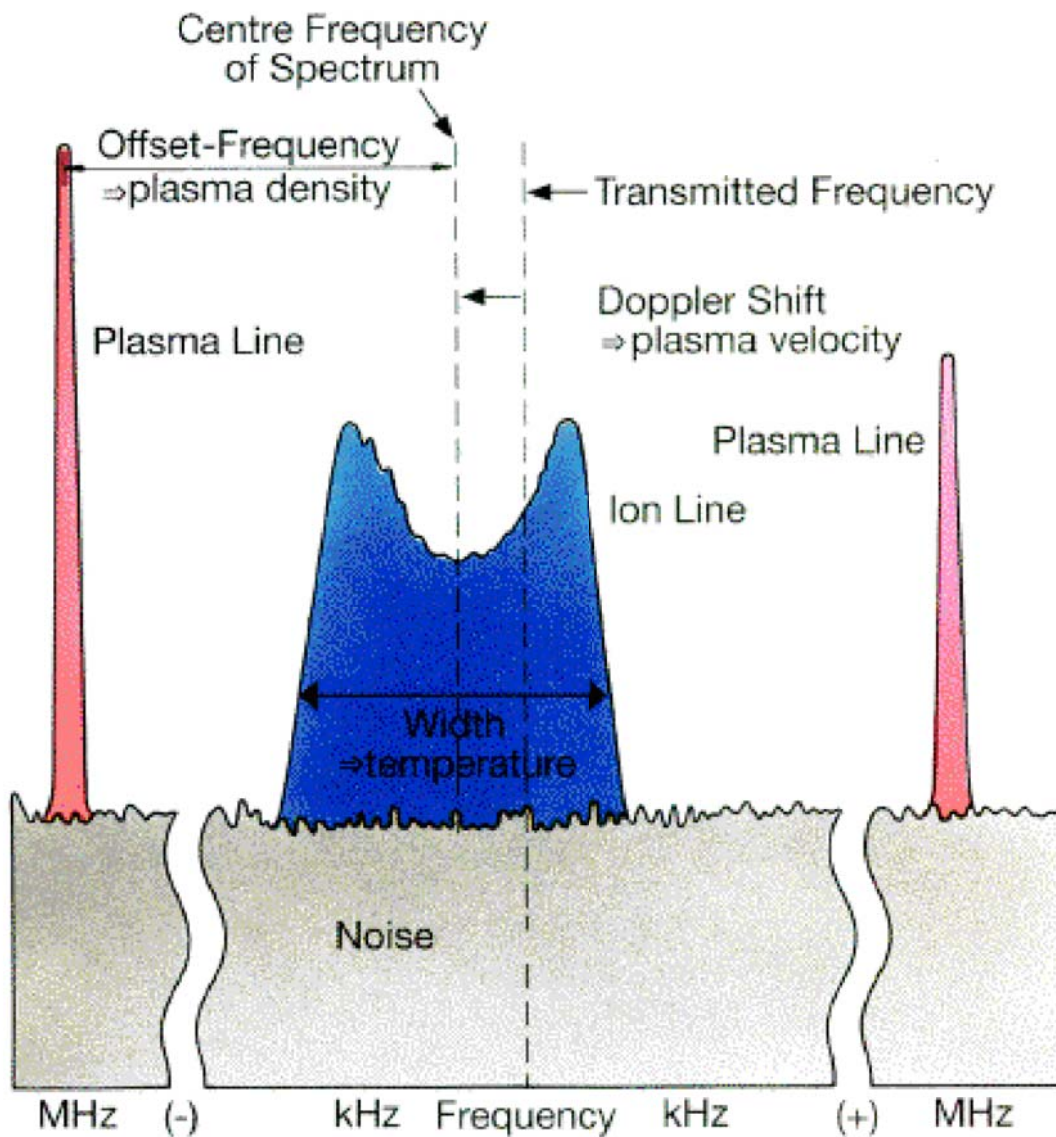


Figure 4.3: Cartoon of an incoherent scatter radar backscatter spectrum. The line encompassing the blue region represents the merged up and down shifted ion lines, from which electron and ion temperatures and ion-neutral collision frequency may be derived. The red regions represent plasma lines, which reveal electron density and the central shift from transmission frequency gives the L-o-S plasma flow velocity. Image credit: Eiscat Scientific Association.



Figure 4.4: Images of the EISCAT Svalbard Radar dishes taken on experimental campaign in February 2007. Upper plate shows the 32 m fully steerable dish, lower plate the fixed field-aligned 42 m dish.

operating frequency of 500 ± 2 MHz and an average operating power of 250 kW, the ESR has an observable range that extends across the entire ionosphere from ~ 70 km – >1300 km. The ESR allows for a great range of experimental set-ups, executed as Special Programmes (SP) but operates routinely in a number of Common Programs (CP) Figure 4.5 and table 4.2 show the Radar efficiency – range profile and pulse schemes for four ESR Common Programmes.

4.2 Space based instrumentation

4.2.1 The OMNI dataset

The interplanetary data used throughout this work are derived from the four spacecraft, Advanced Composition Explorer (ACE; Stone *et al.*, 1990), Wind (Franz *et al.*, 1998), Interplanetary Monitoring Platform 8 (IMP-8; King, 1971) and Geotail (Nishida *et al.*, 1992), that comprise the High Resolution OMNI (HRO) dataset (King and Papitashvili, 2010). ACE and Wind currently occupy Lissajous orbits about the L1 Earth-Sun Lagrange point, whereas the geocentric orbital paths of IMP-8 and Geotail are eccentric and inclined. From the multitude of measurements made by each satellite, the current studies are concerned only with the magnetic field and particle data products. For a more comprehensive description of instrumentation, the interested reader is directed to King (2010) and references therein.

Although differing in design, sensitivity and sample rate, each spacecraft carries a triaxial flux gate magnetometer capable of sub-minute sampling. Plasma data are obtained using a range of instrumentation; however, the positive ion measurements of relevance to the OMNI dataset are made in the following manner: ACE and Geotail employ electrostatic analysers, whereas Wind and IMP-8 use Faraday cups to derive temperature, density and 3-dimensional velocity information.

One minute resolution magnetic field and plasma values are then constructed from the native data, which are then time shifted to the Earth's Bow Shock Nose (BSN) and their time tags reordered accordingly. The method of time shifting applied to the original data is based upon the determination of the magnetic field Phase Front Normal

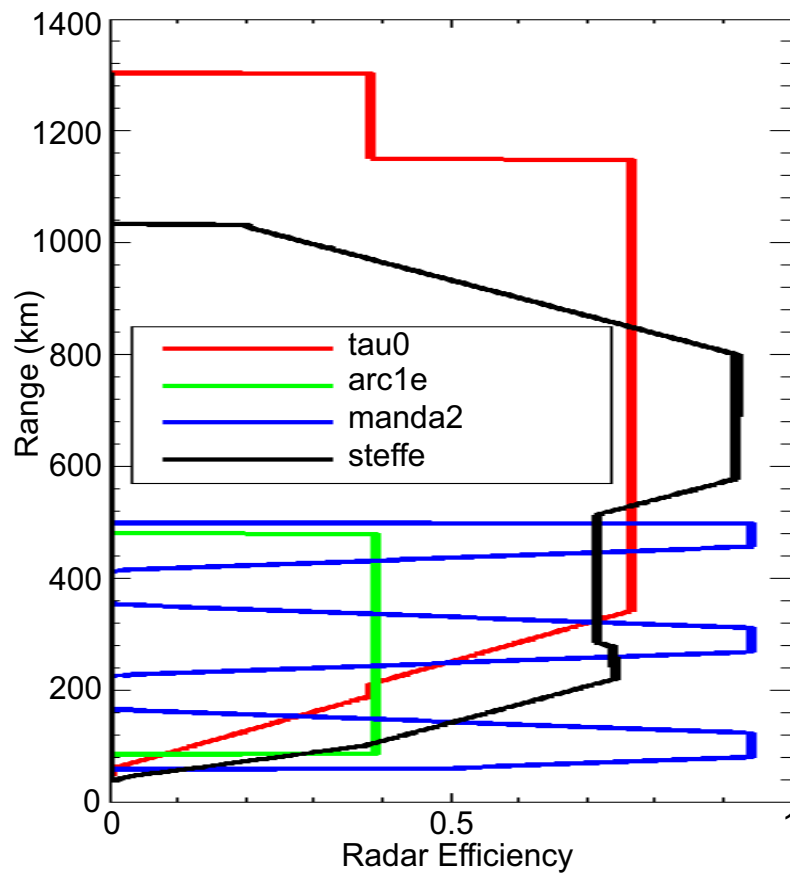


Figure 4.5: ESR Common Program Radar efficiency - range profile

Experiment name	Dish	Pulses (μs)	Sampling rate (μs)	Resolution (km)	Ranges (km)	Plasma line	Time resolution (s)
steffe	single, switchable	16x30 + 16x105 AC	15	2.2 - 16	36 - 1034	2x2x1.7 MHzHz	6
tau0	single, switchable	two 16x60 AC	20	3-9	58 - 1304	-	6.4
manda	single	59x5 AC	5	0.75	60 - 499	-	4
arc_slice	single, switchable	64x6 AC	6	0.9	85 - 481	-	0.5

Table 4.2: ESR Common Program pulse schemes.

(PFN) direction and linear extrapolation to the BSN position at the solar wind flow velocity,

$$\Delta t = \frac{n \cdot (R_{BSN} - R_{sc})}{n \cdot V}, \quad (4.5)$$

where Δt is applied time shift, R_{BSN} and R_{sc} are the positions of the bow shock nose and space craft, V is solar wind flow velocity and n is the PFN direction derived in the following fashion.

PFN determination is achieved with a combination of two independent methods; the Cross Product (CP; Knetter *et al.*, 2004) and Kharbrov or MVAB-0 (Haaland *et al.*, 2006, Sonnerup and Cahill Jr, 1968) techniques. The CP technique computes the cross product of the magnetic field components before and after a tangential discontinuity. MVAB-0 is Minimum Variance Analysis under the condition that the average field in the direction of the PFN is zero, which may be stated as $\langle B \rangle \cdot n = 0$, where B is magnetic field. The CP method is preferentially applied; however, when it fails to yield an acceptable result the MVAB-0 derived PFN is used.

The OMNI data team (King and Papitashvili, 2010) emphasise that this method of data propagation does allow “out of sequence” measurements to occur in final OMNI data products, where the time shift of one datum is greater than that of the preceding time shift plus the sample interval. This effect is not mitigated for; hence, caution must be exercised when applying periodic time series analysis techniques to any OMNI data product. It is for this reason that such analysis is not directly attempted in any of the current studies, which only use OMNI data as approximate indicators of solar wind behaviour.

4.2.2 Los Alamos National Laboratory (LANL) geosynchronous satellites

The current fleet of LANL satellites make continuous energetic particle measurements at geosynchronous orbital altitude. 19 LANL satellites have flown since their introduction in the mid 1970s, of which 5 are currently operational. All satellites are earthward axis-spin stabilised with a period of ~ 10 s. Each of the current LANL satellites is equipped with three instruments: a Synchronous Orbit Particle Analyser

(SOPA), a Magnetospheric Plasma Analyser (MPA) and an Energy Spectrometer for Particles (ESP).

The ESP instrument measures electron and ion energies in the MeV range, which is above that necessary for the current studies, hence, the interested reader is directed to (Meier *et al.*, 1996) for further information. MPA (Bame *et al.*, 1993) has an axis-normal field of view that allows 90% of the unit sphere to be sampled during each rotation using a set of six Channel Electron Multipliers. It is capable of fully determining 3-dimensional ion and electron distributions in an 8-spin cycle of 86 s. The energy range of this instrument, for both ions and electrons, is $\sim 1\text{eV} - 40\text{ keV}$. The SOPA instrument (Belian *et al.*, 1992) consists of three solid-state detector telescopes of 11° Fields-of-View and pointing directions, 30° , 90° and 120° to the satellite's spin axis. The combined use of thin front and thick back detectors allows Pulse Height Analysis (Krimigis *et al.*, 1977) to be performed, enabling the detection and discrimination of heavy ion species as well as electrons and protons. Its energetic range is $50\text{ keV} - 2\text{MeV}$ for electrons, $50\text{ keV} - \sim 50\text{ MeV}$ for protons and $0.5\text{ MeV} - \sim 15\text{ MeV}$ for heavier ions and it is capable of measuring the full spatial particle distribution in each $\sim 10\text{ s}$ spin period.

4.2.3 Defence Meteorological Satellite Program

From their inception in mid 1960s, the DMSP series of satellites have provided global meteorological, oceanographic and solar terrestrial measurements. In near circular, quasi-sun synchronised orbits of ~ 100 minute period and altitude of $848 \pm 22\text{ km}$, at any one time at least two DMSP satellites are operational and are out of orbital rotational phase by $\sim 90^\circ$ (Rich and Hairston, 1994).

This thesis considers data from two of the multitude of instruments aboard the DMSP-F15 satellite, those of the Special Sensor Precipitating Electron and Ion Spectrometer (SSJ/4) (Hardy *et al.*, 1984) and the Ion Drift Meter (IDM), which is part of the SSIES suite of plasma sensors. The SSJ/4 instrument consists of two sets of electrostatic analysers, one set ion and one set electron, with a combined detection range of 30 eV to 30 KeV measured over 20 logarithmically spaced channels at 1 s temporal resolution. The IDM calculates ion angle of arrival by comparing the ion current falling

on each of its detector's four sectors, from which it derives the cross track vertical and horizontal drift velocities at 6 Hz temporal resolution. All IDM data used in this thesis are averaged to 4 s.

Chapter 5. Pulsation Analysis Techniques

This chapter investigates the techniques that were developed to process and analyse the geomagnetic pulsations of interest in subsequent chapters. Although the techniques described here may be applied to a range of geophysical timeseries, all data used in this chapter were recorded by the Finnish Pulsation Magnetometer Chain (FPMC), details of which may be found in Ch. 4.1.1.

5.1 Introduction

The characteristics of the multitude of waves that propagate throughout the terrestrial magnetosphere-ionosphere system provide diagnostics of their generation mechanisms and propagation modes. The nomenclature of ULF waves and the frequency boundaries that define their subclassifications were chosen to enable meaningful discussion of their driving phenomena (IAGA, 1981). Similarly, analysis techniques have evolved to maximise the useful information that can be extracted from observation. When investigating global scale wave phenomena such as Field Line Resonances, it is useful to consider each component of the magnetic field variation independently as well as the overall polarisation of the observed wave (Chisham and Orr, 1997). However, for small-scale travelling wave phenomena such as Pc1-2 it is more useful to gain knowledge of the polarisation characteristics that may reveal information on their source or propagation media.

Satellite measurements of electric and magnetic fields must be transformed into meaningful coordinate systems, hence full 3-dimensional analysis is appropriate. However, observation on the ground is prone to interference from the contribution of the electrically conducting earth, more so in coastal areas where the similarly conductive ocean may introduce significant electric current flows. In general, the vertical component suffers greatest from ground contamination (Raita, T., personal communication).

The ever-growing quantity of magnetometer observations calls for efficient and appropriate processing methodology. This chapter outlines the spectral methods

employed throughout this thesis and the techniques developed to extract and categorise pulsation events of interest. Consideration is made of the merits of treating the horizontal (H & D) components of magnetic field variation independently, requiring two Fourier transforms, or as a single combined complex signal, requiring only one. The use of frequency domain cross-phase analysis as a method of determining the time delay between spaced observations is also discussed. The derived time delays are subsequently used in a simple triangulation technique to highlight their potential usefulness.

5.2 Spectral analysis techniques

The magnetic field time-series analysis employed throughout this thesis is primarily based on the Fourier transform of digitised data from the time to the frequency domain. The aim of such analysis is to derive an estimate of the characteristics that appropriately describe the ULF wave activity driving the observed magnetic perturbations.

5.2.1 Fourier analysis

Historically, a number of time-domain, analogue methods have been used to extract similar estimates (e.g. Webster, 1982, Fraser, 1975, Summers and Fraser, 1972). However, these techniques assume analysis of singular, monochromatic waves, which, as shall be seen in subsequent chapters, is rarely the case. The availability of economical computation in the late 1960s saw a flourish of techniques emerge that employ frequency-domain manipulation to derive spectral parameters. This section will briefly discuss the more common methods of polarisation analysis in the (assumed) principal plane of propagation.

The forward Fourier transform, F , of an infinitely long, continuous time-series, f , is given by:

$$F = \int_{-\infty}^{\infty} f e^{-i\omega t} dt, \quad (5.1)$$

its reverse transform being given by:

$$f = \frac{1}{2\pi} \int_{-\infty}^{\infty} F e^{i\omega t} d\omega, \quad (5.2)$$

where t is time and ω is angular frequency. Hence, for each value of ω in the spectrum, the Fourier amplitude, $F(\omega)$, which is generally complex, is given by

$$F(\omega) = r(\omega) e^{i\theta(\omega)}, \quad (5.3)$$

where r is the modulus of the Fourier coefficient and the complex phase angle, θ , is given by $\theta = \omega t$. However, sampled at intervals of δ , at times t_j , where $j = 0, 1, 2, \dots, N-1$, the digitised magnetometer data analysed here represents a discrete, finite data-set, for which the Discrete Fourier Transform (DFT) must be used. The DFT (F_k) is given by

$$F_k = \sum_{j=0}^{N-1} f_j e^{\frac{-2\pi i k j}{N}} = \sum_{j=0}^{N-1} f_j e^{-i\omega_k t_j}, \quad (5.4)$$

where N is the total number of samples (f_j) and

$$\omega_k = \frac{2\pi k}{N\delta}. \quad (5.5)$$

For speed of computation, the Fast Fourier Transform (FFT) (Cooley and Tukey, 1965) is routinely used. The Cooley-Tukey FFT operates a Decimation In Time algorithm that is optimised when the number of points in the time series is a power of 2, 3 or 5, which has dictated the window length of routinely analysed data.

The temporal evolution of derivable parameters is of great interest to the following studies; hence, the commonly applied (Song and Russell, 1999) dynamic spectra method has been used throughout. With the exception of cases where the effects of windowing were investigated, the number of points, N , in each FFT window, n , was governed by aforementioned constraints of the FFT algorithm. The overlap of each window was generally governed by the process under inspection, with care being taken when interpreting neighbouring spectra that share a significant number of data. Equation 4.3.4 may be restated for the case of the dynamic spectra as

$$F_n(\omega) = r_n(\omega) e^{i\theta_n(\omega)}. \quad (5.6)$$

Although the instruments used in the following chapters record three orthogonal components of magnetic field, the following discussion is restricted to the components in the horizontal plane. The Z component of FPMC data is known to be relatively more susceptible to ground effects, which vary from site to site and are yet to be quantified. Subsequently, full tri-axial analysis (Arthur *et al.*, 1976) will not be addressed here.

5.2.2 Spectral Matrix Analysis (SMA)

Originating in the field of optics, the spectral or coherence matrix (Born *et al.*, 1959) has been at the heart of polarization analysis in the field of electromagnetic wave propagation for many decades. The method of spectral matrix construction is ultimately unimportant in the context of this discussion; however, for continuity the Fourier transform and associated notation is employed throughout. The following outline assumes wave propagation in the z direction. Hence, without transforming to the principal axis of propagation this analysis solely describes the polarisation characteristics in the horizontal plane.

The magnetic field components in the horizontal plane, h and d, may be used to construct a spectral matrix of the form,

$$J(\omega) = \begin{bmatrix} H(\omega)H^*(\omega) & H(\omega)D^*(\omega) \\ D(\omega)H^*(\omega) & D(\omega)D^*(\omega) \end{bmatrix}, \quad (5.7)$$

where $H(\omega)$ and $D(\omega)$ represents the Fourier transform of the h and d time-series, respectively and * denotes the complex conjugate.

The total intensity (I) of the input signal is given by the diagonal elements of the matrix as:

$$I(\omega) = J_{11}(\omega) + J_{22}(\omega) \quad (5.8)$$

and the ratio, R , of polarised to total intensity is given by:

$$R(\omega) = \left[1 - \frac{4|J(\omega)|}{(J_{11}(\omega) + J_{22}(\omega))^2} \right]^{\frac{1}{2}}. \quad (5.9)$$

The angle between the semi-major axis of the polarization ellipse and the h axis, its orientation, α , is derived from:

$$\tan(2\alpha(\omega)) = \frac{2|J_{12}(\omega)|}{J_{11}(\omega) - J_{22}(\omega)} \sin(\theta_D(\omega) - \theta_H(\omega)), \quad (5.10)$$

where $\theta_D(\omega) - \theta_H(\omega)$ represents the complex cross-phase angle between the two components. Similarly, the ratio of semi-minor to semi-major or ellipticity, ε , can be derived from

$$\sin(2\varepsilon(\omega)) = \frac{2|J_{12}(\omega)|}{J_{11}(\omega) + J_{22}(\omega)} \sin(\theta_D(\omega) - \theta_H(\omega)), \quad (5.11)$$

where the sign of ε indicates the direction of polarisation with respect to the assumed plane of propagation, negative (positive) indicating right-hand (left-hand) polarisation.

This method is robust, although, requires an FFT of each component to be performed, which can become computationally restrictive when analysing large datasets.

5.2.3 Complex Input Spectral Analysis

If, as with the spectral matrix method above, it is assumed that the plane of polarisation is close to horizontal or at least that analysis in the horizontal plane is of deductive value, then a spectral technique that has its origins in oceanographic flow analysis proves computationally advantageous with minimal loss of useful information.

The rotary-component method (Gonella, 1972, Mooers, 1970), which is similar in construction to the goniometry method (Fraser and Webster, 1979), combines the real orthogonal components of a vector time series to form a complex signal that is then Fourier transformed in the usual manner. In the present case, the H and D components of the measured magnetic field fluctuations form the complex time series:

$$f_{(t)} = h_{(t)} + id_{(t)}, \quad (5.12)$$

which is displayed graphically in the Argand diagram of figure 5.1. This method has previously been applied to heater induced ELF/VLF wave analysis (Rietveld *et al.*, 1987) and more recently to naturally occurring waves in the same frequency range by Maninnen (2005), whose scheme is approximately outlined here.

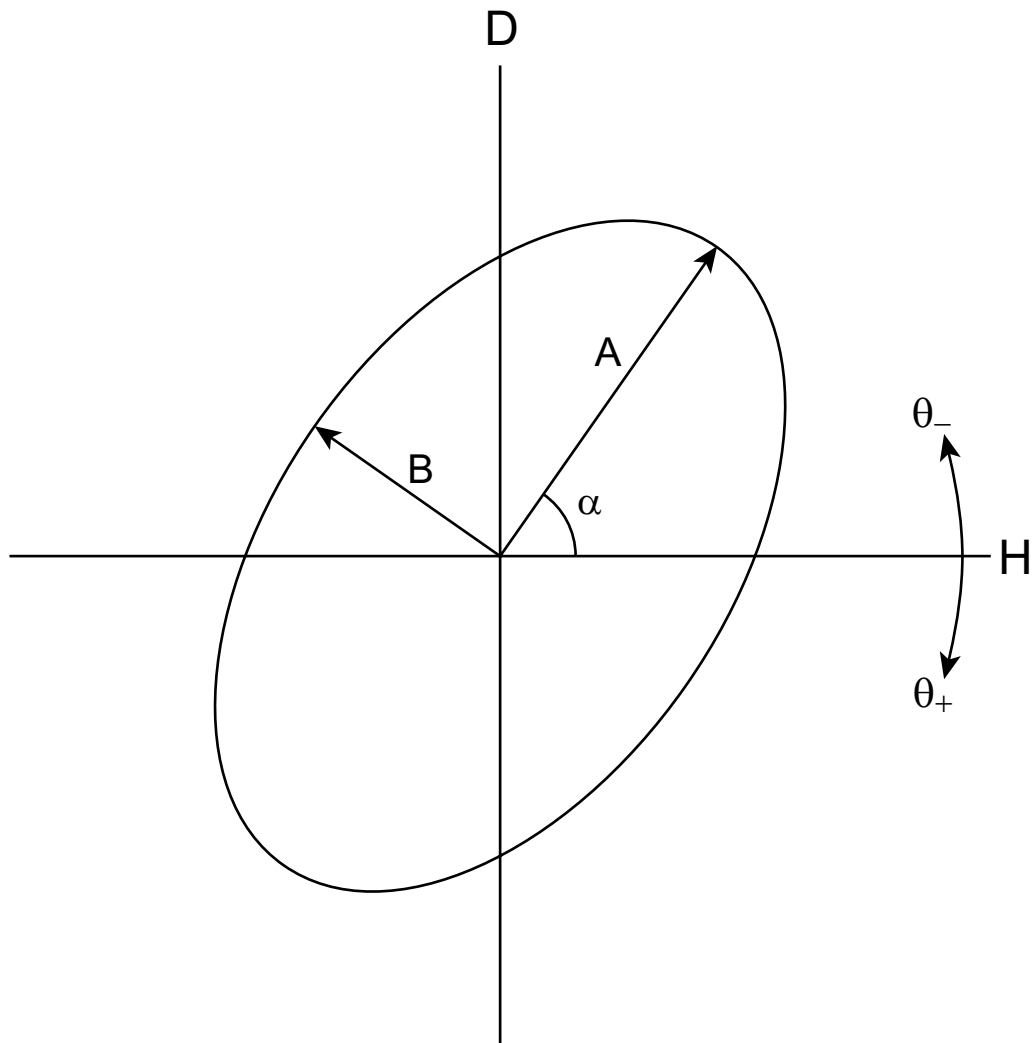


Figure 5.1: Magnetic field polarisation ellipse for an idealised ULF wave, recorded by an instrument of the FPMC aligned along the H and D directions; adapted from Manninen (2005). The ellipse may be completely described by two vectors, rotating in opposite directions with phase angles θ_+ and θ_- . The length of the semi-major and semi-minor axes, A and B, are given by the sum and difference of the Fourier coefficient moduli for that frequency. The angle α is the orientation of the polarisation ellipse and is given by the mean value of the phase angles for each polarisation vector at that frequency.

Unlike the symmetrical spectrum of the purely real time-series in the previous section, the Fourier transform of this complex input has unique amplitudes for both positive and negatives values of angular frequency, such that equation 5.3 must be restated as:

$$\begin{aligned} F(\omega) &= r_+ e^{i\theta_+} \\ F(-\omega) &= r_- e^{i\theta_-} \end{aligned} \quad (5.13)$$

Applying the reverse Fourier transform, it can be seen that the input signal is completely described by the sum of two oppositely rotating vectors that represent the left- and right-hand polarisation components,

$$S_\omega(t) = r_+ e^{i\omega t + i\theta_+} + r_- e^{-i\omega t + i\theta_-} . \quad (5.14)$$

The semi-major and semi-minor axes of the ellipse they sweep out are given by the sum and difference of the Fourier coefficient moduli. As with the spectral matrix method, its ellipticity is given by the ratio of semi-minor and semi-major axes, which can be calculated directly as,

$$\varepsilon = \frac{r_+ - r_-}{r_+ + r_-} ; \quad (5.15)$$

its value ranging from -1 (right-hand circular) to +1 (left-hand circular), with zero denoting linear polarisation. The polarisation ellipse orientation angle is given by the mean phase angle of the two rotating vectors, hence,

$$\alpha = \frac{\theta_+ + \theta_-}{2} . \quad (5.16)$$

The total power spectral density or intensity, I_T , of the signal is given by the sum of the squared moduli of both polarisation components:

$$I_T = r_+^2 + r_-^2 , \quad (5.17)$$

from hereon in, unless explicitly stated, “total power” will refer to vaule of this parameter. The squared difference in polarisation component moduli (the squared length of the semi-minor axis) represents the purely circulatory element of the total power spectral density and is given by

$$I_C = (r_+ - r_-)^2 , \quad (5.18)$$

Subsequently, the linear element of power spectral density must be the remainder,

$$I_L = 2r_+ r_- . \quad (5.19)$$

The degree to which a wave is circularly polarised is then given by

$$PR_c = \frac{I_c}{I_T}. \quad (5.20)$$

5.2.4 Complex input versus spectral matrix analysis

The merits of digital spectral analysis over analogue methods were discussed the section 5.2.1 and while the techniques discussed here may be applied to analogue data, only digital analysis will be considered. Although the techniques under consideration here both employ the Cooley-Tukey Fast Fourier Transform (5.2.1) and derive polarisation parameters in mathematically equivalent manners they differ in the number of transforms and matrix multiplications and additions necessary for their derivation; hence, their computation times are significantly different.

The SMA method requires a minimum of 4 complex arrays, 7 floating-point arrays, 39 multiplications, 7 additions and 2 trigonometric operations whereas the CISA method requires at least 2 complex arrays, 11 floating-point arrays, 12 multiplications, 6 additions and 1 trigonometric operation. However, the processing time in IDL is significantly affected by the execution of the FFT algorithm, which with moderately optimised coding accounts for ~25% of the total processing time. The overall processing time when using the SM method is empirically found to be ~1.6 that of the CISA method. Hence, use of the CISA method represents a considerable absolute saving, when analysing large datasets.

The output from each method differs only in the value of total power and the polarisation ratio, where SMA (CISA) calculates the linear (circular) polarisation content. To illustrate the equivalence and differences between these methods, the following section applies the progressive background extraction technique, which will be outlined in section 5.3.1, to the example pulsations that will be considered fully in sections 5.3.2 and 5.3.3 and to a third, multi-structured pulsation recorded on 24th of May 2006. The IVA observation of this multi-structured pulsation is displayed in figure 5.2. Although rising tone dispersion can be seen throughout this event, its fine element structure appears to be significantly more varied than the previous simple example.

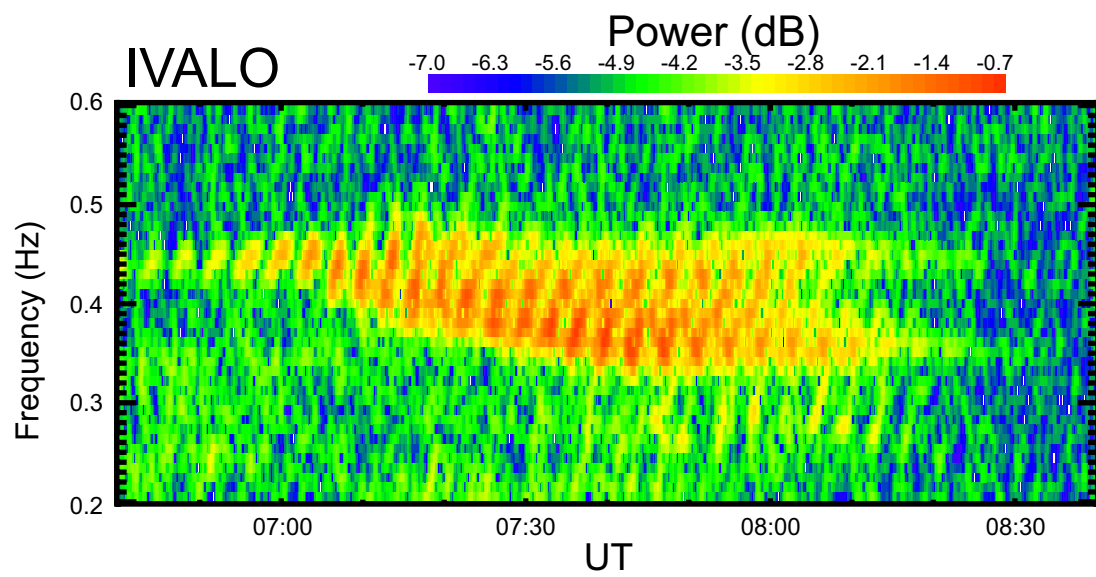


Figure 5.2: Dynamic spectrum for the 24th of May 2006, in which can be seen a Multi-structured pulsation, commencing at ~06.40 UT.

Each method's susceptibility to noise may be assessed by adding uniformly distributed random noise to both components prior to FFT and thresholding. To demonstrate this, increasing levels of noise were added to both the unstructured and simple structured pulsations recorded again at the IVA station. The results of which are shown figures 5.3 and 5.4, for the structured and unstructured cases, respectively. The left hand columns of both figures display the output from the CISA method and right hand columns the output from SMA. The uncontaminated signal is shown in the top panels, with increasing levels of noise added to each subsequent panel below. The CISA method appears to be more resistant to random noise than SMA.

Figure 5.5 presents the processed dynamic spectra and polarisation parameters, ellipticity, polarisation ellipse semi-major axis angle and polarisation ratio for the multi-structured pulsation shown in figure 5.2. The upper-left set of six panels consists of total power spectra from KIL (upper), IVA (middle) and ROV, (lower) processed with the CISA (left column) and SMA (right column) methods. Each set of six panels displays a given polarisation parameter and is of the same layout as the power spectra. The figure demonstrates the equivalence of the derived spectral parameters from each method. However, slight deviations in the extracted frequency limits can be seen, most notably in the lower frequencies at KIL. Evident from the figure is that the multi-structured pulsation has distinct regions of consistent polarisation parameters, unique to each station. The parameter coherence of such regions allows the isolation of multiple superimposed pulsations.

5.2.5 Correlation analysis

The multi-station nature of the magnetometer networks utilised in this thesis allows spatial comparison of a single event at multiple locations. This may be achieved in either the time or frequency domain. However, if performed in the time domain, the same restrictions would apply as with the polarisation analysis outlined above. Hence, cross-correlation is performed in the frequency domain, using the Fourier coefficients generated from the polarisation analysis procedure.

The cross-correlation coefficient of two time series, f_1 and f_2 , is

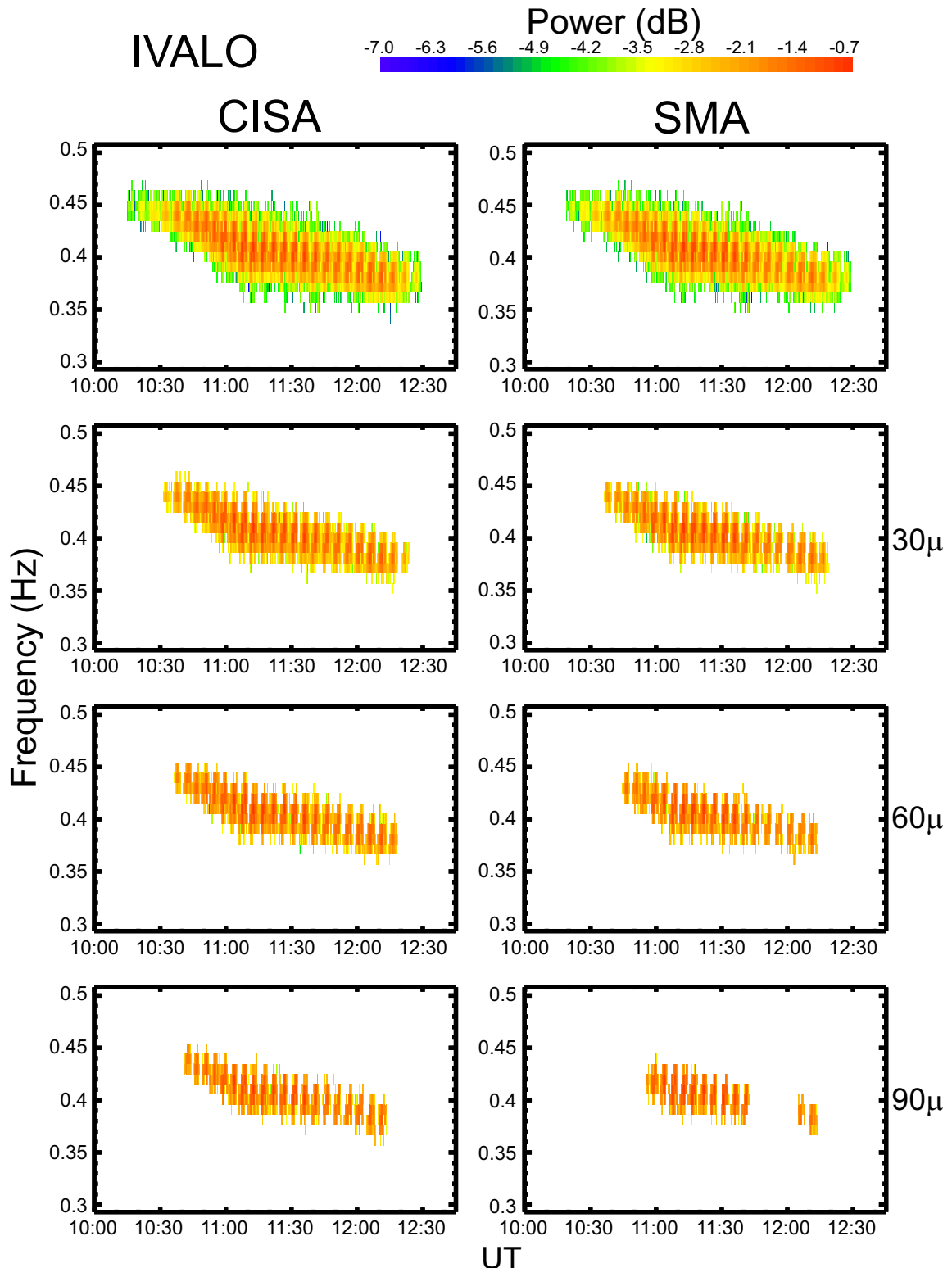


Figure 5.3: Dynamic spectra of the structured pulsation recorded on 03/05/2006 at Ivalo. The left (right) hand column has been generated with the CISA (SMA) method. Each spectrum has been thresholded with the technique described Ch. 5.3.1. The top panels are uncontaminated; uniformly distributed random noise is injected at greater magnitudes with each successive panel downward. The level of noise is indicated at the side of each row, where μ is the standard error of the original signal. The CISA method appears to be more resistant to this type of noise than the SMA method does.

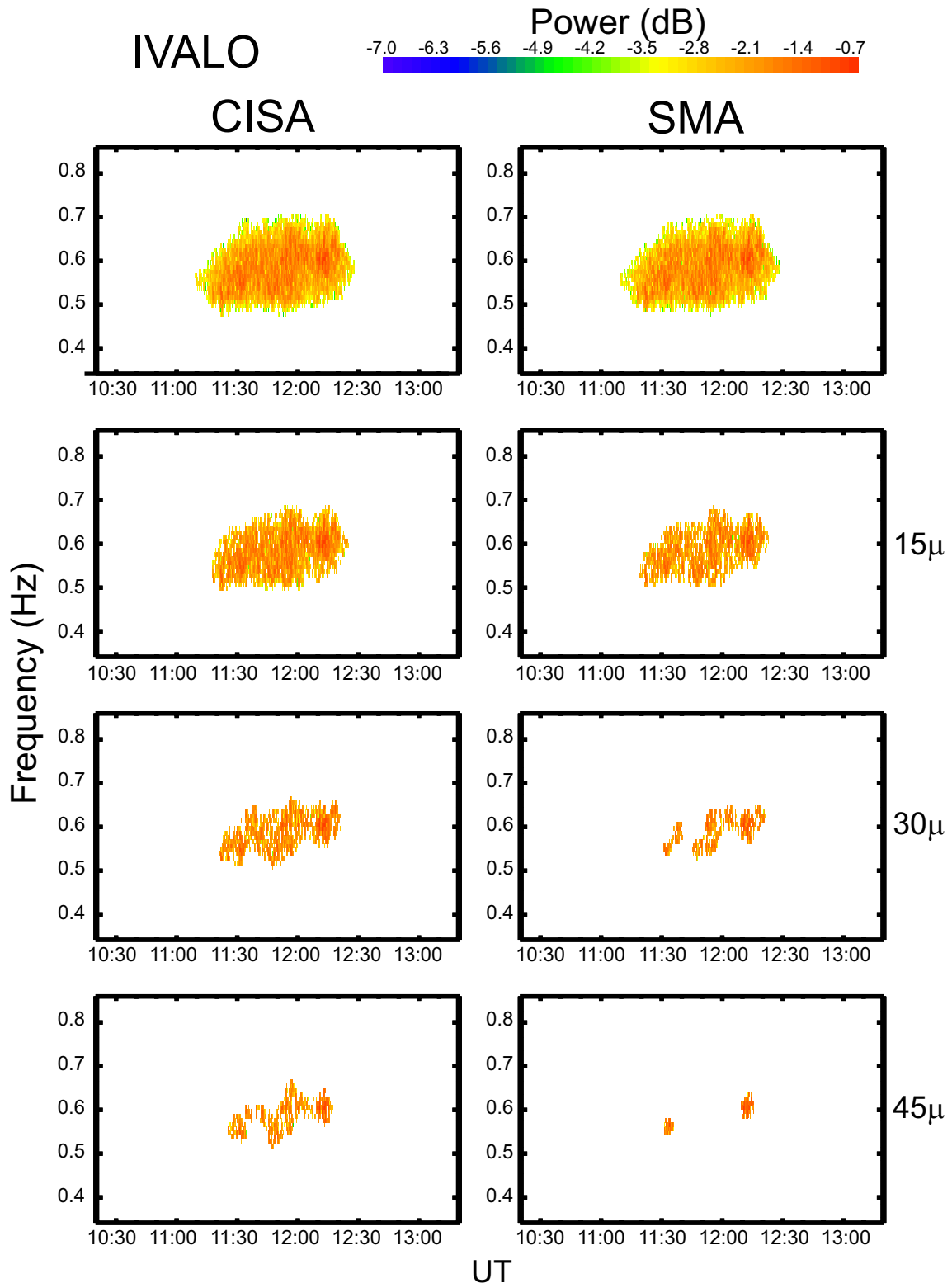


Figure 5.4: Following the format of figure 5.3, an unstructured pulsation recorded on 24/09/2005 at Ivalo is displayed above. Increasing levels of noise are injected with each row, again showing that the CISA method is more resistant to uniformly distributed random noise than the SMA.

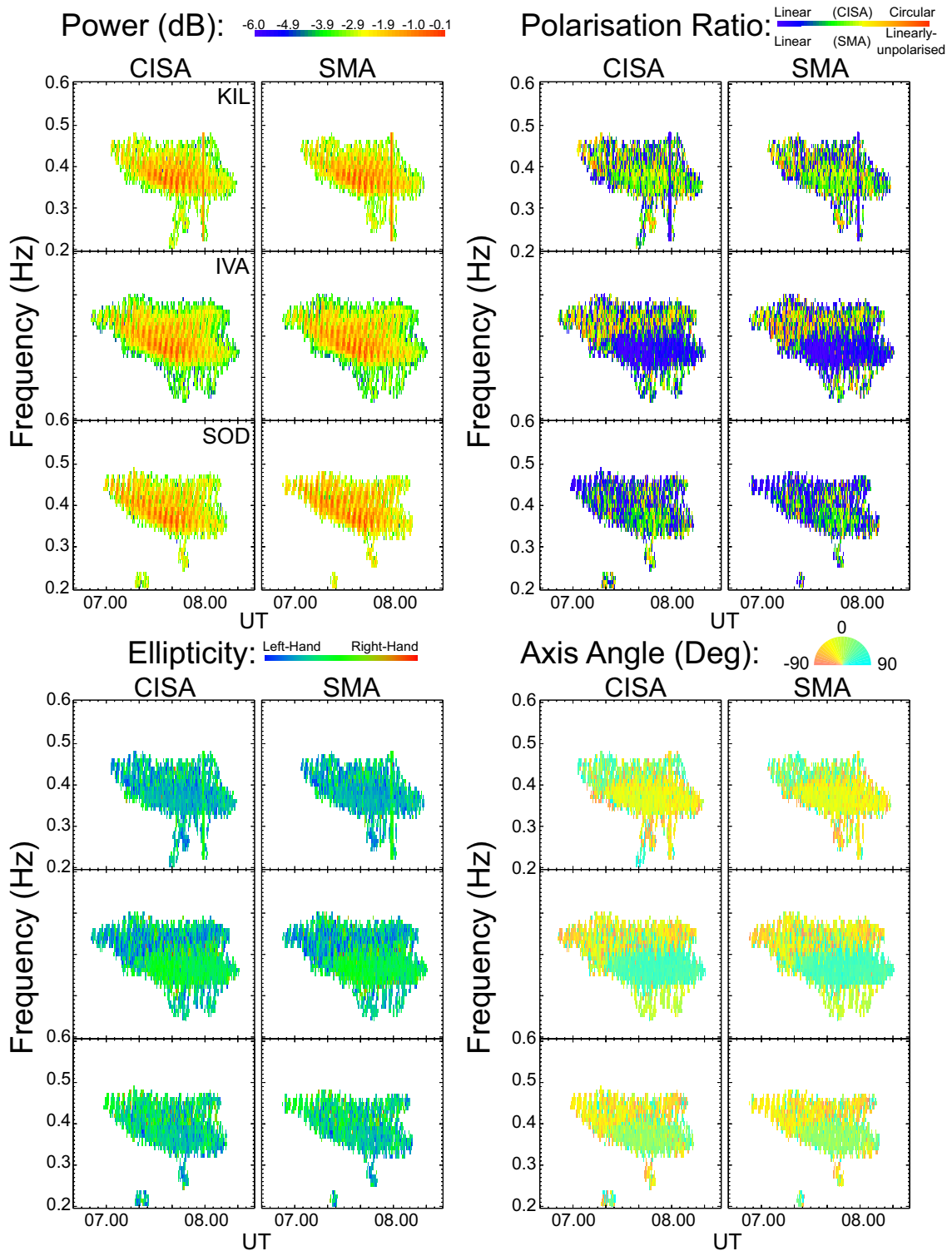


Figure 5.5: Dynamic spectral parameters of a multi-structured pulsation. Each set 6 panel contains information from stations of the FPMC, KIL (upper), IVA (middle) and SOD (lower), processed with the CISA (left) and SMA (right) methods. Each panel has been thresholded to 3 standard deviations above the progressive mean power. The upper-left set of panels show the spectral power used for extraction. The lower sets of panels show ellipticity (left) and polarisation ellipse axis angle (right). The upper right set of panels display the polarisation ratios, which appear to be opposite for each method as the ratio calculated by the SMA method is a measure of linear polarisation.

$$C_{12}(\omega) = F_1(\omega)F_2^*(\omega), \quad (5.21)$$

which is generally complex and may be written as

$$C_{12}(\omega) = |C_{12}(\omega)|e^{i\theta_{12}(\omega)}. \quad (5.22)$$

The complex phase angle θ_{12} is known as the cross-phase angle and can be used to calculate the time delay between observations by dividing it by angular frequency:

$$\Delta t = \frac{\theta(\omega)}{\omega}. \quad (5.23)$$

This does, of course, depend on the wavelength of the observed wave being larger than the separation of the observing stations and that they emanate from a single point source. These conditions are not necessarily met when analysing real data, hence, manual intervention is almost always necessary to ensure a realistic result.

5.3 Pulsation processing

Having described how spectral power and polarisation parameters may be derived, attention can now be focused on the methods used to extract this information from a dynamic spectrum for a given pulsation event. Throughout this thesis, a discrete pulsation is defined as a continuous region in frequency space that is of significant spectral power and distinct, slowly varying spectral characteristics. An individual pulsation must, therefore, exceed some power threshold and be bound by quasi-continuous frequency limits. Unless explicitly stated, spectral analysis is conducted in this section with the CISA method

5.3.1 Pre-processing and background extraction

Power thresholding for background removal has previously been approached in a number of manners. Integrated power in each time increment (Erlandson *et al.*, 1992), frequency dependent signal to noise ratio (Loto'aniu *et al.*, 2005) and frequency band-integrated mean power (Bortnik *et al.*, 2007) have previously been successfully used to determine acceptable power thresholds. However, when applied to data from the FPMC such methods yield inconsistent results, owing to the nature of the local pulsation environment and instruments used. Naturally, the frequency response of each

instrument must be considered, however, discussion of this aspect is reserved for the following chapter. The contribution of non Pc1-2 pulsations to the total power in each analysis epoch further complicates the determination of an acceptable power threshold. The time-increment threshold determination of Erlandson *et al.* (1992) was found to be critically dependent on lower frequency wave activity, irrespective of the width of increment chosen. The frequency band-integrated mean power method of Bortnik *et al.* (2007) was found to overestimate the mean power in cases where true Pc1-2 pulsations endured for a significant fraction of the analysis window. This overestimation appeared not to affect those authors' analysis too greatly, as they used a variable analysis window and the duration of their longest event was of the order 4 hours.

The routine analysis conducted throughout this thesis, however, employs a fixed 24-hour analysis window and in the period of consideration, July 2005 to December 2008, has registered continuous events of durations exceeding 13 hours. In a number of cases this heightened activity raised the mean power to a level that excluded genuine shorter, less intense pulsations in the same day. Given the nature of the current dataset, a statistical approach to background determination and power thresholding was developed that allowed a slightly more objective comparison of wave powers. The 3rd of May 2006 is used in the following section to illustrate this method.

A preliminary dynamic spectrum was created in the following manner. Hourly raw data files were checked for continuity and quality. Using the CISA technique defined in section 5.2.2, a dynamic spectrum was generated with a sliding Fast Fourier Transform (FFT) window, computed using the standard IDL FFT routine. IDL employs the Cooley-Tukey, Decimation In Time algorithm that is optimised when the number of data points in the transform window is a power of 2. Subsequently, a default window length of 102.4 s (9.76 mHz resolution), corresponding to 4096 (2^{12}) data points was chosen. A Kaiser-Bessel window function was applied to each window. The alpha parameter of the Kaiser-Bessel window dictates its shape and subsequently the height and width of its side lobes when transformed into the frequency domain (Nuttall 1981). An alpha value of 7 was chosen as it offers an acceptable trade off between power loss and spectral leakage in the Pc1-2 frequency range.

Data storage capacity and display screen resolution (for visual inspection) led to the selection of a $\sim 41\%$ overlap in a standard 24-hour analysis interval, resulting in a spectrogram of 60 s temporal resolution, containing 1440 time increments. Data values in the 24-hour dynamic spectrum were then ordered according to power and their statistical moments progressively calculated. This was achieved by sequentially including values and recalculating the moments of all included points. The daily threshold was defined as the power level that exceeded the progressive mean by three progressive standard deviations. Figure 5.6 displays the result of this process for the 3rd of May 2006. Panel (a) shows a dynamic spectrum between the frequencies of 0.1 Hz and 1.1 Hz, restricted thus to avoid consideration of the instrumental frequency response that will be addressed in Ch. 6. Panel (b) displays an ordered power curve (solid line) and the values of the statistical limit (asterisks), which is set at the mean plus three standard deviations of all included datapoints. The irregular spacing of the asterisks is due to the thresholding algorithm's iterative process. The algorithm determines the exact threshold value by calculating the statistical moments of all the points, up to and including n , at increments of 10^x . The initial value of x is the order of magnitude of the total number of data points, which in this case is 5; hence, the first calculated threshold value is at $n=1 \times 10^5$. This calculation is repeated until the datum value exceeds the statistical limit or n is greater than the total number of points in the distribution. When this occurs an incremental step back is made and x is reduced by one; hence, the next calculated limit is at $n=11 \times 10^4$. This process is repeated until $x=0$ and the precise threshold value is determined. Panel (c) displays a thresholded dynamic spectrum, in which can be seen the now isolated periodic pulsation; however, a few regions of sufficient spectral power remain that must be given further consideration and removed if appropriate. This method proves extremely robust in providing an acceptable threshold in all scenarios, as it remains indicative of the background noise level irrespective of the duration or intensity of any significant pulsation.

5.3.2 Discrete event parameter characterisation

For simple cases, such as that shown in the previous section, it is possible to extract spectral parameter information for an entire event directly from the thresholded spectrum. However, determining the characteristic values of the four basic derivable parameters, total power (I_T), ellipticity (ε), ellipse orientation (α) and polarisation

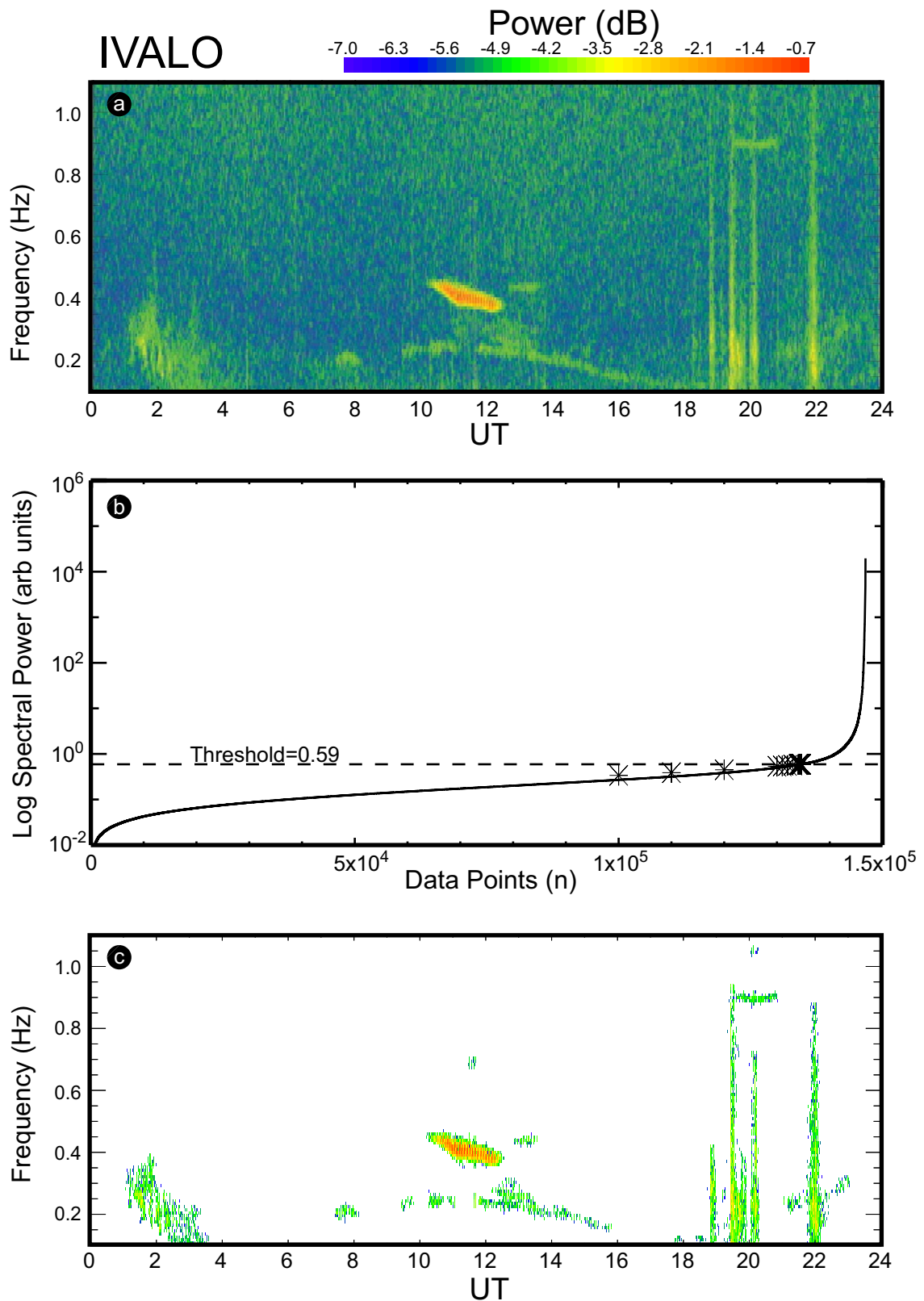


Figure 5.6: Dynamic spectra and progressive power level threshold curve. Panel (a) shows a dynamic spectrum for the 3rd of May 2006, in which can be seen a periodic pulsation centred on ~ 0.4 Hz, initiating at ~ 10.15 am. Panel (b) shows each datapoint, ordered according to power. Each asterisk represents the mean plus three standard deviations of all points up to and including its n value. Panel (c) displays the thresholded spectrum.

degree (PR_c) is somewhat less straightforward. The variation of each parameter within a pulsation event may be great and the presence of random noise may distort their distributions. For these reasons, the following method was adopted to determine the characteristic parameter values for a discrete event. The event isolated in the previous section, will be used to demonstrate the technique.

The pulsation interval was reanalysed with the same window length (frequency resolution) but increased overlap, generating a dynamic spectrum of 10 s temporal resolution. The previously determined threshold was then used to isolate the data of interest. The event value of I_T was taken as the mean of all sufficiently powerful datapoints. Event values of the spectral parameters ε , α and PR_c were derived by constructing total power-weighted histograms with 21 equally spaced bins; the result being a composition of the quasi-random background distribution and a peak representing the characteristic value of the event. Subsequently, a Gaussian plus quadratic function was then fitted to resultant distribution. Figure 5.7 shows the fitted curve for α . The peak of the fitted Gaussian was taken to be the characteristic value of the event, $\alpha = 0.74$ rad in this case.

When fitting to angular parameters such as α , which may take values between $\pm\pi/2$, fitting failure due boundary proximity was mitigated for by shifting the distribution sufficiently in either direction until a fit was achieved. In practice this was not an issue for the determination of ε and PR_c as their values were never sufficiently close to their limits to hamper a fit.

5.3.3 Determination of the degree of structuring within a pulsation

The distinction between structured (pearl) and non-structured pulsations has historically been made by visual examination of dynamic spectra, a process that is inherently subjective, rendering comparison between studies difficult at best. Consequently, a method of objectively determining the degree to which a pulsation is periodic was constructed in the following manner. The visually structured event isolated in section 5.3.2 and a visually unstructured event that occurred on the 24th of September 2005 are

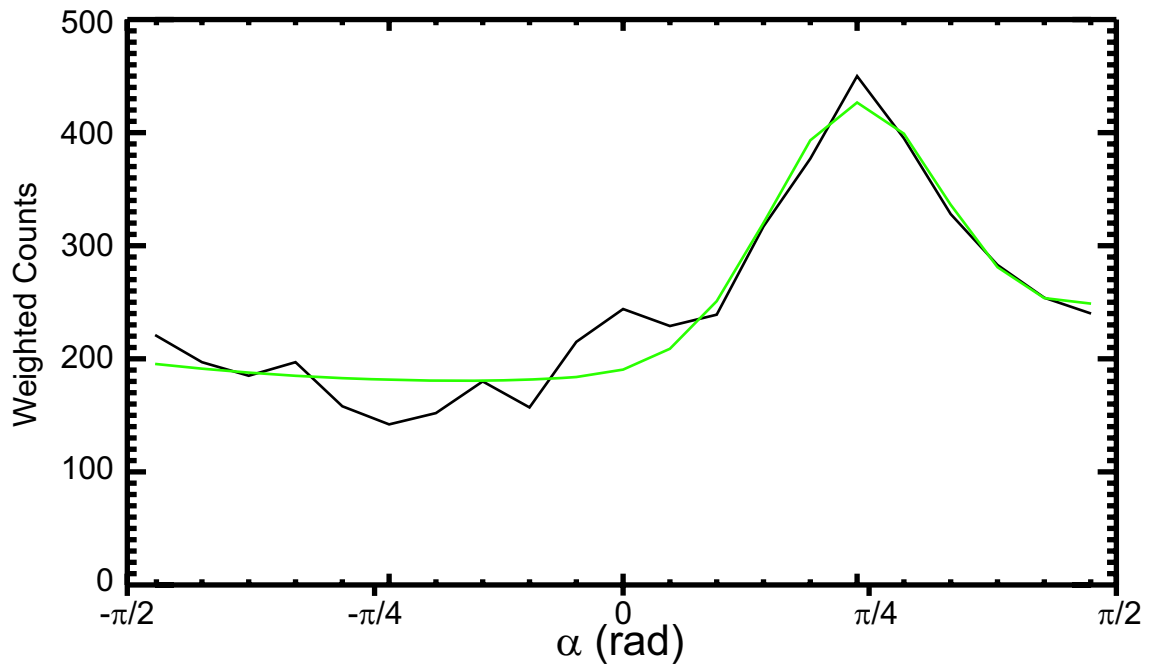


Figure 5.7: Power weighted histogram of semi-major axis angle orientation for a pulsation event on the 3rd of May 2006. Upward directed tick marks indicate the centre of each histogram bin. The green curve represents a fitted Gaussian plus quadratic function, the peak of which (0.74 rad) was taken to be the characteristic value of α for the entire event.

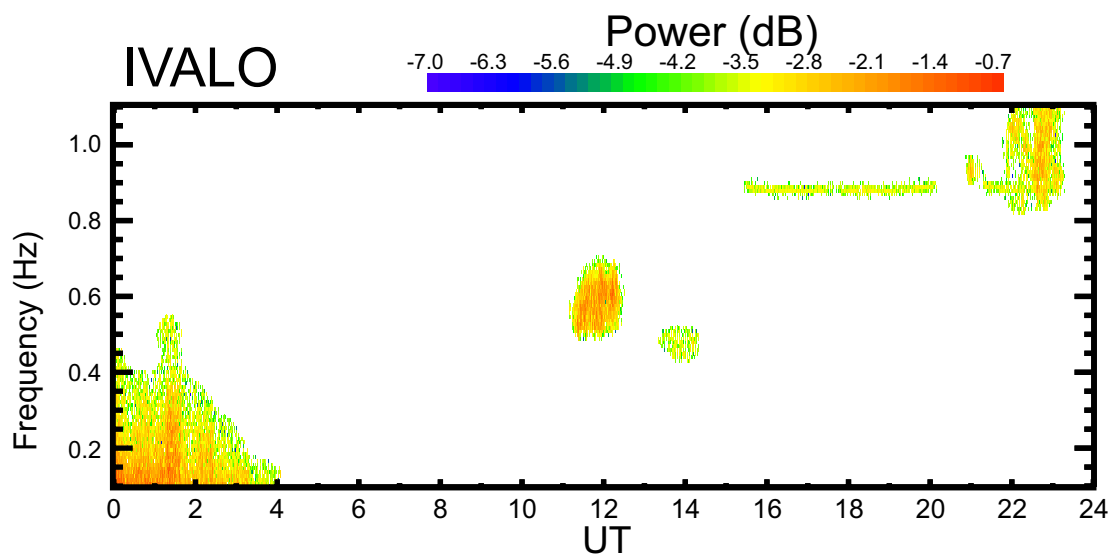


Figure 5.8: Thresholded spectrum for the 24th of September 2005, in which can be seen a pulsation, commencing at ~ 11.00 UT, that visually contains no significant regular structuring.

used to outline this procedure. A dynamic spectrum of the unstructured event, registered at IVA, may be found in figure 5.8.

From the 10 s dynamic spectrum described in the previous section, a timeseries consisting of the mean values of I_T for each time increment was generated, which can be seen in figure 5.9. Although weak rapid fluctuations are present, large amplitude intensifications appear to be regular throughout the event. A second dynamic spectrum was generated from this timeseries of window length 2560 s (256 point) and 640 s window advance. This second dynamic spectrum was then averaged across all time increments for each frequency to generate a single spectrum, which is presented in figure 5.10. A Gaussian function was then fitted to the lowest frequency peak of the averaged spectrum above 2 mHz, represented by the green curve. The peak of the fitted Gaussian was taken to be the fundamental repetition frequency, F_R , of the structured pulsation. Subsequent fits, where possible, were made to higher frequency portions of the curve to assess the contribution of harmonic frequencies to the total spectrum. The blue curve in figure 5.10 is the second fitted Gaussian. In this case the second fit was not a harmonic of the fundamental, hence that portion of the spectrum was treated as part of the background.

A periodic parameter, P_p , was then defined as the ratio of the area under the Gaussian fit to the total area under the spectrum, excluding the contribution of subsequently fitted harmonics, should they exist. P_p , scaled according to the FWHM of the fundamental fitted curve, thereby represents a seemingly adequate indication of the monochromaticity of intensity repetition for an event. Cases where the fundamental fit failed to converge were assigned a value of zero. For events where the determination of P_p was possible, a value of $P_p=1 \times 10^6$ was set, by inspection, as the boundary between structured and non-structured pulsations, where such a distinction was necessary. A P_p value of 4.97×10^6 was reached for the visually structured event in figure 5.6, which suggests that $F_R=3.8$ mHz is a reasonable representation of the overall repetition frequency of the event..

Figures 5.11 and 5.12 display the secondary timeseries and the result of this method applied to the unstructured event in figure 5.8. A Gaussian fit was also achieved in this case; however, the fit did not represent a single significant spectral peak but

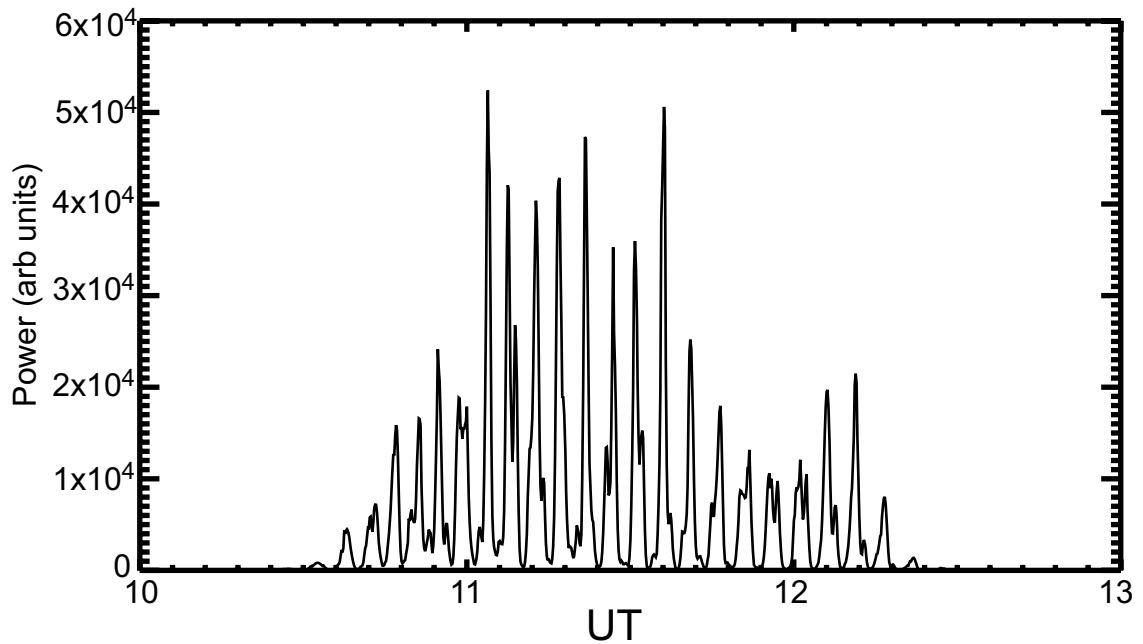


Figure 5.9: Mean I_T for each dynamic spectral window of the structured event on the 3rd of May 2006, with a temporal resolution of 10 s. Although small rapid fluctuations are present, large-amplitude periodic intensifications can be seen throughout.

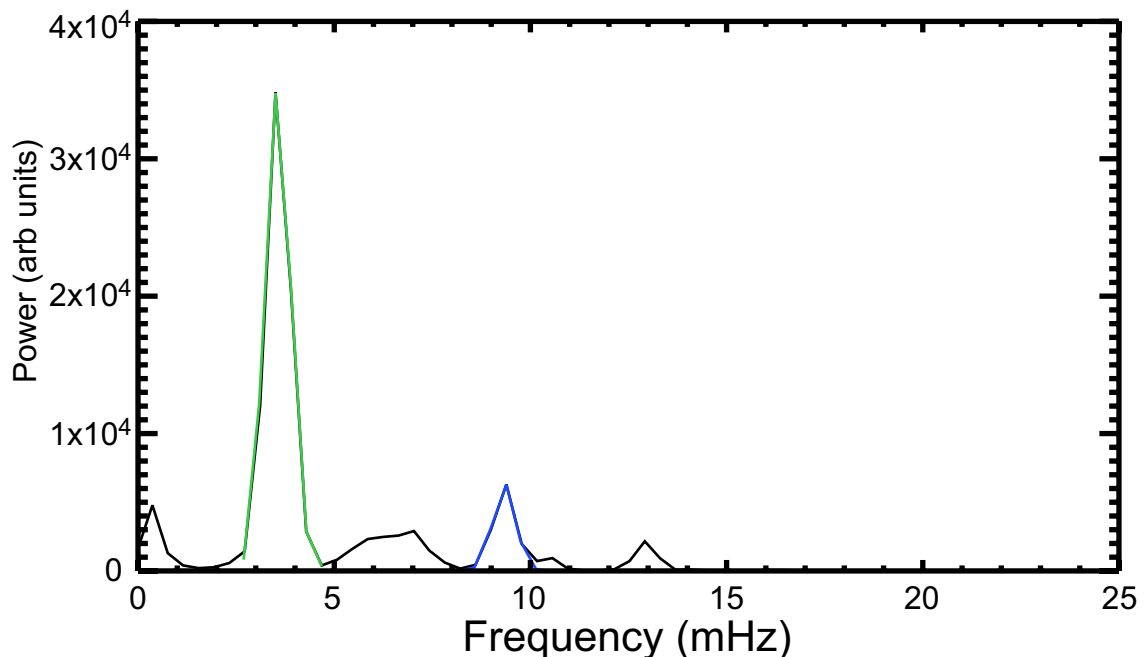


Figure 5.10: Frequency spectrum of the total power variation (Figure 5.9) for the visually structured pulsation event on the 3rd of May 2006. The black line represents unaltered spectral power, the green curve represents a Gaussian fit to the lowest frequency (fundamental) peak. The blue curve represents the next achievable Gaussian fit to higher frequencies. In this case, the second fit (blue curve) was determined not to be a harmonic of the fundamental fit and was treated as part of the background spectrum. The values of repetition frequency and periodic parameter for this event were 3.8 mHz and 4.97×10^6 respectively.

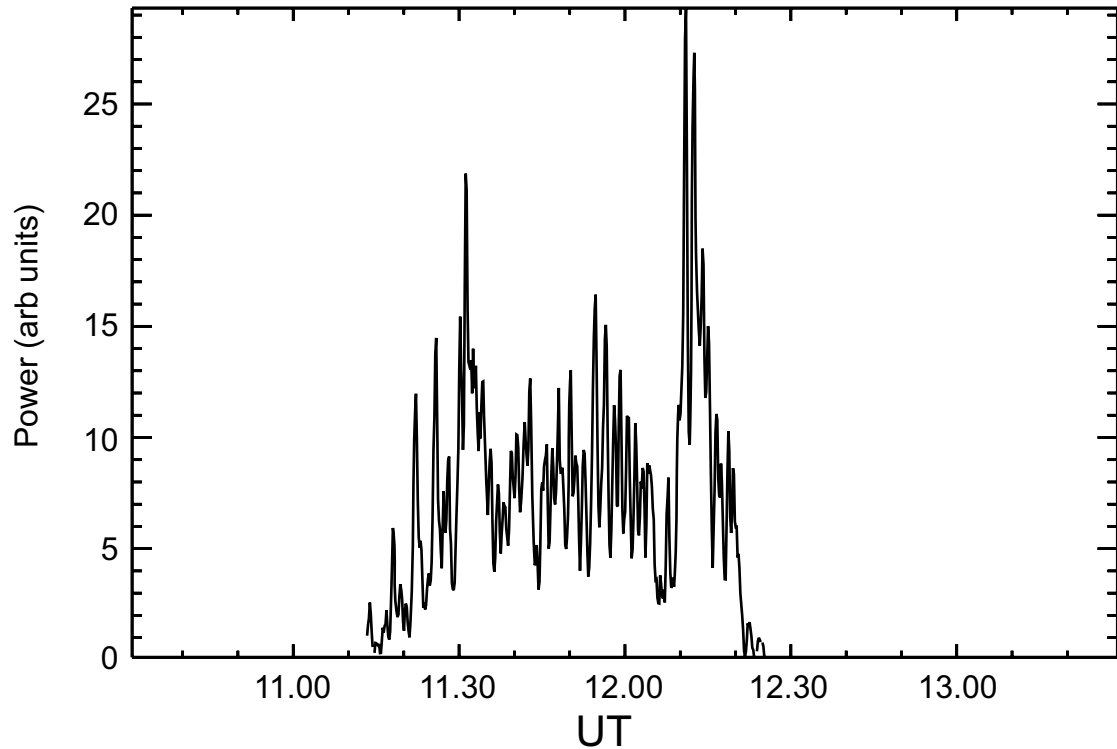


Figure 5.11: Of the same format as figure 5.9, displayed here is the mean I_T for each dynamic spectral window of the structured event on the 24th of September 2005, with a temporal resolution of 10 s. Unlike the previous example, no significant periodic behaviour can be seen.

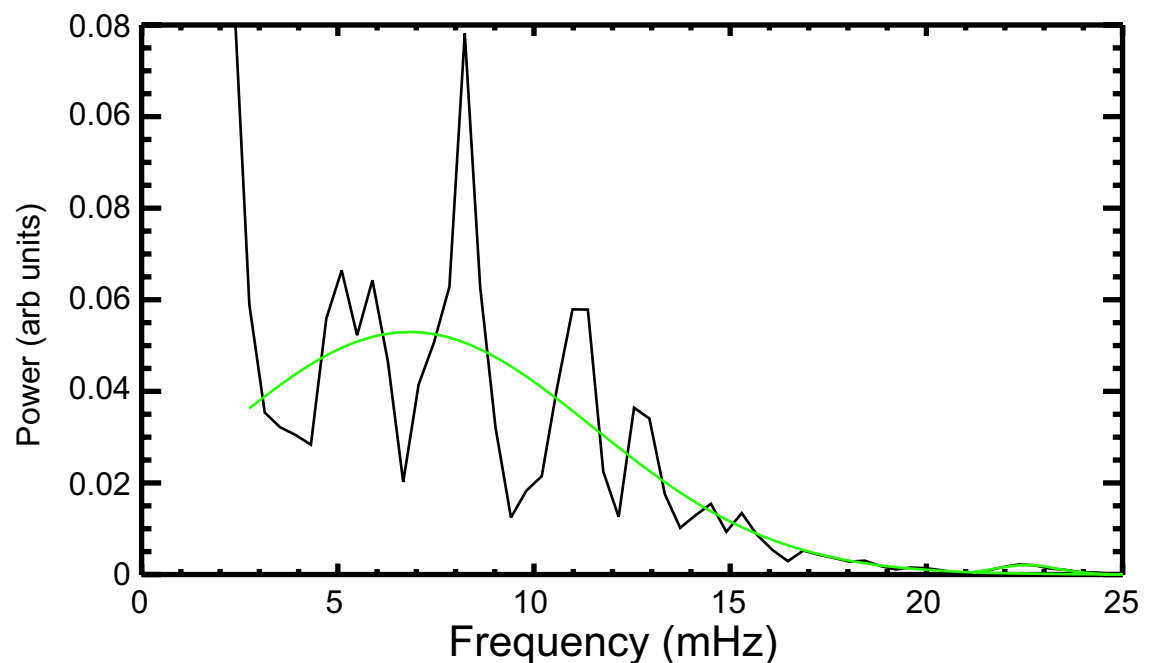


Figure 5.12: Of the same format as figure 5.10, the black curve represents the Fourier spectral power for the event on the 24th of September 2005. In this example a fit to a defined spectral peak is not achieved, subsequently its periodic parameter value was determined to be 4.08×10^4 , 2 orders of magnitude below the 1×10^6 structured cutoff.

several low amplitude peaks that were approximately 6 orders of magnitude smaller than the fundamental of the previous structured event. The value of P_p for this event was 4.08×10^4 , which is well below the structured cut-off of 1×10^6 .

5.3.4 Spectral parameter continuity as an event discriminator

As discussed in section 5.3.2, the variability of each parameter within a given event may be relatively high; however, the discontinuity in parameter values between events that are superimposed on one another in frequency space is generally sharp enough to be used to discriminate between them. In the multi-structured case of figure 5.5, the two distinct regions of pulsation characteristics will hereafter be referred to as the upper, which initiates first at ~06:55 UT and is centred on 0.44 Hz and the lower pulsation, which begins at ~07:20 UT and is centred on 0.38 Hz. Manual selection of frequency boundaries (see section 6.2.2) for each of these pulsations and the methods described in the previous sections allowed the derivation of the parameter values displayed in table 5.1. The derived parameter values were significantly different for the lower and upper pulsations; most notably, with the value of α differing by as much as ~90 degrees at Ivalo. The frequency of repetition, F_R , appeared to be slightly higher, by 0.3 mHz, for the upper pulsation.

5.4 Inter-station time delay determination

As discussed in Ch. 3.6, a number of authors have inferred the location of the ionospheric footprint of an EMIC wave's magnetospheric source region using inter-station time delay of arrival (TDOA). Historically, this delay has been calculated using time domain cross correlation of frequency band filtered data, an effective method for singular quasi-monochromatic pulsations; however, this is frequently not the case. The following section demonstrates that frequency domain inter-station cross-phase analysis may be employed to determine the TDOA of multi-structured pulsations.

Firstly, the equivalence of the two approaches is demonstrated by applying both to the case of the simple structured pulsation (first displayed in figure 5.6, panel a), using the three stations with the clearest observations, KIL, IVA and SOD. Using a

method similar to that described in Ch. 5.2.3, TDOA timeseries were derived by computing the cross-phase of manually selected pulsation data and multiplying by the central frequency of the data increment, the results of which for each horizontal component and polarisation sense can be seen in figure 5.13. A window length of 360 s with a 50% overlap was used, generating values of TDOA at intervals of 180 s.

To generate a comparable timeseries of time domain derived TDOA, dynamic inter-station cross correlation was employed, in which the same 360 s and 180 s window length and overlap were maintained. Given that the central frequency of the pulsations under scrutiny was of the order 1 Hz it was only necessary to calculate correlation coefficients for maximum lags of ± 3 s, meaning that each cross correlation calculation contained in excess of 1400 points. The results of this procedure are shown in figure 5.13 as dashed lines.

5.5 Source triangulation

The triangulation method of Fraser (1975) is employed here to simply illustrate a potential usage of Pc1-2 TDOA. The triangulation geometry of this method, applied to the three-station array of KIL, IVA and SOD, is shown in figure 5.14. This scheme assumes a coherent source and plane wave propagation at a constant velocity. In the following examples, the station locations are gnomonically projected on to the plane of wave propagation, on which all calculations are made.

The station separations are given by R_{12} , R_{23} and R_{13} , and their internal angles by the corresponding θ values. V is the phase velocity of the plane wave, with δ values representing the measured time delays between stations. The angle of arrival with respect to the bearing SOD->IVA is given by:

$$\phi_2 = \tan^{-1} \left(\frac{R_{12} \delta_{13}}{R_{13} \delta_{12} \sin \theta_1} - \frac{1}{\tan \theta_1} \right) \quad (5.24)$$

and subsequently the phase velocity is found using:

$$V = \frac{\cos \phi_3 R_{13}}{\delta_{13}}. \quad (5.25)$$

	KIL	IVA	SOD	
α	13.44	-36.66	-40.78	upper
	-23.84	53.36	16.38	lower
ε	0.44	0.45	0.27	upper
	0.56	0.17	0.40	lower
PR_c	0.39	0.41	0.25	upper
	0.42	0.16	0.33	lower
P_p ($\times 10^6$)	0.11	2.6	3.3	upper
	2.8	3.9	3.8	lower
F_R (mHz)	4.90	5.09	5.09	upper
	4.84	4.83	4.84	lower

Table 5.1: Values of Semi-major axis angle (α), Ellipticity (ε), degree of polarisation (PR_c) and periodicity for each of the discrete regions of frequency space that comprise the multi-structured event recorded on the 24th of September 2006. Values were derived with the methods described in sections 5.3.2 and 5.3.3.

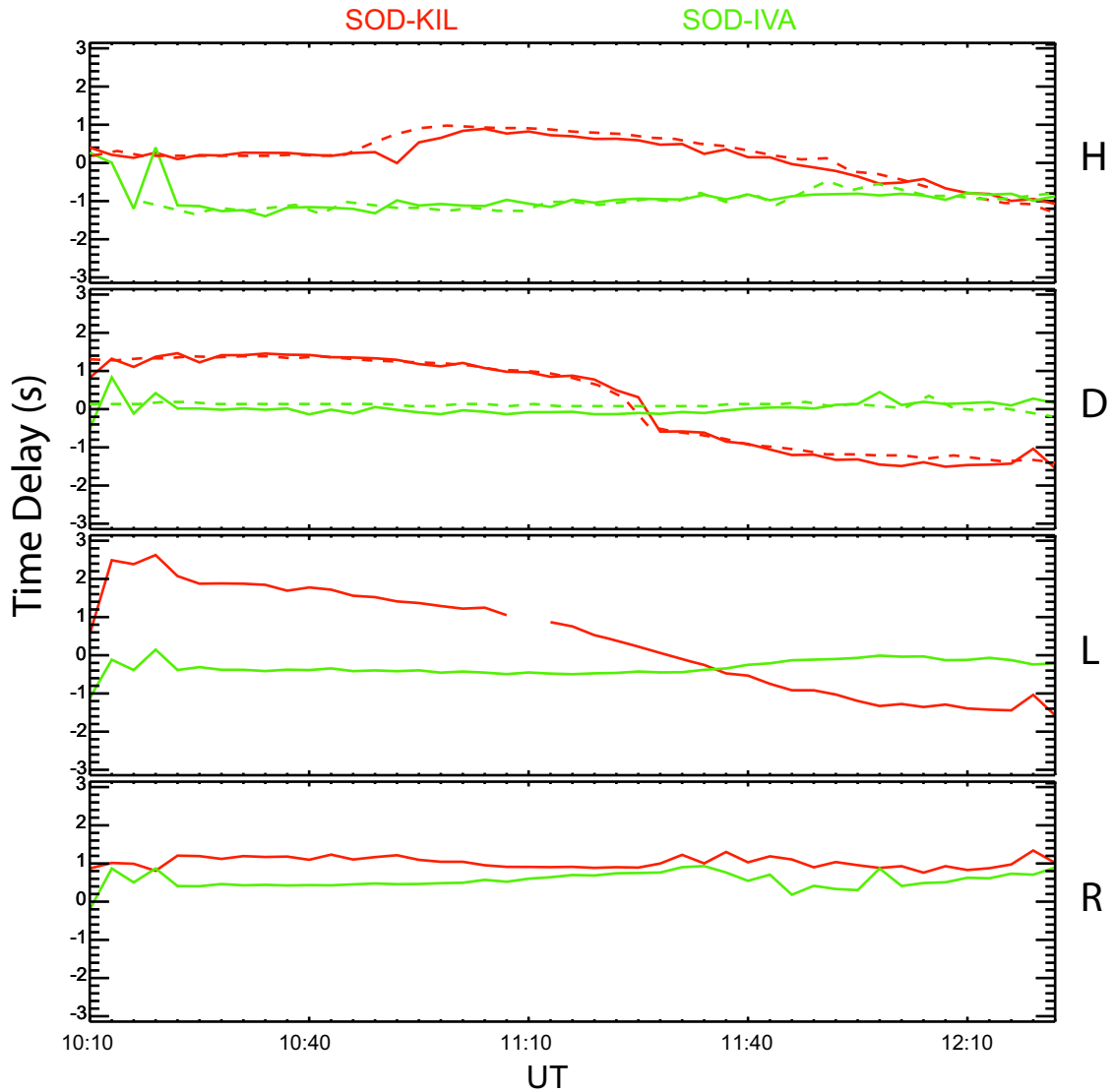


Figure 5.13: Time delays from SOD to KIL and SOD to IVA for the simple structured on the 3rd of May 2006. In the upper two panels, solid (dashed) lines represent frequency (time) domain derived values. The lower two panels display the left- and right- polarisation component delays.

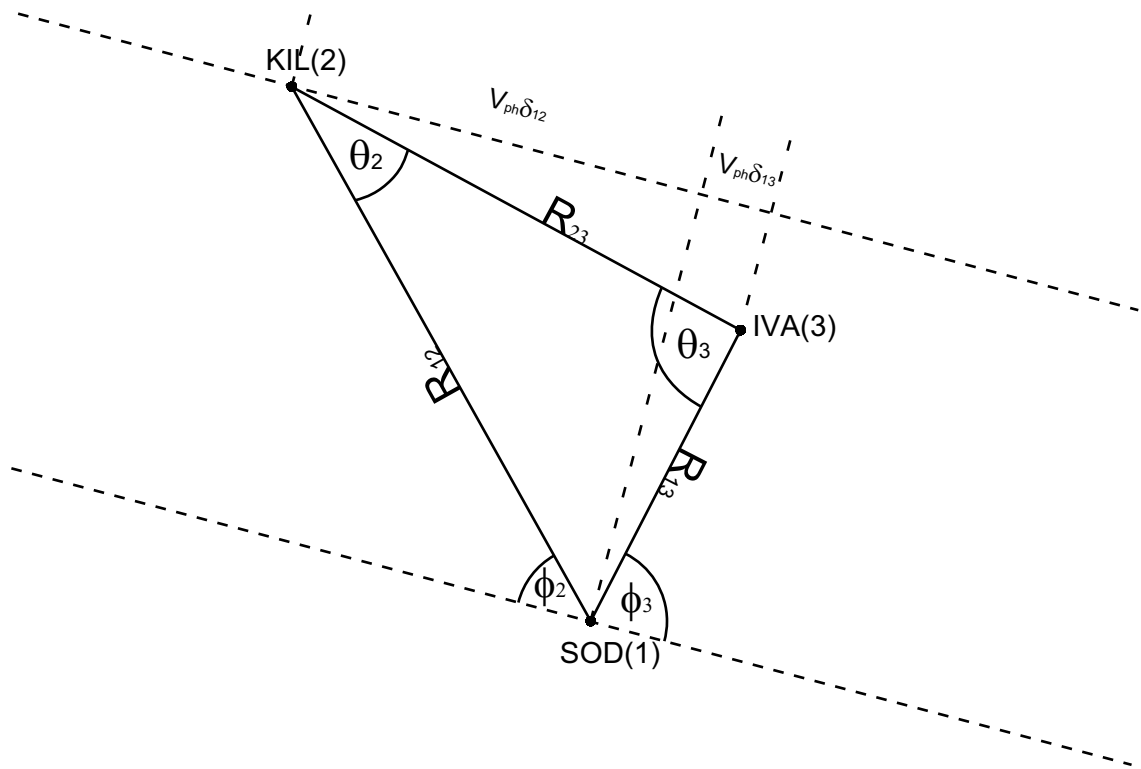


Figure 5.14: FPMC triangulation geometry.

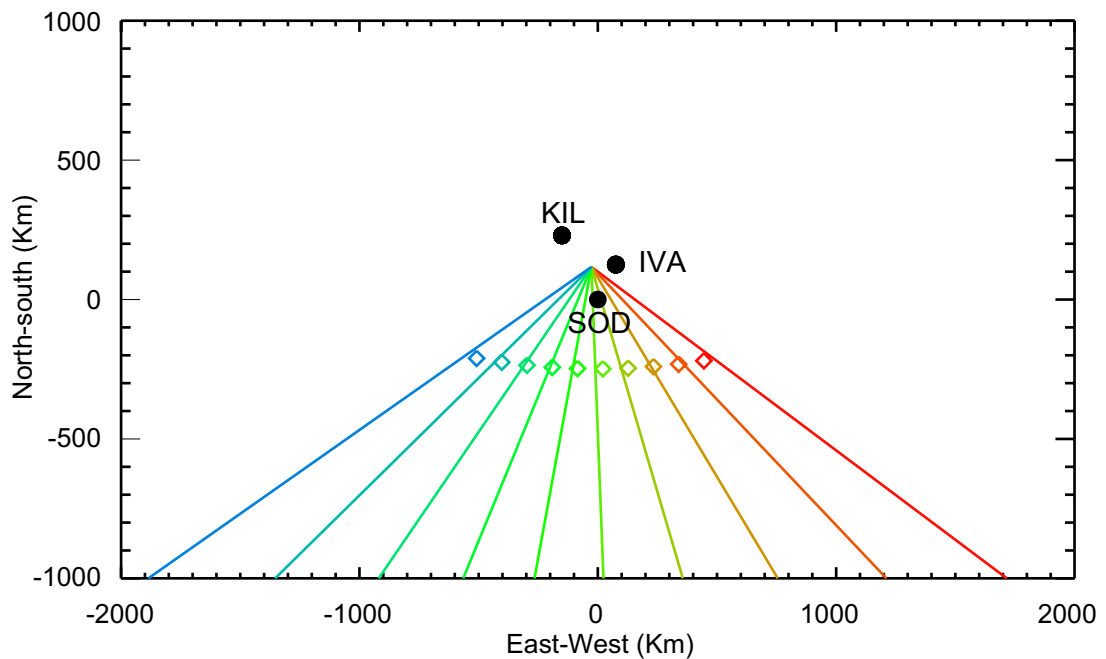


Figure 5.15: Simulation of DTOA triangulation of a moving point source, after Fraser (1975). Station locations have been gnomonically projected on to a plane, centred on SOD, in which it is assumed a plane wave is propagating at a constant velocity. Diamonds indicate simulated source positions and the corresponding coloured lines indicate the triangulated directions of arrival.

Figure 5.15 illustrates a simulated point source (diamonds), moving zonally at a constant latitude of 62 degrees, gnomonically projected on to the plane of the array. This method is applied to the derived delays of each component of the simple-structured pulsation in figure 5.16; the direction of arrival vectors are colour coded such that red (blue) indicates the start (end) of the event and green the middle. Immediately evident from figure 5.16 is that each component returns a different result. However, for the majority of the event the derived velocity was consistently between approximately 100 and 200 kms^{-1} as seen in figure 5.17. One might expect the ionospheric source to migrate westward with the drift of the magnetospheric energetic ion population generating the incident EMIC waves, and indeed there is suggestion of this in the H component and L polarisation data. However, this is not reflected in the D component or R polarisation data.

The results of triangulating the upper and lower portions of the multi-structured pulsation are displayed in figure 5.18. This figure, similar in format to figure 5.16, shows each component for both segments of the pulsation. There appears to be a distinct difference in direction of arrival between the upper and lower pulsations most markedly so in the R polarisation result. A remarkable difference is seen in the derived velocities (figure 5.19), with the lower pulsation displaying a high level of consistency throughout the event and the upper pulsation varying considerably in all components

5.6 Discussion

The predominately polarised nature of Pc1-2 pulsations brings about a need for routine knowledge of polarisation characteristics. Although previous studies have investigated such characteristics, little information on the dynamic nature, evident in their derivable parameters, of Pc1-2 pulsations has been reported. The example events in this chapter highlight the complexity of pulsations both spatially and temporally, emphasising the need for the dynamic analysis methods outlined above.

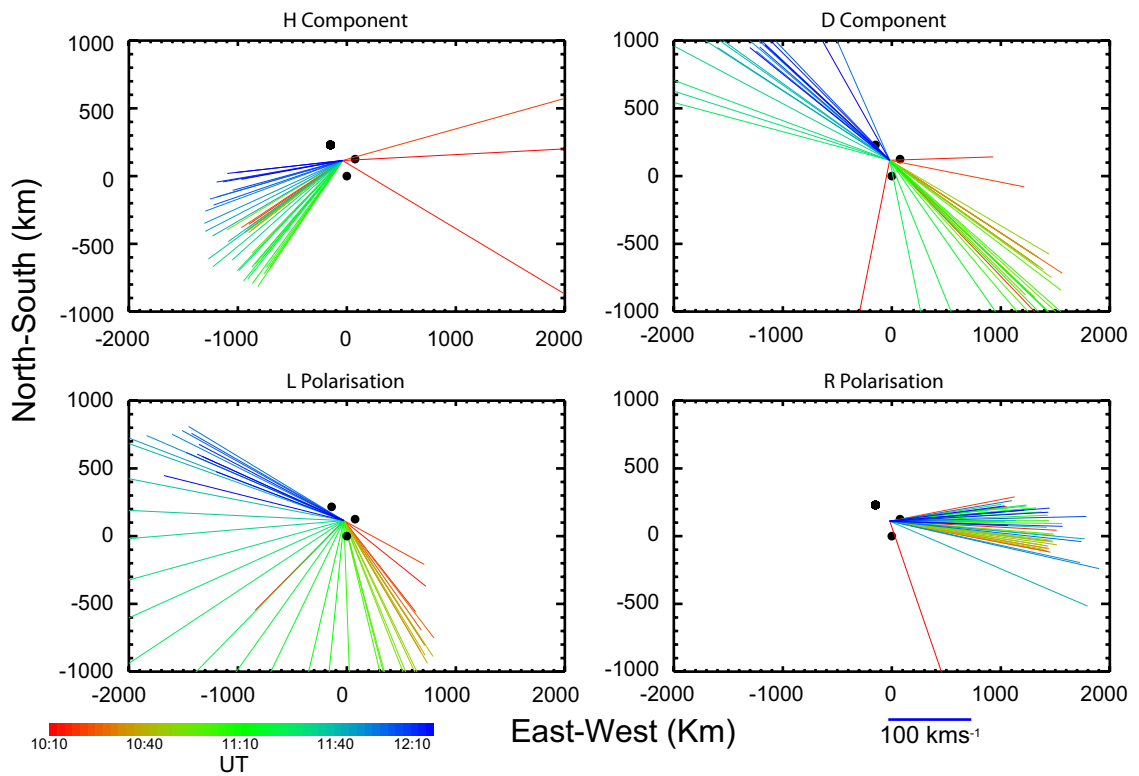


Figure 5.16: Cross-phase-TDOA plane wave triangulation of the quasi-monochromatic Pc1 event on the 3rd of May 2006. Triangulated direction of arrival is indicated by each vector emanating from the centre of the array with its length indicative of the derived phase velocity.

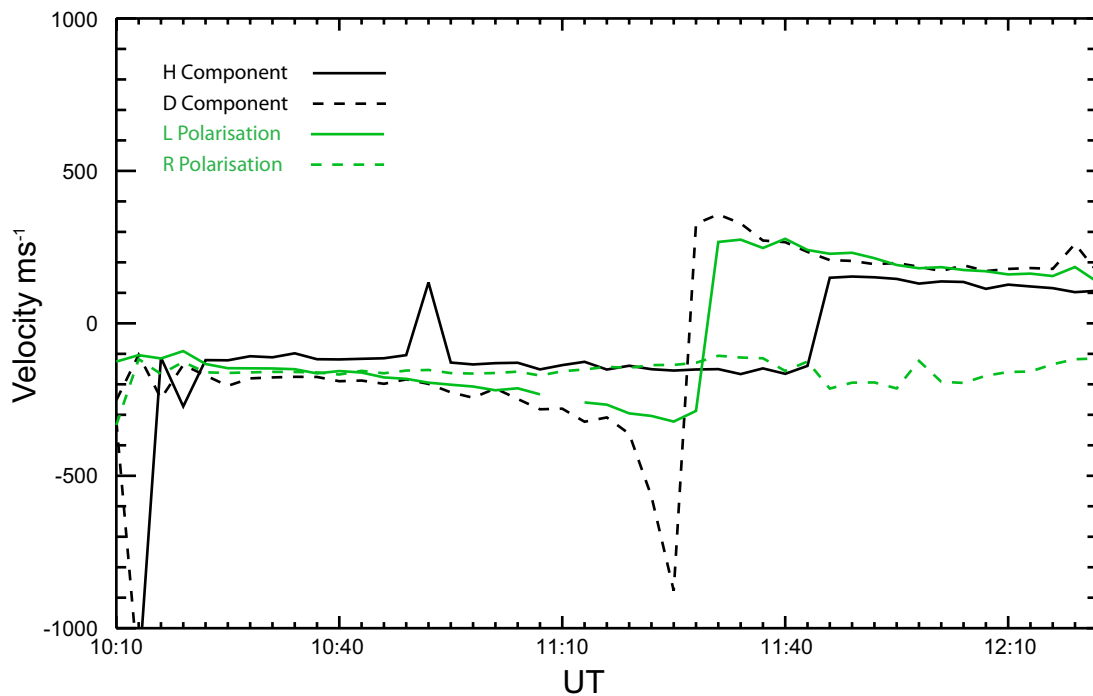


Figure 5.17: Phase velocities for the event in Figure 5.16

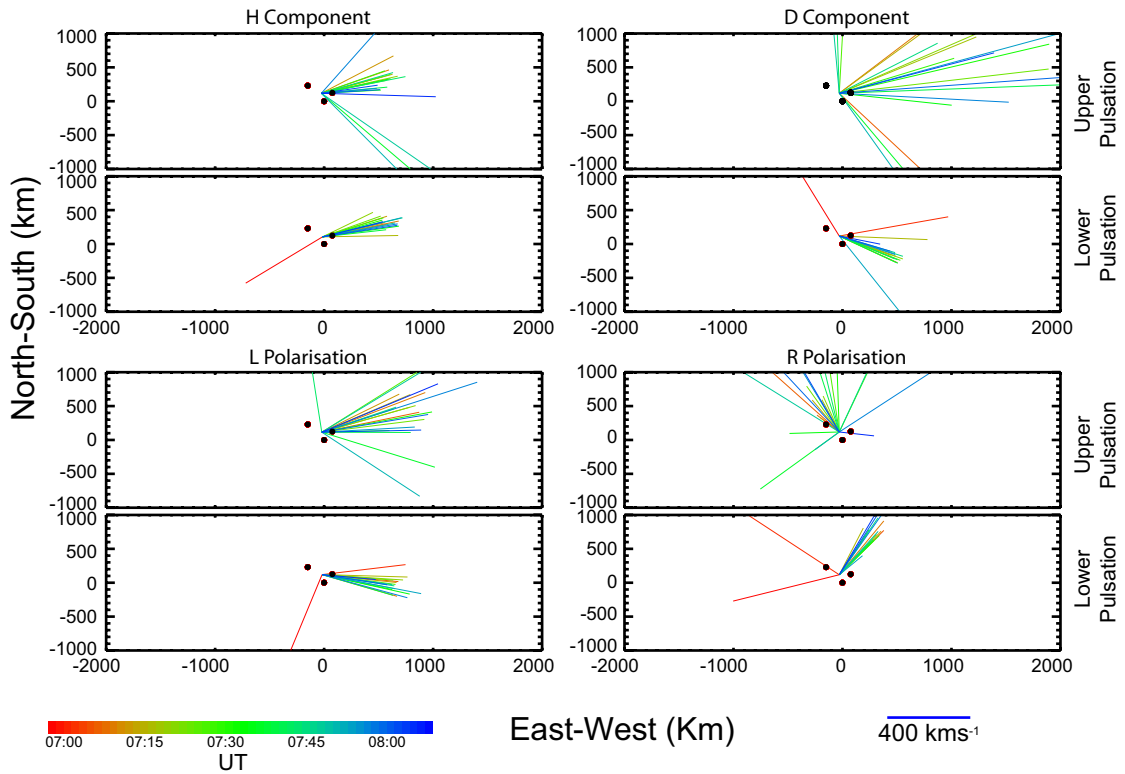


Figure 5.18: Cross-phase-TDOA plane wave triangulation of the multi-structured Pc1 event on the 24th of September 2005, similar in format to figure 5.16, each pair of projections depicts the upper and lower pulsation frequency bands identified in section 5.3.4.

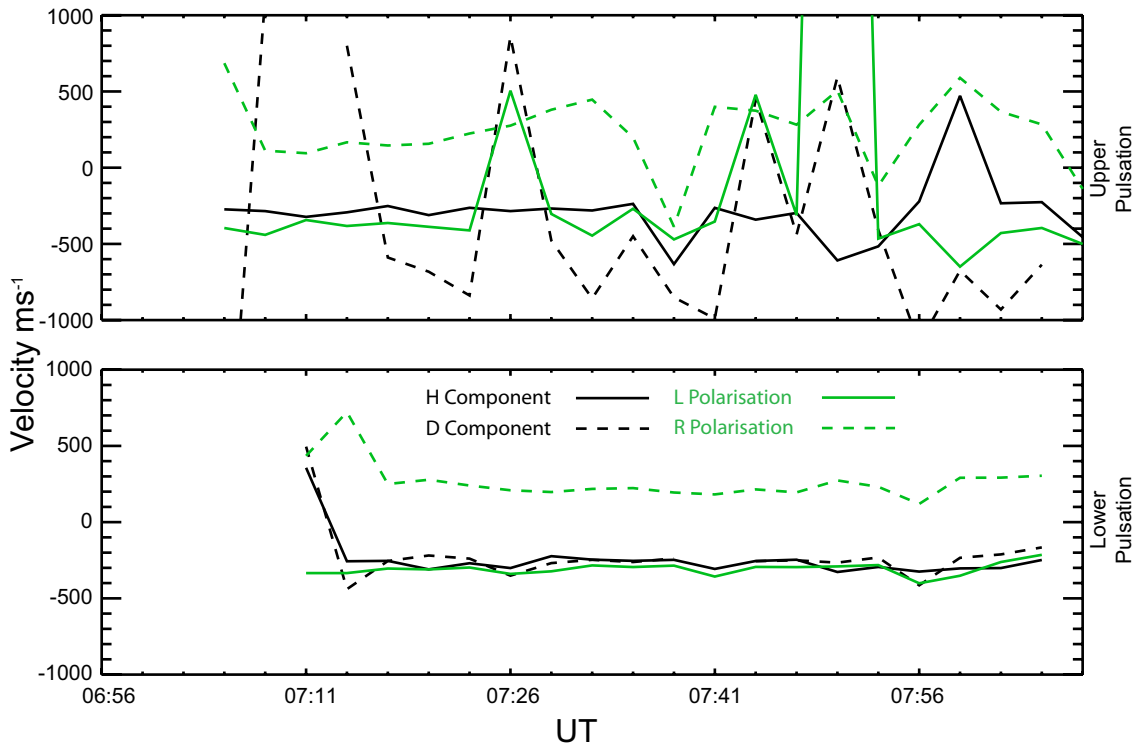


Figure 5.19: Phase velocities for the event in Figure 5.18.

5.6.1 Analysis techniques and processing

The CISA technique (section 5.2.3) requires considerably less computation than the full 3-component spectral matrix method (Means, 1972, Born *et al.*, 1959) adopted by Bortnik *et al.* (2007) yet is liable to phase ambiguity owing to the omission of a third component, in this case the Z component. This chapter has demonstrated that the CISA and the 2-component SMA techniques produce equivalent polarisation parameter outputs, as seen in figure 5.11. However, comparison of CISA with the full 3-component SMA method on ~200 sample intervals (not presented) showed that the two methods produce nearly equivalent outputs in all sampled cases.

Figures 5.3 and 5.4 showed the SMA technique to be more susceptible to random noise than the CISA method. This is presumably due its use of the diagonal elements of the spectral matrix (the auto spectra). The CISA technique exclusively uses the component cross-spectra; hence, theoretically, would be more susceptible to sources of noise that are coherent between components. However, naturally occurring noise is usually relatively incoherent (Arthur *et al.*, 1976). Subsequently, as long as the dominant source of noise is natural, the CISA technique is more appropriate for routine analysis.

A significant difference between the method adopted above and those of previous authors when isolating discrete events is the use of progressive power thresholding, which affects both time and frequency boundaries of a given pulsation. Visual boundary detection methods, such as those described by Kerttulla *et al.* (2001a, 2001b) and Engebretson *et al.* (2008), are prone to saturation by surrounding high spectral power; hence, the current technique is likely to resolve a greater number of events and consistently higher events durations in a given interval. As the ordered power curve in figure 5.6 displays, the method adopted here reaches a threshold value that is irrespective of the higher value data points. It is, however, dependent on the standard deviation of the included distribution; hence, as the number of points is increased a threshold value is more likely to be reached. This dependence becomes important when analysing intervals of considerably differing durations.

The power weighted histogram method of section 5.2.2 is more effective in producing a characteristic value of polarisation parameter than the analogue methods employed by previous authors, e.g. Fraser (1975) and the averaging method favoured by recent authors, e.g. Bortnik (2007), which treat low-power, and potentially noisy signals, indiscriminately. Given the conclusions drawn by previous authors on the source location and propagation mode of a variety of Pc1-2 phenomenon, the implications of this improvement may prove to be vast. For example, the relationship of the magnetospheric source region to the plasmopause has been inferred from such values. It may be of great interest to revisit this relationship using this technique coupled with the ever-growing repository of in situ satellite data now available.

Using polarisation parameters use as a discriminator between concurrent events may have great implications for multi-structured events. The dynamic polarisation data in figure 5.5 and differing repetitive values presented in table 5.1, strongly suggest that the multi-structured pulsation under investigation is a superposition of independent pulsations.

The quantitative determination of the structured nature of an event (section 5.3.3) is more a test of pulsation monochromaticity. This distinction may categorise what appears to be a legitimately structured pulsation as unstructured in cases where the structure repetition period is non-stationary. Repetition period non-stationarity is in itself of interest but will not be addressed here. As the bandwidth of a pulsation increases so does the potential overlap of successive wave-packets; hence, when a total-power timeseries is constructed a second oscillation is introduced, which is arguably present in figure 5.9. This is partially mitigated for by removing the contribution of higher order harmonics of the fundamental repetition frequency, as displayed in figure 5.10; however, the true effect of bandwidth increase and wavepacket dispersion on this method is unknown. This remains a subject for further study.

5.6.2 Inter-station time delay and source triangulation

Dynamic cross-phase analysis of these high frequency pulsations was made possible by the GPS timing and subsequent synchronicity of the entire FPMC chain. The agreement between the time-domain and frequency-domain derivations of TDOA

in the simple-structured case, displayed in figure 5.13, is encouraging. The frequency domain method introduced in section 5.4 allows the consideration of individual pulsations that are partially superimposed on one another; this may shed further light on their origin and propagation mode. This method may prove useful in examining the goose pulsations of Feygin (2009) and provide limits for the theory that has proposed for their generation.

As evidenced by the greatly varied results for each component of a given pulsation, it is clear that TDOA triangulation alone may not prove as useful as one might have hoped. Further investigation of the TDOA derived from each sense of polarisation seems a worthwhile endeavour as it might be expected that the most consistent result should come from the isotropically propagating R-mode assuming of course that the observing array is outside the near-field of the source region. Investigation of the usefulness of cross-phase analysis for Pc1-2 study, beyond simple contribution to the identification process, is the subject of a future study.

Alternative methods of TDOA ionospheric source location are currently under development. Multilateration, using four stations to obtain the three independent equations necessary to solve for the unknown latitude, longitude and velocity has currently proved unable to yield consistent results. An iterative method of expanding circles on the surface a sphere that employs the iterative formula of Vincenty (1975) shows somewhat more promise but has yet to bear fruit. However, all of these source location methods rely on constant velocity and plane or spherical wave front propagation and as the mixed results from simple case presented 5.16 suggests, this may never be an acceptable assumption. Subsequently, the natural progression from this approach would be to model the ionospheric density profile through which ray tracing may be attempted. As suggested by the vector plots of figure 5.18, there is some promise in applying triangulation methods to prove that multi-structured pulsation are in fact the superposition of multiple pulsation of independent source regions.

5.7 Summary

Three events of differing characteristics have been used in this chapter to demonstrate the techniques that were developed to analyse Pc1-2 pulsations recorded by the induction coil magnetometers of the FPMC. A power thresholding technique has been introduced that is less prone to contamination by higher-powered pulsations in the analysis interval than previously published methods. A method for objectively determining the degree to which a pulsation is periodic has been described and applied to unstructured, structured and multi-structured pulsations. This method showed that it is possible to parameterise consistently the periodicity of a pulsation albeit it at the expense of knowledge of its repetition frequency stability.

Given the relative computational efficiency of the CISA method compared to SMA and its better performance in the presence of noise, it has been concluded here that the former method is the most appropriate for Pc1-2 studies of this nature.

Frequency-domain cross-phase analysis has been employed to determine the Time Delay Of Arrival between a triangular sub-array of the FPMC. The TDOA values have subsequently been used in a simple triangulation scheme to highlight its potential usefulness. The varied results of triangulation for each component and polarisation sense suggested that using such methods independently may be inappropriate for even the most simple of cases.

Chapter 6. Characteristics of Pc1-2 Pulsations from Multi-station Data

This study investigates the properties of high-latitude ULF pulsations in the frequency band 0.1-5Hz, using the ground-based pulsation magnetometers of the Finnish Pulsation Magnetometer Chain (FPMC, Ch. 4.1.1), over the calendar year 2007. Owing to the demise of the Barentsberg magnetometer in March 2007, only data from the six remaining stations of the FPMC, Kilpsjarvi to Nurmijarvi inclusive, will be presented, for which a local time of UT + 1hr 40min will be used throughout, fixing local noon at 10.20 UT. Complex Input Spectral Analysis (CISA), Cross-Phase analysis and a manual selection process were employed to derive pulsation occurrence and polarisation parameters. Further details of the FPMC and analysis techniques employed may be found in chapters 4 and 5. Pulsation behaviour in time, space, frequency and polarisation is characterised and compared with geomagnetic activity and solar forcing via the SYM-H (Sugiura and Poros, 1971) index and OMNI combined solar wind parameters (King and Papitashvili, 2005).

6.1 Introduction

The behaviour of Pc1-2 pulsations has been the subject of a number of statistical studies that have considered timescales ranging from diurnal to multiple solar cycle and spatial occurrence in latitude and local time (Kangas *et al.*, 1998 and references therein).

The inverse relationship between Pc1-2 occurrence and sunspot number, first reported by Benioff (1960), has been verified on the ground at low (Fraser-Smith, 1970) and high latitudes over two (Kangas *et al.*, 1999) and four (Mursula *et al.*, 1991) successive solar cycles. Ionospheric attenuation has been suggested as the origin of ground-based observational Pc1-2 occurrence variation (Fraser-Smith, 1970), as theory (Greifinger and Greifinger, 1968) and observation (Appleton and Piggott, 1954) indicate that it is correlated with sun spot number. However, to date, no quantitative evidence in the Pc1-2 frequency band has been presented to confirm this assertion. Solar cycle dependency has been shown to hold true for in situ-magnetospheric Pc1-2s also, albeit using a vastly reduced dataset that did not allow continuous comparison over

a full solar cycle (Mursula *et al.*, 1996). Magnetospheric composition and response, in particular the dynamics of the plasmopause, to solar cycle driving has been suggested as a more likely Pc1-2 controlling factor (Daglis *et al.*, 1999, Mursula *et al.*, 1996). Irrespective of the cause of this inverse relationship, it is certainly true that selecting a period surrounding solar minimum offers the greatest probability of maximising Pc1-2 observation.

The relationship of Pc1-2 pulsations to geomagnetic storms and substorms is a longstanding quandary (Kangas *et al.*, 1998 and references therein). Substorms have been directly associated with the Irregular Pulsations of Diminishing Period (IPDPs) that frequently accompany Pc1-2s and increased auroral activity has been implicated in the modification of central pulsation frequency (Mursula *et al.*, 2000). However, a quantitative relationship between substorm activity and Pc1-2 occurrence is yet to be determined.

The propensity for pulsations to occur during the recovery phase of a geomagnetic storm is well documented (Bortnik *et al.*, 2008b, Engebretson *et al.*, 2008, Kerttula *et al.*, 2001a, Kerttula *et al.*, 2001b, Heacock and Kivinen, 1972, Wentworth, 1964). Occurrence has been shown to increase during and maximise within the 2-8 day period following storm onset.

Determining the propagation mode of a magnetospherically generated wave may yield information on the driving instability and medium through which it travels yet achieving this from the ground is nontrivial for a number of reasons. Measureable parameters such as the ratios of circular to linear and left to right hand polarisation, and orientation of the polarisation ellipse are only truly indicative of the transmitted signals emanating from the ionosphere (Tamao, 1984). Ionospheric waveguide propagation (Greifinger and Greifinger, 1968, Manchester, 1966) may alter wave characteristics such that the orientation of the polarisation ellipse aligns with the direction of propagation, hence, at sufficient distance, this information can be used to infer its source location (Fraser, 1975). The predominant source of Pc1 pulsations at the latitude of interest to this study are Electromagnetic Ion Cyclotron Waves (EMIC) that have been shown to be generated in the equatorial region near, but not bound, to the plasmopause (Loto'aniu *et al.*, 2005, Fraser and Nguyen, 2001). These left-handed,

field-guided mode waves are thought to intersect the ionosphere at the magnetic footprint of their magnetospheric source region and interact in the aforementioned manner. It has been shown, however, that a multitude of EMIC wave characteristics exist in the magnetosphere (Anderson *et al.*, 1992b). It is clear that each stage in a Pc1-2 pulsation's journey to the ground adds an additional level of complexity to its final appearance. Both ground- (Bortnik *et al.*, 2007, Webster and Fraser, 1985, Fraser, 1975, Fraser, 1975a, Summers and Fraser, 1972) and space-based (Anderson *et al.*, 1992b) studies have investigated Pc1-2 polarisation characteristics but have generally involved either small sample sizes or limited spatial coverage.

Few statistical studies (Kerttula *et al.*, 2001a, Kerttula *et al.*, 2001b) have made the distinction between structured pulsations that display a periodic intensification in spectral power and unstructured pulsations that exhibit no regular intensity modulation. The mechanism responsible for the structured nature of some pulsations has not yet been conclusively determined (Demekhov, 2007) and is beyond the scope of this chapter.

This study combines simultaneous, multipoint observations across an extended latitudinal range with high temporal resolution analysis over a full calendar year. The resulting dataset has provided a statistically significant number of events, from which further insight in to the behaviour of Pc1-2 pulsations has been drawn.

Given the size of the dataset used for this study, an automated identification algorithm would have been an obvious choice of method for event selection. The following sections discuss the reasoning for not automating the event selection process and outline the manual approach taken.

6.2 Event identification and processing

As has been discussed, a number of authors have adopted automated algorithms with varying degrees of success. Each of the aforementioned automated techniques has their merits; however, they all share a common inability to isolate discrete pulsations that appear to have central frequencies that converge or bifurcate. The success of an

algorithm rests firmly with the assumptions that constrain its behaviour. As constraints are tightened, homogeneity of extracted events increases; conversely, as limits are relaxed the greater the probability of incorrect or false extraction. As the polarisation characteristics of such a spatially extended dataset have yet to be quantified, a posteriori limits could not be adequately defined and a priori limits prove overly restrictive when hastily applied.

For the purpose of this study, as outlined in the previous chapter, a discrete pulsation is defined as a continuous region in frequency space that is of significant spectral power and distinct, slowly varying spectral characteristics. Similarly, an individual pulsation must exceed some power threshold and be bound by continuous frequency limits.

6.2.1 Pre-processing and background extraction

Preliminary daily dynamic spectra were created using the CISA technique described in section 5.2.3 and the method outlined in section 5.3.1. The daily threshold was defined as the power level that exceeded the progressive mean by three progressive standard deviations. The data below each threshold was then extracted and averaged over the entire year of 2007 in each frequency increment to create a statistical calibration curve. Figure 6.1 displays these curves from 0-3 Hz, in which can be seen the instrumental frequency response and a number of instrumentally attributed spikes. These curves were then used to normalise each power spectrum, enabling a frequency independent threshold to be set for event extraction. This method proves extremely robust in providing an acceptable threshold in all scenarios, as it remains indicative of the background noise level irrespective of the duration or intensity of any significant pulsation.

6.2.2 Manual frequency boundary selection

Having acceptably defined a dynamic power threshold, the concept of continuity of spectral characteristics, the next condition of a discrete pulsation, must be considered. Using the CISA (5.2.3) and Cross-Phase (5.2.5) techniques each data point has associated with it a minimum of four basic parameters, total power (I_T), circular

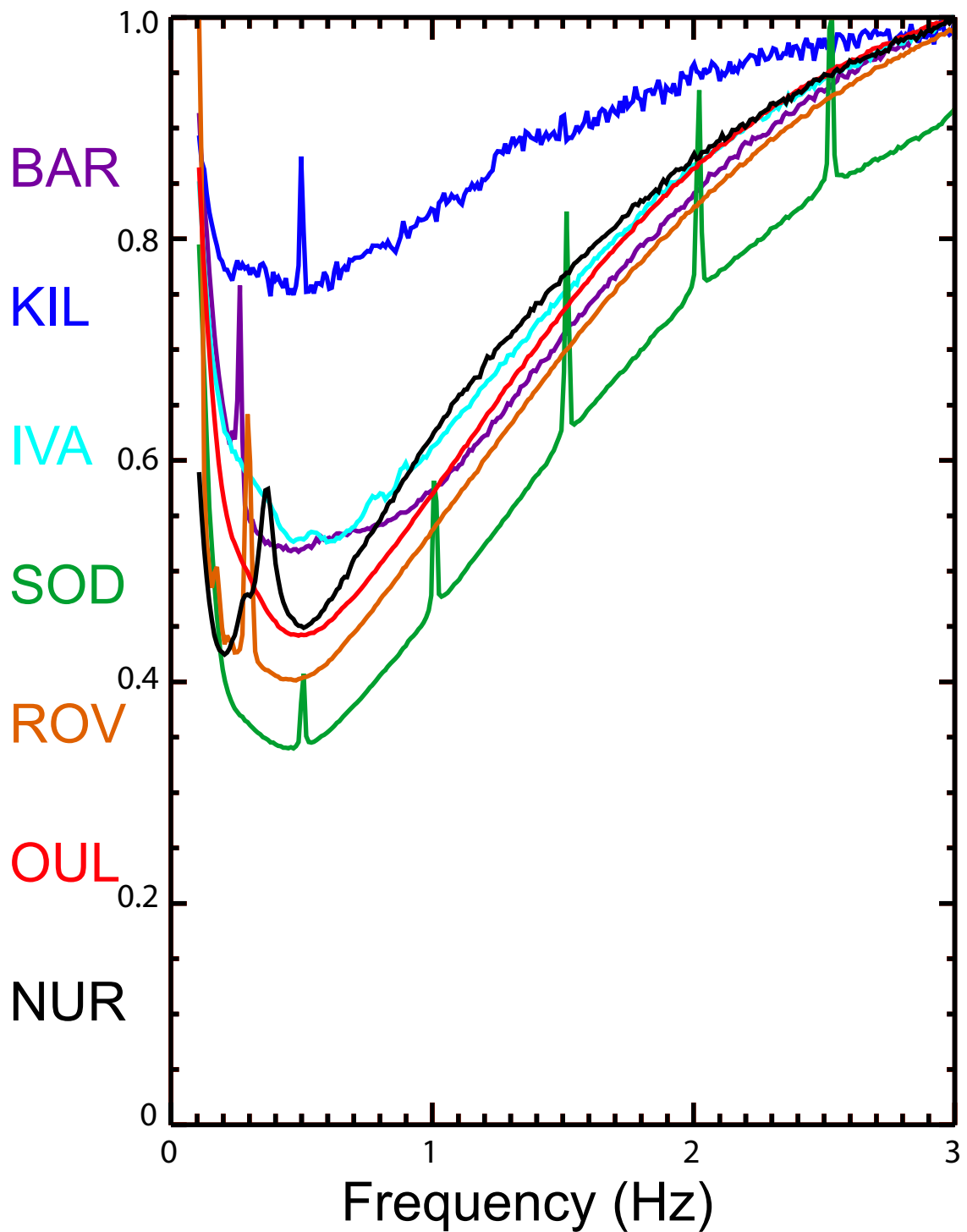


Figure 6.1: Normalised background level for each station in the FPMC. Each curve is derived from the full 2007 dataset. A threshold level of 3 standard deviations above the progressive mean was used.

polarisation ratio (PR_c), ellipticity (ε) and semi-major axis angle (α) plus a possible $\sum n-m$, $m=n-1..1$ values of cross-power (I_{cr}) and $-$ phase (Ph_{cr}), where n is the number of stations at which the pulsation is registered. For a pulsation to be considered discrete each of these parameters must display an adequate degree of continuity. It was found that the variation of each of these parameters within a given event may be greater than that between closely occurring events. It is for this reason that no fixed values of parameter gradient could be found that consistently differentiated between adjacent events and why an automated algorithm was not applied to the current dataset. Subsequently, manual event selection was necessary and was conducted in the following manner, which uses the first day of analysis, Jan 1st 2007 as an exemplum.

Each standard daily spectrogram, with its background removed, using the aforementioned method, was displayed on a tablet PC, where regions of interest were selected using a stylus. Figure 6.2 shows initial dynamic spectra for Jan 1st 2007, repeated in figure 6.3 with their backgrounds removed. Given that no quantitative coherence analysis will be presented here, to gain a better estimate of spectral characteristics, each selected region was reanalysed with the same window length and 10 s resolution. It was found that inter-station cross-phase was the most stable (i.e. of lowest standard deviation for a given event) parameter and hence most useful for discrete event identification. Subsequently, the cross-phase of each station's data with that of the most powerful normalised station was computed. The resultant thresholded spectrum, ellipticity, semi major axis angle, polarisation ratio and cross-phase were plotted for each station. Frequency limits were selected, for each event and station, again with a tablet PC and stylus. Selection was based on visual continuity of α , ε and PR_c for the most intense station and continuity of $Ph_{cr(R-H)}$, ε and PR_c for all others.

Figure 6.4 contains total-power dynamic spectra for region 2 of figure 6.3. This region contains pulsations that would have previously been categorised as a single event (Feygin *et al.*, 2009, Fukunishi *et al.*, 1981); however, consideration of all the available parameters show it to be comprised of two discrete events, of which the lower frequency pulsation will serve as exemplar and is overlaid with its manually selected frequency boundaries. The spectral information in the encircled region of frequency space was then extracted for further analysis. The parameters used for selection are

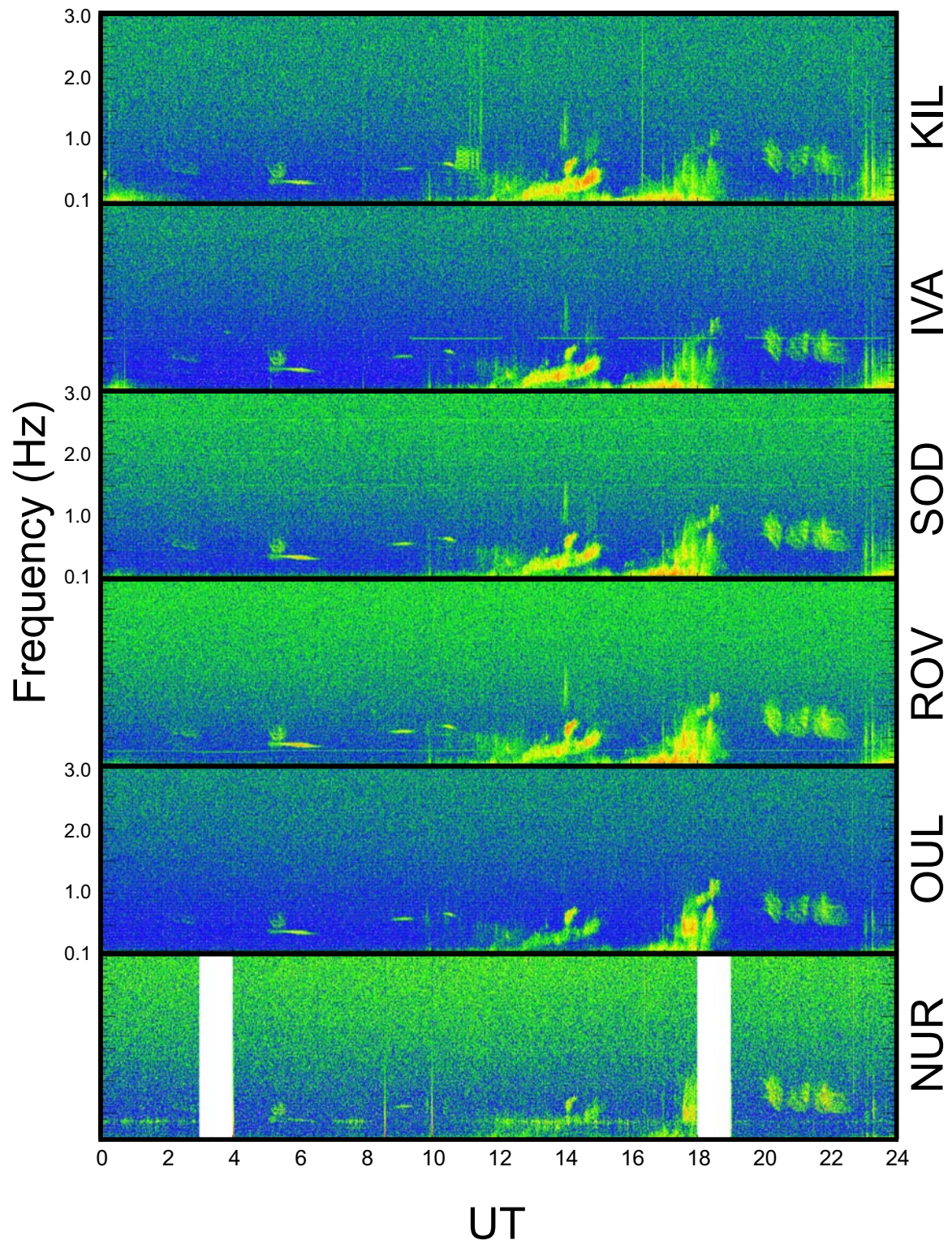


Figure 6.2: FPMC dynamic spectra for the 1st Jan 2007, between the frequencies of 0.1 Hz and 3 Hz. An FFT window of 102.4 s with an overlap of 42.4 s was used. A number of distinct, continuous and pulsations IPDP and instrumental artefacts are evident in all stations.

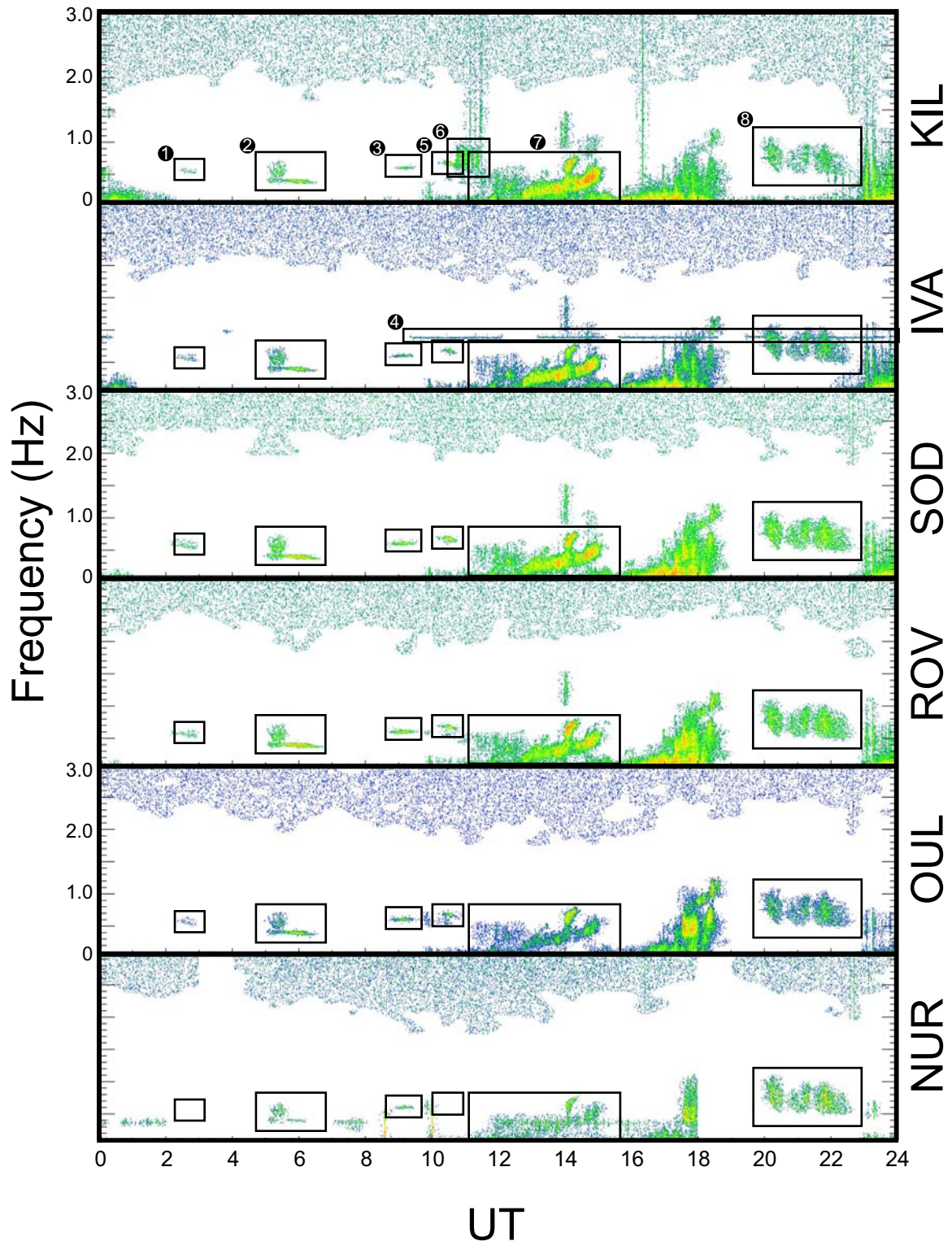


Figure 6.3: FPMC dynamic spectra for the 1st Jan 2007 with their background noise extracted. The regions of interest enclosed in black boxes were selected for higher temporal resolution analysis. Regions 4 and 6 were determined to be artefacts, which will not be further considered, and region 7 as an IPDP. Residual noise can be seen above 2.0 Hz.

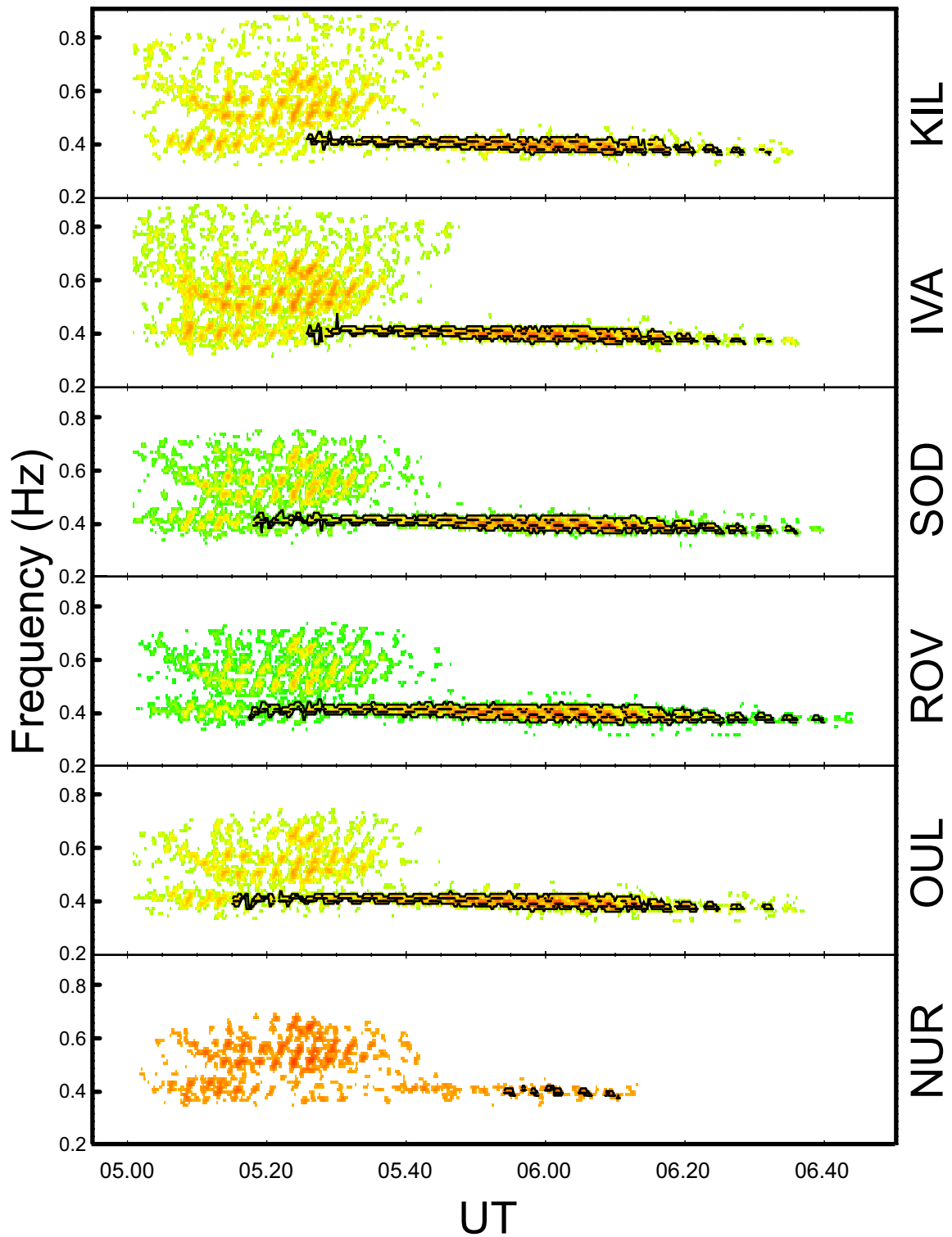


Figure 6.4: Dynamic spectra of figure 6.3 region 2 with background noise removed and frequency boundaries for a discrete pulsation with central frequency of ~ 0.4 Hz overlaid.

displayed in Figure 6.5, which show distinct spectral characteristics for each pulsation present.

6.2.3 Statistical parameter determination

The directly extracted values for each time increment are as follows: central frequency (F_c) and frequency width (ΔF) are defined as the average and difference of the frequency limits, respectively, with the parameter F_p defining the frequency of the increment's peak power. These values for SOD are displayed in panels a-c of figure 6.6. The difference in event start and end times, denoted by vertical dashed lines, define event duration (Δt). Statistical moments for each time increment were computed for each spectral parameter; panels d-i show their means and standard deviations.

As previously noted, each parameter may be highly variable within a given event, to the point where characterisation by a single value becomes questionable. Total event statistical moments were computed, however, variability with intensity, frequency and time, meant that without knowledge of the standard deviation, skew and kurtosis, the mean was often uncharacteristic of the entire event. Hence, the method outlined in section 5.3.2 was used to derive characteristic event values.

To gain further insight into each event's general trend, parameter gradients were calculated either using the time increment mean or dynamic histogram derived values, depending on which method was used for their initial derivation.

6.2.4 Event categorisation and degree of structuring

Figure 6.3 clearly shows several, morphologically dissimilar, varieties of pulsation, each of significant power and spectral continuity yet clearly not all are of Pc1-2 type. Rather than visually discriminate during the selection process, the methodology outlined in section 5.3.3 was applied to event categorisation. Events of the type in region 4 were recorded only at Ivalo (IVA) and were of a consistent $F_c = 0.9$ Hz and $\Delta F < 0.15$ Hz. Events of the type in region 6, which were recorded only at Kilpisjarvi (KIL), exhibited sharp spectral boundaries. Both event types were subsequently excluded from the Pc1-2

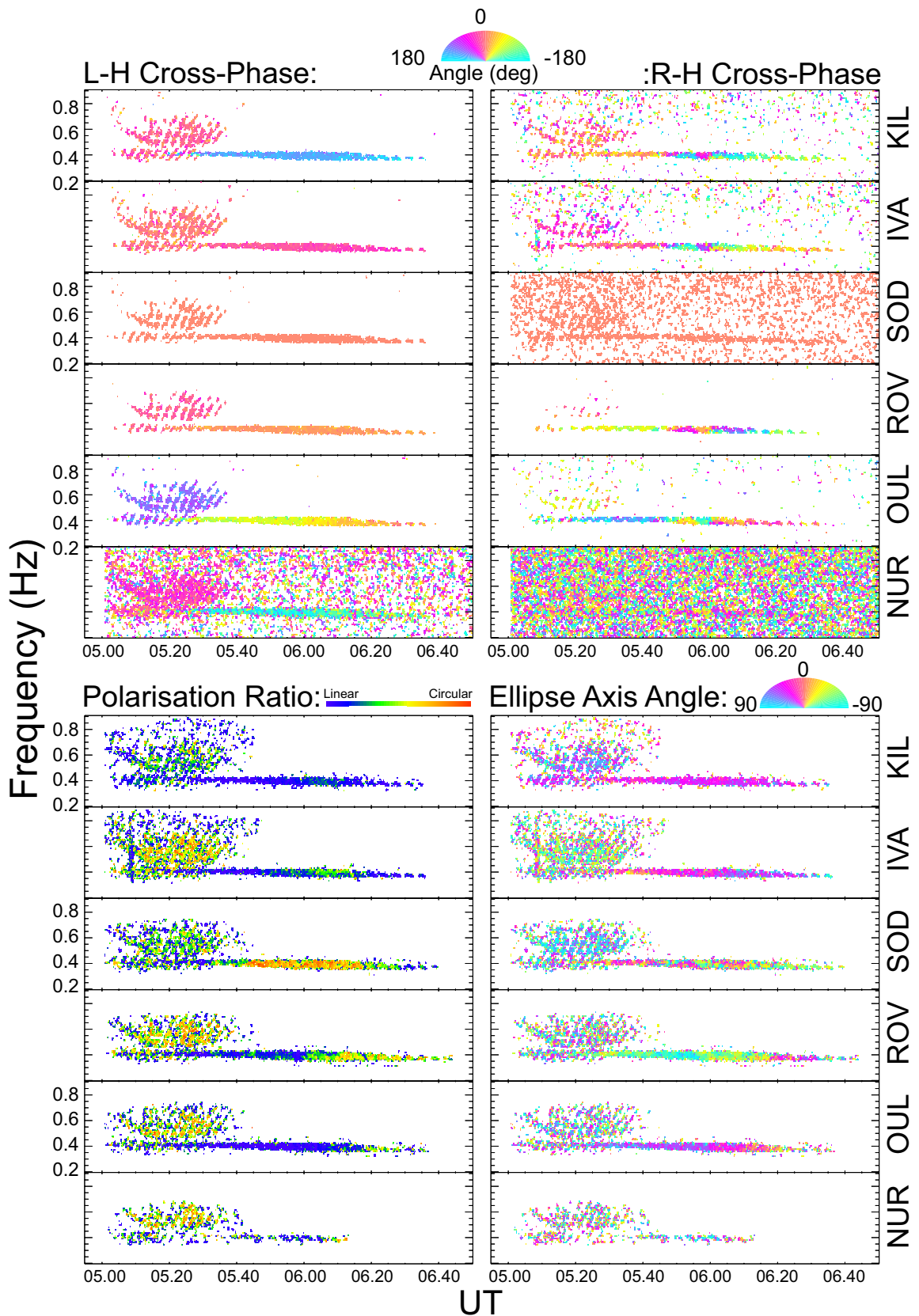


Figure 6.5: Spectral selection parameters for Figure 6.3 region 2. Cross-phase (top panels) plots show that two distinct pulsations are present. Significant variation can be seen in the polarisation ratio and semi-major axis angle throughout the lower frequency event at all stations.

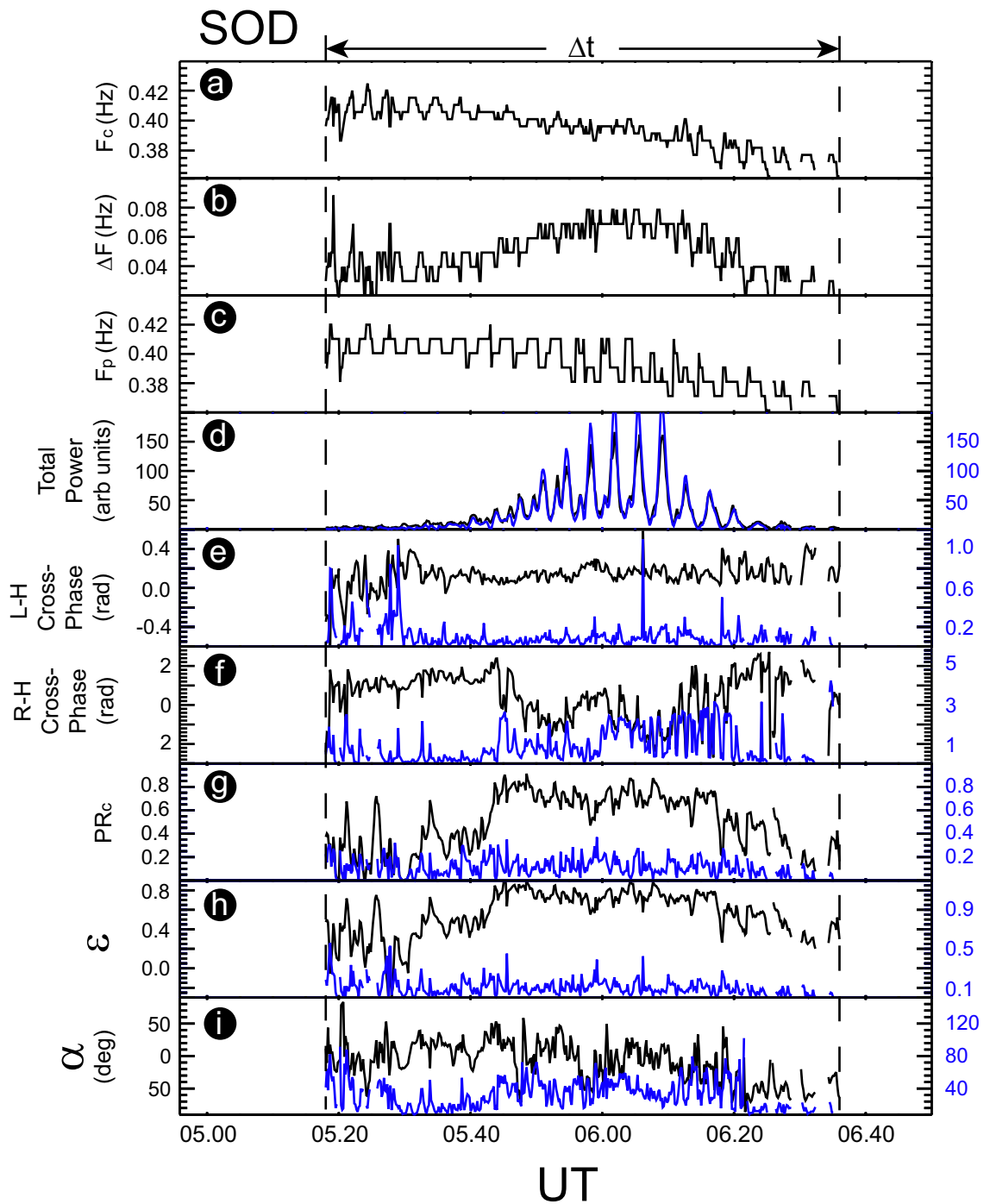


Figure 6.6: Statistical parameters for the discrete event in region 2 of figure 6.3 for SOD. Parameter values are black, their standard deviations blue.

dataset and their origins will remain unaddressed in the current work. Irregular Pulsations of Diminishing Period (IPDP), such as those enclosed in region 7 were excluded by applying the collective conditions that the gradient of F_c must not exceed $1.5 \times 10^{-5} \text{ Hz s}^{-1}$, $F_c - 0.5dF > 0.3\text{Hz}$ and $\Delta F > 0.3 \text{ Hz}$.

An immediately apparent feature of the extracted Pc1-2 dataset, independent of FFT input parameters, was that the distinction between structured and unstructured pulsations was less than clear. To investigate this phenomenon the periodic parameter (P_p) introduced in section 5.3.3 was calculated for each event with a cut-off value of $P_p = 1 \times 10^6$ for structured event identification. This condition identifies the apparently periodic, narrow band pulsations of figure 6.3 in regions 1, 2, 3 and 5 as structured and that of region 8 as unstructured.

6.2.5 Identification of geomagnetic storm activity and determination of solar wind driving structures.

Identification of the geomagnetic storms used in this study loosely follows the scheme set out in the Gonzalez *et al.* (1994) review paper. The Sym-H index has been used as a de facto high temporal resolution Dst index as its value remained modest for entire interval of study (Wanliss and Showalter, 2006). Correction for the magnetopause current contribution to the Sym-H index has been made using the empirical formula of Burton *et al.* (1975) with OMNI solar wind data (Gonzalez *et al.*, 1994). Following the scheme of Gonzalez *et al.* (1994), the lower limits of small, moderate and intense storms were set at -30 nT, -50 nT and -100 nT respectively. The minimum Sym-H value (SH_{peak}) and onset (T_{sto}), main (T_{stm}) and recovery phase (T_{str}) times were recorded for each storm. Since the focus of this study is Pc1-2 behaviour over a full calendar year, storm isolation was not a selection criterion. Exclusion of this condition allowed the effects of multiple storms to contribute to the storm-time rather than the nonstorm-time distributions described in the following sections. It has been noted that magnetospheric storm response differs according to the causal solar wind structure, e.g. (Tsurutani and Gonzalez, 1997). To investigate this effect the solar wind structure responsible for each storm was determined based upon the criteria of (Xu *et al.*, 2009). In addition to the aforementioned criteria, Minimum Variance Analysis (MVA) (Sonnerup and Cahill Jr, 1967) was employed to isolate magnetic clouds (MC), Cross Correlation Analysis

(CCA) of Omni and Stereo data was used to detect CIRs and similarly CCA of IMF and solar wind velocity components was used to determine the presence of Alfvén waves.

6.2.6 Magnetopause and plasmapause positions

The magnetopause standoff distance has been calculated, using OMNI solar wind data, according to the empirical fit of Shue *et al.* (1997) and is used throughout as an indicator of dayside magnetospheric compression. Similarly, the position of the plasmapause has been calculated using the empirical model of O'Brien and Moldwin (2003). These authors used in situ CRRES satellite crossings of the plasmapause to generate a model position that is dependent upon geomagnetic indices. Three local time dependent model functions were prescribed, based upon the Kp, AE and Dst indices respectively. Given the association of Pc1-2 pulsations to ring current energy content (Daglis *et al.*, 1999), the Dst model was chosen as default in the current study.

6.3 Statistical results

The methods and conditions described in the previous sections identified 1416 discrete Pc1-2 events, of which 16 IPDPs and 203 KIL/IVA artefacts were excluded. Of the remaining 1197 events, which from this point onward will be referred to as the dataset, 405 and 792 were categorised as structured and unstructured respectively. This information is summarised in table 6.1

6.3.1 Pc1-2 dataset statistics

Mean dataset values of the basic occurrence, frequency and polarisation parameters for each station are also given in table 6.1 and box and whisker plots of their distributions are shown in figure 6.7. The solid boxes represent the inter-quartile ranges of each distribution and their whiskers extend to the full range of the dataset; outlying data exceeding three standard deviations of the median are represented by diagonal crosses. A number of gaps in the Sodankylä dataset during the month of July account for the comparatively low number of recorded events; the bracketed numbers in table 6.1 indicate the true count, based upon those events registered at both IVA and ROV during

Station	Events		F_c (Hz)		ΔF (Hz)		F_p		Δt	
	KIL	1131		0.500		0.080		0.497		76.6
IVA	383	748	0.493	0.503	0.067	0.087	0.491	0.500	77.3	76.3
	1119		0.502		0.075		0.499		71.1	
SOD	375	744	0.493	0.506	0.063	0.081	0.491	0.504	71.4	70.9
	928 (1069)		0.522		0.065		0.520		63.8	
ROV	324 (371)	604 (698)	0.528	0.519	0.055	0.070	0.526	0.517	68.7	61.2
	1071		0.522		0.067		0.520		65.8	
OUL	379	692	0.504	0.532	0.056	0.073	0.056	0.530	66.0	65.7
	901		0.526		0.064		0.524		64.4	
NUR	278	623	0.542	0.519	0.062	0.065	0.539	0.518	62.1	65.4
	463		0.596		0.061		0.594		51.0	
	122	341	0.608	0.592	0.057	0.063	0.606	0.590	43.2	53.8

Table 6.1: Basic occurrence and frequency parameters (mean values) of the full (upper value), structured (left) and unstructured (right) datasets. Interpolated values from SOD are bracketed.

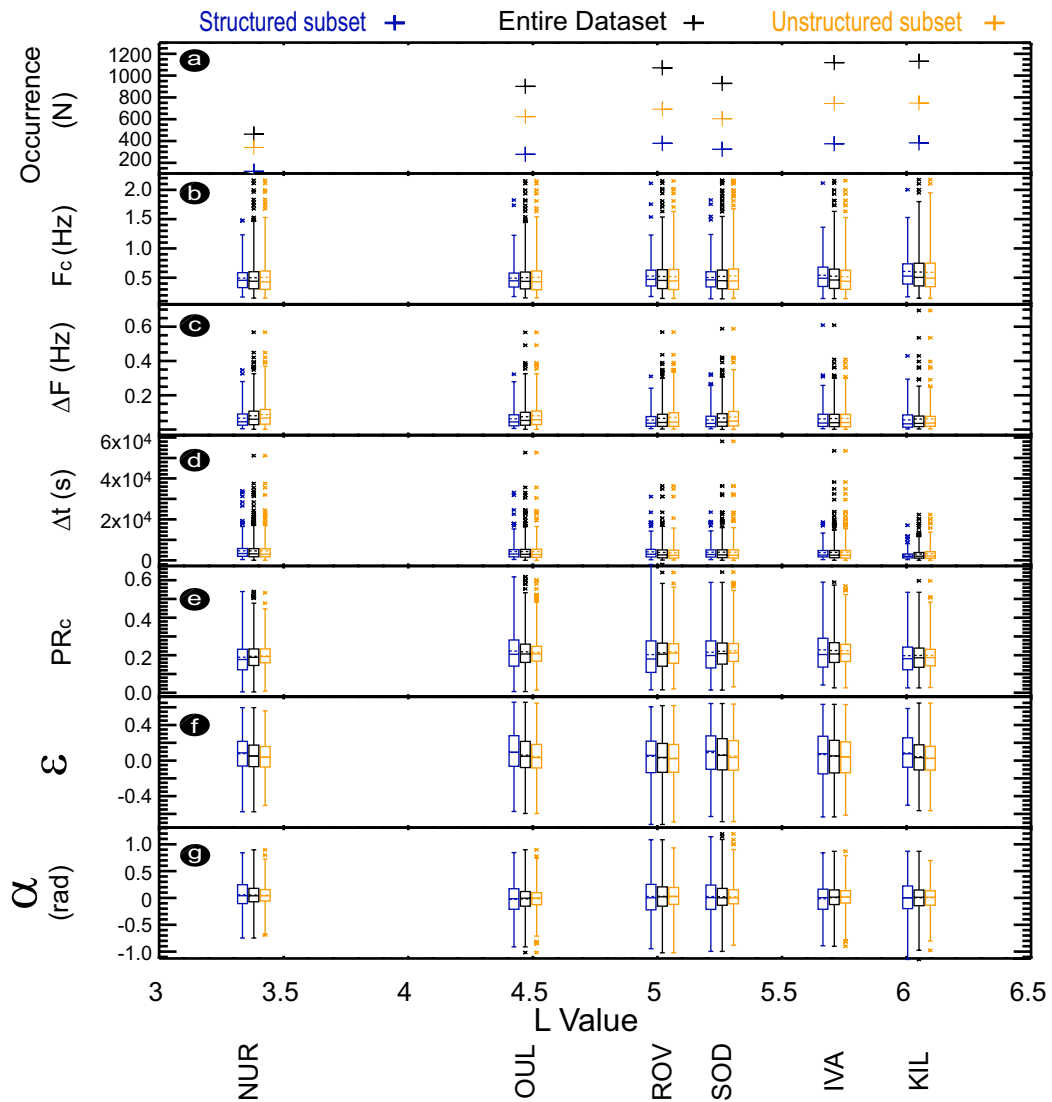


Figure 6.7: Panel a displays the number of pulsations in the entire dataset plotted against L-shell value. Panels b-g are box and whisker plots of the distribution of frequency and polarisation parameters. The total distribution is shown in black, structured blue and unstructured orange.

these times. Each value or box and whisker plot is derived for the entire dataset and for the structured and unstructured subsets as defined in section 6.2.4.

The box and whisker plots displayed in figure 6.7 do not interpolate the missing data for Sodankylä, which, given the heightened activity during those periods, is seen to have an effect on all parameters. Panel a of figure 6.7 shows that there is a general increase in the number of recorded events with latitude. Unstructured events are more numerous at all stations yet their dominance shows no clear latitudinal dependency. Event bandwidth (panel c) and duration (panel d) also increase with latitude. Structured events appear more band-limited than their unstructured counterparts. Although the difference between subset durations shows no systematic variation with L-shell, the difference in mean bandwidth does display a slight dependency, increasing with latitude. Panel b also confirms an approximately inverse relationship of F_c with L value, in agreement with previous observation and theory (Kangas *et al.*, 1998). Panel e shows the mean values of PR_c , which indicates that the two extreme stations, NUR and KIL, are less circularly polarised than the central four. Panel f displays mean values of ϵ , which suggests a slight systematic preference for left-hand polarisation and again, more so in the central than the extreme stations, with the structured/unstructured difference being more pronounced at the extremes. Structured events are of greater left-handedness at all stations. Little may be assumed from the distribution of α , as an evenly distributed angular dataset would naturally average to zero.

In figure 6.8 are superposed monthly occurrence histograms for the full calendar year, in which can be seen the well documented increased occurrence surrounding the equinoxes. For effective comparison of monthly values, a month is from hereon in defined as one twelfth of a year. The month of July, however, contains an unexpectedly high number of events, which, as shall be seen, may be attributed to a rapid succession of low intensity storms. The aforementioned missing and subsequently interpolated Sodankylä data is not reproduced in these histograms. The annual distribution of total, structured and unstructured pulsations are shown in blue, red and yellow respectively and where the distributions overlap orange is used. Error bars for each of the distributions are plotted centrally, to the left and to right of centre of each column for the total, structured and unstructured pulsations respectively. The mean value for each category is plotted on all columns as an appropriately aligned cross. The figure suggests

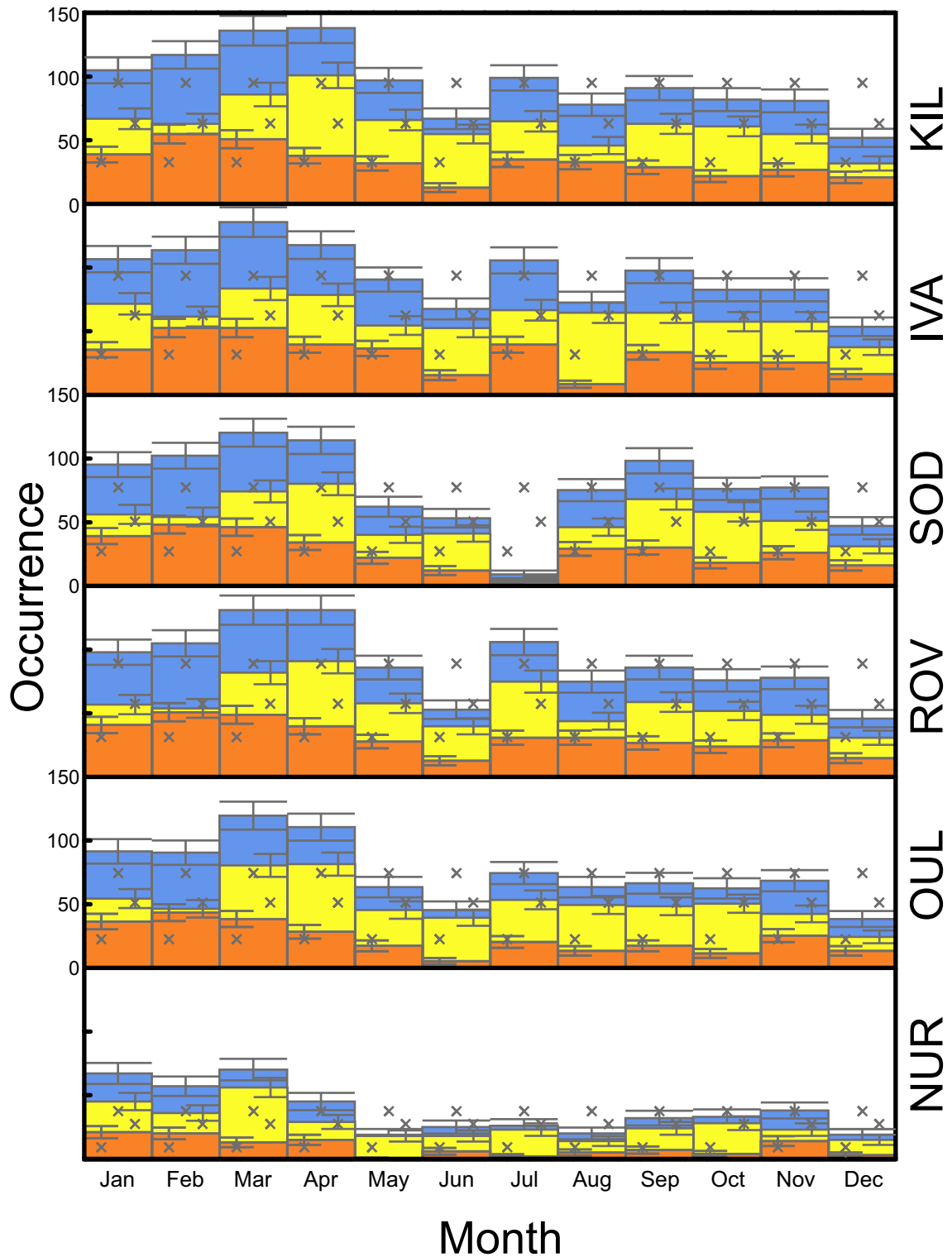


Figure 6.8: Pc1-2 occurrence histograms for six stations of the FPMC in the year 2007. Each bin is populated with the total number of discrete pulsations, irrespective of duration. Total occurrence is coloured blue, structured red, unstructured yellow and where the distributions coincide the overlap is coloured orange, which in this figure is exclusively the case. Error bars for the total distribution span the full width of each bin, whereas the structured (unstructured) distribution's error bars are half width and aligned to the left (right). The mean value of each distribution is plotted in each column aligned to the relevant error bar.

that the peak monthly occurrence is pre-equinox for structured and post-equinox for unstructured pulsations, in the vernal case, evidenced by significant increases in occurrence above the mean for those respective months. However, the autumnal variation is less pronounced.

In a similar format to figure 6.8, the diurnal distributions of total (blue), structured (red) and unstructured (yellow) pulsations are represented in figure 6.9, which show that the local noon prevalence in occurrence is composed of a pre-noon structured and post-noon unstructured peak.

Figure 6.10 contains an annual-diurnal-total occurrence plot for each station. With month on the vertical and universal time on the horizontal axis, each data point represents a bin of 12 minutes width and one month height and contains the total number of whole pulsation minutes within that bin. Each histogram shows the evolution of diurnal occurrence throughout the year. Similarly, figures 6.11/6.12 present the structured/unstructured distributions and clearly show the differences in peak occurrence between the two subsets. Structured (unstructured) pulsations favour pre- (post-) noon and pre- (post-) equinox. The contribution of intense activity surrounding the equinoxes is apparent in both the structured and unstructured distributions, in both cases accounting for the majority of counts and thus heavily influencing the overall shape of each diurnal distribution.

Histograms of event F_c are shown in figure 6.13, which retains the colour scheme of 6.8. The modal frequency range for structured pulsations is 0.380-0.474 Hz at all but the highest latitude station, which very slightly favours the lower frequency bin of 0.286-0.380 Hz. Unstructured events are slightly more numerous in the 0.286-0.380 Hz range at all stations except for two central stations, SOD and IVA, which favour the lower band: 0.190-0.285 Hz. These distributions show that the arithmetic mean values in table 6.1 overestimate characteristic central pulsation frequencies; more so in the unstructured case, which are generally more positively skewed.

F_c variation with universal time is shown in figure 6.14, which adopts the colour scheme of 6.7. The figure consists of a series of box and whisker plots, each of which represents 2 hours of UT. An increase of central frequency may be seen as a positive

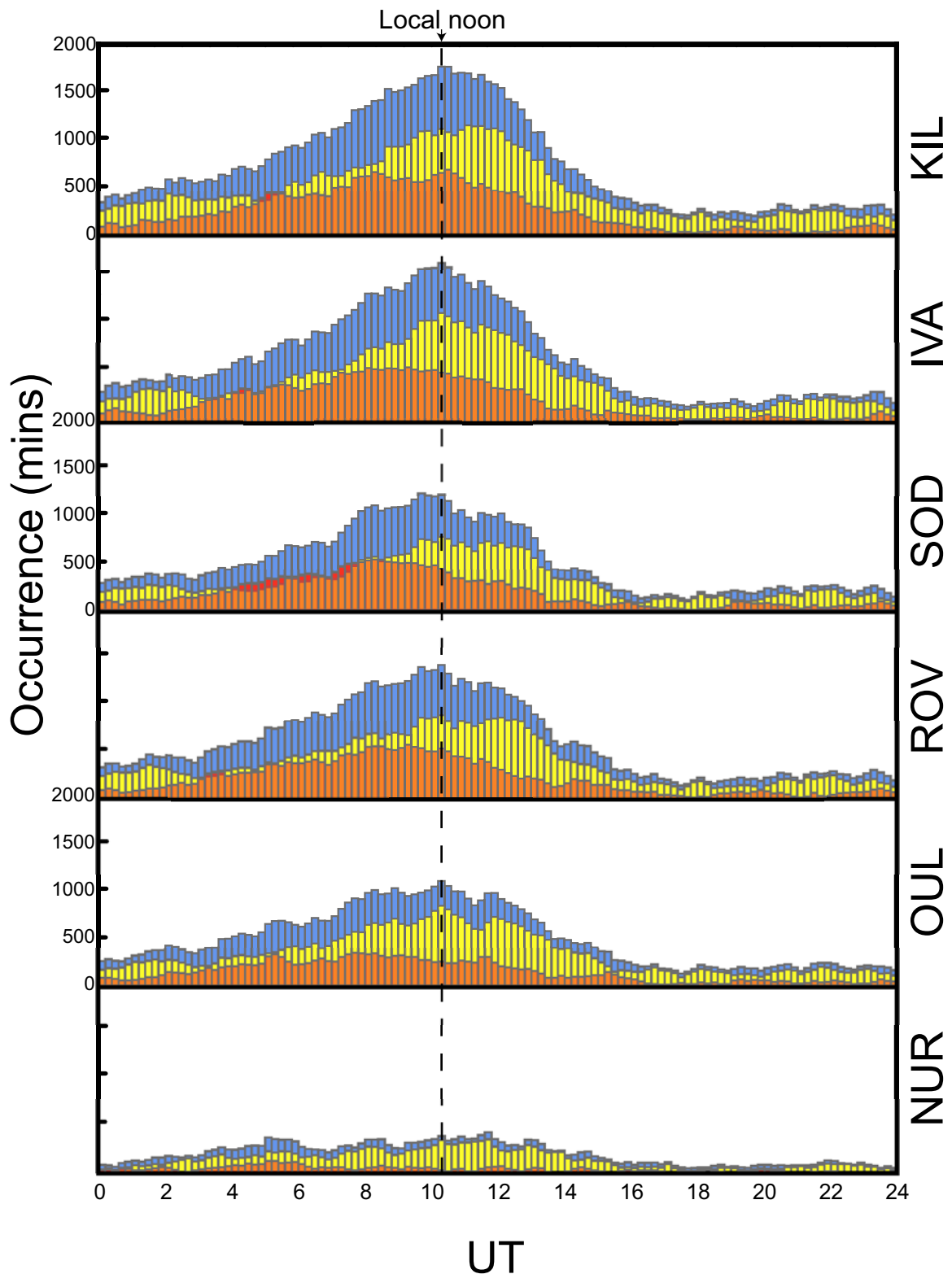


Figure 6.9: Diurnal Pc1-2 occurrence histograms for six stations of the FPMC in the year 2007. Total occurrence is coloured blue, structured red, unstructured yellow and orange their overlap. Structured and unstructured pulsations show a preference for pre- and post-local noon, respectively. Local noon is marked with a vertical dashed line as will it be in all subsequent plots.

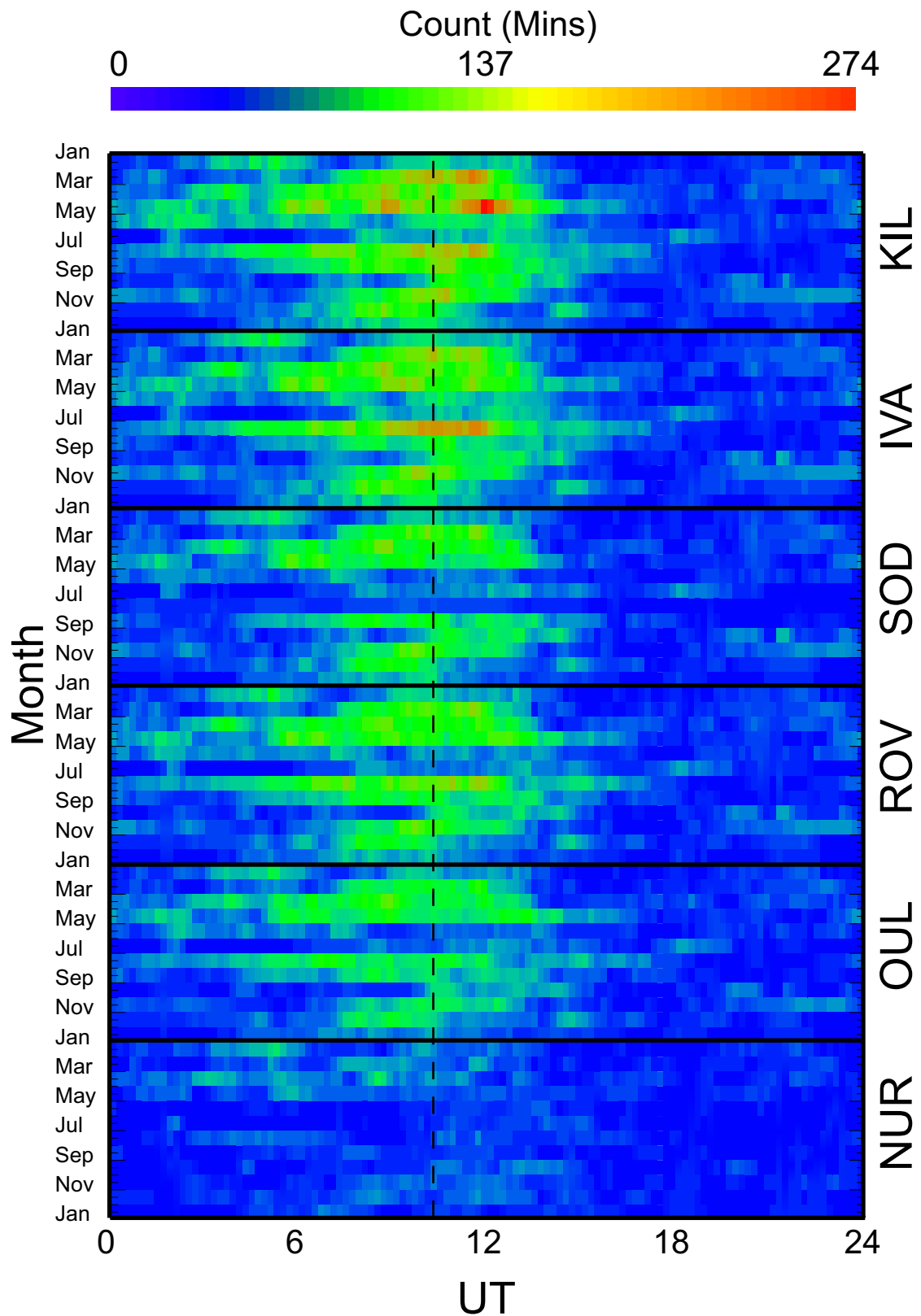


Figure 6.10: Pc1-2 Annual-diurnal-occurrence plot for six stations of the FPMC in year 2007. Each bin is of 12 minutes width and 1 month height and is populated with the total number of pulsation minutes in that bin.

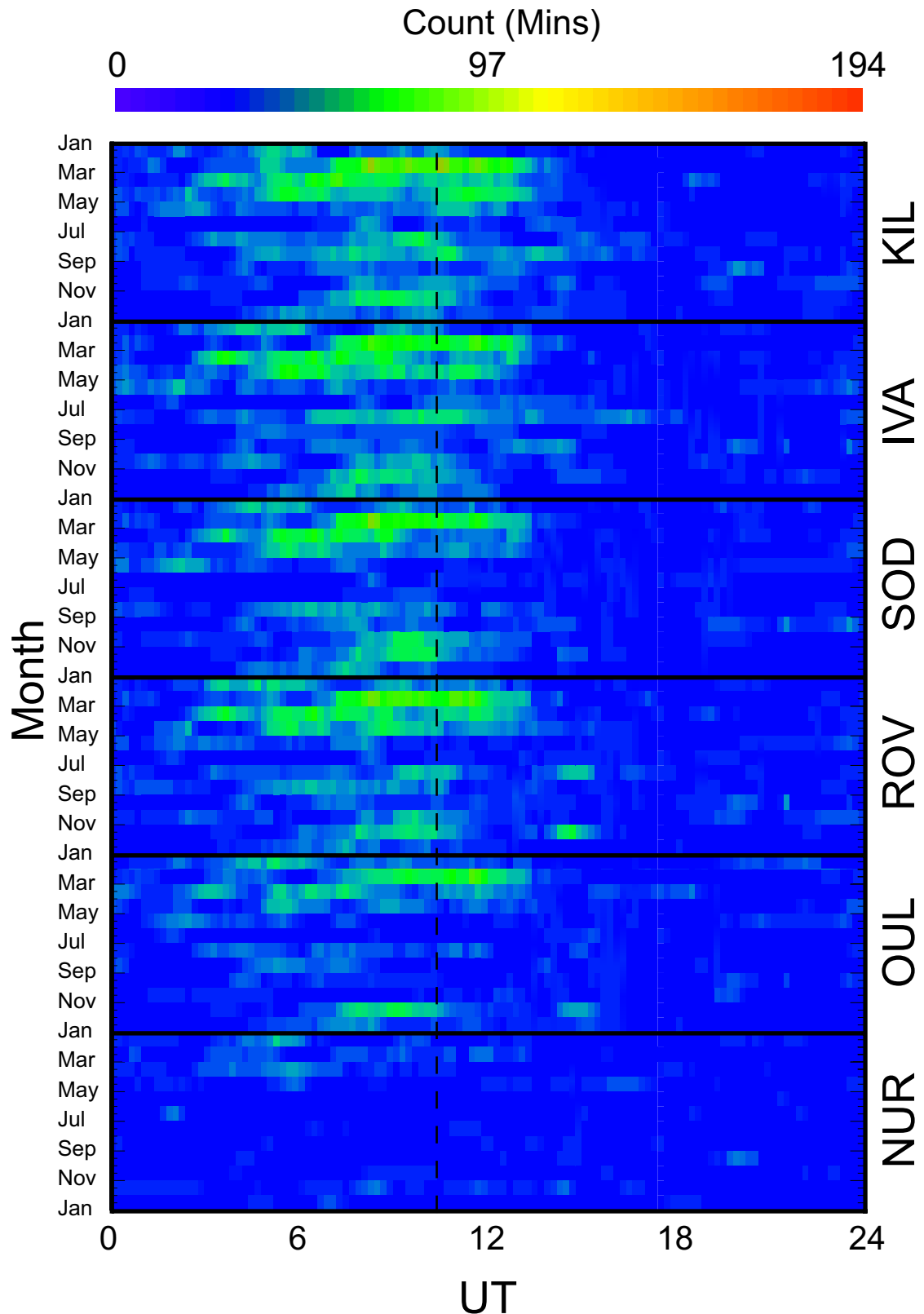


Figure 6.11: Annual-diurnal-occurrence plot of structured Pc1-2 occurrence for six stations of the FPMC in year 2007. Each bin is of 12 minutes width and 1 month height and is populated with the total number of pulsation minutes in that bin.

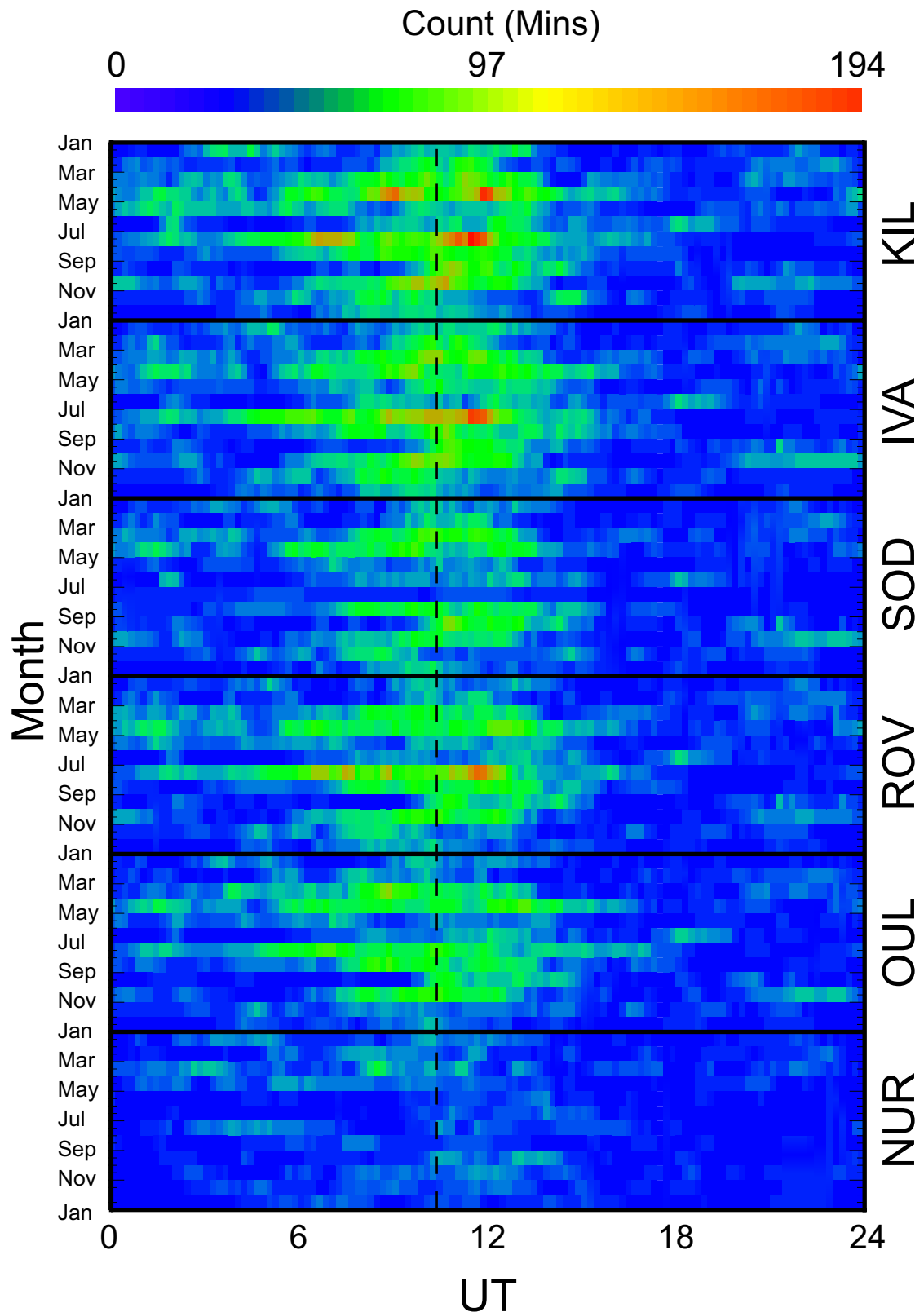


Figure 6.12: Annual-diurnal-occurrence plot of unstructured Pc1-2 occurrence for six stations of the FPMC in year 2007. Each bin is of 12 minutes width and 1 month height and is populated with the total number of pulsation minutes in that bin.

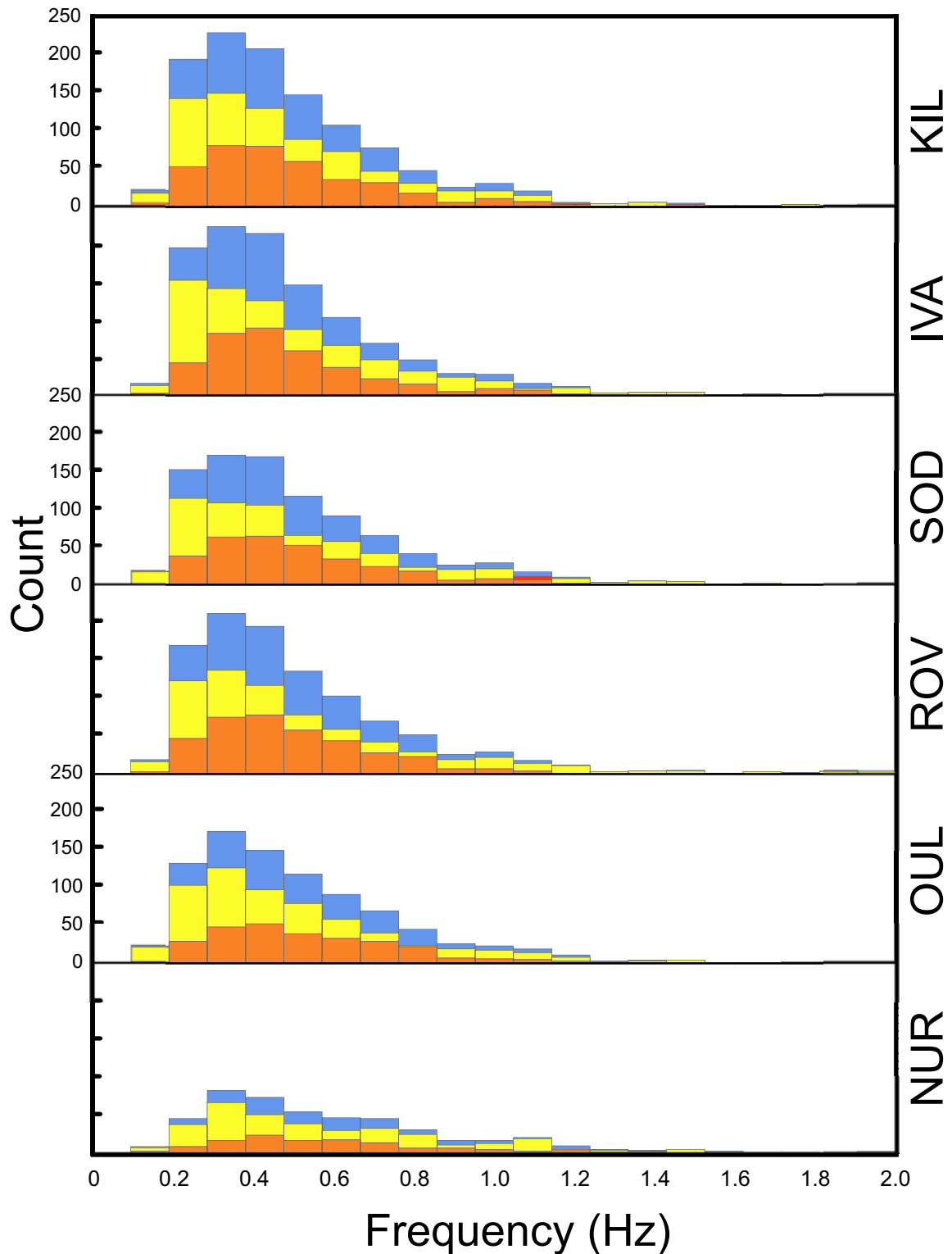


Figure 6.13: Central frequency histograms for six stations of the FPMC in the year 2007. Total occurrence is coloured blue, structured red, unstructured yellow and orange their overlap. Structured pulsations appear more band-limited and of slightly higher modal frequency than unstructured at all stations.

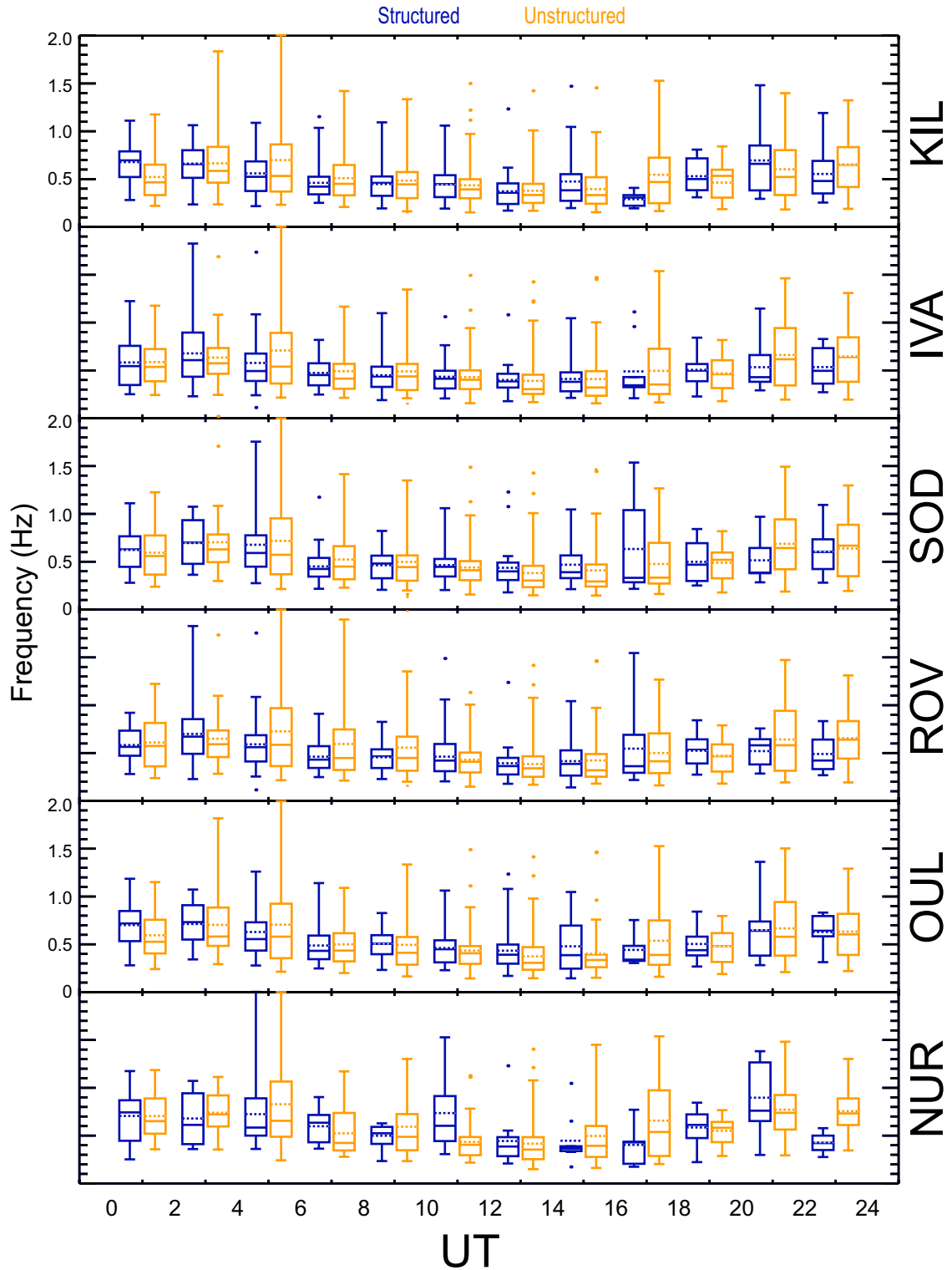


Figure 6.14: Box and whisker plots of the diurnal central frequency variation for the entire dataset. Each box plot represents a 2 hour data-bin containing all the structured (blue) and unstructured (orange) events that occurred in that UT interval.

shift in both the median value and inter-quartile range surrounding local dawn and midnight. A pronounced trough in the post-noon and early evening sectors is also apparent, where the data's 75th percentile falls below that of the 25th percentile of the dawn peak. The dawn sector peak is predominantly populated with structured events and the midnight peak with unstructured. Most high latitude deviations from this pattern are unstructured, which is converse to the low latitude case. Figure 6.15, which is a plot of the annual distribution of pulsations of similar format to figure 6.14 but with each box and whisker plot representing one month, indicates that the epoch surrounding and immediately following summer solstice experiences the lowest frequency events at all latitudes for both species.

Event duration histograms are shown in figure 6.16, which are, given the large range of durations and the predominance of sub 100 minute long pulsations, logarithmically binned. The distributions of both subsets are similar and do appear, as their mean values in table 6.1 suggest, to favour shorter durations with decreasing latitude. Figure 6.17 presents histograms of the degree to which an event is circularly polarised. The structured event distribution displays a small positive skew suggesting that most events tend to be more linearly polarised. The unstructured distribution appears near symmetrical; although, the central stations do display a slight negative skew suggesting that pulsations registered there show a tendency to be more relatively circularly polarised. The histograms in figure 6.18 show unstructured event ϵ to be symmetrically distributed about zero implying no preference for left- or right-handedness. However, the structured event high latitude, negatively skewed distribution suggests a preference for left-handedness there, less so at the lowermost station. Histograms of the semi-major axis angle of polarisation ellipse are displayed in figure 6.19. Although each of the histograms does display a central peak and most are somewhat negatively skewed, their more uniform-like distribution suggests that no systematically preferred orientation exists at any latitude.

The diurnal variation of PR_c is represented as series of box and whisker plots, of similar form to figure 6.14, in figure 6.20. The figure shows little systematic variation of polarisation degree with time of day. However, as depicted in figure 6.21 in similar form, there exists a quasi-sinusoidal diurnal variation of ellipticity that is more pronounced in the central stations. Pre-dawn to mid-morning pulsations appear to be

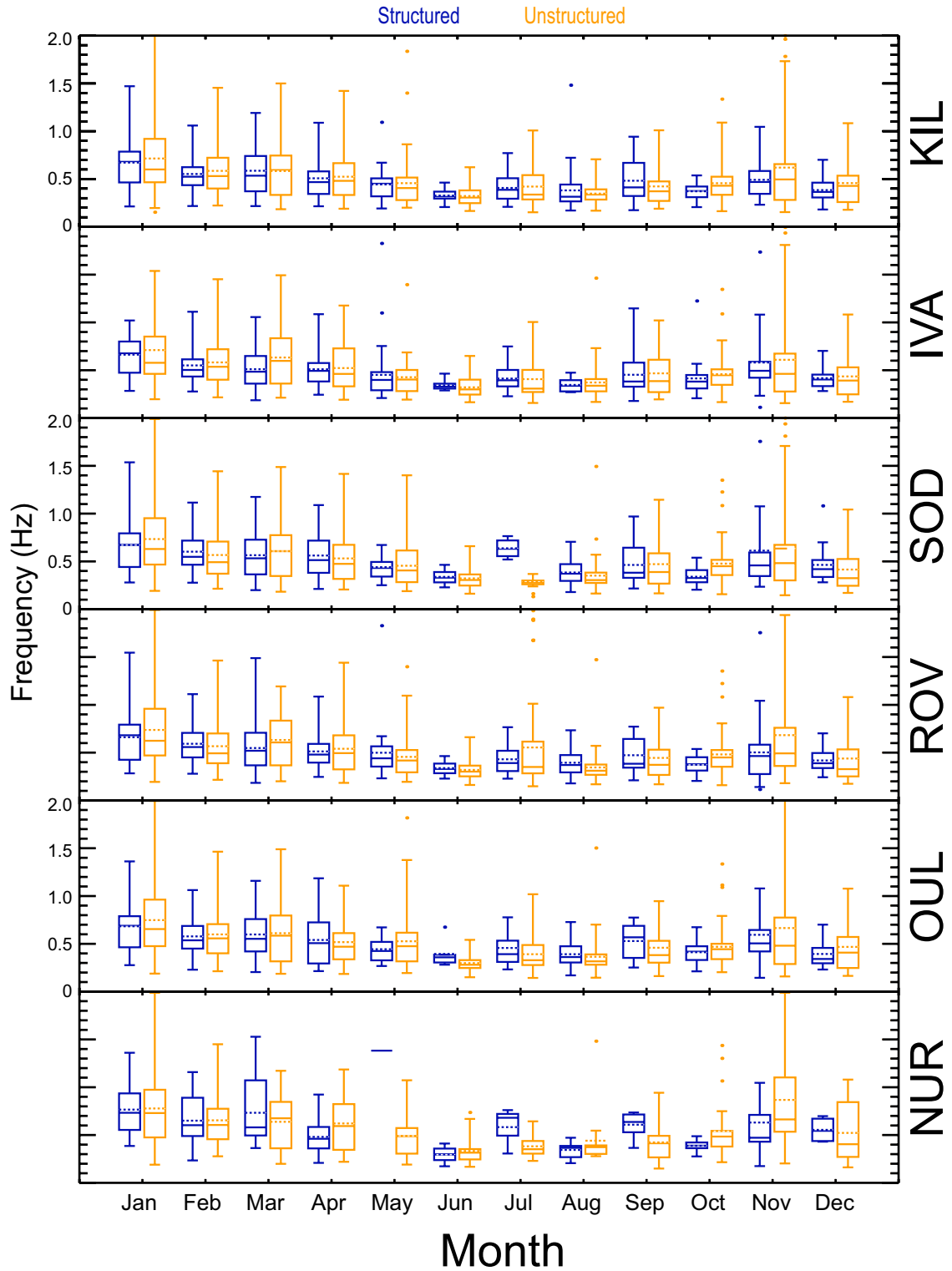


Figure 6.15: Box and whisker plots of the annual central frequency variation for the entire dataset. Each box plot represents a month wide bin containing all the structured (blue) and unstructured (orange) events that occurred in that interval.

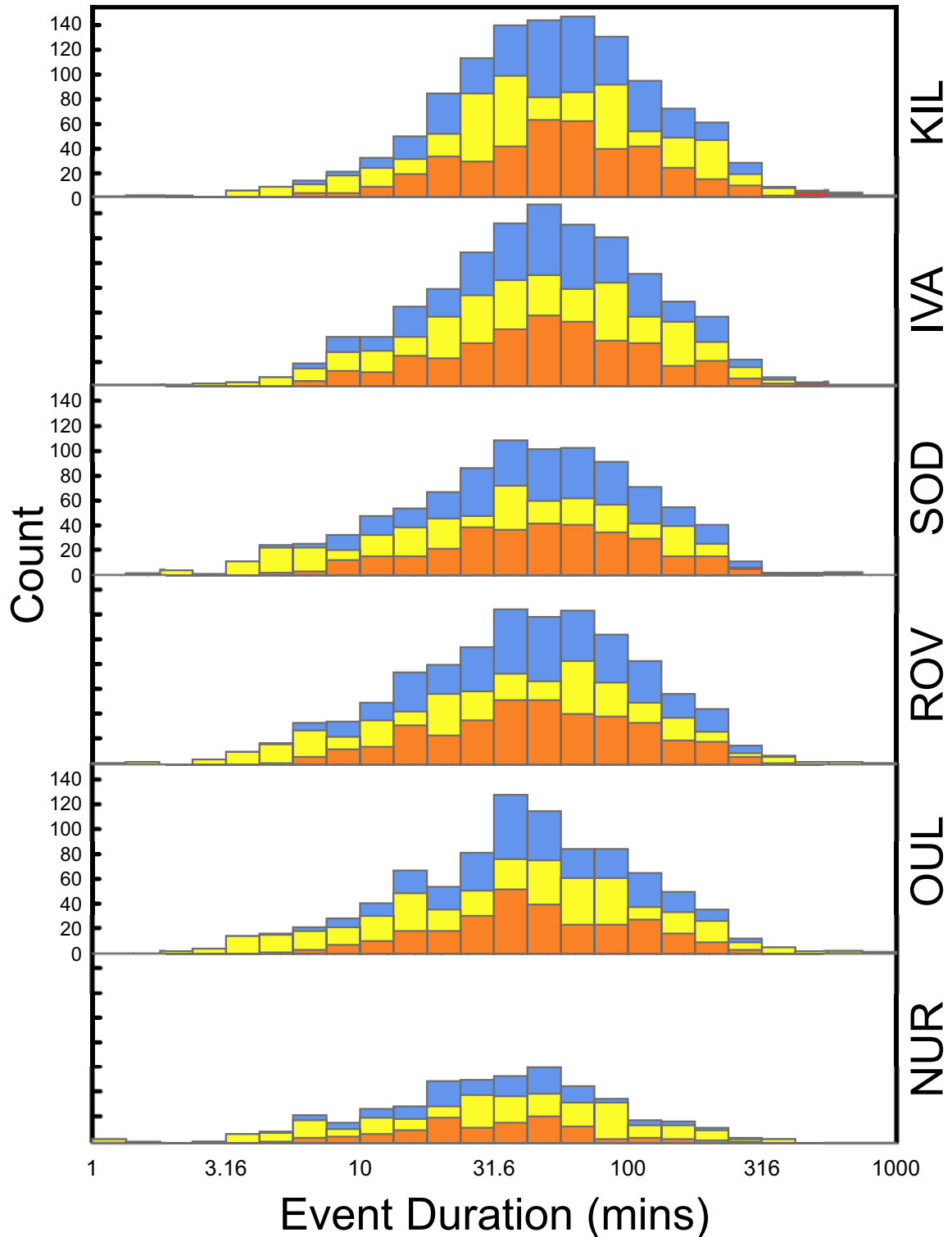


Figure 6.16: Event duration histograms for six stations of the FPMC in the year 2007. Total pulsation count is coloured blue, structured red, unstructured yellow and orange their overlap. Given the large spread yet low modal duration, bin intervals are logarithmic.

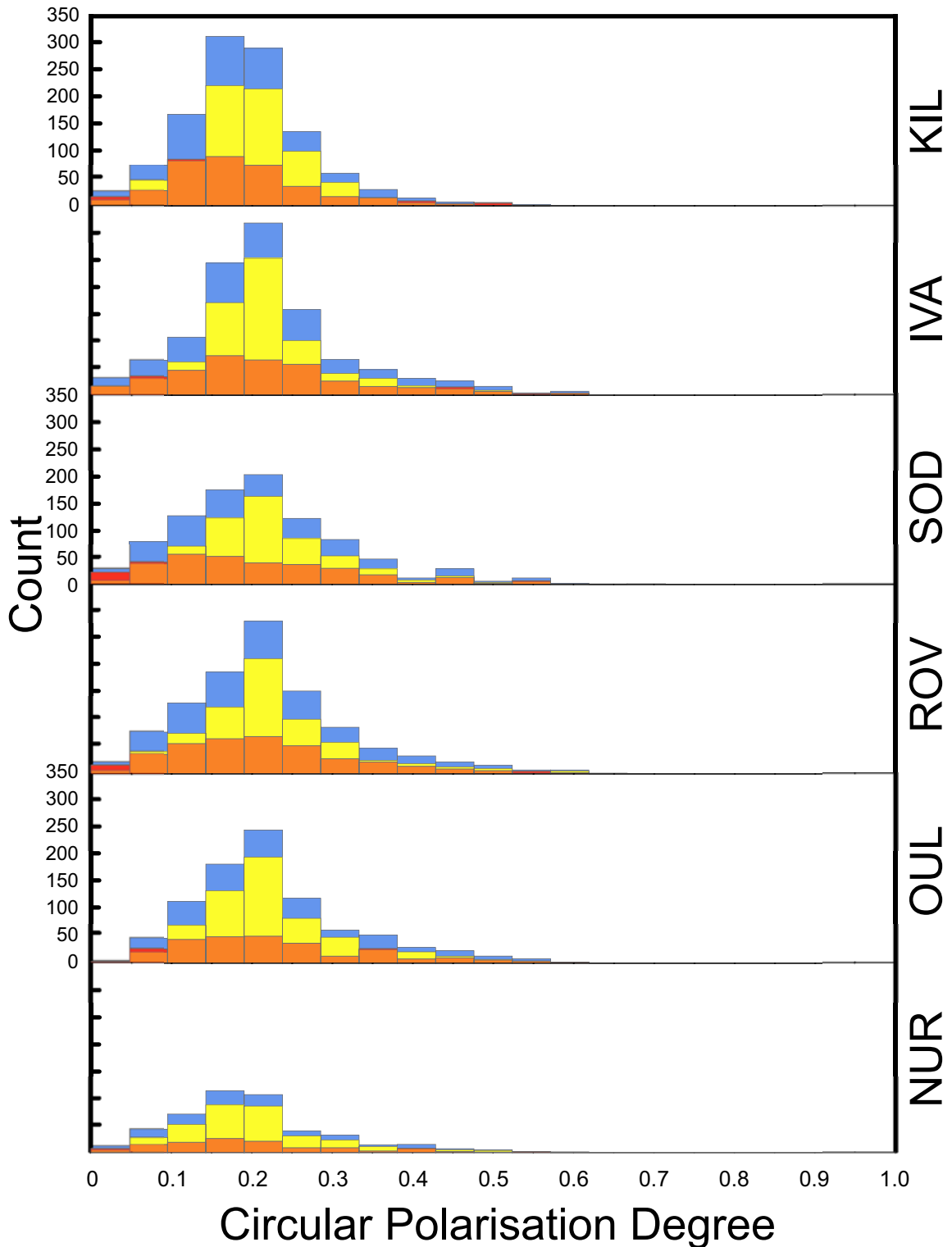


Figure 6.17: Polarisation histograms for six stations of the FPMC in the year 2007. Total pulsation count is coloured blue, structured red, unstructured yellow and orange their overlap. Structured pulsations display a small positive skew relative to the near normal unstructured distributions, which appear to be slightly negatively skewed at higher stations.

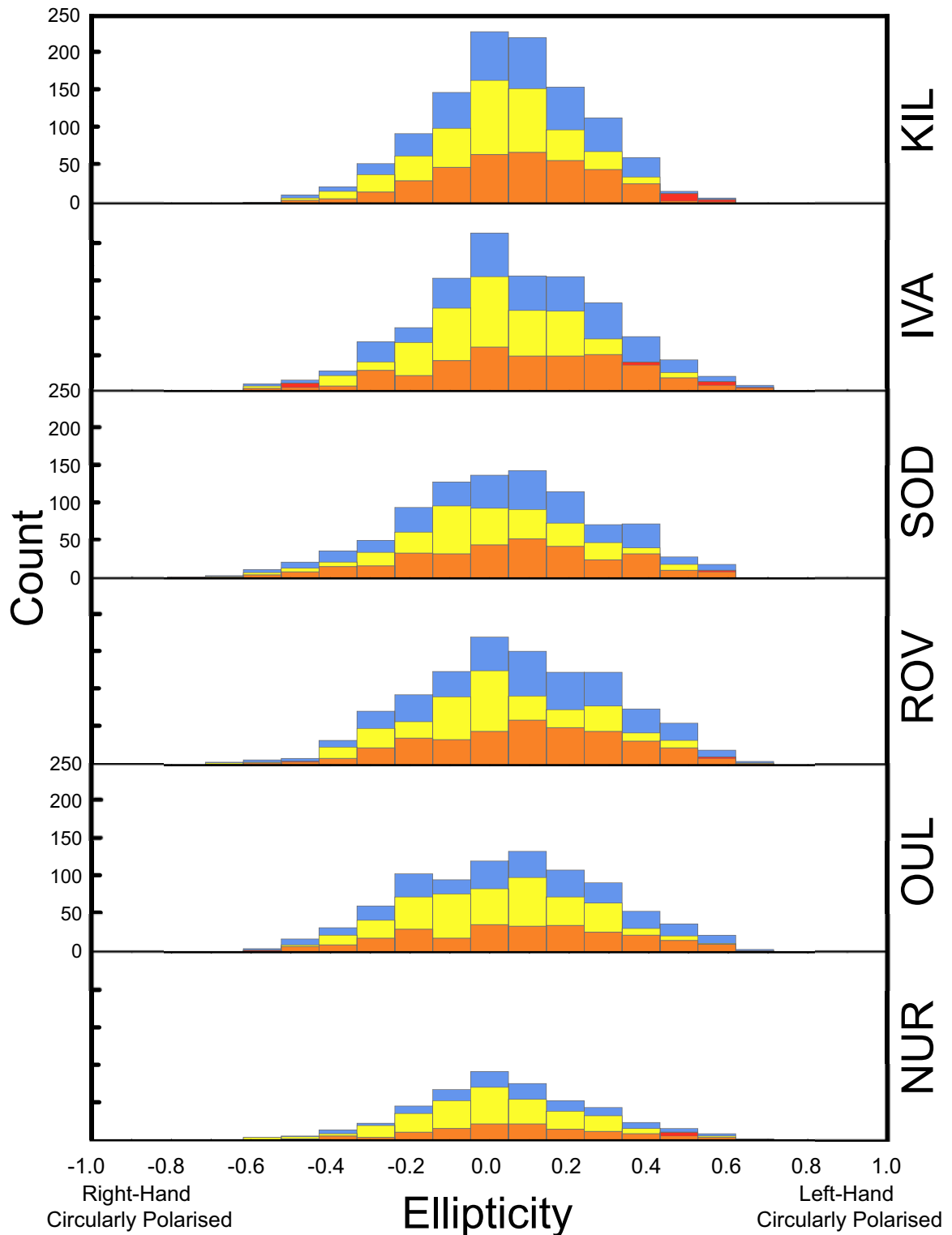


Figure 6.18: Ellipticity histograms for six stations of the FPMC in the year 2007. Total occurrence is coloured blue, structured red, unstructured yellow and orange their overlap. Unstructured pulsations are near normally distributed about zero ellipticity, whereas structured pulsations display a negative skew suggesting a preference for left-handedness at all but the most equatorial station.

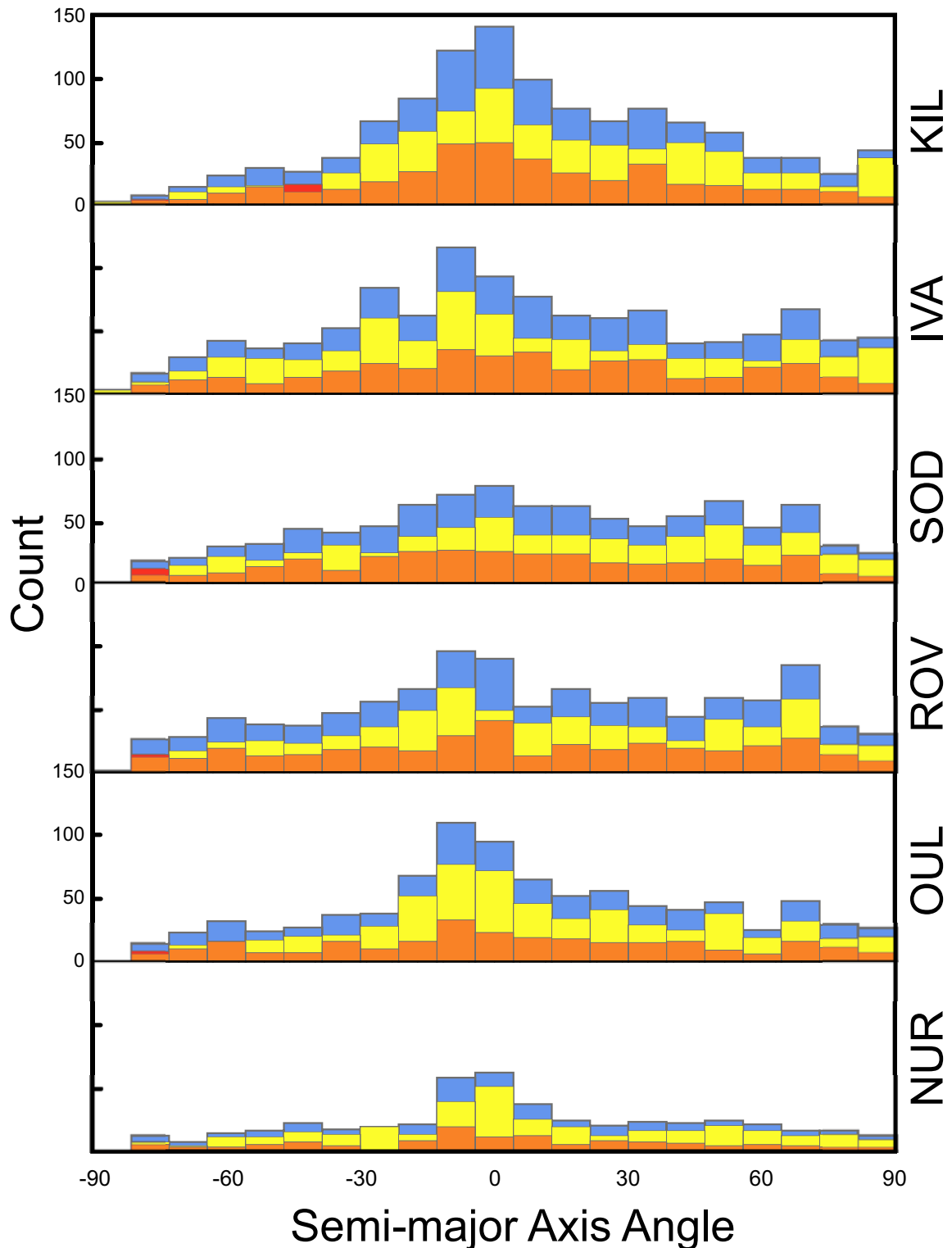


Figure 6.19: Polarisation ellipse semi-major axis angle histograms for six stations of the FPMC in the year 2007. Total occurrence is coloured blue, structured red, unstructured yellow and their overlap orange. The small kurtosis and similarity of all histograms implies that the orientation of the polarisation ellipse has no significant preferred orientation.

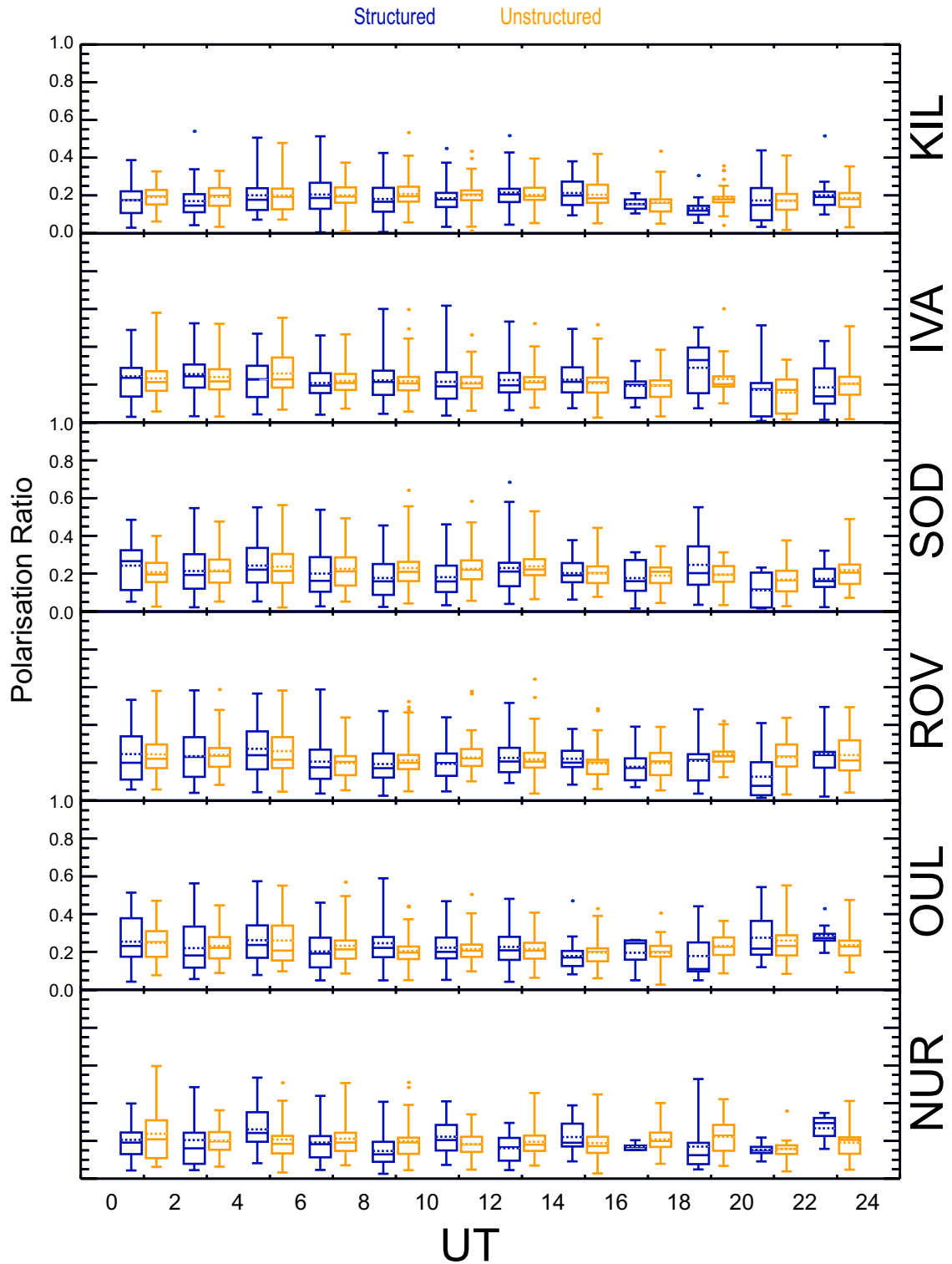


Figure 6.20: Box and whisker plots of the diurnal polarisation ratio variation for the entire dataset. Each box plot represents a 2 hour data-bin containing all the structured (blue) and unstructured (orange) events that occurred in that UT interval.

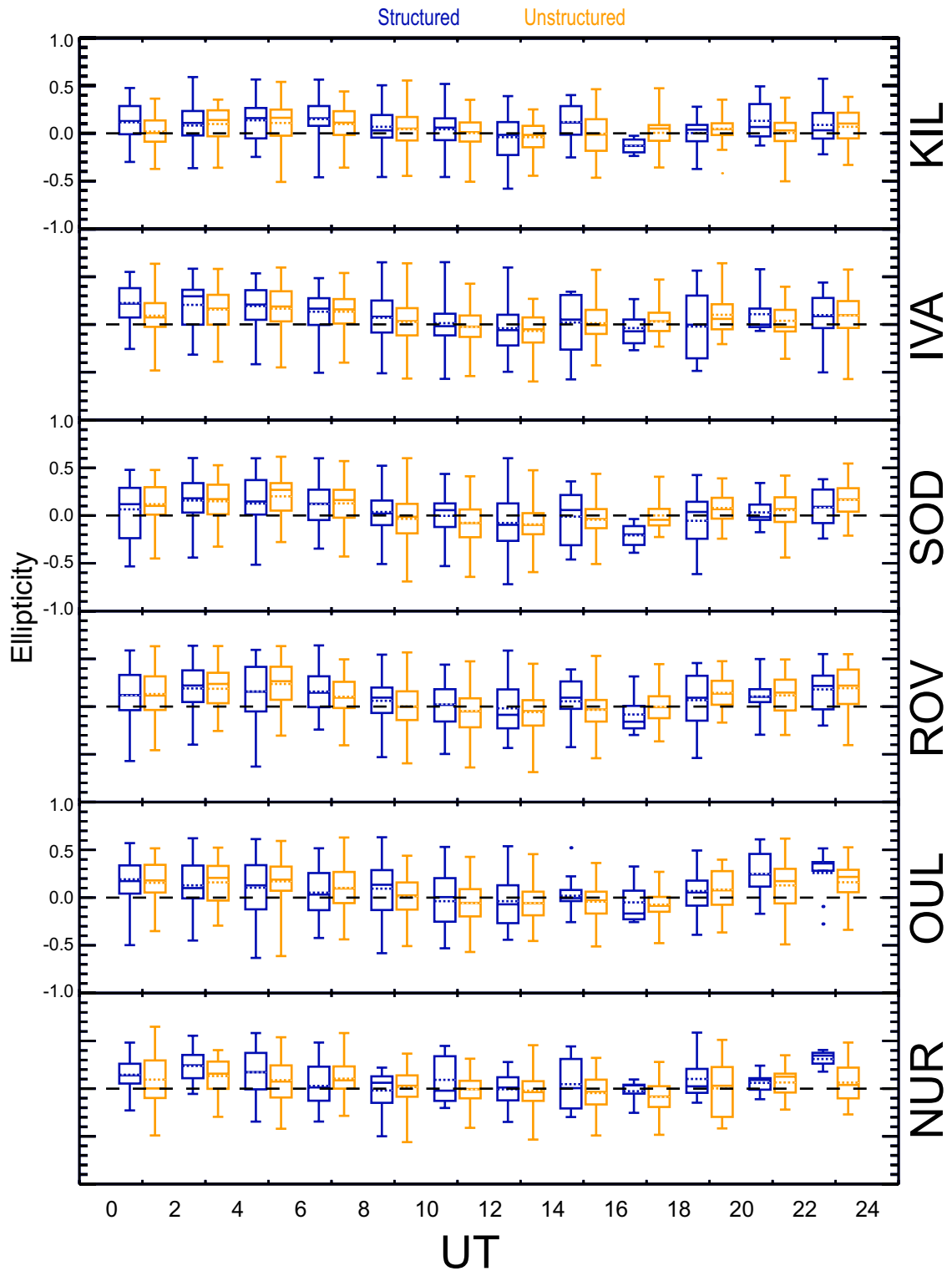


Figure 6.21: Box and whisker plots of the diurnal Ellipticity variation for the entire dataset. Each box plot represents a 2 hour data-bin containing all the structured (blue) and unstructured (orange) events that occurred in that UT interval.

predominantly L-H circularly polarised, evidenced by the 25 percentile of most 2 hourly bins in that time period taking a positive value. However, post-local noon events become less dominantly polarised, shown by the median value of their distributions falling close to zero, remaining so until late evening where a further increase in L-H polarisation dominance is seen.

6.3.2 Geomagnetic storm statistics

The criteria and techniques outlined in section 6.2.5 isolated 26 discrete storm events, of which 19 were of small and 7 of moderate intensity. No large storms were recorded for the interval of study, which is unsurprising given the declining phase of the solar cycle. 23 of the recorded storms were driven by CIRs, the remaining 3, all of which were of moderate intensity were CME (all of MC type) induced. The basic measured parameters are outlined in table 6.2. Mean durations of 102 and 165 hrs for weak and moderate storms respectively were observed. Figure 6.22 shows the total number of storms and the number of storm hours in each month of the year. An immediately apparent feature in the storm monthly histogram is that occurrence does not consistently follow the well-documented equinoctial variation (Gonzalez *et al.*, 1994) but displays a higher than expected number of storms in the months of July, August and December. July and August saw a rapid succession of small storms surrounding a single moderate storm in mid-July, whereas December saw two lengthy yet small intensity storms.

6.3.3 Storm-time pulsation occurrence

Pulsation properties during storm-times and their temporal evolution have been compared to the non-storm-time case, the results of which will follow a description of a quasi-randomly selected, typical storm event.

On the 27th of February 2007 at approximately 18.00 UT, a geomagnetic storm was initiated by a CIR impinging on the Earth's magnetosphere. It was characterised by a gradual rise in solar wind velocity from 350 kms⁻¹ to 650 kms⁻¹, increased magnetic field strength and temperature, and concurrent density and temperature discontinuities (not shown); this CIR induced a magnetospheric compression immediately prior to storm onset. Panels a and b of figure 6.23 show the position of the model magnetopause

Onset Date	Solar Wind Structure	Max Sym-H* (nT)	Min Sym-H* (nT)	Onset (decimal hour of day)	Main Phase Duration (hours from onset)	Recovery Phase Duration (hours from main phase)	Total Duration (days)
02/01/2007	CIR	14.9	-32.6	11.9	3.57	118.53	5.09
29/01/2007	CIR	0.1	-55.4	13.9	8.20	123.80	5.50
13/02/2007	CIR	8.7	-41.4	14.7	9.30	101.10	4.60
27/02/2007	CIR	15.4	-36.3	17.9	6.48	93.13	4.15
12/03/2007	CIR	1.8	-46.3	23.9	1.90	114.65	4.86
23/03/2007	CIR	-2.9	-63.0	20.8	9.82	127.98	5.74
31/03/2007	MC	22.0	-75.6	23.9	8.67	147.87	6.52
17/04/2007	CIR	19.2	-30.7	5.7	7.05	66.37	3.06
23/04/2007	CIR	9.5	-34.9	0.5	2.30	36.05	1.60
27/04/2007	CIR	12.8	-37.3	16.0	8.28	143.68	6.33
07/05/2007	CIR	22.1	-41.0	11.9	9.92	79.35	3.72
22/05/2007	MC	22.8	-55.6	16.8	20.37	169.73	7.92
21/06/2007	CIR	11.4	-36.6	20.8	2.98	52.82	2.33
10/07/2007	CIR	24.7	-44.8	19.8	10.02	71.85	3.41
14/07/2007	CIR	6.7	-58.6	7.4	18.90	81.42	4.18
20/07/2007	CIR	21.4	-45.7	6.6	4.20	99.55	4.32
06/08/2007	CIR	16.5	-36.6	19.8	6.50	70.42	3.20
10/08/2007	CIR	-0.8	-41.8	3.6	11.18	98.20	4.56
27/08/2007	CIR	-0.6	-38.5	10.8	14.08	76.12	3.76
01/09/2007	CIR	7.4	-31.9	15.4	13.87	61.48	3.14
06/09/2007	CIR	1.1	-31.0	8.8	13.83	54.08	2.83
27/09/2007	CIR	24.3	-47.0	13.6	42.38	196.02	9.93
25/10/2007	CIR	4.5	-59.8	3.2	17.72	151.55	7.05
20/11/2007	MC	26.1	-67.3	4.4	16.10	255.47	11.32
10/12/2007	CIR	4.4	-34.0	20.3	10.33	119.37	5.40
17/12/2007	CIR	25.8	-45.1	5.6	10.50	222.28	9.70

Table 6.2: Storm occurrence statistics.

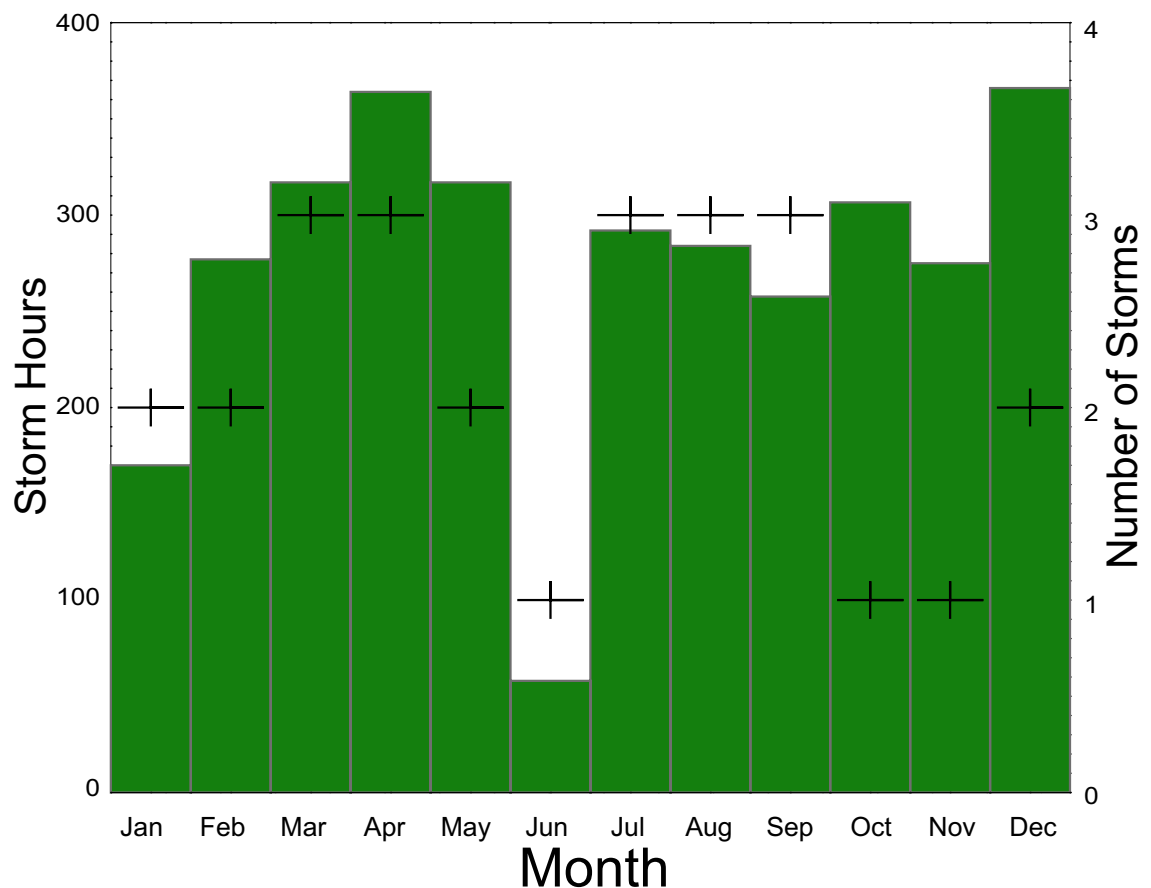


Figure 6.22: Storm occurrence statistics. The histogram represents the number of storm hours, irrespective of their start times, and the crosses the total number of storms initiated within a given month.

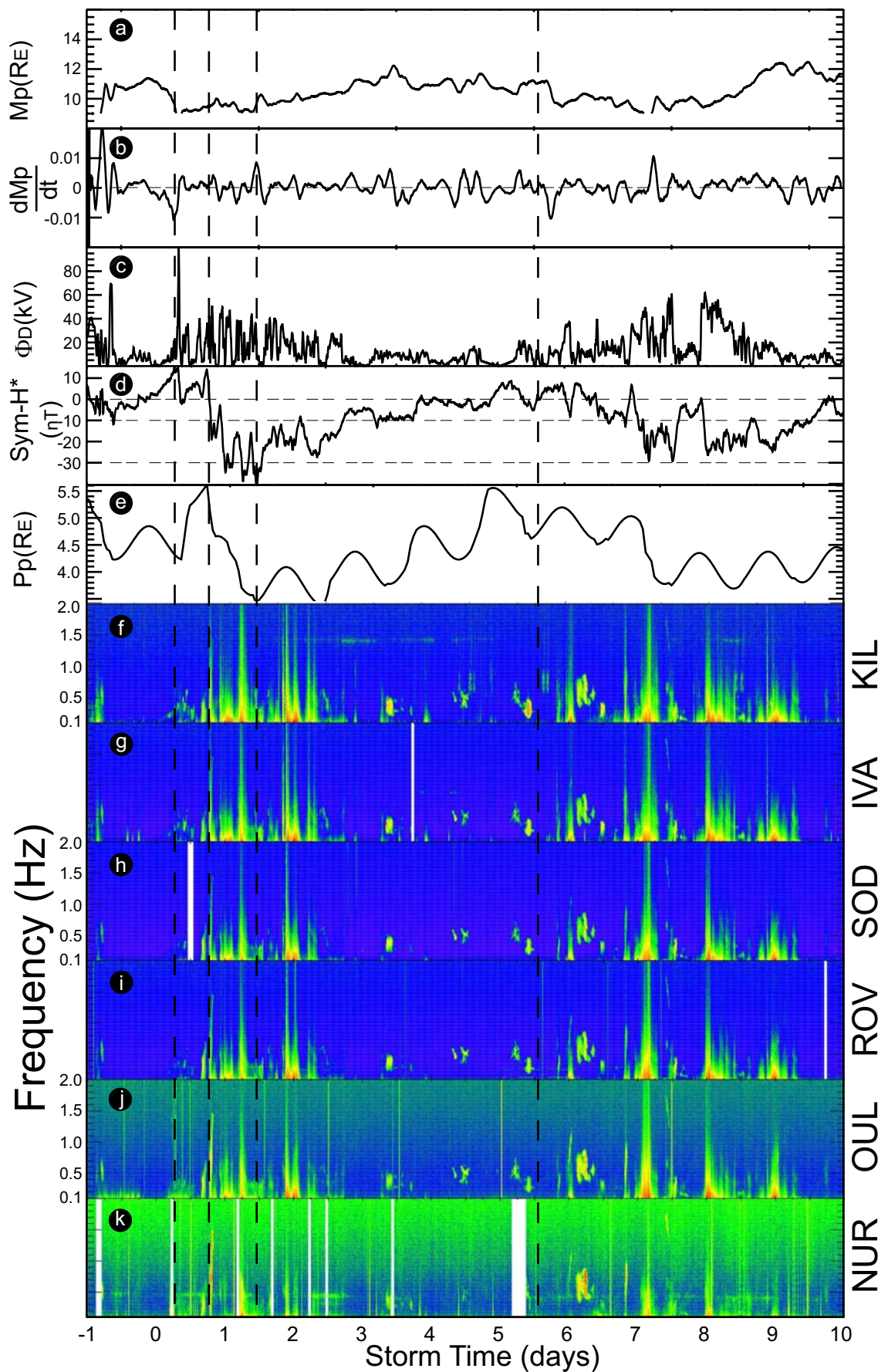


Figure 6.23: Magnetospheric parameters and Pc1-2 dynamic spectra for a geomagnetic storm, initiated 27th Feb 2007 (day 0).

(Shue *et al.*, 1997) and its temporal derivative, in which can be seen the compression from $\sim 11.5 R_e$ to $\sim 9.5 R_e$ (panel a) at ~ 07.00 UT of day zero and its largely negative gradient (panel b). This compression, indicated by the first dashed line, induced a number of high to upper-mid latitude discrete, continuous pulsations (panels f-i) which endured until storm onset, demarcated by the second dashed line. Panel c presents an estimate of the dayside reconnection voltage (Milan *et al.*, 2008, Kan and Lee, 1979), which indicates heightened reconnection at the times of compression and storm onset, remaining so well into recovery. At the time of onset, broadband, irregular pulsations also initiated and continued throughout the storm's main phase and for more than a day into its recovery phase, during which time no Pc1-2s were registered. Although no quantitative spectral power comparison will be attempted here, these irregular pulsations appeared with greater spectral power and over a greater frequency range at the higher latitude stations.

Panel d shows the adjusted Sym-H index, which can be seen to increase in response to magnetospheric compression then fall sharply, indicating storm onset. Sym-H minimised at ~ 01.00 UT the following day, indicated by the third dashed line, marking the beginning of recovery to a pre-storm level. Panel e displays the Sym-H dependent model plasmapause position for the mean local time of the FPMC, which shows the plasmaspheric contraction and subsequent expansion during the full storm cycle. Pulsation activity, seen in panels f-k, can be seen to emerge surrounding local noon of day 2 from onset and remain bound to that local time sector until day 5 where pulsations occur at a greater range of local times.

Immediately following the end of storm recovery, at the end of day 5, a further dayside magnetospheric compression, increased reconnection and a Sym-H negative excursion can be seen. The minimum value of Sym-H, in this case, was not low enough to classify as a potential storm nor did it follow the predefined storm pattern. This does, however, illustrate the potential for storm related yet non-storm time activity to contribute to pulsation occurrence and highlights the inappropriateness of considering pulsation behaviour relative to onset alone, ignoring duration, history and subsequent activity.

Figure 6.24, which retains the panel designations of, and for the upper five panels the same format as, figure 6.23, presents scatter plots of pulsation F_c for the full year of 2007 (panels f-k). Each data point is colour coded according to the storm phase in which it occurred. Non-storm time, pre-storm Sudden Commencement (SC), main phase and recovery phase are coloured black, blue, green and red respectively. The plots show that dramatic increases in F_c are commonly, although not exclusively, coincident with a low model plasmopause position, following prolonged periods of estimated day side reconnection and subsequent negative excursions of Sym-H*.

Occurrence probability histograms for non-storm and storm time intervals can be found in figure 6.25. Retaining the histogram colour scheme of figure 6.8, each distribution is normalised against the total possible number of minutes in which a pulsation may occur. The histograms imply that structured (unstructured) events are more likely during non-storm (storm) times and that both species are more probable earlier (later) in the day. The peak probability of structured events is higher during non-storm than storm time; its pre-local noon peaked distribution also appears more pronounced and shows greater decay with decreasing latitude, the two distributions showing a reasonable degree of similarity at OUL and NUR. Unstructured pulsations exhibit somewhat converse behaviour, with the non-storm time distribution retaining its shape, reducing only in magnitude with decreasing latitude; whereas the storm time distribution becomes more uniform with latitude, similar to the non-storm time structured distribution. The more pronounced bimodal appearance of the non-storm time distribution also implies that the local midnight associated unstructured pulsations seen at all latitudes occur less probably during storm times, the converse being true for morning sector unstructured pulsations. As the current method of Pc1 identification allows the discrimination of multiple pulsations in a given minute, the contribution of these concurrent events to each distribution can be found in figure 6.26. Multiple concurrent events appear more likely to be structured and to occur during non-storm times.

A number of previous storm related Pc1-2 studies have used superposed epoch analysis to characterise pulsation behaviour in the aftermath of storm onset, using days from onset day 00.00 UT as their temporal unit of consideration (Bortnik *et al.*, 2008b, Engebretson *et al.*, 2008, Kerttula *et al.*, 2001a, Kerttula *et al.*, 2001b). As table 6.2

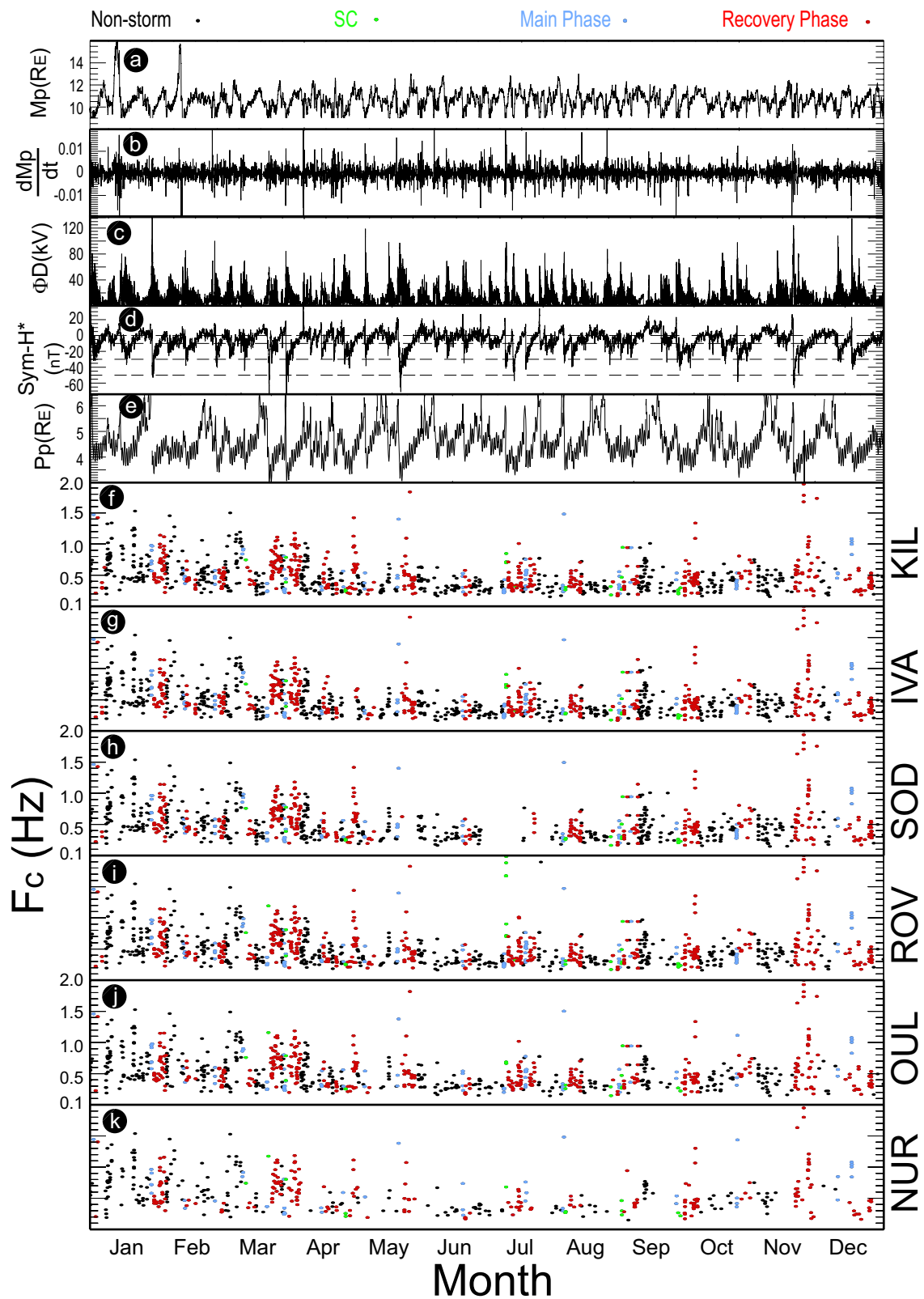


Figure 6.24: 2007 model magnetospheric boundary position, activity indices and storm occurrence-frequency behaviour. Each data point in the lower six panels represent a single event, its colour indicates the storm phase in which it occurred.

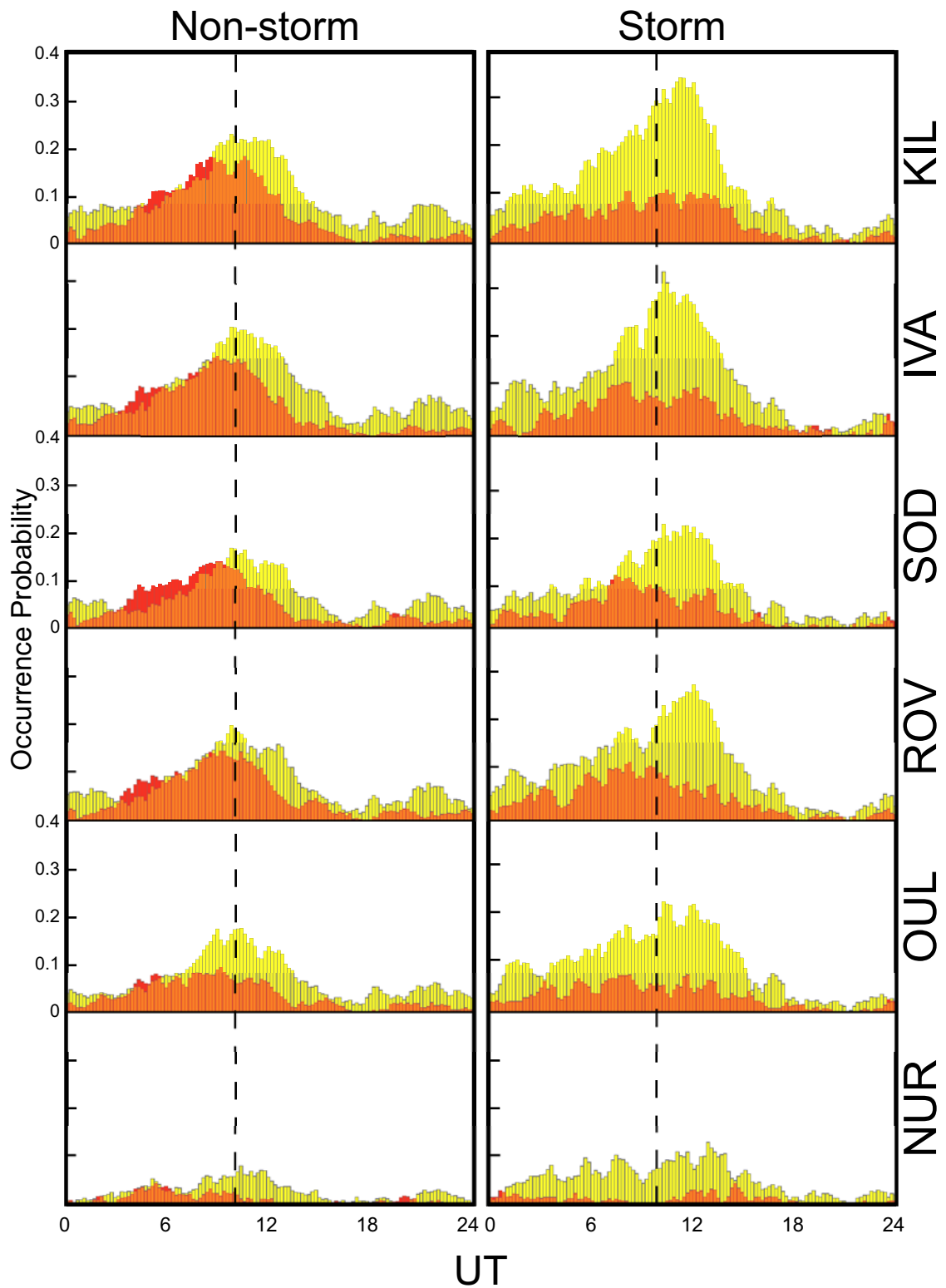


Figure 6.25: Occurrence probability histograms of non-storm and storm time pulsations. Each histogram is normalised against the total number of possible minutes a pulsation may occupy. Structured pulsations are coloured red and unstructured yellow.

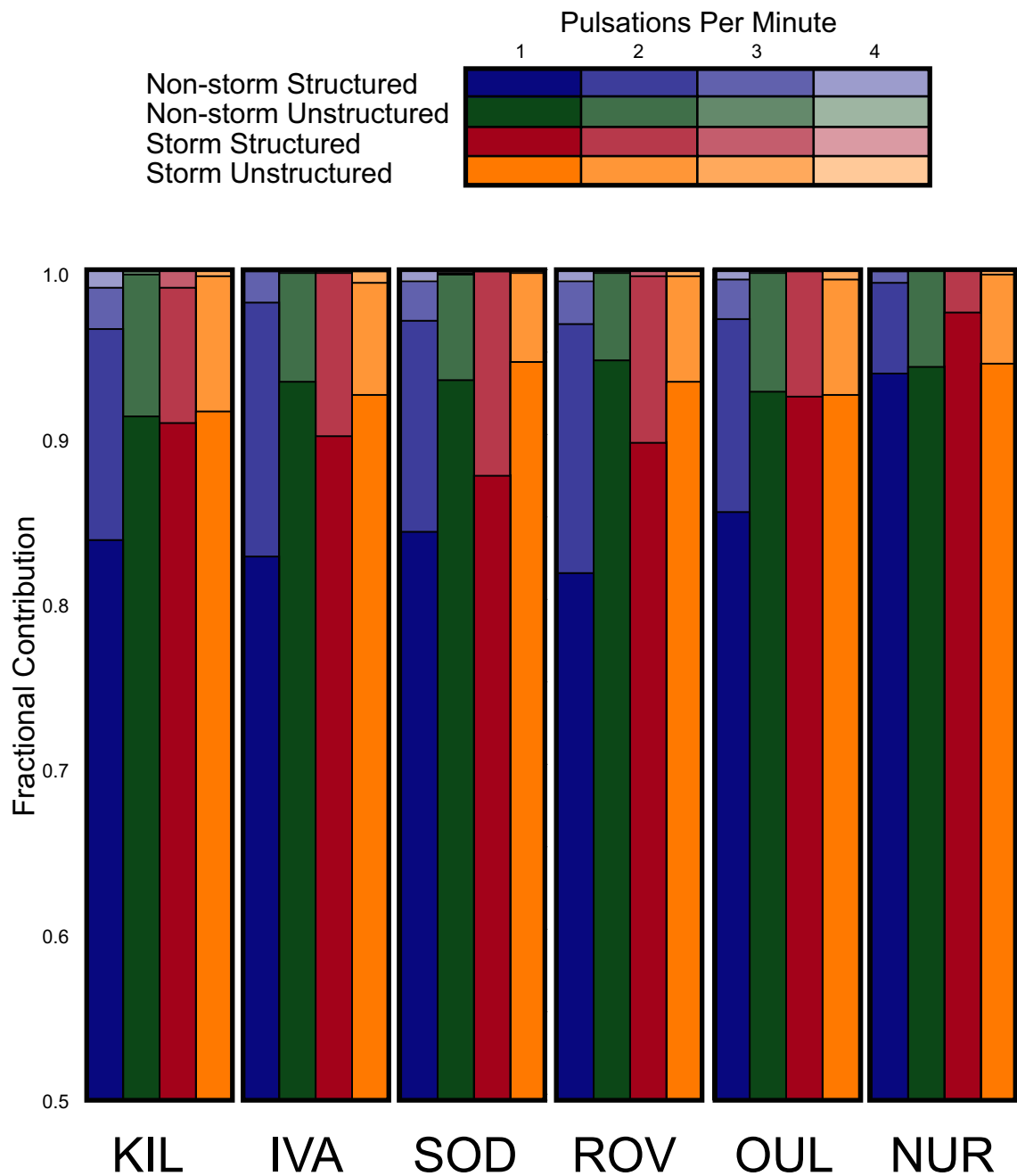


Figure 6.26: Fractional contributions to total minute count from concurrent pulsations. Contribution from concurrent pulsations is most probable for non-storm time structured events, which reduce in likelihood with decreasing latitude.

reveals, even if subdivided in to small and moderate intensity, the maximum difference between storm durations is of the order ~ 7 -8 days, which, as highlighted in the example storm description at the beginning of this section, would superpose contributions from a fully recovered ring current population over those from a highly disturbed one. It is for this reason that the current dataset is divided not into increments of days from onset but in to storm phase segments consisting of a main phase and three, equal length, recovery phase intervals. Figure 6.27 presents Storm phase-UT-Occurrence probability plots for the structured and unstructured cases of the storm-time pulsation subset. To enable meaningful diurnal occurrence assessment, each interval is individually normalised against the total number of possible minutes for each storm in each bin.

The main phase distribution shows a post-local noon unstructured peak and, with the exception of a small probability of post midnight pulsations, is restricted to its few surrounding hours, diminishing considerably with latitude. Structured pulsations in this phase follow a similar diurnal pattern, although, relatively are not as dependent on latitude. As recovery initiates, unstructured pulsations begin to occur at a greater range of local times and appear to favour latter than main phase occurrence. As recovery develops, greater still is their local time extent, however, the peak in occurrence appears to shift forward, favouring near post-local noon. In the final stages of recovery, unstructured pulsations occupy almost all local times yet remain most probable throughout the morning and at noon itself. Structured pulsations, again, follow a similar pattern, although, they appear to shift to earlier local times sooner than their unstructured counterparts.

The storm time temporal evolution of F_c , Δt , PR_c , ε and α for each station is shown in figures 6.28 to 6.32, all of which are comprised of 21 bins (with the exception of Δt , which has 24 bins) spanning each parameter's range per storm segment. The unstructured F_c modal group is relatively low during storm main phase at all stations and roughly doubles following the initiation of recovery. As recovery continues, F_c (modal group) returns gradually to pre storm values yet its range becomes greatly increased, mid recovery, lessening as recovery nears completion. The low number of structured events makes interpretation questionable; however, their distribution appears to follow a similar pattern to the unstructured case. Structured event duration, seen in figure 6.29, does seem to increase as storms progress yet no distinct evolution is

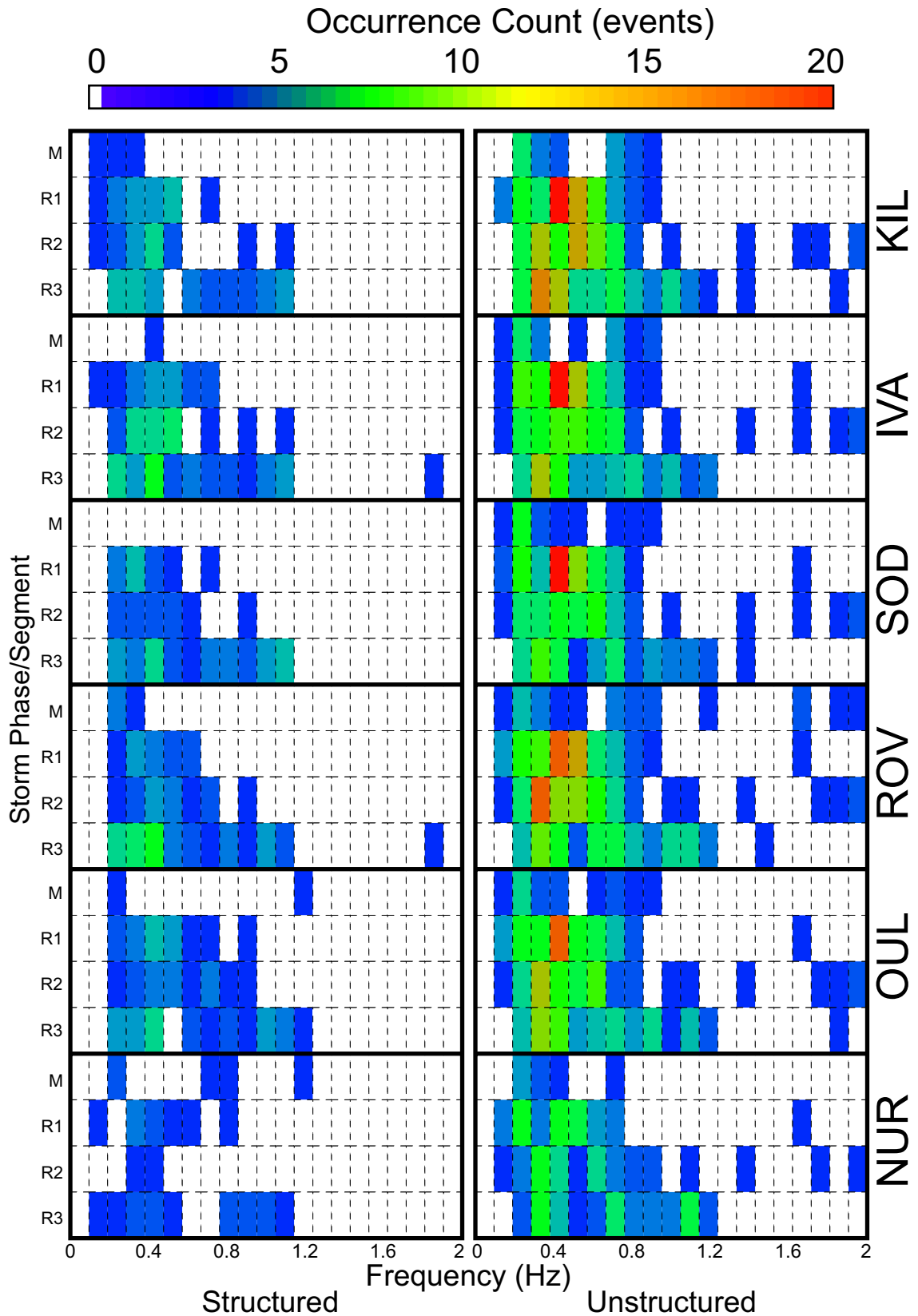


Figure 6.28: Storm phase-Frequency-Occurrence probability plots of storm time structured and unstructured Pc1-2 central frequency. Each bin contains the total number of events in that storm segment. Storm main phase is labelled M and each 1/3 recovery phase segment R1, R2 and R3 respectively.

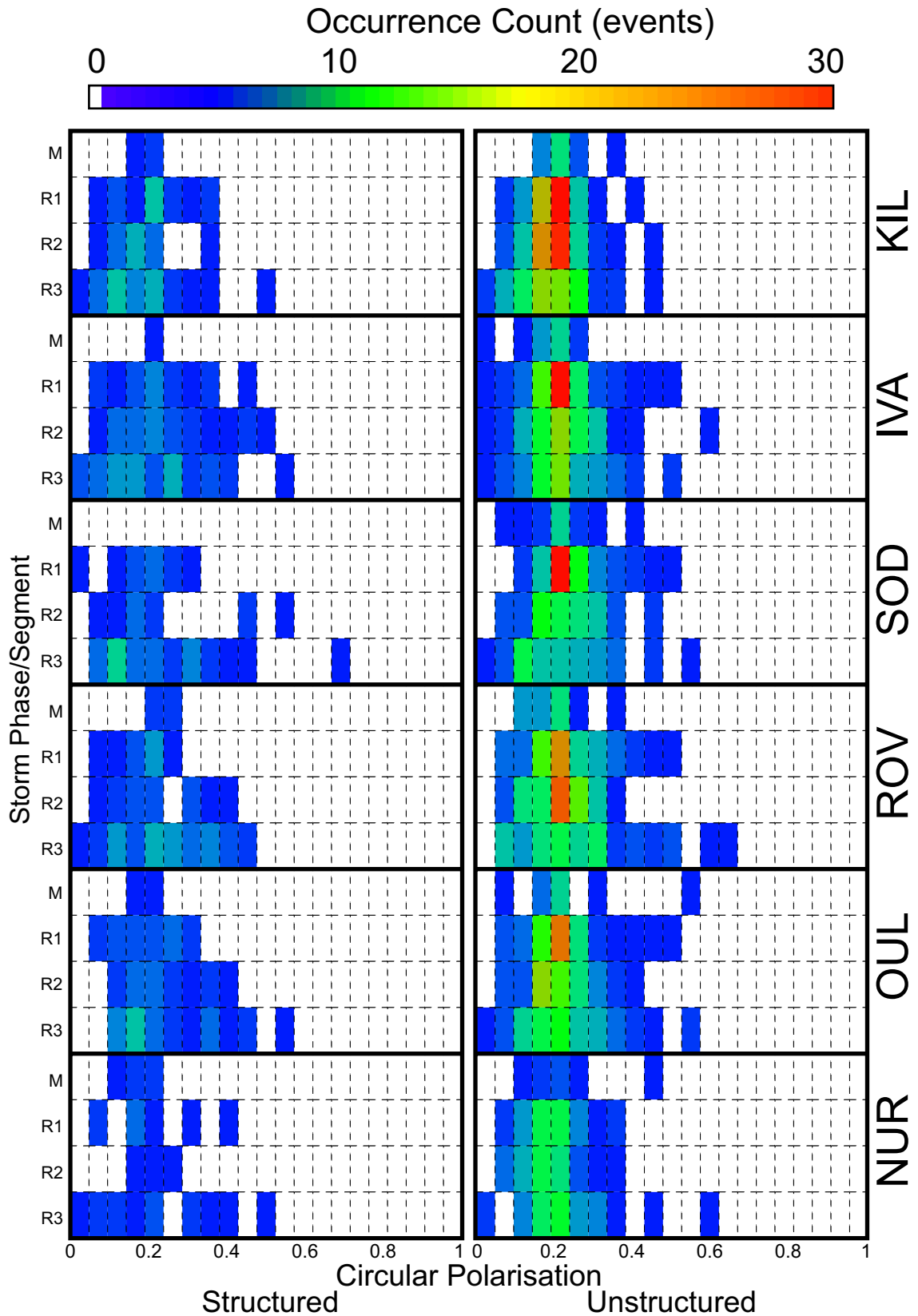


Figure 6.30: Storm phase-Polarisation Degree-Occurrence probability plots of storm time structured and unstructured Pc1-2 pulsation circular polarisation degree. Each bin contains the total number of events in that storm segment. Storm main phase is labelled M and each 1/3 recovery phase segment R1, R2 and R3 respectively.

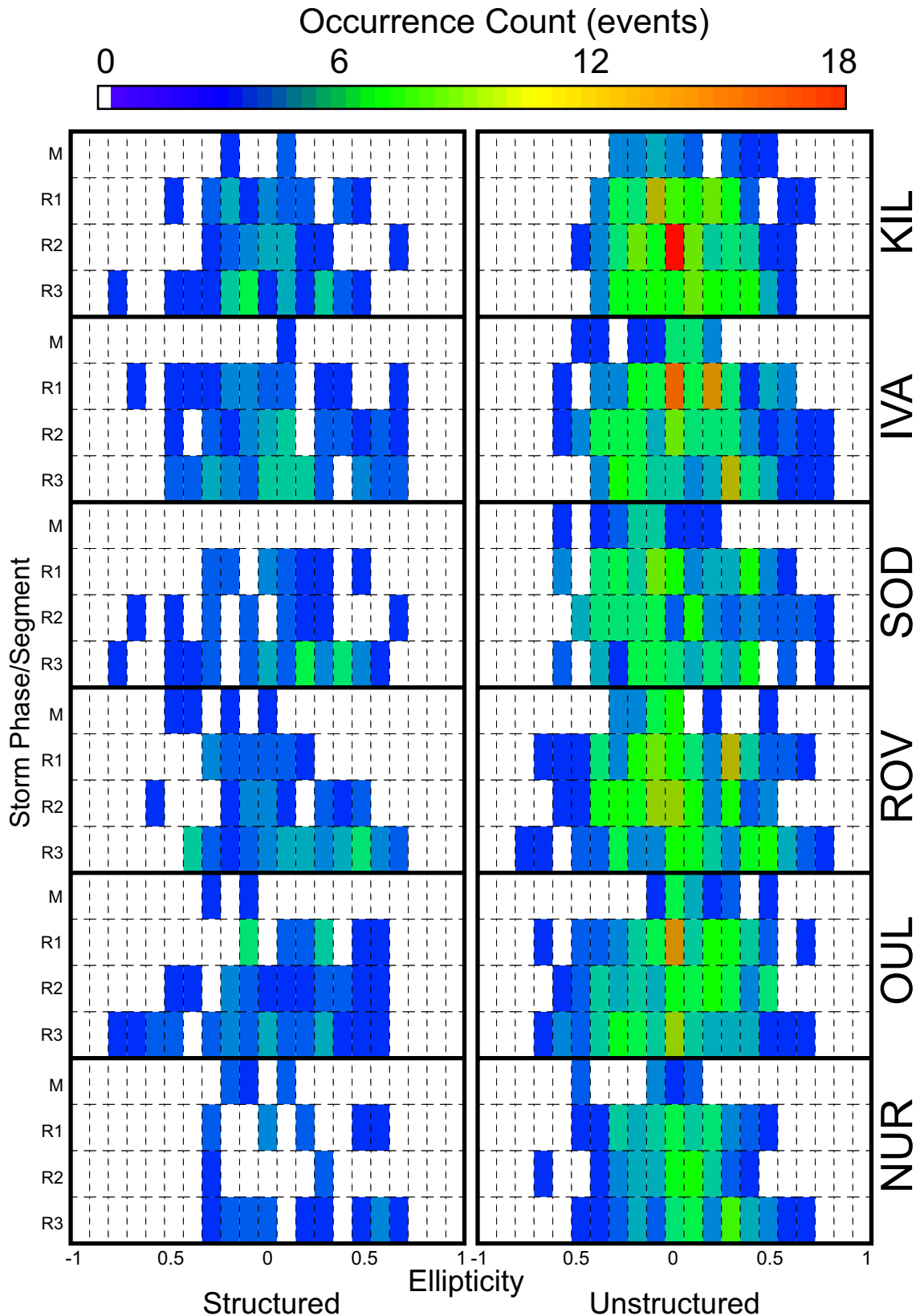


Figure 6.31: Storm phase-Ellipticity-Occurrence probability plots of storm time structured and unstructured Pc1-2 pulsation ellipticity. Each bin contains the total number of events in that storm segment. Storm main phase is labelled M and each 1/3 recovery phase segment R1, R2 and R3 respectively.

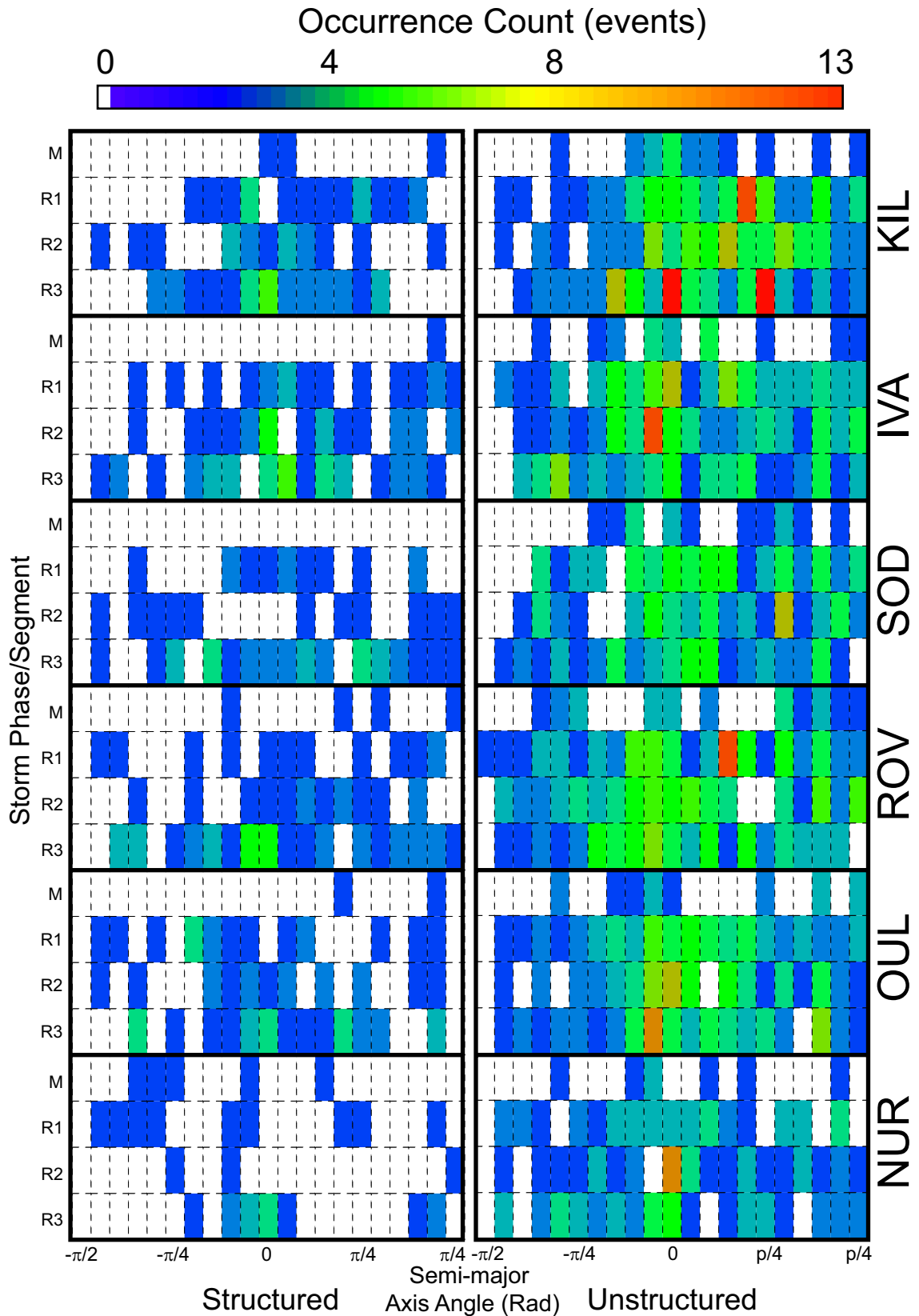


Figure 6.32: Storm phase-Polarisation Axis Angle-Occurrence probability plots of storm time structured and unstructured Pc1-2 pulsation polarisation ellipse semi-major axis angle. Each bin contains the total number of events in that storm segment. Storm main phase is labelled M and each 1/3 recovery phase segment R1, R2 and R3

exhibited for unstructured events and it may be argued that the reverse is true, that modal duration decreases with storm recovery. In figure 6.30 the range of PR_c for structured events increases with storm evolution more dramatically, although, it is unclear whether this is simply a consequence of the low number of recorded events. Pulsation ellipticity (6.31) for both species at high latitude appears not to evolve greatly and its distribution remains generally centred on zero throughout. The SOD and ROV distributions indicate that in early recovery right-handedness is favoured, which evolves in to a preference for left-handedness, the converse being true for OUL, with NUR exhibiting similar behaviour to the high latitude case. In figure 6.32 the haphazard nature of the α distribution's temporal evolution, again, suggests that no preferred orientation of polarisation ellipse exists for either species.

To assess the dependence of central pulsation frequency on the radial position of the plasmopause, figure 6.33 displays scatter plots of non-storm and storm time events. A linear fit to the data, achieved by minimising the Chi-squared statistic, reveals a positive (negative) storm- (non storm-) time dependence on the model plasmopause position for both subsets of pulsations.

6.4 Discussion

6.4.1 Analysis technique

The methods used to derive the occurrence and polarisation parameters presented above are not, individually, new or unique yet their combined application to Pc1-2 pulsations warrants a cautionary note as comparison to previous works will be made in the following section. The selection process itself may improve the latitudinal extent of detection for a given event, as each potential pulsation was analysed simultaneously across the entire magnetometer chain. The use of progressive power thresholding avoids the high spectral power saturation present in earlier studies (Kertulla et al., 2001a, 2001b) and is likely to resolve a greater number of events and consistently higher event durations than previously reported.

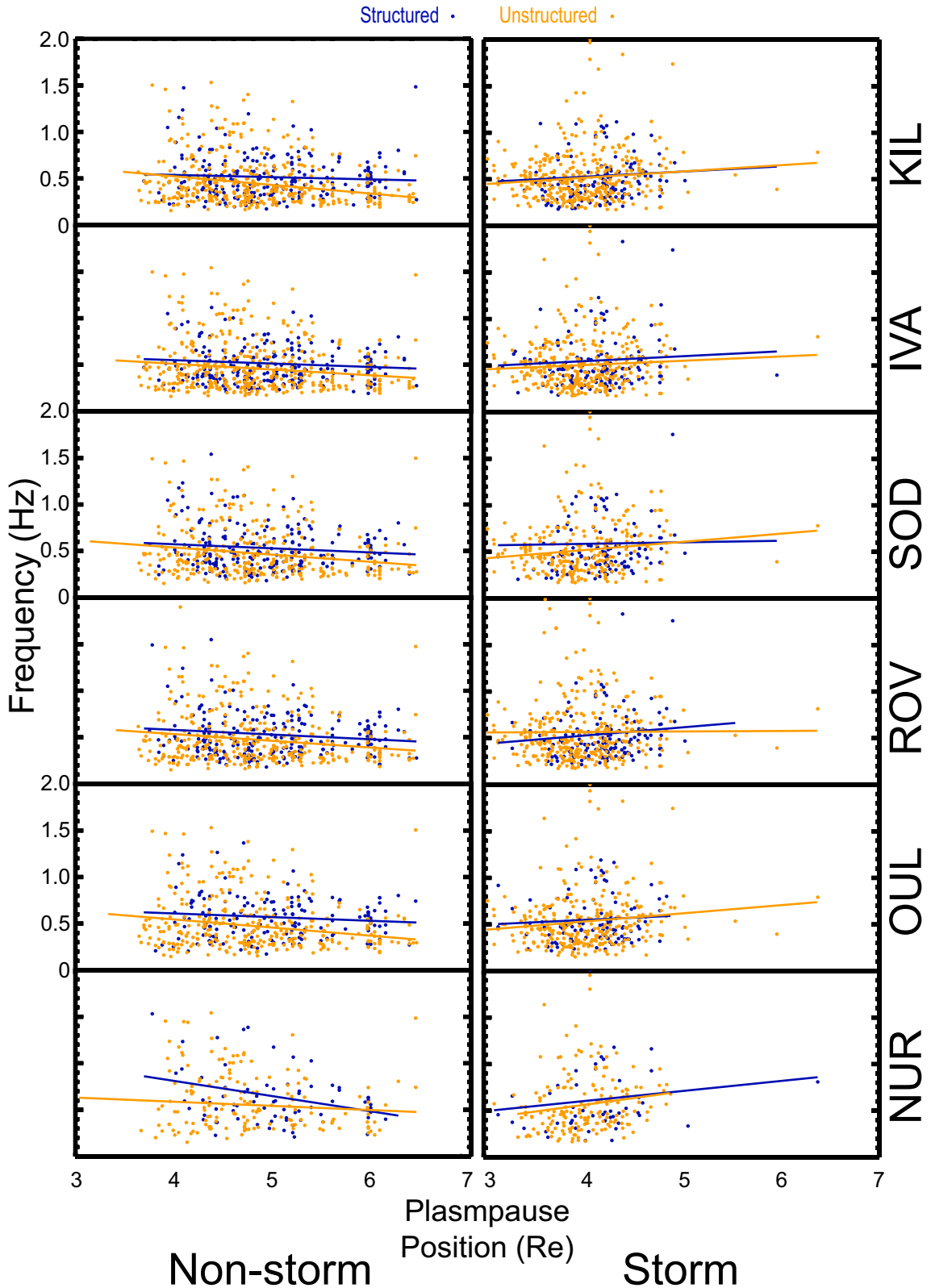


Figure 6.33: Central frequency against model plasmopause position for non-storm and storm intervals. Structured events are coloured blue and unstructured orange. Chi-squared minimisation linear fitting reveals a weekly negative dependence on plasmopause position for the non storm cases and a positive dependence for storm time events. All fits are significant to the 99% confidence level.

The use of inter-station cross-phase continuity where the semi major axis angle, polarisation ratio and ellipticity were excessively varied, again, increases the likelihood of event detection, even when compared to the automated approach of Bortnik *et al.* (2007). This technique may slightly skew the occurrence and frequency distributions of identified events, compared to previous works, by isolating individual concurrent pulsations. Subsequently, a greater number of events may be registered, of which some will be of shorter duration and/or narrower bandwidth. This effect, as implied by figure 6.26, is small for most cases, perhaps with the exception of non-storm time structured pulsations, for which >16% of cases were in some way concurrent. Figure 6.4 aptly highlights how this method may aid understanding of multifarious pulsations by providing information of their polarisation component phase propagation. What is shown in the figure to be two separate events, with distinct polarisation characteristics and differing repetition periods, bears a great resemblance to the goose pulsations of Feygin *et al.* (2009). It is unclear at this stage how the causal nonlinear effects suggested by Feygin *et al.* (2009) might manifest themselves in the polarisation and phase characteristics of a pulsation, hence, further theoretical work must be conducted before conclusions may be drawn on its applicability to that particular phenomenon. Investigation of the usefulness of cross-phase analysis for Pc1-2 study, beyond simple contribution to the identification process, is the subject of a future study.

As noted in section 5.6.1, the parameterisation of event structuring is more a test of pulsation monochromaticity, which may categorise what appears to be a legitimately structured pulsation as unstructured in cases where the structure repetition period is non-stationary, thus bolstering the unstructured event distribution. This effect may partly explain the disagreement of this finding with that of previous work that purport structured pulsation domination. Repetition period non-stationarity is in itself of interest but will not be addressed here.

6.4.2 Pulsation dataset

Historically, ground based studies have compared low-mid and mid-high latitude observations. The multi-station approach of this study allows consideration of Pc1-2 characteristics across most of the latitudinal range of the ionospheric footprint of the plasmopause, which although may not be the preferred site of EMIC wave generation is

an important region to its behaviour (Fraser and Nguyen, 2001). As implied by panels a and d of figure 6.7, the number and duration of events increases with latitude, up to the highest station in the chain (KIL). This is in agreement with previous ground-based studies that have considered the variation of Pc1-2 occurrence with latitude. However, such studies have reported this relationship using either two stations (NUR and SOD; Kerttula *et al.*, 2001a, Kerttula *et al.*, 2001b) or a number of stations (ranging from mid to high latitude; Guglielmi *et al.*, 2006) of differing origin, construction and operation, which brings in to question their comparability. This result is phenomenologically consistent with in-situ studies showing that magnetospheric EMIC waves predominate in the outer magnetosphere, with their occurrence increasing with L-shell value up to at least L=9 (Anderson *et al.*, 1992a). Of the entire dataset, 26% (32%) of events were seen at all stations, a further 28% (33%) were exclusively registered by the upper five and a mere 6% by the highest two (KIL-IVA), where the bracketed percentages are adjusted for missing SOD data. Events detected at one of the central stations in the chain (IVA - OUL) were generally, 64% (71%) of cases, registered at all four, 86% (93%) for at least three out of four. Given the suggested narrow spatial extent of the magnetospheric EMIC source region (Loto'aniu *et al.*, 2005), these figures may be testament to a stable and well-developed ionospheric duct (Fraser, 1975, Greifinger and Greifinger, 1968, Manchester, 1966), as might be expected at solar minimum. This suggests that the parameter distributions discussed below are representative of a significant degree of ducted behaviour.

The seasonal occurrence variation seen in figure 6.8 agrees in form with previous observation (Fraser-Smith, 1970), although, direct comparison is inappropriate as the Fraser-Smith (1970) distribution contained data from a full solar cycle. There appears to be no obvious dependence of seasonal variation on latitude, the distribution displaying only the aforementioned equatorward occurrence decay.

The diurnal distributions agree with previous observation (Mursula *et al.*, 1994b) in form although not in relative magnitude. The diurnal distribution at SOD is similar to earlier observations made at solar minimum (Kerttula *et al.*, 2001a, Mursula *et al.*, 1996). A pre-local noon peak in structured, as well as a post-local noon peak in unstructured, pulsations can be seen at all stations, however, the current dataset possesses a secondary peak in unstructured events in the pre dawn sector, similar to that

of the sunspot maximum distribution of Mursula (1994). Mursula (1994) attributes this bimodal behaviour to the erosion of the ionospheric duct surrounding local noon, affecting propagation from a high latitude unstructured source. This is supported by the current observation if two conditions hold true; firstly, that it is solely the high latitude duct that is eroded and secondly, that the source of structured (unstructured) pulsation is at a consistently lower (higher) latitude than the affected propagation region, neither of which will be addressed here. It is also evident that the local time peak of both species remains constant with latitude. This finding contradicts earlier reports of a maxima shift from morning to noon with increasing latitude (Kangas *et al.*, 1998). The dynamic nature of diurnal occurrence for both species of pulsation is emphasised by figures 6.10 – 6.12, which show its evolution over the course of the year. The aforementioned structured occurrence peak can be seen to occupy both post and pre-local noon, most notably across the vernal equinox. Unstructured occurrence is seen to shift dramatically in local time, presenting three maxima in a number of months, of which July is the clearest example. Again, it is unclear from the considered data whether this is a source or propagation effect, further investigation is clearly needed to elucidate this behaviour.

The consistently higher modal frequency of structured compared with unstructured pulsations (figure 6.13), with the exception of the highest latitude observations (KIL), may be further evidence of their lower magnetospheric source region (Anderson *et al.*, 1992a). This may, however, also be caused by the earlier local time prevalence of structured pulsations and the filtration affect of the Ionospheric Alfvén Resonator (IAR) (Prikner *et al.*, 2001, Demekhov *et al.*, 2000, Mursula *et al.*, 2000). Although contradictory evidence exists on the mechanism of IAR control over Pc1 ionospheric transmission, it is not hastily discounted as a possibility, given that Spectral Resonance Structures (SRS) were observed for ~25% of the analysed year (not presented). Furthermore, the Pc 1-2 diurnal frequency distribution shown in figure 6.14, which concurs with that of Kenney and Knaflich (1967), qualitatively agrees with frequency behaviour of the observed SRSs. Although the annual frequency distributions presented in figure 6.15 do suggest that lower frequencies are present in the summer months, the contribution from storm time activity is more than likely masking any genuine annual variation.

The ratio of linear to circular polarisation (PR_c) has historically been used as a proxy for distance from the observer to a pulsation's ionospheric source, whose location is subsequently inferred from the semi-major axis angle (α) of the polarisation ellipse (Webster and Fraser, 1985, Fraser, 1975b, Summers and Fraser, 1972). Figures 6.17 and 6.19 show that the values of PR_c for the events in this study are generally low, mostly below 0.3, and that the values of α are not significantly ordered at any latitude but do exhibit moderately, centrally peaked distributions, implying a preferential magnetic north-south orientation. Structured events exhibit a lower modal value of PR_c than unstructured events at IVA and SOD yet these stations display the most uniform of structured α distributions. This is contradictory to earlier evidence as it suggests that at these stations the prevailing source region for unstructured is closer than that for structured pulsations. A number of explanations for this exist. Either, linearity is not a good proxy for great distance of propagation, the source region for unstructured pulsations is not at extremely high latitude, the orientation of the magnetometer is no longer cardinally aligned or the method used to derive PR_c and/or α is incorrect. Given the variability of α within an event, it would be unsurprising if even a power-weighted modal value could not adequately represent an entire event. Given the uncertainty of instrument alignment, derivation technique and natural variability, drawing conclusions based the values of α presented here would be somewhat questionable. PR_c and ϵ are not similarly affected by such ambiguity as neither absolute nor relative orientation affect their values.

Unstructured pulsations show no preference for left- or right-handedness at any latitude yet structured events show a slight preference for left-hand polarisation, as evidenced by their negatively skewed distributions in figure 6.18. The diurnal variation of ϵ agrees in form with the in situ observations of Anderson *et al.* (1992) for the L= 5-6 subset of pulsations, however, the magnetospheric distribution appears to lag the ground by ~ 2 hours. It is worth noting that Anderson *et al.* (1992) used a ~ 450 day interval from two full solar cycles before the present study. Although evident in all stations, this variation is most pronounced in ROV, SOD and IVA that span the range $L = 4.5-5.7$. This observation brings in to question whether the observation of left- (right-) hand polarisation implies proximity (distance) from the ionospheric footprint of a pulsation's magnetospheric source region.

6.4.3 Storm characteristics

Xu *et al.* (2008) showed that towards the end of the declining phase of solar cycle 23 CIRs and Sector Boundary Crossings (SBCs) became the dominant solar wind structures to impact upon the earth as the number of ICMEs (including magnetic clouds) declined. It was also shown that the geoeffectiveness, a structure's ability to induce a magnetic storm, of CIRs was far greater than that of SBCs. The number of geomagnetic storms isolated in this study is greater than that reported for 2007 by Xu *et al.* (2008). This may be due to the current study using the OMNI solar wind dataset and the Sym-H index to derive Sym-H*, where Xu *et al.* (2008) uses only data from the ACE satellite to compute Dst*, removing any interval containing missing or unreliable information. Presently, one extra moderate and four extra small storms were registered; unfortunately, storm dates and times were not included in Xu *et al.* (2008) for comparison, which is unsurprising given the ten-year extent of their study. An element of caution must be exercised when comparing the present storm-set to those of previous Pc1-2 studies as all aforementioned works have considered intervals in different phases of their respective solar cycles and given the depth of cycle 23, a direct "like for like" comparison may, therefore, prove rather uninformative. The present range and values of storm intensities ($-75.5 \text{ nT} < SH_{\text{peak}} < -30.7 \text{ nT}$), falls consistently and considerably below those of previous studies, which potentially restricts the energy of resonant ions responsible for EMIC wave growth (Dessler and Parker, 1959), the position of the plasmopause (O'Brien and Moldwin, 2003) and magnetosphere composition (Daglis *et al.*, 1999). Given the modest range of storm intensities, no attempt to present any dependence on intensity has been made.

6.4.4 Storm related pulsations

When undertaking this study it was hoped that a discernable response to storms induced by different solar wind structures could be found. Of the twenty six storm intervals recorded only three were ICME induced, which were also the most intense and longest, hence, no conclusions about general Pc1-2 response can be made without further observations.

The role of EMIC waves in the decay of the storm time ring current has received a great deal of attention, both theoretically and observationally e.g. (Daglis *et al.*, 1999) and references therein. Resonant interaction with anisotropic ions provides a direct ring current loss mechanism through pitch angle scattering and subsequent precipitation. The findings of this study agree in part with previous observations yet its representation in terms of fraction of storm length rather than day from onset produces a somewhat clearer picture of pulsation evolution.

Compared to non-storm intervals, the overall storm time probability of observing a Pc1-2 pulsation does not significantly differ at high latitude; however, an increase is seen in mid latitude observations. The relative fraction of structured events and the diurnal variation of both pulsation species changes dramatically throughout the storm cycle. As shown in figure 6.25, the occurrence probability of unstructured pulsations is increased during storms in the local time range of early morning to post noon yet is decreased surrounding local midnight. Peak unstructured occurrence can also be seen to shift from pre to post noon and exhibits comparatively greater enhancement at higher latitude.

Mechanisms for the evolution of this diurnal occurrence with storm progression, as seen in figure 6.27, have been suggested by a number of authors. Kurttula *et al.* (2001) suggested that decreased Pc1-2 activity in the early recovery phase is due to reduced transmission and duct propagation through the ionosphere. This is not fully supported by the current data set as SRSs are observed in the early recovery phase, however, some support could be argued as they do appear more frequently in the later stage of recovery (not shown). This mechanism clearly requires further quantitative investigation before conclusions may be drawn on its contribution to the observed pulsation behaviour. The observations of Engebretson *et al.* (2008) that EMIC wave associated proton precipitation is absent during the main and early recovery suggests that it is generation rather than propagation that suffers a reduction at these times, it is however noted by those authors that further observation is necessary to confirm this assertion.

The association of EMIC wave generation with plasmaspheric plumes (Engebretson *et al.*, 2008, Fraser *et al.*, 2005, Spasojevic *et al.*, 2004) may provide a

partial explanation for the Pc1-2 characteristics seen here. Spasojevic (2004) showed that the sunward motion of plasma on the dayside, in response to the inward migration of the nightside plasmopause, may lead to the formation of a post noon plasmaspheric plume on the time scale of a few hours. This cold dense plume can be maintained for a considerable number of hours as continued storm-related sunward convection and co-rotation stabilise its configuration. The earthward motion of ring current ions on the nightside causes an increase in temperature anisotropy through adiabatic heating. When this, now highly anisotropic, population drifts westward and intersects the cold dense plume, EMIC waves may favourably interact with these energetic ions causing wave growth, pitch-angle scattering and precipitation. Given that a plume may extend out past $L=7$ and differential drift separation may further elevate the anisotropic particle population, there is potential for this mechanism to generate the high latitude pulsations observed. The plume forms in the afternoon sector, which for the FPMC roughly corresponds to midday UT, then as storm induced convection relaxes, co-rotation dominates and the plume shifts to later local times. This is consistent with the current observation only if the plume has dissipated by the second recovery segment (R2 of figure 6.27) as pulsation activity begins to shift towards the morning.

6.5 Summary

This statistical study has investigated the behaviour of Pc1-2 pulsations over the course of a single year (2007) in the late declining phase of solar cycle 23. Complex Input Spectral Analysis, a novel method of spectral power thresholding, inter-station cross-phase and polarisation property continuity have been used to identify 1197 distinct events corresponding to 5728 independent observations over 6 stations of the Finish Pulsation Magnetometer Chain, spanning the latitudinal range $L = 3.4-6.1$.

The observed pulsations displayed a high degree of cross-phase continuity throughout each event. This continuity enabled the extraction of multiple individual pulsations from what would have previously been considered single yet complicated events.

Diurnal occurrence, frequency and polarisation characteristics have been presented. The basic measured parameters agree with previous ground based observations, however, it has been shown that arithmetic mean values are often unrepresentative of true behaviour. Pulsation central frequency has been shown to vary sinusoidally in a similar fashion to the fundamental SRS frequency and hence qualitatively supports the suggestion of IAR control of ionospheric transmission. The box and whisker representation of ellipticity revealed that its diurnal variation is also sinusoidal and is in agreement with that of in situ observations, which questions the validity of the assertion that L-H polarisation implies proximity to the ionospheric footprint of the magnetospheric source region.

Geomagnetic storm time pulsations were compared to those of non-storm times. It was found that the relative fraction of unstructured pulsations increased during storm time, more so at high latitude. A positive relationship was found between storm time pulsation frequency and plasmapause position that is significant for both structured and unstructured events. The diurnal evolution of pulsation parameters throughout the storm cycle was presented and some support was found for the association of afternoon sector plasmaspheric plumes with recovery phase Pc1-2 activity.

Chapter 7. Coordinated Observations of the Cusp Region

7.1 Introduction

The interplay between the solar wind the terrestrial magnetosphere remains a subject of impassioned debate. However, an undisputed fact in this quagmire of complexity is that the region of the magnetospheric cusp is of great importance to this highly dynamical system. The magnetic reconnection between the Interplanetary Magnetic Field (IMF) and geomagnetic fields that occurs in the cusp region creates free flowing conduits through which magnetosheath plasma populations may gain direct access to depths of the magnetosphere. The field-parallel acceleration of plasma in the reconnection process on these now open field lines may be sufficient to allow particle precipitation to occur in the low altitude ionosphere (Rosenbauer *et al.*, 1975). The often transient nature of this reconnection is well documented, e.g. (Russell and Elphic, 1979, Haerendel *et al.*, 1978, Russell and Elphic, 1978), and one of its physical manifestations, flux transfer events (FTEs) continue to be an area of active research e.g. (Fear *et al.*, 2009).

The ionospheric counterpart of FTEs has long since been recognised as the anti-sunward flows in radar (Rodger and Pinnock, 1997, Pinnock *et al.*, 1993, Goertz *et al.*, 1985, Van Eyken *et al.*, 1984) and optical data (Moen *et al.*, 1995). In radar observations, these transient features are termed Pulsed Ionospheric Flows (PIFs) (Provan and Yeoman, 1999) if they are within a consistent region of backscatter or Poleward Moving Radar Auroral Forms (PMRAFs) (Wild *et al.*, 2001, Milan *et al.*, 1999) if the regions between successive flows lack backscatter power. Poleward Moving Auroral Forms (PMAFs) in optical observations are adept at tracking cusp precipitation but are limited to times of darkness.

The multitude of interactions taking place in the cusp region generate a cacophony of electromagnetic wave activity. Much is known about the ground signatures of waves in the cusp and historically they have been used as a proxy for its position (Fraser-Smith, 1982 and references therein). However, most studies have focused on either continuous pulsations (Pc) or lower frequency irregular (Pi) ULF waves. Recently, investigations both on the ground, e.g. Engebretson *et al.*(2009,

Safargaleev *et al.* (2004), and in situ, e.g. Nykyri *et al.* (2006), Le *et al.* (2001), have been conducted that associate Pc1-2 with cusp particle precipitation particularly during enhanced ionospheric convection. It has been suggested this region could also be the source of high frequency broadband irregular wave activity (Engebretson *et al.*, 2009). Using all-sky optical imagery it was shown by the latter authors that broadband noise in the frequency range 0-1 Hz is not always seen within the cusp proper. Similarly, they showed that the mantle waves, also observed by the former authors, were present only under intense particle precipitation at the poleward edge of the cusp.

This case study provides coordinated observations of the cusp region during a period of enhanced dayside reconnection and polar cap expansion, followed by substorm onset and subsequent polar cap contraction. A correspondence between flow enhancement and sustained broadband irregular pulsations (Pi1-c, hereafter Pi) in the 50 mHz to 1.5 Hz frequency band observed on the ground is reported. Birkeland currents generated in the dusk flank convection reversal boundary of the ionospheric cusp/cleft are simultaneously implicated in the generation of both the observed Pi and the spectral width enhancements in SuperDARN backscatter that are so often used as a proxy for the position of the cusp.

7.2 Instrumentation and data acquisition

7.2.1 Interplanetary and geomagnetic data

The solar wind and IMF data presented throughout this study were obtained from the OMNI-HRO database (King and Papitashvili, 2010). For the month of September prior to the interval of interest the OMNI dataset is composed of measurements from the ACE (Stone *et al.*, 1998) and Geotail (Nishida *et al.*, 1992) satellites. Geotail's eccentric orbital path at that time placed it outside the bow shock and in the upstream solar wind for approximately 50% of its orbit, during which time particle and field measurements were made by the CPI (Frank *et al.*, 1994) and MFE (Kokubun *et al.*, 1994) instruments respectively. For the periods where Geotail was within the bow shock, data was taken from ACE, which resides in a lissajous orbit about the L1 Earth-Sun Lagrange point at ~240 Re from Earth in the upstream solar wind. For the specific interval of interest to

this case study, 2005/09/25-04:00 - 2005/09/25-20:00, data are exclusively from Geotail, which was no further than 10 R_E from the bow shock throughout. The propagation time (King and Papitashvili, 2010) from Geotail to the bow shock position was of the order of a few minutes.

The Sym-H and AE indices (see 4.1.3 for a description of indices and references), which are used as indicators of storm and substorm activity were obtained from the World Data Centre for Geomagnetism, Kyoto.

7.2.2 Coherent scatter radar

During the period of this study the Super Dual Auroral Radar Network (SuperDARN; Greenwald *et al.*, 1995b, see Ch. 4.1.4 for further details), consisted of 17 HF coherent-scatter radars, 10 in the northern and 7 in the southern hemisphere. This case study is concerned solely with northern hemisphere ionospheric flows. Hence, only data from the northern hemisphere will be presented. Of the 10 operational northern hemisphere radars, 7 were collecting data during this time, all of which were operating at least at 1 minute full scan resolution. The Map Potential routine (Ruohoniemi and Baker, 1998), using all available SuperDARN radar data, has been employed here to derive the northern hemisphere ionospheric electric potential distribution from which convection maps were generated.

Line-of-Sight (L-o-S) velocity and spectral width information from the two SuperDARN radars that form the Co-operative Twin Located Auroral Sounding System (CUTLASS; 4.1-4) are presented in this study. The location of these Radars, Hankasalmi (HAN) and Þykkvibær (PYK) are shown in figure 7.1, which is a geographic projection of their Fields-of-View (F-o-Vs). In the figure, concentric dotted lines represent 10° of latitude, with radial dotted lines denoting 15° of longitude: geographic features are outlined in grey. The F-o-Vs are demarcated by solid black lines, beams 5 and 9 of PYK and HAN respectively are shown by dotted black lines, which can be seen to intersect in the ionospheric volume over the locations of the EISCAT Svalbard Radar (ESR) and the Barentsberg magnetometer (BAR). CUTLASS was, at the time of analysis, operating in stereo (see section 4.1.4) mode, with channel A of both radars performing a 1 minute cadence full beam sweep, while channel B camped

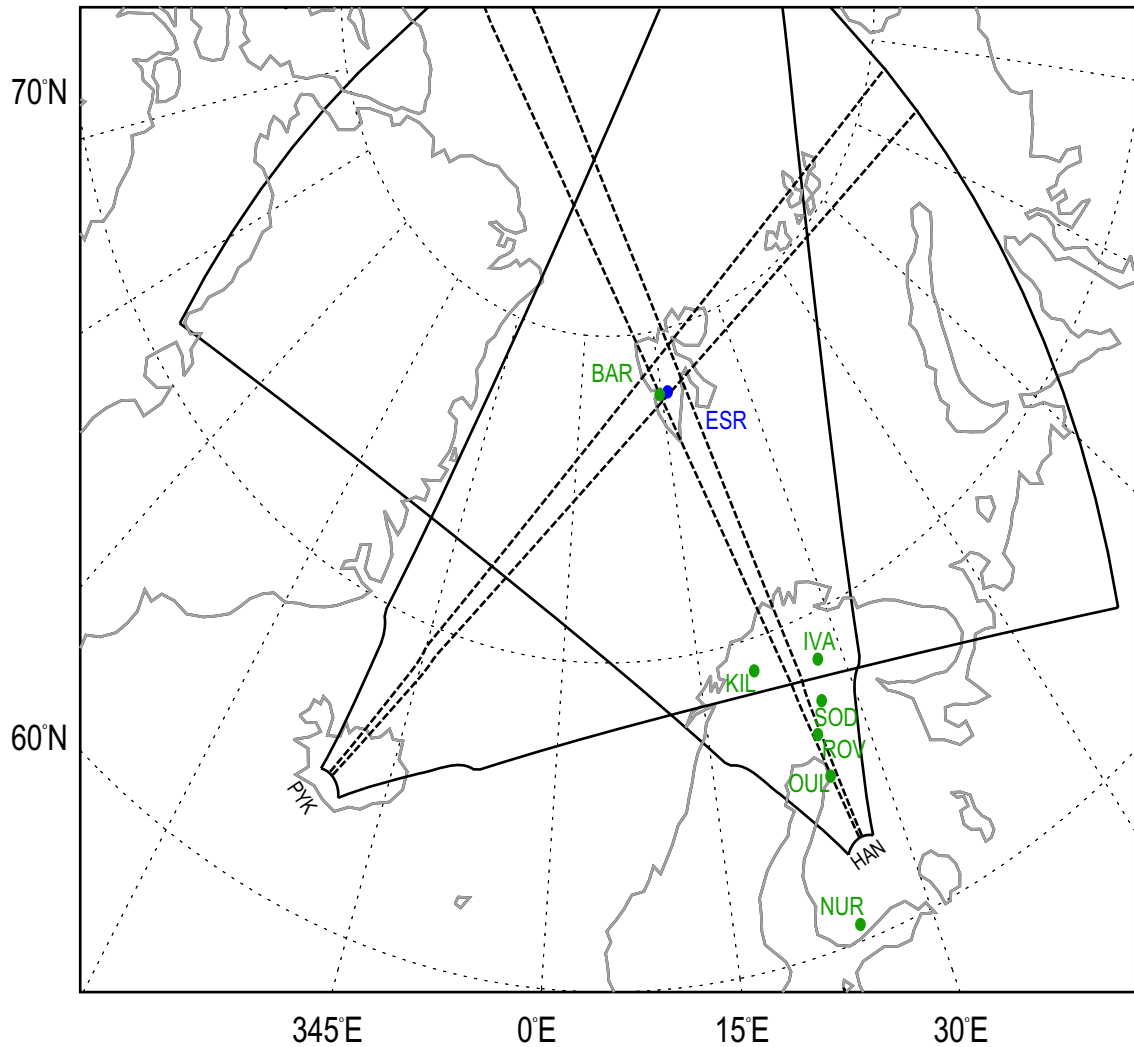


Figure 7.1: Geographic locations of the FPMC (green dots) and Eiscat Svalbard Radar (blue dot). This schematic outlines geographical coastlines in grey. The projected fields of view of the PYK (63.8° N, 20.5° W) and HAN (67.3° N, 26.6° E) CUTLASS radars are shown with solid black lines. Beams 5 of PYK and 9 of HAN, which intersect over the integration volumes of the BAR magnetometer and the Eiscat Svalbard Radar (ESR), are highlighted with dashed lines.

on beams 5 (PYK) and 9 (HAN) in high temporal resolution mode with 3 second cadence. Both radars and channels employed the same number of gates and range resolution, 75 gates of 45 km length. The Virtual Height model of Chisham *et al.* (2008) was used to determine geographic backscatter location in all of the following sections.

7.2.3 The Finnish Pulsation Magnetometer Chain (FPMC)

At the time of this study the FPMC (as described in 4.1.1) was comprised of seven pulsation magnetometer stations spanning $\sim 18^\circ$ of geographic latitude from Nurmijärvi, Finland at L-shell value (McIlwain, 1966) of $L \sim 3.4$ to Barentsberg, Spitsbergen which occasionally resides within the polar cap region. With a sampling rate of 40 Hz these tri-axial induction coil magnetometers are optimised to provide a resolution of 1 pT s^{-1} at 1 Hz. Fourier spectral analysis was performed via the CISA technique (4.3.1), using a sliding window of 102.4 s (4096 data points) to create dynamic spectra of 1 minute temporal resolution. Although no frequency dependent or relative power spectral density phenomena are investigated here, a statistical approach, described in section 4.3.4, was used to account for instrumental frequency response.

7.2.4 The EISCAT Svalbard Radar (ESR)

Throughout the day of analysis, the ESR incoherent scatter radar (4.1.5), located a few tens of kilometres from Barentsberg in Longyearbyen, operated in Common Program (CP) 2 using the Steffe modulation scheme on both the fixed 42m and steerable 32 m dishes to provide continuous measurements over the altitude range 77 km to 900 km. As part of the URSI Incoherent Scatter Observation Days, the 32 m dish cycled through three positions defined in geographic polar coordinates: Mainland EISCAT facility intersect (171.6° az, 63.2° el), geomagnetically south (144.0° az, 66.7° el) and vertical (171.6° az, 90° el). Data from both radars, which provide range resolutions of 2.4 km, were altitude gate analysed with the GUISDAP analysis package to form two continuous (in time and altitude) altitude profiles of ion temperature (T_i) and L-o-S velocity (V_i), and electron temperature (T_e) and density (N_e). The resultant times series were of 128 s temporal resolution and an altitude resolution that decreases linear with height from ~ 4 km at 100 km to ~ 40 km at 900 km.

7.2.5 In situ particle data

Particle data from the SSJ/4 and IDM instruments aboard the DMSP-F15 satellite (see section 4.2.3 for further details) are used to provide information on the locations of the low altitude cusp and magnetospheric boundaries. The low energy ion electrostatic analyser of the SSJ/4 instrument on this spacecraft has been faulty since its launch in 1999; hence, caution is exercised when interpreting its spectra.

Ion information from the LANL-01 and -02 (4.2.2) geostationary satellites are used here to infer a source population for EMIC wave generation. Data from the SOPA and MPA instruments on LANL-01 are merged to form a single energy-time spectrogram spanning the energy range ~ 1 eV to 5 MeV, with temporal resolution ~ 86 s.

7.3 Observations

7.3.1 Interplanetary and geomagnetic conditions

On the 9th of September 2005, a moderate intensity geomagnetic storm initiated, causing a significant ring current enhancement and subsequent Dst index minimum of ~ -130 nT. Figure 7.2 shows the interplanetary and geomagnetic conditions from the 8th to the 26th of that month. The magnitude of the IMF can be seen in panel a and SW velocity, density, temperature and plasma beta in panels b – e. The sharp concurrent increase in measured SW parameters indicate the impact of a Coronal Mass Ejection (CME; Xu *et al.*, 2009). This CME in turn induced an impulsive increase in dayside reconnection and earthward retreat of the magnetopause as indicated by the Milan *et al.* (2008) reconnection voltage proxy and the Shue *et al.* (1998) model standoff position shown in panels f and g. The cross correlation of IMF and SW velocity components shown in panel h indicates the presence of Alfvén waves (Xu *et al.*, 2009) immediately prior to a second magnetospheric impact, on the 15th of September. The recovery phase of this compound storm lasted well in to the evening of the 23rd, with Sym-H returning to positive values. At this time the magnetopause standoff position gradually begins to

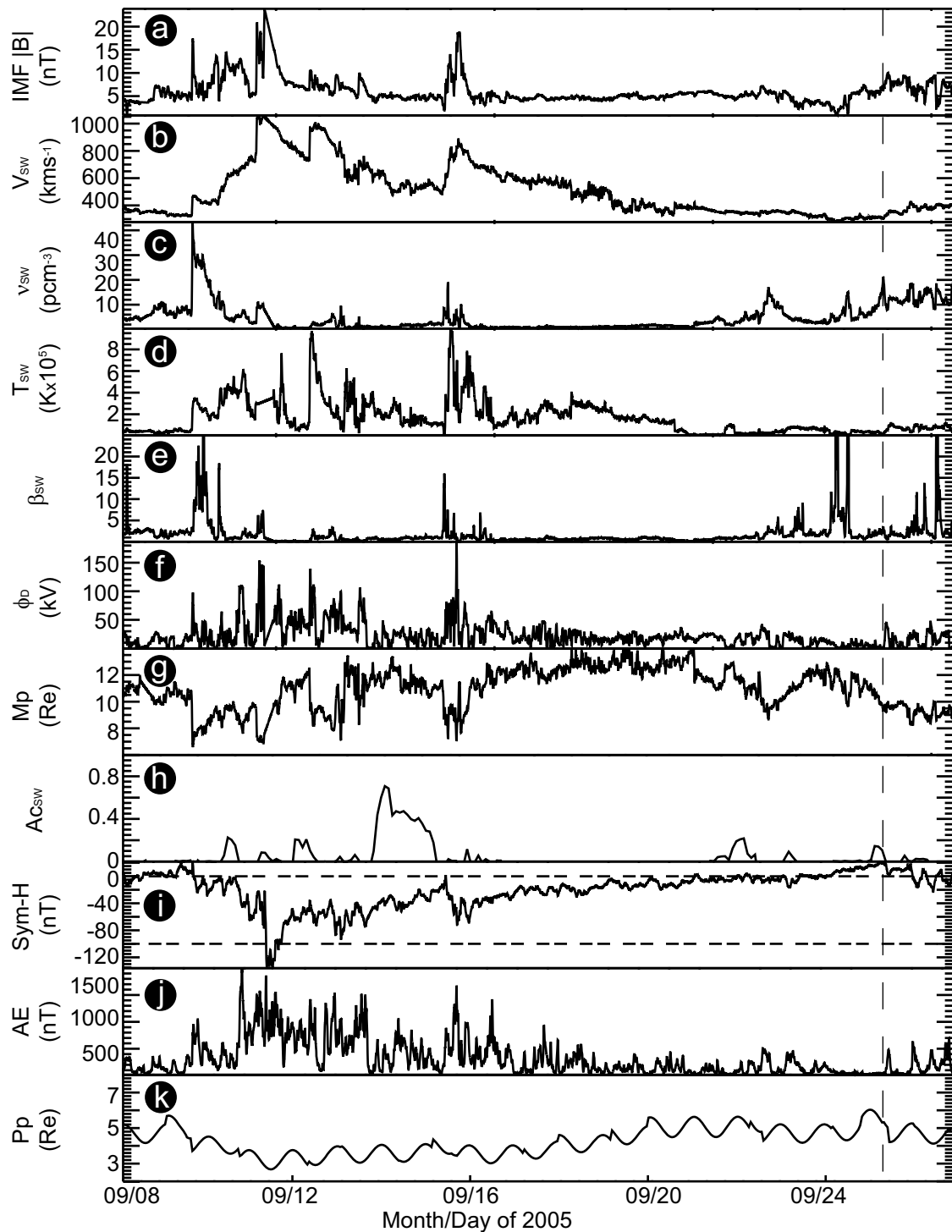


Figure 7.2: Solar Wind (SW) and geomagnetic indices for the period 2005/09/08-2005/09/27. SW parameters were derived from the OMNI dataset lagged to the magnetopause. Panel a show the magnitude of the IMF. SW velocity, temperature, particle density and plasma beta are shown in b - e. Panels f - h show an estimate of the dayside reconnection voltage, the model radial magnetopause position at the sub solar point and the three-component cross correlation of IMF with SW velocity as a measure of Alfvén wave activity. Panels i - k show the Symmetric-Horizontal storm time disturbance, the Auroral Electrojet associated magnetic disturbance and a model plasmopause position. A CME with foreshock induced a moderate intensity geomagnetic storm on 2005/09/08 with a secondary Alfvén wave and shock associated intensification on 2005/09/15. Pulsed Ionospheric Flows begin at the dash vertical line.

recede earthward from $\sim 12.5 R_E$ to $\sim 10.5 R_E$ by the morning of the 25th, which is marked with dashed vertical line.

These conditions show that a recently energised ring current population was steadily subjected to dayside magnetospheric compression prior to interval of interest. Figure 7.3 shows the period 04:00 to 20:00 UT on the 25th of September in a similar format to figure 7.2, except for the omission of the Alfvén coefficient panel and inclusion of the IMF clock angle, now in panel b. IMF clock angle is given here as degrees from north in GSM coordinates. Marked with dashed vertical lines are the times of behavioural change in the IMF. The first time of interest, $\sim 10:05$ UT, (t1) marks an increase in IMF magnitude and the beginning of a change in orientation to a largely southward direction. The second vertical line, at $\sim 10:50$, (t2) marks the start of a period of strong southward direction where the IMF clock angle is $\sim 190^\circ$. The third interval, $\sim 11:30$ - ~ 1315 (t3 - t4) shows a gradual anti-clockwise rotation IMF. The dayside reconnection voltage proxy in the eighth panel suggests that a moderate level of reconnection initiates at t1 and endures until t4. The Sym-H index (panel i) responds with a reduction from +20 nT to 5 nT, which subsequently invokes an inward movement of the plasmopause position shown in the bottom panel.

7.3.2 Ground based radar and pulsation magnetometer observations

Figure 7.4 presents geographic latitude/longitude-time plots of L-o-S Doppler velocity and spectral width data from three beams of each of the CUTLASS radars on the 25th of September 2005. The channel-A beams shown are 8-10 from HAN and 4-6 from PYK, the central beams from which intersect the integration volumes of the ESR and Barentsberg (BAR) pulsation magnetometer. The figure presents the period 04:00 UT to 20:00 UT and provides an overview of radar observations throughout the ionospheric sunlit hours of the day of interest. Indicated with a horizontal dashed line on each panel is the latitude/longitude of the ground-based instrumentation on Spitsbergen at $\sim 78.2^\circ$ N. The approximate local time of their location is also shown. The colour scales of these overview plots have been standardised for comparison and range from -1000 m s^{-1} to 1000 m s^{-1} in velocity, negative values indicating flows away from the radar, and 0 m s^{-1} to 500 m s^{-1} in spectral width. Negative values of velocity regularly exceed this range, however, in this plot, for illustrative purposes it is

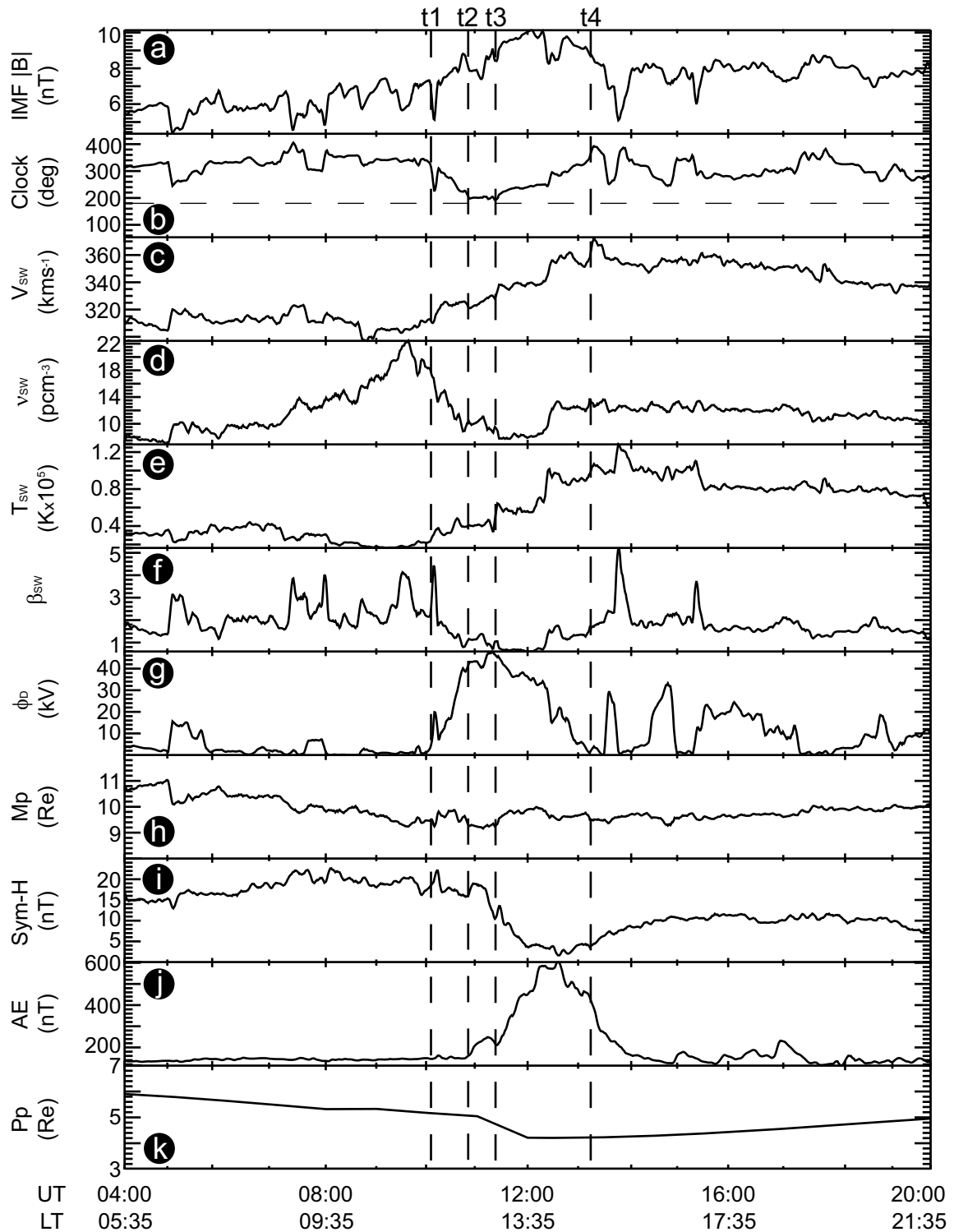


Figure 7.3: Solar wind and geomagnetic parameters for the period 04:00-20:00 UT on the 25th of September 2005. Similar to figure 7.2 in all panels bar the addition of IMF clock angle in GSM coordinates (panel b) and removal of the Alfvén wave coefficient, these time-series show an increase in the estimate of dayside reconnection voltage (first to fourth dashed line), a period of significantly southward IMF (second to third dashed line) and a period of IMF anticlockwise rotation (third to fourth dashed line). During the demarcated interval, a reduction in Sym-H and corresponding inward migration of the plasmapause can be seen.

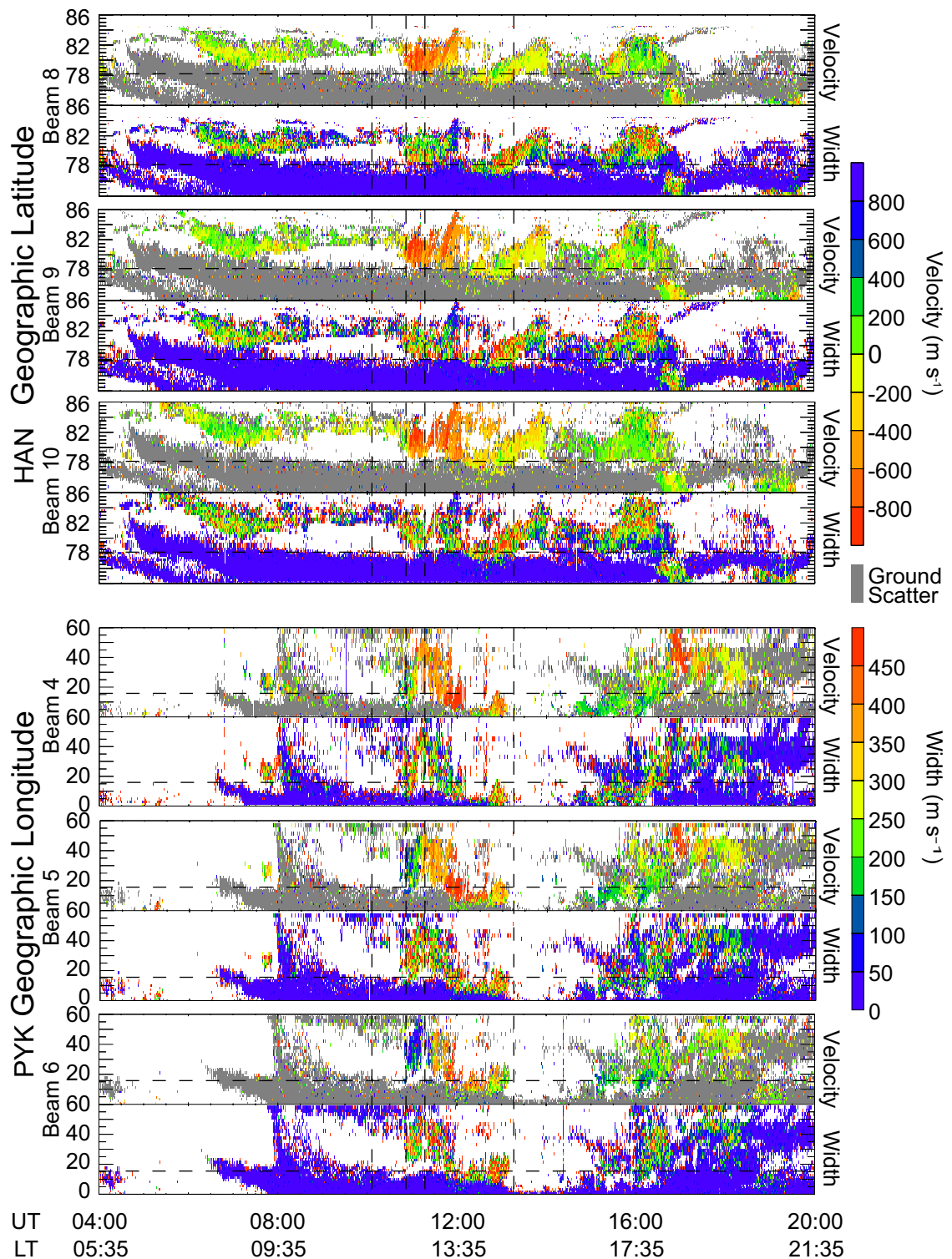


Figure 7.4 Line of sight Doppler velocity and spectral width data from channel A of the CUTLASS radars for the same interval as figure 7.3. The upper six panels show HAN data from beams 8,9 and 10, and the lower six panels PYK data from beams 4, 5 and 6. As before, changes in IMF behaviour are marked with vertical dashed lines. The geographic longitude or latitude of the Svalbard instruments is marked on each panel with a horizontal dashed line.

beneficial to restrict it thus. Data points of extremely low velocity and spectral width backscatter are flagged as ground scatter and coloured grey in all velocity panels. The key times of interest (t1-t4) as noted in figure 7.4 are marked with vertical dashed lines, which will be present on all future parameter-time plots. Given the -12° (geographically west of north) boresight direction of the HAN radar, phenomena that are stationary in local time appear first in higher numbered beams that look further eastward. HAN observations show high-latitude low-velocity F-region backscatter as early as 06:00 UT in beam 10 appearing within a few minutes in beams 9 and then 8. The latitude of this early scatter is too high to appear in any of the chosen PYK beams. From $\sim 07:00$ the equatorward edge of this patch of scatter slowly migrated northward until $\sim 10:45$, when a region of high spectral width in excess of 250 m s^{-1} extended down to $\sim 78.5^\circ \text{ N}$. Evident in all displayed beams and radars, this patch exhibited high negative velocities in HAN data, indicating strong poleward flows (in excess of -1500 m s^{-1}) and the expansion of the polar cap until approximately midday. Following these flows, a region of scatter with a strong eastward velocity component, peaking at $\sim 1200 \text{ m s}^{-1}$ (as seen in PYK data), and moderate poleward velocity of $\sim 350 \text{ m s}^{-1}$ persists until approximately 14:00, disappearing from the PYK field of view by $\sim 13:15$ as it migrated northward under polar cap contraction. Further discussion of this interval will be made once the large-scale ionospheric flow regime has been addressed. After this period, conditions become quieter with flow velocities and spectral widths subsiding. Even though significant enhancements in width, indicative of the Open Closed field line Boundary (OCB), were seen at high latitude well into the early evening they were not accompanied by high velocity flows.

Figure 7.5 displays full beam sweep fan plots from both CUTLASS radars for the interval 10:40 UT to 13:21 UT. These pairs of scans are geomagnetically projected and orientated such that magnetic local noon is at the top of each map. Concentric dashed lines mark 10° of magnetic latitude, the innermost denoting 80° N , with radial lines marking 15° of magnetic longitude, or one hour of local time. Each scan represents 1 minute of data, with their start times separated by 20 minutes. For clarity, ground scatter has been removed from all maps. The first scan (10:40-10:42) exhibits limited backscatter in both radars. The 11:00 UT HAN scan reveals the azimuthal extent of the poleward flows, which appear to extend some 3 hours in local time. The locations of the ESR and BAR are initially seen to lie beneath the equatorward edge of this high

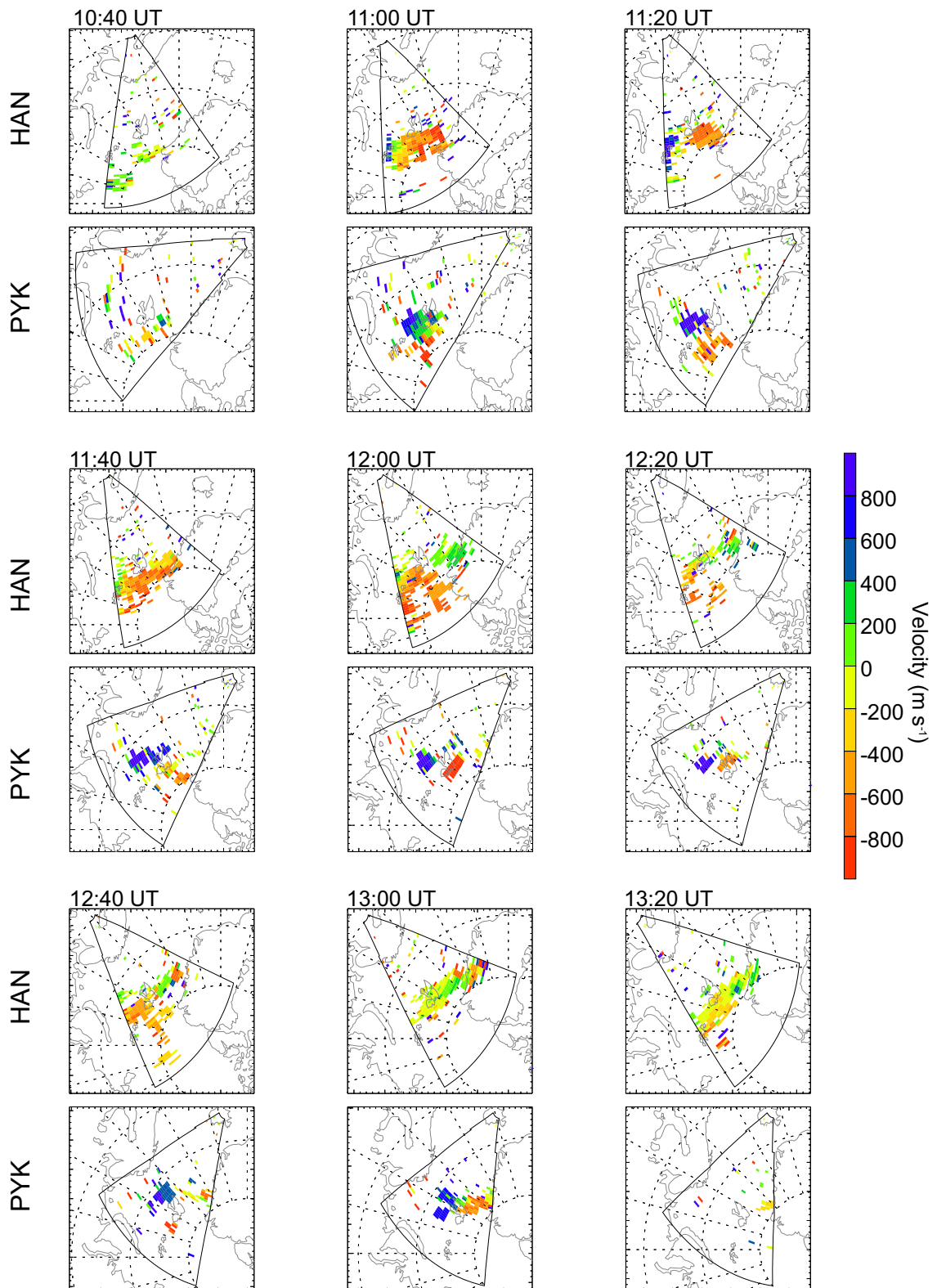


Figure 7.5: CUTLASS L-o-S velocity scans for the interval 10:40-13:21. Scan resolution is one minute with a separation of 20 minutes between each successive scan display. Scan projections are Geomagnetic-Magnetic Local Time, orientated with local noon at the top. Each concentric dashed line represents 10° of latitude and each radial dashed line 1 hour of local time. Poleward flows can be seen over Svalbard in the HAN scans: however, PYK data reveals the development of a shear flow overhead.

velocity region and are engulfed in the polar cap as enhanced dayside reconnection drives its expansion. From 11:20 onwards, oppositely directed L-o-S velocities are seen in PYK scans, showing flow away (towards) from the radar at higher (lower) latitude. This apparent shear flow, signifying the dusk convection reversal boundary, endures until PYK backscatter disappears ~13:00.

Global ionospheric convection maps for the same interval are shown in figure 7.6. Each convection map is similar in format to those in the previous figure and contains data from all available SuperDARN radars in the interval. The start times are again separated by 20 minutes, although, each of these maps contain 2 minutes of radar data. UT, IMF orientation and cross-polar cap potential are given in the top left-, top right- and bottom left-hand corner of each map respectively. Ionospheric flow vectors are scaled and colour coded by velocity. Positive (negative) equipotential contours are shown with dashed (solid) black lines and the Heppner-Maynard convection boundary (Heppner and Maynard, 1987) with a solid green line. A lack of global backscatter results in potential maps that are more representative of the IMF dependent statistical model constraining their form. This appears to be the case in the first map, which contains relatively few vectors of limited magnitude. The beginning of this interval sees Spitzbergen located at the eastward edge of the throat of the developing convection pattern. As the IMF began rotating anticlockwise from a predominantly B_y negatively direction to largely B_z negative, the cross-polar cap potential increased up to maximum value of 91 kV at 11:34 UT (not shown), flow velocities increased and a twin celled convection pattern was set up, indicating enhanced dayside reconnection. As the IMF rotated back towards dusk, pushing the cusp/cleft duskwards (Cowley *et al.*, 1991), previously anti-sunward dayside flows were directed eastwards creating a region of high velocity flow over Spitsbergen somewhat later than might be expected. At ~ 13:00 UT, global convection began to relax, with the cross-polar cap potential falling to below 40 kV. Throughout this interval, Spitzbergen remained within the convection reversal subject to occasionally intense shear flows overhead.

Focussing now on the high velocity poleward flows that were highlighted earlier but not discussed, figure 7.7 concentrates on the interval 10:30 UT to 12:00 UT. The figure displays data from channel B of the HAN and PYK radars, which were camped on beams 9 and 5 respectively in high temporal resolution mode. The times and

25/09/2005 10:40-13:22 UT

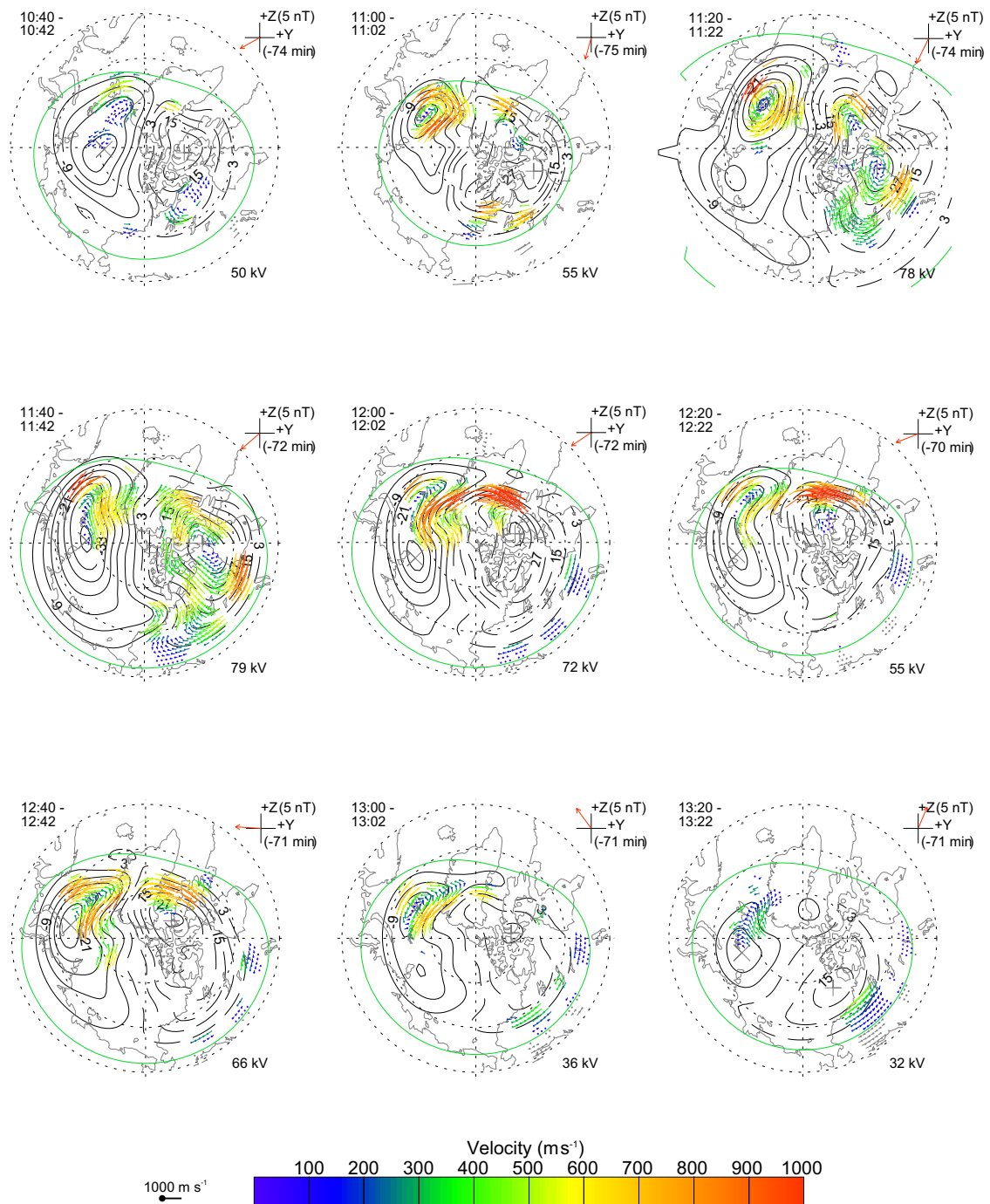


Figure 7.6: Geomagnetically mapped ionospheric flow vectors, derived from the APL Map Potential model using all available SuperDARN data. Negative (positive) equipotential contours are shown by solid (dashed) black lines. Each map contains two minutes of radar data and is separated by 20 minutes. Concentric and radial dashed lines mark 10° of latitude and 6 hours of magnetic local time respectively. All maps show geographic outlines in grey and are orientated with 12 noon at the top. Scan time in UT, IMF orientation and cross polar cap potential are indicated in the top left-, top right- and bottom right-hand corner of each panel respectively.

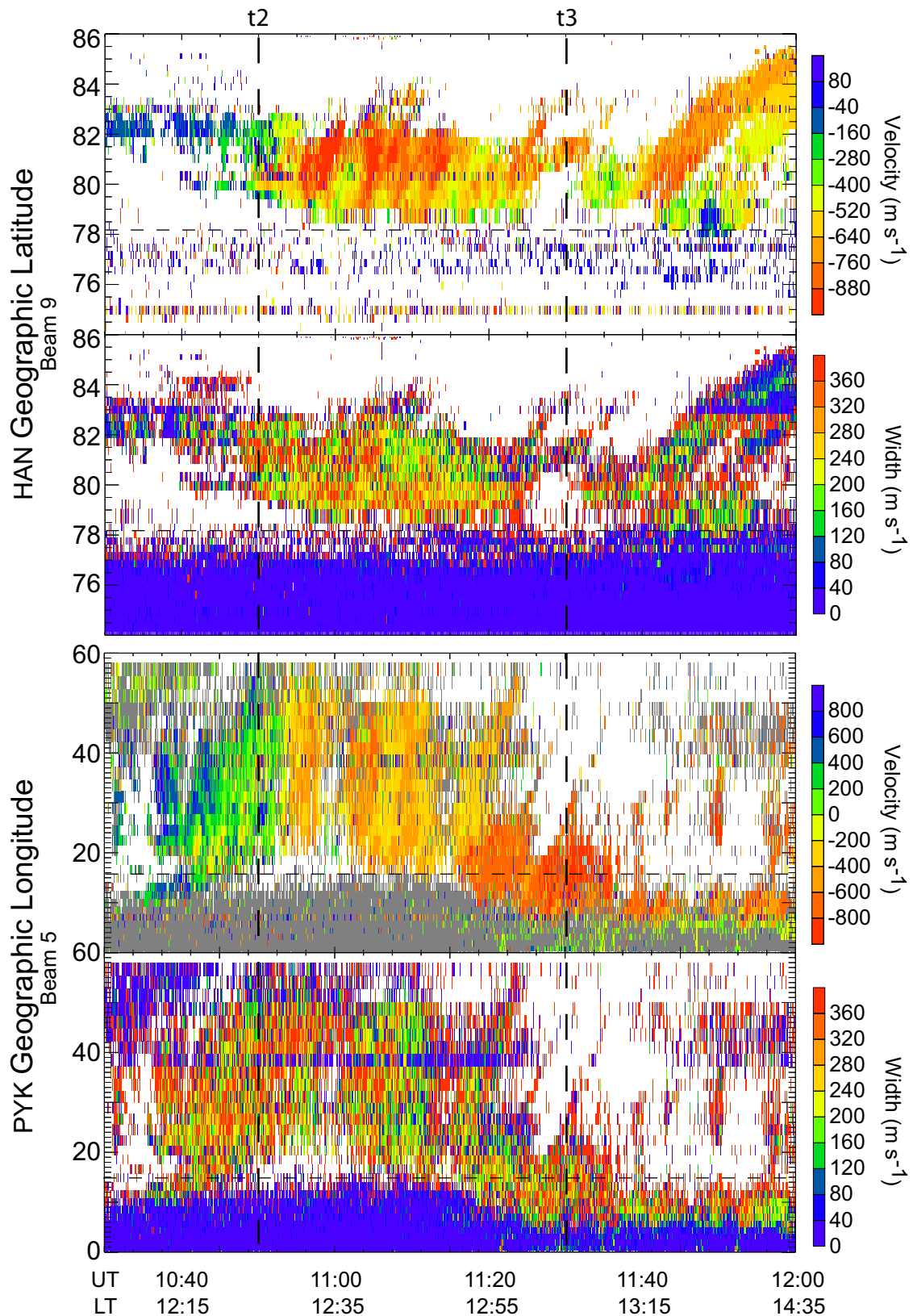


Figure 7.7: Stereo fast mode L-o-S Doppler velocity and spectral width data from Channel B of the CUTLASS radars for the interval 10:30 - 12:00 UT. Velocity scales have been adjusted to highlight the PIFs that initiate at approximately 10:50. The times of IMF behavioural change identified in figure 7.3 are, as before, marked with dashed lines as is the latitude of the ground based instrumentation.

latitude/longitude of interest are again marked with dashed lines. The HAN L-o-S Doppler velocity colour scale has been altered to accentuate the PIFs that initiated at t_2 and persisted until t_3 . During this period, L-o-S velocity oscillated between $\sim -300 \text{ m s}^{-1}$ and $\sim -1500 \text{ m s}^{-1}$. Although a visual regularity may be attributed to these PIFs, when subjected to Fourier analysis no significant periodicity emerged, which is unsurprising given the small number of enhancements. Further pulsed flows can be seen at $\sim 11:39$ UT, however, they are imbedded within what appears to be a PMRAF. A velocity reversal at 11:10 UT in PYK data is approximately coincident with a reduction in peak poleward flow velocity seen in HAN backscatter.

Parameters measured by the ESR 42 m fixed, field aligned dish for the period 04:00 UT to 20:00 UT are shown in figure 7.8. Displayed in descending order are T_i , V_i , T_e and N_e as functions of altitude and UT. It must be noted here that the ESR velocity convention is opposite to that of SuperDARN, meaning that negative flows are towards the radar. However, the colour scale has been reversed in this figure, and all ESR figures that follow, such that red (blue) still indicates flow away from (towards) the radar. Elements of these data display synergy with the intervals t_1 - t_4 , which are again marked with dashed lines. N_e is presented in the fourth panel with a logarithmic colour scale from 10^{10} to 10^{12} particles per cubic metre. N_e remained reasonably constant from $\sim 07:00$ until t_2 when low and high altitude density began to fall. t_2 also coincides with enhancements in T_i , V_i and T_e . A uniform increase in T_i , to greater than 2000 K, occurred down to E-region altitudes and upward ion flows from ~ 350 km began sporadically, reaching velocities exceeding 250 m s^{-1} . A slight increase in T_e was seen down to ~ 200 km but it was not until t_3 that temperatures exceeding 3500 K were reached. At t_3 , upward ion velocity increased further, approaching 400 m s^{-1} and at times could be seen to originate from as low as 300 km altitude. At this time N_e decreased considerably above 300 km and the bulk of the F-region electron population could be seen to descend. Oscillatory enhancements, which were weakly mirrored in T_e , could be seen in N_e as it began to recover to its pre t_3 distribution. At $\sim 12:50$ a sharp increase in electron density and temperature was seen; density enhancement was most pronounced at low altitude (~ 250 km), whereas electron temperature maximised at higher altitudes. Conversely, an enhancement in upward ion velocity was accompanied by a reduction in T_i . t_4 was roughly coincident with the end of these enhancements.

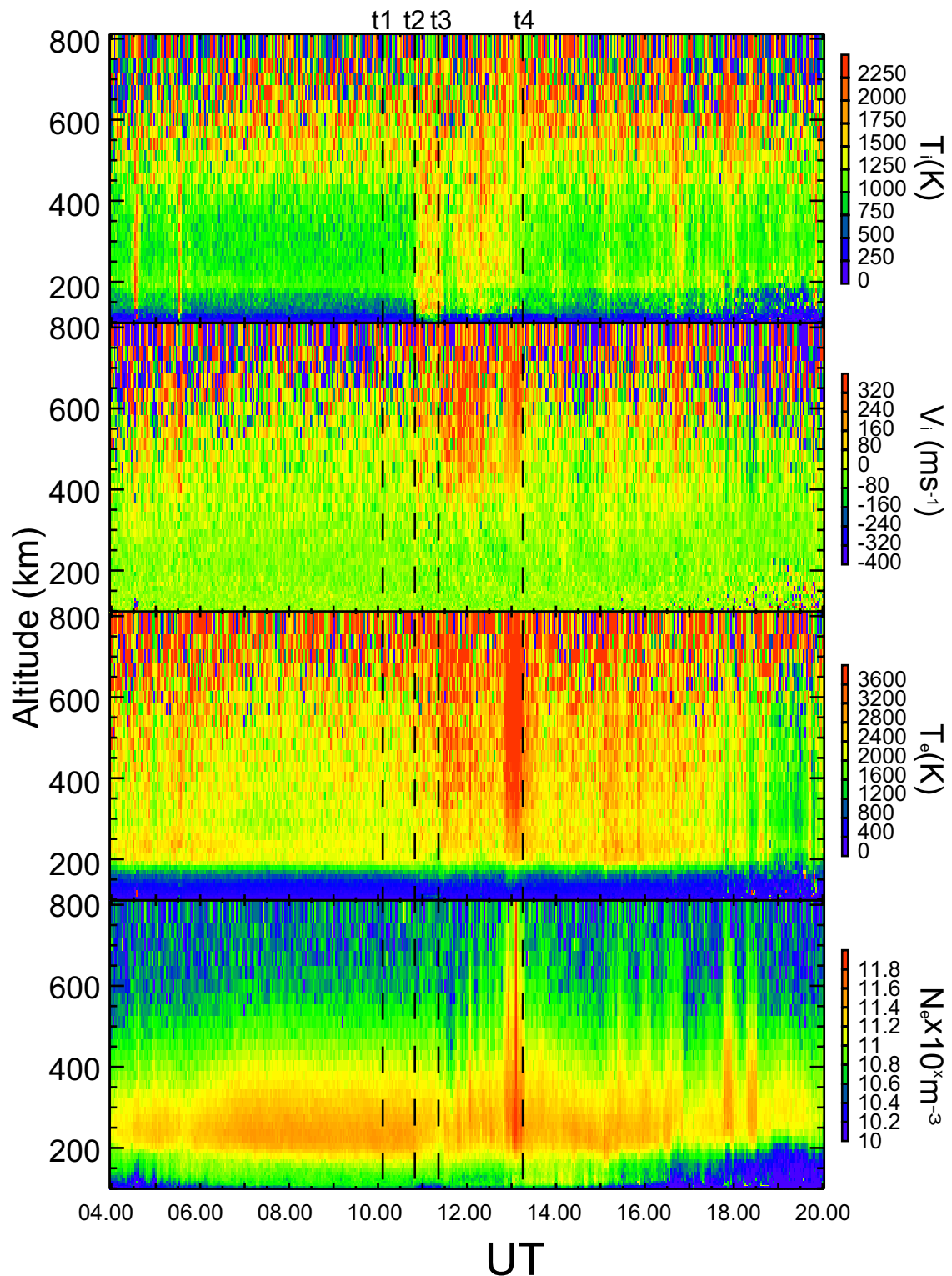


Figure 7.8: 128 s post integrations of the ESR 42 m field aligned dish. L-o-S ion temperature and velocity are shown in the first two panels, electron temperature and concentration in the third and fourth. The Steffe pulse scheme, providing 2.4 km range resolution, has been altitude gated, such from 100 km to 900 km, gate size increases linearly from ~ 4 km to 40 km. Ion temperature is seen to increase during the period of PIFs seen in Han radar data. Ion upwelling from 300 km is seen during the period of IMF anti-clockwise rotation as is electron temperature enhancement. A significant enhancement in electron temperature and density can be seen towards the end of the demarcated interval.

Figure 7.9 focuses on the parameters measured by the ESR 32 m steerable dish during the interval 10:00 UT to 14:30 UT. Of similar format to figure 7.8, these panels display the four basic parameters along the three directions given in 7.2.4. Ion velocity measurements along LD2 (approximately geomagnetically southward) indicate northward flows towards the radar between 10:50 UT and UT 11:40, which concur with CUTLASS poleward flows during this interval and indicates a equatorward migration of the OCB. From ~11:00 UT, Low altitude flow towards the radar can be seen in the LD1 (slightly westward looking) data also, which over the course of a few tens of minutes appear up to a similar altitude as in LD2. LD1 is of lower elevation angle than LD2, hence, the component of a horizontal flow in L-o-S of LD2 would be expectedly lower. This does however signify that the region of enhanced flows is moving in a direction that is approximately perpendicular to LD2 and has a component in the direction of LD1, hence, duskward. However, from 12:00 UT L-o-S velocity along LD2 is reversed until ~13:00 UT when a further reversal sees a return to flows toward the radar in a northerly direction, which persist until ~14:10 UT. Enhanced electron temperatures in the third set of panels reveal the motion of the OCB as the polar cap firstly expands to include the ESR at ~11:20 UT, then again at ~13:20 UT. Given the long effective integration time and three-position scan pattern, observation of individual pulsed flows are not directly possible from these data, however, they do reveal the large-scale flow reversals in this interval.

A wealth of noteworthy Pc1-2 pulsations occurred throughout the analysis interval that may elucidate the global magnetospheric state. Figure 7.10 contains dynamic spectra from all seven stations of the FPMC. These frequency-time-spectral intensity plots are independently, logarithmically scaled such that red (blue) denotes high (low) spectral intensity. At 04:10 UT, a narrow-band, structured Pc1 pulsation seen at all stations initiated with central frequency ~0.25 Hz. Polarisation parameter and cross-phase analysis (not shown) revealed that as this pulsation continued for over 5 hours its parameters became multifarious, complicating its spectral boundaries and smearing its periodic appearance. Occurring at the most statistically likely time of day for its class (see chapter 6), this pulsation began to diminish in power at 10:00 UT and ceased entirely by 10:40 UT. Figure 7.11 displays dynamic spectra and polarisation parameters for the sustained pulsation elements in the period of interest recorded at Ivalo; these were extracted with the techniques outlined in Ch.6.2. Given the length of

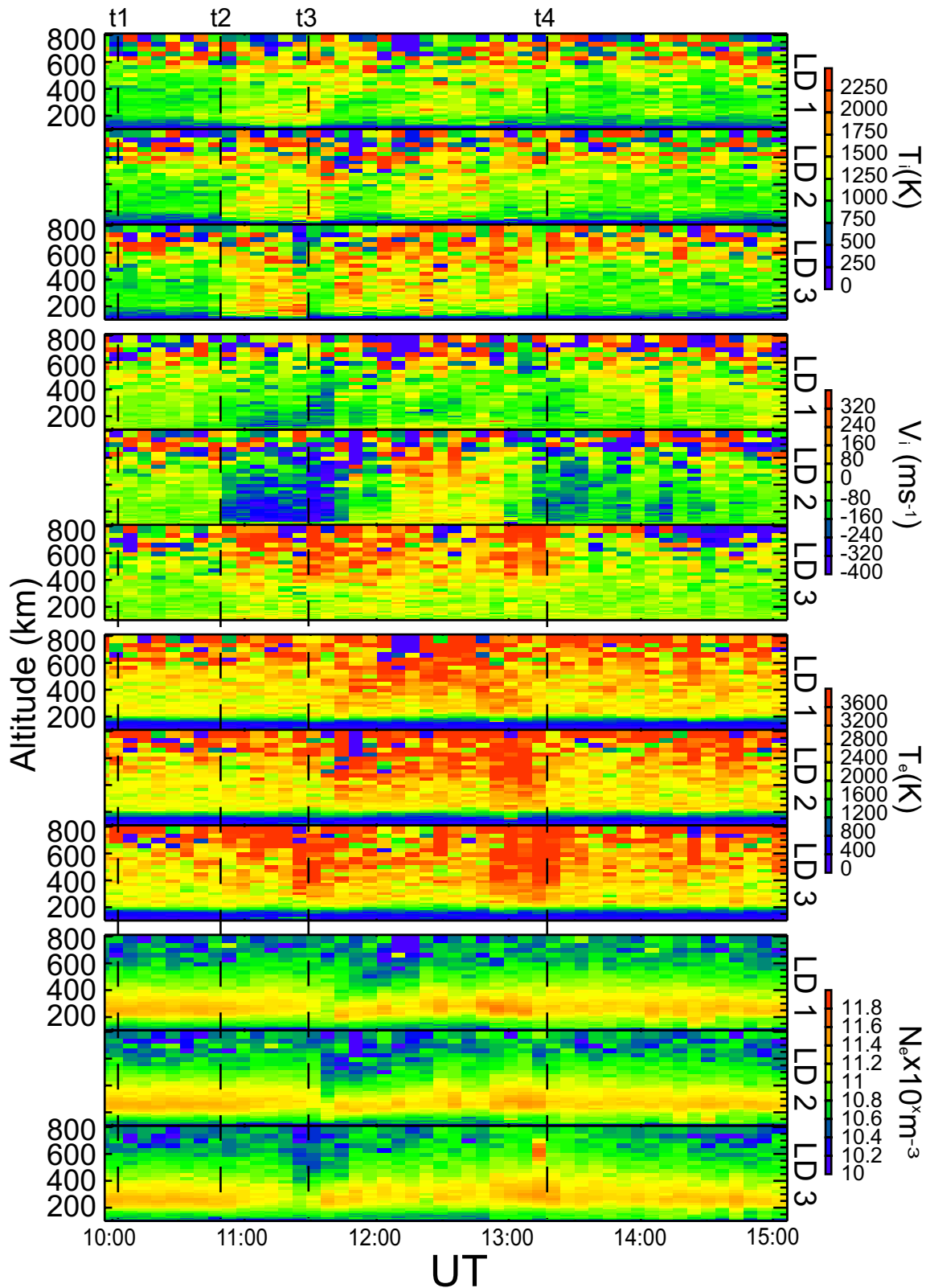


Figure 7.9: 128 s post integrations of the ESR 32 m steerable dish, similar in format and analysis to figure 7.8. Operating in common program 2, three look directions (LD) are cycled through: LD1 (171.6° az, 63.2° el), LD2 (144.0° az, 66.66° el) and LD3 (171.6° az, 90° el). During the period of PIF seen in the HAN radar data flows towards ESR can be seen in the southward looking scan intervals.

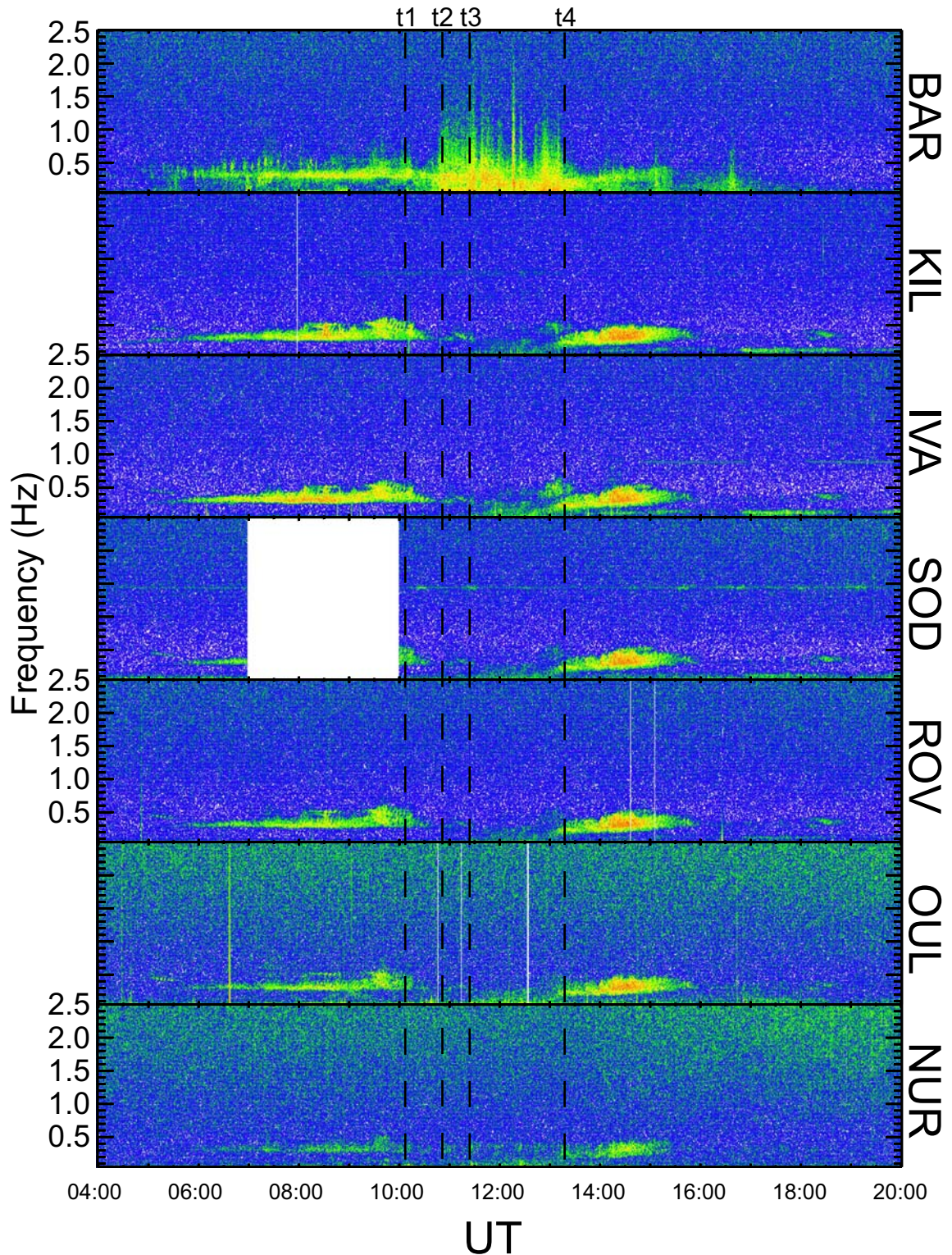


Figure 7.10: FPMC dynamic spectra for the period 04.00-20.00 UT on the 25th of September 2005. Multiple periodic, continuous pulsations can be seen at all stations from 05.00 UT onward, persisting until ~10.40 UT. Narrow band irregular pulsations initiate at high latitude at a similar time. Continuous pulsations re-emerge at ~13.00 UT and display a moderate increase in central frequency until termination at ~16.00 UT. The IMF intervals identified in figure 7.3 are marked with dashed vertical lines.

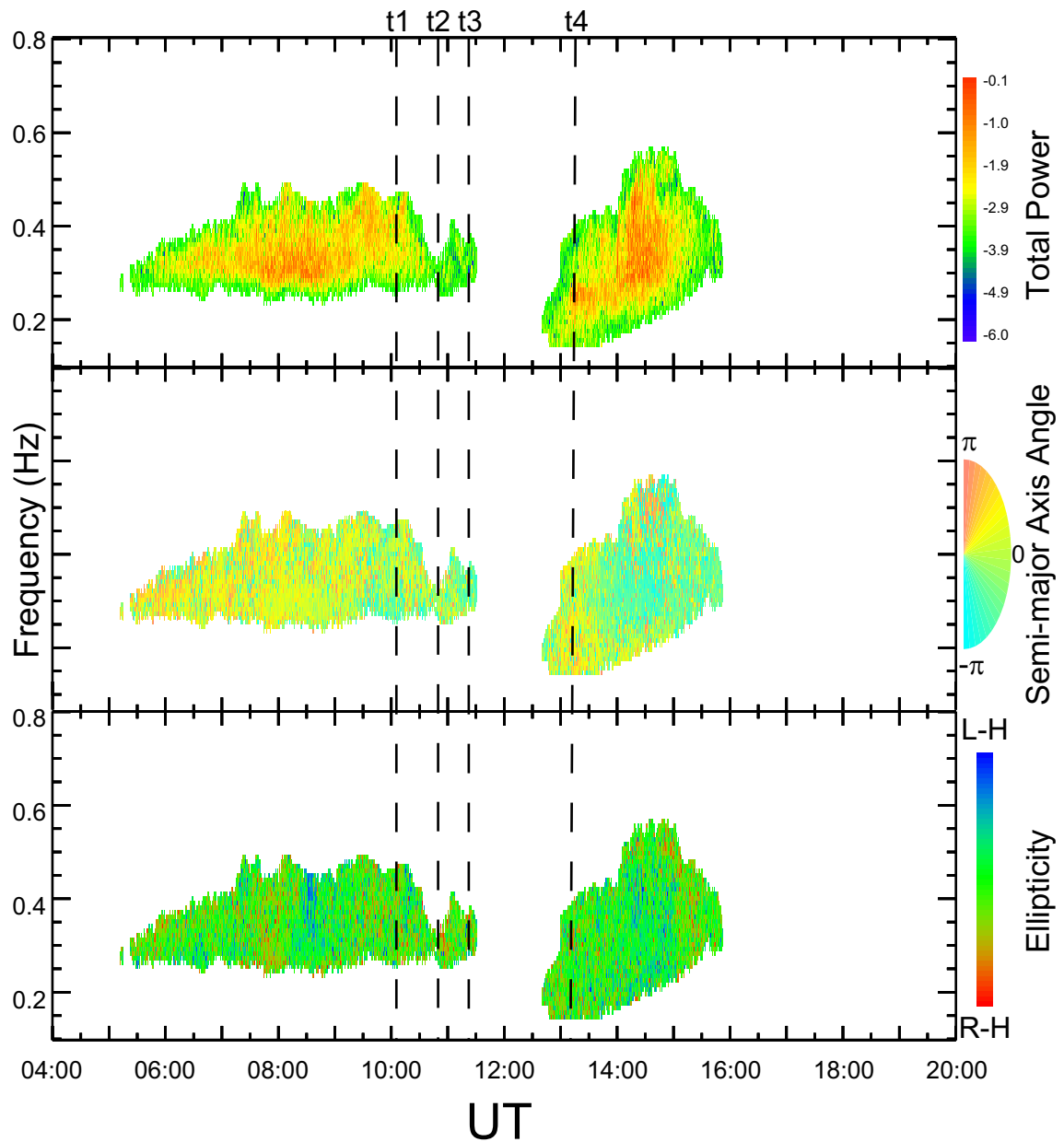


Figure 7.11: Dynamic spectrum and polarisation parameters for the extracted continuous pulsations registered at Ivalo. Some consistency in semi-major axis angle (middle panel) can be seen for both pre and post PIF events.

each pulsation and the non-stationary nature of each parameter, characterisation by a single event values is somewhat uninformative. Consequently, figure 7.12 presents the result of dynamic histogram fitting, which applies the technique outlined in Ch.6.2 to sequential windows of extracted data to derive meaningful timeseries for ellipticity and semi-major axis angle of orientation. The left-hand column of figure 7.12 shows that the orientation of the polarisation ellipse for the pulsation following the period of PIFs differs significantly from the pulsation prior that period. Ellipticity, displayed in the right-hand column, shows that post-PIF pulsations are significantly left-hand circularly polarised at SOD (fourth panel) suggesting that their ionospheric source region is near by.

The focal ULF wave activity of this study occurred at $\sim t_2$, approximately coinciding with Spitzbergen's inclusion in the polar cap, when broadband unstructured pulsations were exclusively seen at BAR. Although these irregular pulsations were not as band-limited as the Pc1s that preceded it, a slight spectral power enhancement can be seen to persist at a similar frequency throughout. They displayed little consistent polarisation, orientation or quantifiable regularity in their intensity; hence, similar analysis to that displayed in figures 7.11 and 7.12 is not presented for this pulsation. Between t_2 and t_3 , the period of PIFs, broadband pulsations are reasonably constant. At t_3 they become less regular, culminating in a final sustained series of bursts from 12:45 to t_4 , coinciding with northward motion of the OCB over the instrument.

Immediately prior to t_4 a second narrow band Pc1 pulsation began, which was again surrounded by multiple shorter duration structured pulsations, giving it the appearance of an Interval of Pulsations of Diminishing Period (IPDP). The 330 and 200 minute durations of the morning and post-noon continuous pulsations place them both at the top of the duration distribution derived in chapter six. The rarity of such enduring pulsations is compounded by their separation. In the aforementioned study, it was generally seen that when multiple pulsations of this length occurred they overlapped, often appearing as a single event.

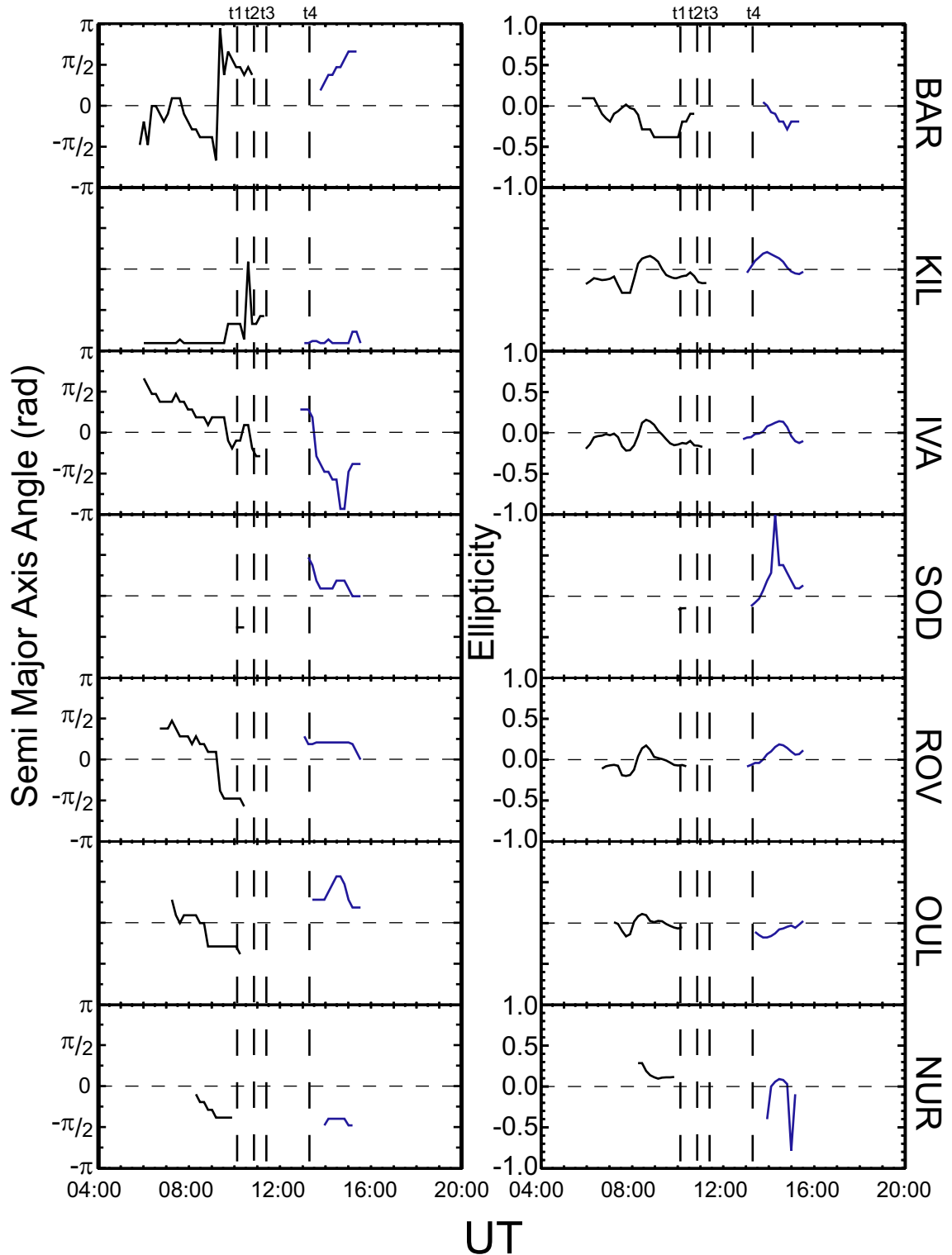


Figure 7.12: Dynamic histogram derived values of Semi-major axis angle and ellipticity for the enduring pulsations in the period 04.00-20.00 UT on the 25th of September 2005. The IMF intervals identified in figure 7.3 are marked with dashed vertical lines. The large duration and non-stationarity of repetition period of each pulsation prevented the determination of singular event repetition frequencies for the visually evident amplitude oscillations evident in the dynamic spectra of figure 7.10.

7.3.3 In situ particle observations

Figure 7.13 presents merged proton spectrograms from the SOPA and MPA instruments on the LANL 01A, 02A, 97A and 084 satellites for the entire 24 hours of the day of analysis. The 01A satellite is in geosynchronous orbit approximately 15° east of the FPMC; the ground track of all the LANL satellites used can be found in figure 7.14. With an energy range of a few eV to several MeV, these flux perturbation maps represent the deviation of flux from an average background level (Henderson *et al.*, 2006). Rigorous interpretation of these particle data is reserved for future work; however, it may be noted that increased differential ion flux of 50 keV to ~ 1 MeV can be seen surrounding local noon in all satellites. These energies are significantly higher than might be expected to generate EMIC waves but without knowledge of their radial profile it cannot be discounted that they are the source of the morning sector Pc1s. A substorm particle injection at 11:30 UT is also evident in the 084 spectrum, which can then be seen to drift westward, with its highest energy components reaching the 02A satellite by 13:00 UT, coinciding with IPDP initiation.

The ground track of the DMSP-F15 satellite between 11:17 UT and 11:33 UT is overlaid on the geomagnetic-MLT map of the northern polar region in figure 7.14, which is of similar format to those in figure 7.5. Cross-track ion velocity vectors measured by the IDM instrument are represented as lines perpendicular to the satellite's track. The ion drift velocities at the altitude of DMSP-F15 were in general agreement with SuperDARN convection patterns, where radar data existed. Low-latitude dusk-sector westward drifts consistent with convection return flows were observed, however, there was a slight drift reversal boundary discrepancy, which may be attributed to a few unreliable IDM datapoints. High latitude drifts were consistent with strong anti-sunward flows at 12 MLT sweeping westward under the influence of an increasing IMF B_y component. The red coloured cross-track vectors mark the cusp region, as identified from the particle spectrograms (Newell and Meng, 1988) in figure 7.15. Electrons are shown in the upper panel and ions in the lower. These spectra show that the satellite passed through the energetic ion region of the low latitude boundary layer (concurrent with sunward flows measured by the IDM), skirted the plasma mantle and entered the cusp just after 11:25. The faulty low-energy ion instrument obscured the full dispersed

LANL Geo. Protons (MPA+SOPA)

September 25, 2005 (2005268)

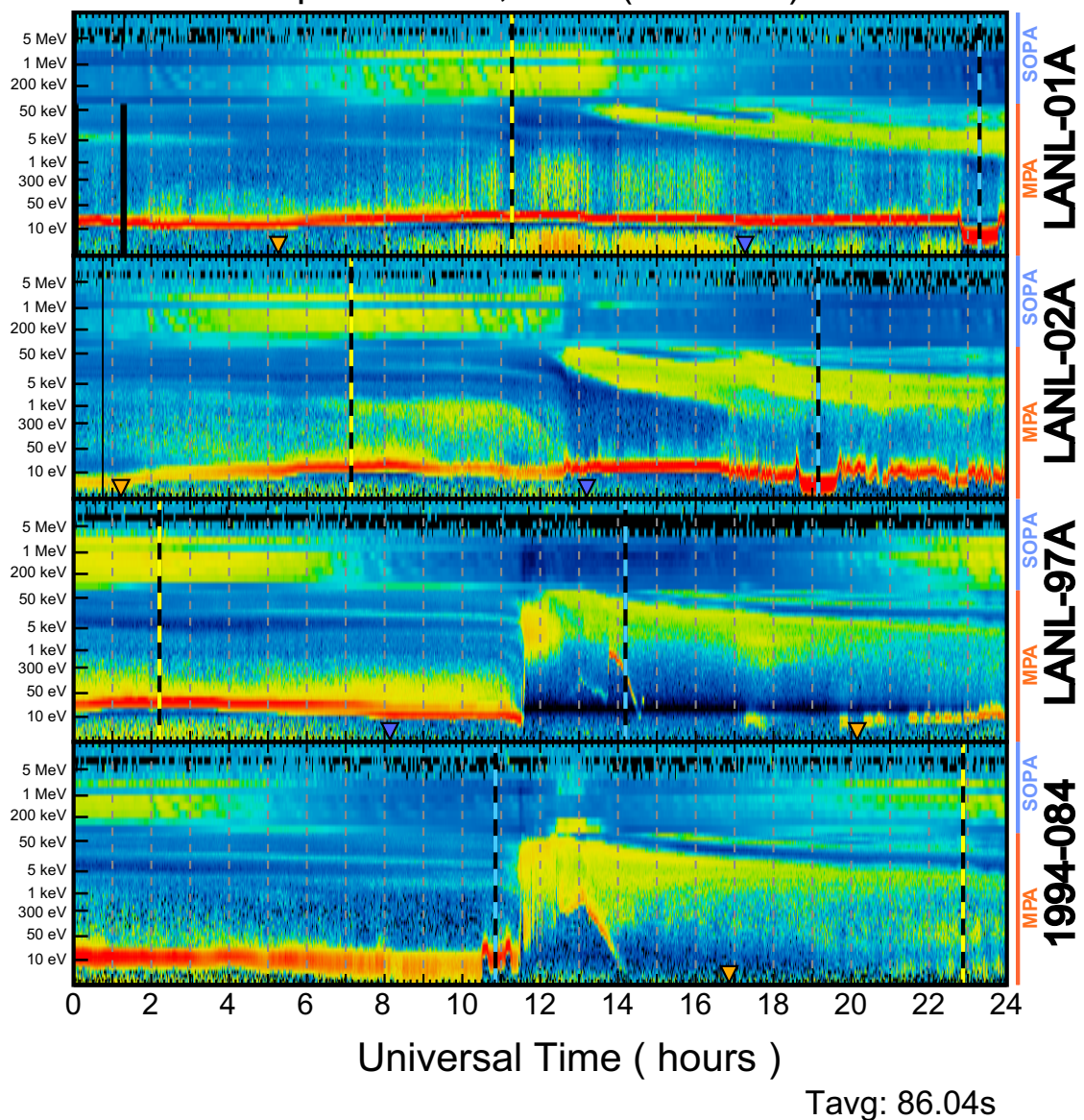


Figure 7.13: Merged ion spectrogram of from the SOPA and MPA instruments aboard the LANL-01A, -02A, 97A and 084 geostationary satellites. The foot prints of these satellites can be seen in figure 7.14. Colour represents the differential flux from an average background level, red signifying a large positive deviation. Increased ion flux of energies between 50 keV and ~1 MeV can be seen by all satellites surrounding local noon. A substorm injection event at 11:30 UT is evident in the 084 spectrum, which can then be seen to drift westward, with its highest energy components reaching 02A by 13:00 UT.

Plot downloaded from <http://leadbelly.lanl.gov/>

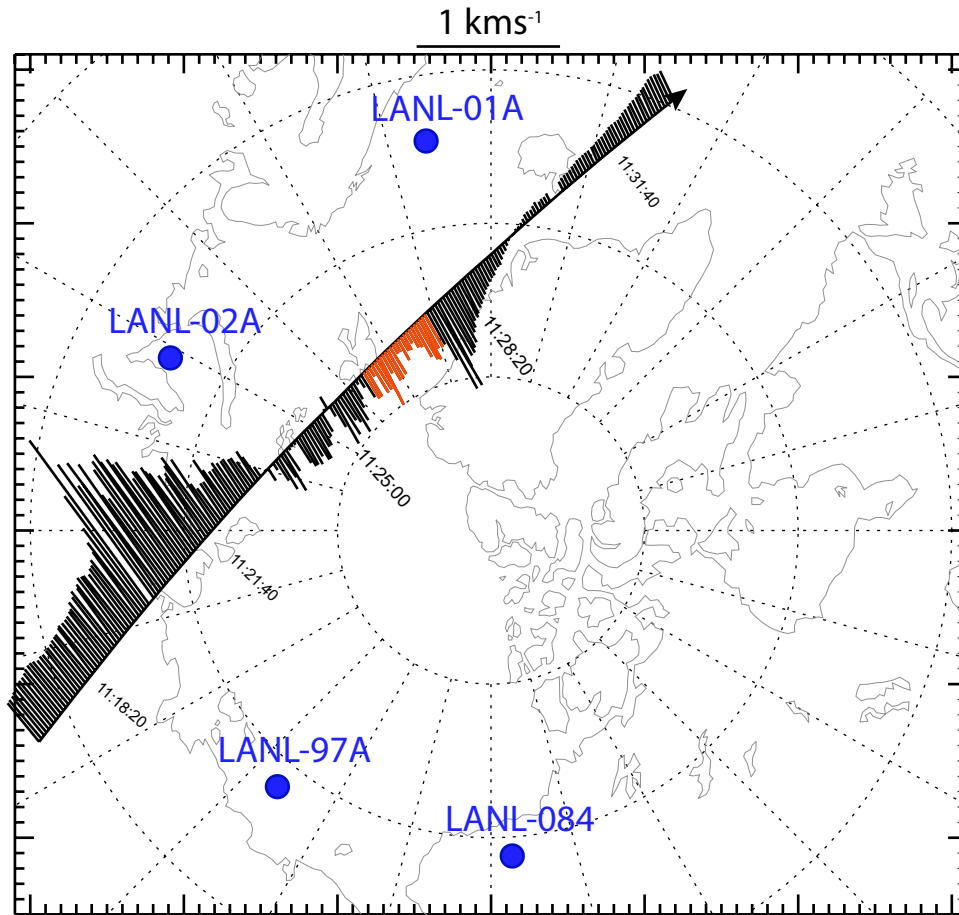


Figure 7.14: Geomagnetic-MLT projection of the DMSP F15 satellite’s IDM cross-track ion drift velocity. Concentric (radial) dashed lines mark 10° (15°) of latitude (longitude). The cusp region (figure below) is shown in red. The footprint of the LANL-01A, -02A, -97A and -084 satellites are also shown in blue.

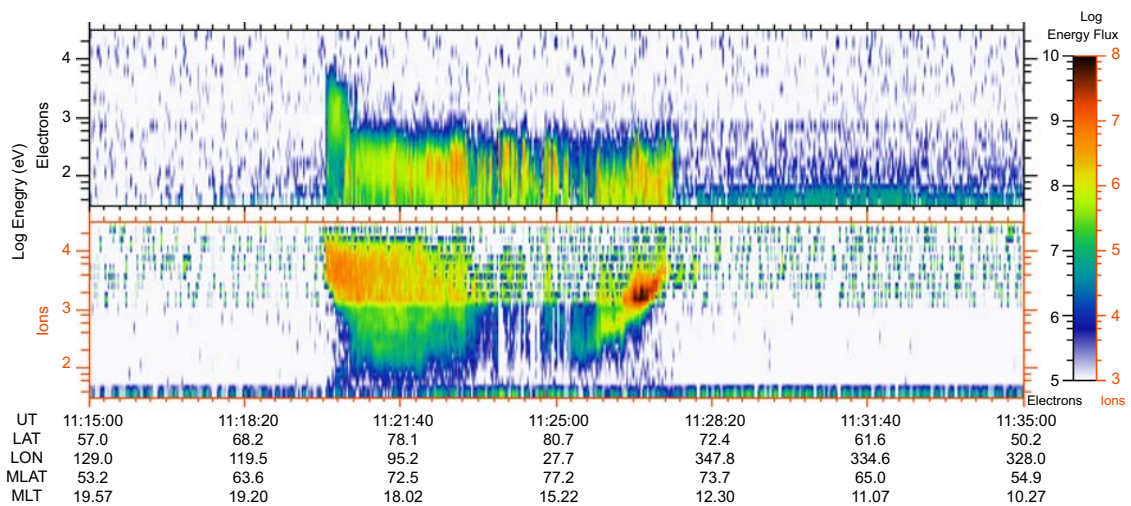


Figure 7.15: DMSP F15 SSJ/4 particle data, provide by JHU/APL and the centre for Space Sciences at the University of Texas at Dallas, showing a dispersed cusp signature ~11:25 slightly to the west of the ground base instrumentation’s integration volumes. It must be noted that the low energy ion instrument is untrustworthy, somewhat hampering precise analysis.

cusp signature and did not allow precise timing to be determined; however, it is clear the satellite exited the cusp region at 11:27:20 at a magnetic latitude of 74.5° .

7.4 Discussion

Observations of IMF control over the position and throat direction of the dayside convection pattern, PIFs and Spectral Width Boundaries (SWB) are commonplace and a number of statistical studies have successfully characterised their behaviour, e.g. (McWilliams *et al.*, 2000, Provan and Yeoman, 1999, Baker *et al.*, 1995). The occurrence of ULF wave activity associated with the cusp/mantle region has also been well reported upon, e.g. (Engebretson *et al.*, 2009, Dyrud *et al.*, 1997). However, as well as each element of this case study is known, the observations presented here provide a coherent scenario, from which support may be found for candidate mechanisms for the generation of the irregular pulsations and spectral width enhancements that have long been attributed to the cusp. An overview of the instrumentation and key data is present figure 7.16

7.4.1 Morphology and motion of the cusp and OCB

A key aspect of this case study is that Spitzbergen remained within the cusp region yet on the fringe of the post-noon convection reversal boundary, depicted as the orange region of figure 7.16, and not at its poleward edge throughout. As enhanced convection began, in response to a largely southward IMF, Spitzbergen was situated on the duskward edge of the convection pattern throat, as shown by the Map Potential contours in figure 7.16. The westward return flows overhead (fig. 7.7, PYK data) suggest that the OCB was slightly northward of the ESR at the time that poleward flows were observed in both HAN and ESR 32 m L-o-S velocity data. As enhanced reconnection continued, opening flux and causing the expansion of the polar cap, ion temperature and upward velocity enhancements signified that the ESR was the on newly opened field lines. The persistent azimuthal shear flows showed that the ESR and BAR remained close to the edge of the convection reversal boundary for the duration of the substorm growth phase. At onset, the cusp was forced eastward by an increasingly negative IMF B_y component, again, keeping Spitzbergen close to the convection reversal boundary.

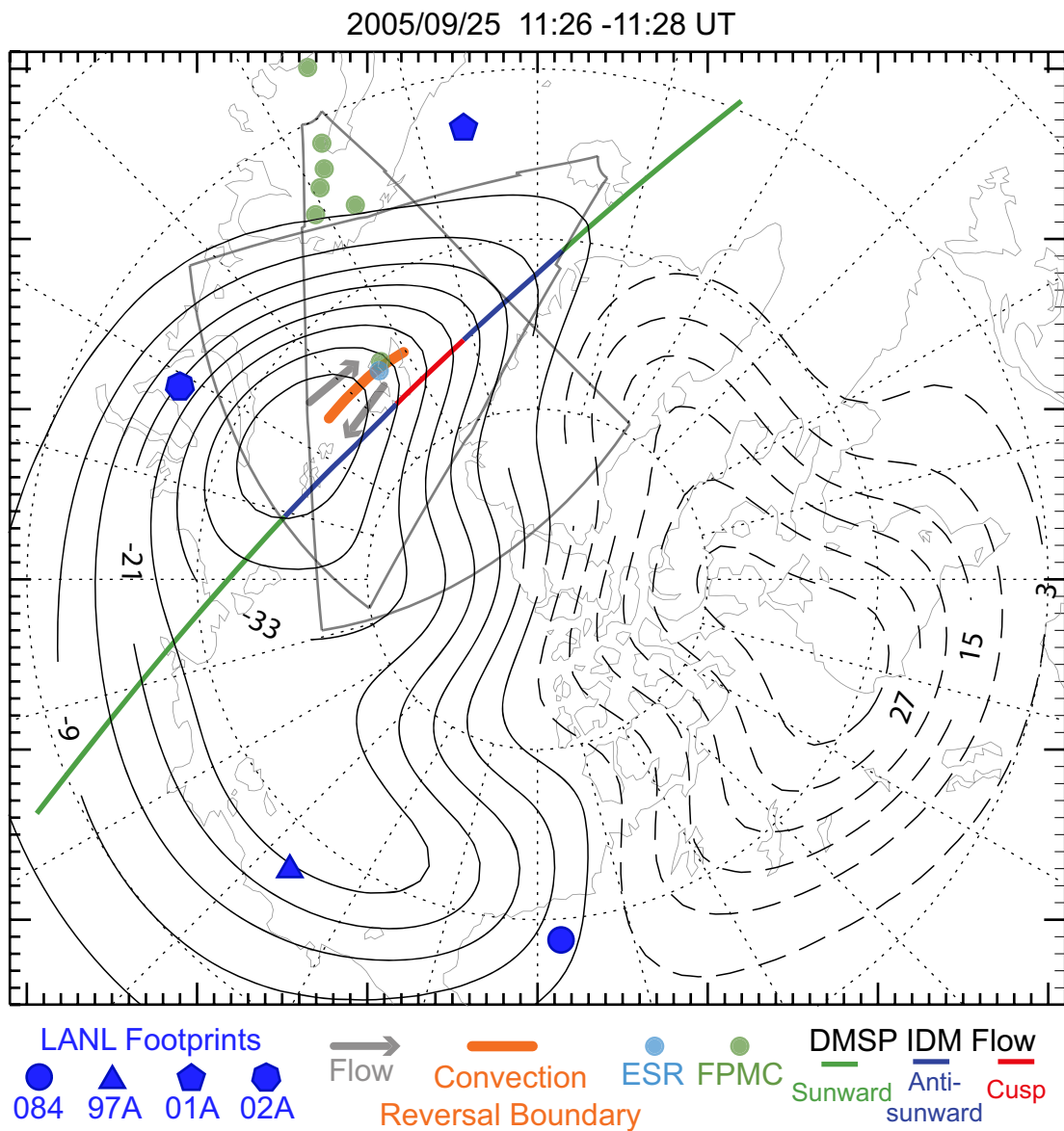


Figure 7.16: Schematic overview of instrument measurement regions and ionospheric flows following the period of pulsed ionospheric flows. Map Potential contours are represented by the continuous and dotted black lines. The fields of view of HAN and PYK are outlined with grey continuous lines and the ground track of DMSP-15 is shown by the green(sunward flow), blue (anti-sunward) and red (cusp) line. Ionospheric flow is indicated by the grey arrows either side of the convection reversal region shown in orange.

Distinct from the region 1 current system, the Birkeland currents generated in and around the cusp have been shown to contain significant substructure and be more variable than previous models of simple current pairs with a downward (upward) directed leading (trailing) edge (Marchaudon *et al.*, 2009). Neubert and Christiansen (2010) suggested that small-scale Birkeland currents in the cusp region may be orders of magnitude more intense than those seen in the OCB elsewhere. Those studies suggest that the field-aligned currents over Spitzbergen may have been highly variable. Ion upwelling and erratically structured electron density imply that field-aligned currents were indeed variable with respect to the position of the ESR.

At approximately the time that a dispersed ion signature, seen in DMSP-F15 spectra, placed the ESR deep within cusp region, the OCB began to retreat poleward. As the cusp began to migrate (fig. 7.7, HAN data), under the influence of night-side reconnection closing flux and contracting the polar cap, the now northward IMF was no longer driving the impulsive reconnection responsible for the PIFs and all that remained were PMRAFs, which are considered to be their fossil remnants (Davies *et al.*, 2002). At this time, electron temperature and density began to fall until the OCB passed over the ESR causing intense electron precipitation, which ceased upon complete traversal.

7.4.2 Correspondence of irregular pulsations to radar measurements

A number of authors have concluded that the unstructured Pc1-2 waves, so frequently associated with the cusp, are generated on its poleward edge (Engebretson *et al.*, 2009, Dyrud *et al.*, 1997, Menk *et al.*, 1992) or in the mantle region (Engebretson *et al.*, 2005). Using a closely spaced array, the latter authors noted the absence of waves, continuous or irregular, directly underneath the cusp.

The relatively broadband nature of the irregular pulsations registered at BAR suggests that they are Pi rather than unstructured Pc1-2. However, the band of peak spectral power, at a similar frequency to the Pc1 either side, suggests either that ionospheric filtering was taking place or underlying Pc1 were contributing to the total spectral power in that interval. Further investigation is clearly needed to draw any further conclusion on this point as, for example, the method of spectral analysis used

does not lend itself to identification of the spectral resonance structures that are indicative of ionospheric filtering in this frequency range.

The observation of Pc1 and possible IPDP at all FPMC stations implies a consistently stable ionosphere, capable of ducting ULF waves of the appropriate propagation mode. Waves of the aforementioned type are generally thought to propagate in the ionospheric duct in fast-magnetosonic mode (Manchester, 1966) as a result of ionospheric coupling of field line guided EMIC waves generated in the non-local magnetosphere (Fujita and Tamao, 1988). The energetic ion populations observed at geosynchronous orbit show that the waves may indeed have been generated in the ring current. It is unclear from the derived values of semi-major axis angle (seen in figure 12) whether the pulsations either side of the interval of enhanced ionospheric flow were generated by the same source population. Although, the pre- and post-PIF pulsations registered at most stations do exhibit a similar drift in orientation angle. The absence of continuous pulsations at all latitudes during the period of high latitude Pi may be indicative of a radial migration, caused by enhanced dayside reconnection, of source particles to a region of less favourable EMIC instability; the re-emergence of Pc signifying its return favourable instability. The morning Pc displayed little significant polarisation dominance; however, the pulsations following the period of pulsed reconnection exhibited the greatest left-hand polarisation (indicative of EMIC mode propagation) at L-shell values of $\sim 5.3 - 5.8$, suggesting a local ionospheric source region. The absence of irregular pulsations in all stations except BAR suggests that the irregular pulsations, in contrast to the band-limited waves, are locally generated and that they do not couple to ducted modes. Although the ubiquitous Pc appear to be suppressed during the period of high latitude Pi, there is no evidence here to suggest a causal relationship between the two phenomena. However, it is possible that enhanced dayside reconnection may be responsible for both.

Recently, Engebretson *et al.* (2009) have reported the absence of continuous and irregular pulsations in the footprint of the cusp. Using the POLAR satellite, these authors report Pc1-2 in the mantle region poleward of the cusp proper. They continued to show with auroral imagery that soft electron precipitation was coincident with these Pc1-2 and that Pi were only observed when energetic precipitation was significantly enhanced. The current observation agrees with these authors' in that no Pc1 was seen

within the cusp region or at least in its dusk flank. The increased electron density and elevated electron temperatures, concurrent with the final bursts of Pi, indicated that intense particle precipitation was occurring above Spitzbergen during those final bursts. However, the band integrated total power of the Pi was best correlated with the variation in upward ion velocity (correlation coefficient of 0.69, compared with a maximum correlation coefficient of 0.39 when correlated with other ESR parameters), which can respond to both ion and electron temperature enhancements (McCrea *et al.*, 2000).

Upward ion flows are frequently implicated in the generation of earthward travelling field-line guided EMIC waves. However, the broadband irregular nature of the currently observed pulsations does not support this mechanism in this case. The lack of consistent wave polarisation of the Pi registered at BAR, evidenced by the failure of the employed histogram fitting technique to derive a satisfactory result, further detracts from this possibility. This is unsurprising as the EMIC instability is inversely proportional to magnetic field strength, hence, is likely to occur at extremely high altitude. This requires the propagation firstly of the ions to altitudes of sufficiently low magnetic field strength then downward propagation of EMIC waves to the ionosphere by which time the newly reconnected field lines may have propagated poleward of the cusp proper.

Engebretson *et al.* (2005) showed that Pi “cusp noise” observed in situ by the POLAR satellite was absent in ground magnetometer data casting doubt on the ability of those waves to reach the ground. A conventional interpretation of the current Pi observations might be that they are the result of ionospheric conductivity modulation by the particle precipitation associated with small-scale pulsed reconnection Birkeland currents. Hosokawa *et al.* (2004) related Birkeland currents and magnetic field fluctuations in the range 0.2 Hz – 5 Hz, measured by the Ørsted satellite, to SWB enhancements along the dawn OCB. Birkeland current instabilities, magnetospheric Afvén waves and small-scale current inhomogeneity were considered yet no firm conclusions were drawn from these observations as to the nature of their relation.

Spectral width enhancement in SuperDARN backscatter is a highly contentious issue and its precise origin remains undetermined. Spectral Width Boundaries (SWBs)

are routinely used to distinguish regions of the ionosphere and overlying magnetosphere. In a statistical study of two periods covering the winter months of 1994 and the Autumn/winter months of 1996/1997, Villain *et al.* (2002) found that regions of high spectral widths (in excess of 350 m s^{-1}) are collocated with the LLBL/cusp/mantle region. These authors concluded that the spectral width characteristics observed could not be explained by geometric or instrumentation effects alone and that they must be indicative of magnetosphere-ionosphere coupling processes. In the formulation of a statistically based algorithm (not employed here) for SWB determination Chisham and Freeman (2003) determined the threshold for cusp backscatter to be as low $\sim 200 \text{ m s}^{-1}$. Many possible mechanisms have been proposed as the cause of SuperDARN spectral width enhancements, including: intense particle precipitation inducing strong spatial and temporal non-uniformity within backscatter targets (Baker *et al.*, 1995), Pc waves (Wright *et al.*, 2004) and small scale vortical structures generated by filamentary Birkeland currents (Huber and Sofko, 2000, Schiffler *et al.*, 1997).

Values of spectral width close to Spitzbergen were generally elevated during the times of Pi. The largest sustained period of high spectral width occurred during the final series of Pi and intense electron precipitation, however no electron precipitation was observed during the initial sequence of PIFs. This suggests that both the small scale vortical flows associated with transient reconnection and intense precipitation may be involved in broadening cusp spectra.

7.5 Summary

This chapter has presented northern hemisphere multi-instrument observations of a period surrounding a geomagnetic substorm, in which irregular pulsations measured on the ground were seen to correspond to both particle precipitation and coherent scatter radar spectral width enhancements.

Utilising the ESR and SuperDARN, the open-closed field line boundary was observed to migrate equatorward, in response to enhanced dayside reconnection, and then poleward as nightside reconnection initiated. The position and flow direction of the cusp responded to changes in the IMF clock angle in an expected manner, shifting

duskward under the influence of strong B_y negative. Pulsed ionospheric flows were observed during the substorm growth phase, whereas poleward moving radar auroral forms were observed post onset. The DMSP-F15 satellite was used to place the location of ESR and BAR southward of the cusp proper. Pc1-2 pulsations were observed at all latitudes throughout the entire analysis interval, with the exception of the period of enhance day-side reconnection. Geosynchronous satellite data showed them to have an equatorial magnetospheric source; hence, their ubiquity demonstrated the stability of the ionospheric duct. Dynamic histogram fitting was used to derive Pc1-2 polarisation parameters, revealing a drift in polarisation ellipse orientation that was common across the enhanced reconnection gap. The continuous pulsation that re-emerged following that gap, displayed significantly left-handed polarisation at an L-shell value of ~ 5.1 , suggesting that the ionospheric footprint of their magnetospheric source region was in close proximity.

Irregular pulsations were recorded exclusively by the BAR induction coil, which shares its integration volume with the ESR. These pulsations were seen to correspond well with local SuperDARN spectral width enhancements and with both ion and electron vertical transport. Small scale vortical flows associated with filamentary Birkeland currents during pulsed reconnection and intense localised particle precipitation are implicated in the generation of both spectral width enhancements and irregular pulsations.

Chapter 8. Summary and Further Work

8.1 Summary

This thesis has investigated the behaviour of ULF pulsations in frequency band 0.1 -5 Hz and their relationship to solar-terrestrial phenomena.

In Chapter five, two techniques for analysing Pc1-2 magnetometer observations have been assessed and it has been shown that for routine data processing the Complex Input Spectral Analysis method is an adequate choice. When processing large datasets, the saving in computation offered by the CISA technique over that of spectral matrix analysis outweighs the loss of information on individual components of magnetic field variation. A novel application of spectral power thresholding has also been introduced. However, given that polarisation and inter-station cross-phase parameters often vary at a greater rate within continuous pulsations than between adjacent ones, it has been concluded that further work must be conducted for an adequate automated algorithm to be found that satisfactorily isolates discrete events. Subsequently, a manual event selection procedure was created, consisting of a graphical interface allowing precise frequency elements to be selected on the basis of visual continuity of polarisation parameters and spectral cross-phase. This procedure allowed the extraction of discrete adjacent pulsations with previously unachievable resolution. Polarisation parameters for each discrete event have been derived with a power weighted histogram fitting procedure that has proven to produce values that are more representative than previously employed methods. This same procedure has been applied to spectral cross-phase analysis, deriving pulsation Time Delay Of Arrival between a network of ground magnetometer stations. The usefulness of these TDOAs has been demonstrated with a simple triangulation scheme that was shown to be capable of suggesting independent source regions for discrete simultaneous pulsations of differing frequency.

A measure of the periodic nature of a pulsation has been introduced that objectively assigns a value of monochromatic structuredness to a given event. This

parameter allows a quantitative assessment of the level of structuring of pulsation, replacing the subjective visual method used in previous studies.

The occurrence and polarisation characteristics of Pc1-2 Pulsations have been investigated in a statistical study of unprecedented detail included in chapter six. A full year of pulsation magnetometer data from 6 stations of the Finnish Pulsation Magnetometer Chain was analysed, from which diurnal, annual and latitudinal distributions were derived. Occurrence and polarisation agreement was found with satellite studies and through the representation of these distributions in box and whisker format, some support was found for the suggestion that the Ionospheric Alfvén Resonator plays a role in the filtration of signal through the ionosphere. The agreement of the current diurnal ellipticity distribution with satellite observation casts doubt on the assertion that the handedness of a pulsation on the ground is indicative of its distance from the ionospheric source region.

The Geomagnetic storm-time behaviour of Pc1-2 pulsations was investigated and it was found that unstructured pulsations are more probable during storm times increasingly so at high latitude. The diurnal pulsation evolution throughout the storm cycle was found to be in agreement with the suggestion of their association with plasmapheric plumes forming in the afternoon sector during storm recovery.

In chapter seven, high-latitude irregular pulsations were investigated during the course of a geomagnetic substorm. This study combined ground-based magnetometer and radar measurements with solar wind and magnetospheric observations to examine the wave-particle interactions associated with transient reconnection. SuperDARN coherent radar observations of Pulsed Ionospheric Flows within a period of enhanced dayside reconnection. EISCAT incoherent scatter radar measurements showed ion upwelling and electron precipitation occurring in the vicinity of the high-latitude magnetometer's integration volume. DMSP particle data placed the magnetospheric cusp slightly to the north of the observed high latitude pulsations, with Map Potential global convection map placing the ground stations in the duskward flank of the dayside convection throat. Continuous pulsations were also observed at all stations of the Finnish Pulsation Magnetometer Chain, which were seen to cease during the period of enhanced reconnection. This cessation may be attributed to the radial migration of

magnetospheric source particles to regions of lower instability during the substorm cycle. These observations provide support for the association of high latitude irregular pulsations, in the frequency band 0.1 Hz -2 Hz, with enhanced Field Aligned Currents and SuperDARN spectral width enhancements seen in the flanks of the cusp proper.

8.2 Further work

The studies conducted in this thesis have predominantly considered Pc1-2 behaviour observed from the ground and it is abundantly clear that much could be gained by including in situ magnetospheric data. The techniques honed throughout the course of these studies provide a set of tools with which further investigation may be made using the multitude of satellite observations currently in existence and those that are upcoming.

The ability to discern consistently pulsations of similar frequency yet independent origin would be a great use to the formation and verification of pearl generation theory; hence, a detection algorithm is a must for future ground based studies. A continuation of the search for an automated pulsation detection algorithm may find success by treating dynamic spectra as images and employing pattern recognition or “edge detection” techniques e.g. Ziou and Tabbone (1998), Kunt, (2003).

A wealth of Cluster satellite - Pc1-2 studies exist, e.g. Engbretson *et al.* (2007); however, ground-satellite conjugate studies using Cluster are few. Cluster’s tetrahedral configuration ideally suits it to isolating the EMIC source region or at least the field-line along which they are flowing. Not only would such information provide further insight into the high-latitude phenomena similar to that presented in chapter 7 but the energetic particle instruments onboard may clarify the frequency behaviour of Pc1-2 on the ground that has driven much pearl generation theory. As a first step to such a study, 18 potential events have been isolated for the year of 2007 and are awaiting analysis. The Cluster mission’s extension to 2014 is an encouraging acknowledgement of the value of Cluster science past, present and future.

An obvious extension to the work in chapter six would be the inclusion of data from the full digital archive of the FPMC, which now consists of observations spanning an entire solar cycle. Such a study may allow a more accurate determination of the storm time Pc1-2 distribution evolution and subsequently shed light on contribution of EMIC waves to the relaxation of the ring current. Similar statistical ground-satellite studies would be of great interest, given that missions such as the Fast Auroral SnapshoT (FAST) have accumulated vast overlapping datasets that are yet to be exploited.

The current inability to determine the ionospheric source region of Pc1-2 observed on the ground with an acceptable degree of accuracy hampers ground-satellite conjugate studies, although many attempts, with varying degrees of success, have been made in the past several decades, no recent studies have been conducted using digital processing techniques. Previous studies have used wavepacket (pearl) envelope time delays between spaced stations to calculate group velocities or have assumed that the semi-major axis angle aligns with the direction of propagation at large distances from their ionospheric source. Neither method is applicable to regions close to the source or multifarious pulsations. In an attempt to assess the viability of using phase velocity as a tool for source location, I have created an iterative trilateration procedure based on the intersection of expanding circles on the surface of a spherical ionosphere. However, as with previous studies it still requires a singular well-behaved pulsation to provide a group delay. Extensions to this study may include the assessment of the use of spectral cross-phase to determine delay and the inclusion of empirical ionospheric data to create velocity maps.

With the growing number of isolated observations that support Equatorial Growth Modulation models of pearl formation, I believe that a logical step towards confirmation of such theories is a statistical comparison of Pc4-5 occurrence with Pc1-2 repetition periods. As a first step towards this goal, I have begun analysing IMAGE magnetometer data using the cross-phase method of Menk *et al.* (2004) for the period of the study presented in chapter in six.

Exciting times lie ahead for radiation belt and ring current studies. With the introduction of several low-latitude radars to the SuperDARN network and the

upcoming Radiation Belt Storm Probe (RBSP) mission, investigations of energetic ring current particles have never looked so promising. In addition to the investigation of storm dynamics, these lower-latitude radars, coupled with the high-resolution TMS radar mode (Yukimatu and Tsutsumi, 2002) offer an excellent opportunity to observe Pc1-2 waves as they propagate through the ionosphere. The effects of Pc1-2 on radar backscatter are still largely unknown and such investigations may provide insight in to this longstanding quandary.

The twin RBSP satellites, due to launch in mid 2012, are tasked with shedding light on the dynamical processes in the radiation belts and, subsequently, are equipped with a full suite of appropriate particle and field instruments. The possibility of conjugate satellite-radar-ground magnetometer studies is truly exhilarating.

Appendix A. Vector Identities

$$\nabla^2 \mathbf{A} = \nabla(\nabla \cdot \mathbf{A}) - \nabla \wedge (\nabla \wedge \mathbf{A}). \quad (\text{A.1})$$

$$\frac{1}{2} \nabla(\mathbf{A} \cdot \mathbf{A}) = \mathbf{A} \wedge (\nabla \wedge \mathbf{A}) + (\mathbf{A} \cdot \nabla) \mathbf{A}. \quad (\text{A.2})$$

$$\nabla \wedge (\mathbf{A} \wedge \mathbf{B}) = \mathbf{A}(\nabla \cdot \mathbf{B}) - \mathbf{B}(\nabla \cdot \mathbf{A}) + (\mathbf{B} \cdot \nabla) \mathbf{A} - (\mathbf{A} \cdot \nabla) \mathbf{B} \quad (\text{A.3})$$

$$\nabla \wedge (\mathbf{A} + \mathbf{B}) = \nabla \wedge \mathbf{A} + \nabla \wedge \mathbf{B}.$$

Appendix B. IMAGE Magnetometer Locations

Station	Code	Geographic		Geomagnetic*	
		Latitude	Longitude	Latitude	Longitude
Ny Ålesund	NAL	78.92	11.95	75.25	112.08
Longyearbyen	LYR	78.2	15.82	75.12	113
Hornsund	HOR	77	15.6	74.13	109.59
Hopen Island	HOP	76.51	25.01	73.06	115.1
Bear Island	BJN	74.5	19.2	71.45	108.07
Nordkapp	NOR	71.09	25.79	67.73	109.39
Sørøya	SOR	70.54	22.22	67.34	106.17
Kevo	KEV	69.76	27.01	66.32	109.24
Tromsø	TRO	69.66	18.94	66.64	102.9
Masi	MAS	69.46	23.7	66.18	106.42
Andenes	AND	69.3	16.03	66.45	100.37
Kilpisjärvi	KIL	69.06	20.77	65.94	103.8
Ivalo	IVA	68.56	27.29	65.1	108.57
Abisko	ABK	68.35	18.82	65.3	101.75
Leknes	LEK	68.13	13.54	65.4	97.5
Muonio	MUO	68.02	23.53	64.72	105.22
Lovozero	LOZ	67.97	35.08	64.23	114.49
Kiruna	KIR	67.84	20.42	64.69	102.64
Sodankylä	SOD	67.37	26.63	63.92	107.26
Pello	PEL	66.9	24.08	63.55	104.92
Dønna	DON	66.11	12.5	63.38	95.23
Rørvik	RVK	64.94	10.98	62.23	93.31
Lycksele	LYC	64.61	18.75	61.44	99.29
Oulujärvi	OUJ	64.52	27.23	60.99	106.14
Mekrijärvi	MEK	62.77	30.97	59.1	108.45
Hankasalmi	HAN	62.25	26.6	58.69	104.54
Dombås	DOB	62.07	9.11	59.29	90.2
Solund	SOL	61.08	4.84	58.53	86.26
Nurmijärvi	NUR	60.5	24.65	56.89	102.18
Uppsala	UPS	59.9	17.35	56.51	95.84
Karmøy	KAR	59.21	5.24	56.43	85.67
Tartu	TAR	58.26	26.46	54.47	102.89

* 2007 Corrected Geomagnetic Coordinates

References

Alfven, H. Existence of electromagnetic-hydrodynamic waves, *Nature*, 150, 405-406, doi:10.1038/150405d0, 1942.

Alperovich, L S, Fedorov, E.N. Hydromagnetic Waves in the Magnetosphere and the Ionosphere, Springer Verlag , 2007.

Anderson, B.J., Erlandson, R.E., Zanetti, L.J. A Statistical Study of Pc 1-2 Magnetic Pulsations in the Equatorial Magnetosphere: 1. Equatorial Occurrence Distributions, *J. Geophys. Res.*, 97 , 3075-3088, doi:10.1029/91JA02706, 1992a.

Anderson, B.J., Erlandson, R.E., Zanetti, L.J. A Statistical Study of Pc 1-2 Magnetic Pulsations in the Equatorial Magnetosphere: 2. Wave Properties, *J. Geophys. Res.*, 97, 3075-3088, doi:10.1029/91JA02697 , 1992b.

Anderson, B.J., Hamilton, D.C., Electromagnetic ion cyclotron waves stimulated by modest magnetospheric compressions, *J. Geophys. Res.*, 98, 11369-11382, doi:10.1029/93JA00605 , 1993.

Anderson, B.J., Recent observations of electromagnetic ion cyclotron waves in space, *Adv. Space Res.*, 17, 41-50, doi:10.1016/0273-1177(95)00693-9, 1996.

André, R., Pinnock, M., Rodger, A.S., On the SuperDARN autocorrelation function observed in the ionospheric cusp, *Geophys. Res. Lett.*, 26, 3353-3356, 1999.

Appleton, E.V., Barnett, M.A.F., Local reflection of wireless waves from the upper atmosphere. *Nature*. 115, 333-334, doi:10.1038/115333a0, 1925.

Appleton, S.E., Piggott, W.R., Ionospheric absorption measurements during a sunspot cycle, *J. Atmos. Solar-Terr. Phys.*, 5, 141-172, doi:10.1038/115333a0, 1954.

Arthur, C.W., McPherron, R.L., Means, J.D., A comparative study of three techniques for using the spectral matrix in wave analysis, *Radio Sci.*, 11, 833-845, doi:10.1029/RS011i010p00833, 1976.

Baker, K.B., Dudeney, J.R., Greenwald, R.A., Pinnock, M., Newell, P.T., Rodger, A.S., Mattin, N., Meng, C.I., HF radar signatures of the cusp and low-latitude boundary layer, *J. Geophys. Res.*, 100, 7671-7695, doi:10.1029/94JA01481 , 1995.

Bame, S.J., McComas, D.J., Thomsen, M.F., Barraclough, B.L., Elphic, R.C., Glore, J.P., Gosling, J.T., Chavez, J.C., Evans, E.P., Wymer, F.J., Magnetospheric plasma analyzer for spacecraft with constrained resources, *Rev. Sci. Instrum.*, 64, 1026-1033, doi: 10.1063/1.1144173, 1993.

Bates, H.F., Albee, P.R., Aspect sensitivity of F-layer HF backscatter echoes. *J. Geophys. Res.*, 75, 165-170, doi:10.1029/JA075i001p00165 , 1970.

- Baumjohann, W., Paschmann, G., Lühr, H., Characteristics of high-speed ion flows in the plasma sheet, *J. Geophys. Res.*, 95, 3801-3809, doi:10.1029/JA095iA04p03801, 1997.
- Belian, R.D., Gisler, G.R., Cayton, T., Christensen, R., High-Z energetic particles at geosynchronous orbit during the great solar proton event series of October 1989, *J. Geophys. Res.*, 97, 16897-16906, doi:10.1029/92JA01139 , 1992.
- Benioff, H., Observations of geomagnetic fluctuations in the period range 0.3 to 120 seconds. *J. Geophys. Res.*, 65, 1413-1422, doi:10.1029/JZ065i005p01413, 1960.
- Bilitza, D., Reinisch, B.W., International reference ionosphere 2007: Improvements and new parameters, *Adv. Space Res.*, 42, 599-609, doi:10.1016/j.asr.2007.07.048 , 2008.
- Born, M, Wolf, E., Bhatia, A.B., Principles of optics, Pergamon press Oxford, 1959.
- Bortnik, J., Cutler, J.W., Dunson, C., Bleier, T.E., An automatic wave detection algorithm applied to Pc1 pulsations, *J. Geophys. Res.*, 112, A04204, doi:10.1029/2006JA011900, 2007.
- Bortnik, J., Cutler, J.W., Dunson, C., Bleier, T.E., The possible statistical relation of Pc1 pulsations to Earthquake occurrence at low latitudes, *Ann. Geophys.*, 26, 2825–2836, doi:10.5194/angeo-26-2825-2008, 2008a.
- Bortnik, J., Cutler, J.W., Dunson, C., Bleier, T.E., McPherron, R.L., Characteristics of low latitude Pc1 pulsations during geomagnetic storms, *J. Geophys. Res.*, 113, A04201, doi:10.1029/2007JA012867, 2008b.
- Bossen, M., McPherron, R., Russell, C., A statistical study of Pc 1 magnetic pulsations at synchronous orbit, *J. Geophys. Res.*, 81, 6083-6091, doi:10.1029/JA081i034p06083, 1976.
- Burckle, L., Grissino-Mayer, H.D., Stradivari, violins, tree rings, and the Maunder Minimum: a hypothesis, *Dendrochronologia*, 21, 41-45, doi:10.1078/1125-7865-00033 , 2003.
- Burton, R.K., McPherron, R.L., Russell, C.T., An empirical relationship between interplanetary conditions and Dst, *J. Geophys. Res.*, 80, 4204–4214, doi:10.1029/JA080i031p04204 , 1975.
- Campbell, W.H., Thornberry, T.C., Propagation of Pc 1 hydromagnetic waves across North America, *J. Geophys. Res.*, 77, 1941-1950, doi:10.1029/JA077i010p01941, 1972.
- Cerisier, J.C., Senior, C., Merge: a FORTRAN program, Tech rep, Centre d'Etude des Environnements Terrestres et Planetaires, 1994.
- Chapman, S., Ferraro, V.C.A., A New Theory of Magnetic Storms. *Nature*. 126, 129-130, doi:10.1038/126129a0, 1930.

Chisham, G. and Orr, D., A statistical study of the local time asymmetry of Pc 5 ULF wave characteristics observed at midlatitudes by SAMNET, *J. Geophys. Res.*, 102, 24339-24350, doi:10.1029/97JA01801, 1997.

Chisham, G., Freeman, M.P., A technique for accurately determining the cusp-region polar cap boundary using SuperDARN HF radar measurements, *Ann. Geophys.*, 21, 983-996, doi:10.5194/angeo-21-983-2003, 2003.

Chisham, G., Lester, M., Milan, S.E., Freeman, M.P., Bristow, W.A., Grocott, A., McWilliams, K.A., Ruohoniemi, J.M., Yeoman, T.K., Dyson, P.L., A decade of the Super Dual Auroral Radar Network (SuperDARN): scientific achievements, new techniques and future directions, *Surv. Geophys.*, 28, 33-109, DOI: 10.1007/s10712-007-9017-8, 2007.

Chisham, G., Yeoman, T.K., Sofko, G.J., Mapping ionospheric backscatter measured by the SuperDARN HF radars—Part 1: A new empirical virtual height model, *Ann. Geophys.*, 26, 823-841, doi:10.5194/angeo-26-823-2008, 2008.

Cliwer, E.W., Feynman, J., Garrett, H.B., An estimate of the maximum speed of the solar wind, 1938-1989, *J. Geophys. Res.*, 95, 17103-17112, doi:10.1029/JA095iA10p17103, 1990.

Cooley, J.W., Tukey, J.W., An algorithm for the machine calculation of complex Fourier series. *Math. Comp.*, 19, 297-301, 1965.

Cornwall, J.M., Cyclotron instabilities and electromagnetic emission in the ultra low frequency and very low frequency ranges, *J. Geophys. Res.*, 70, 61-69, doi:10.1029/JZ070i001p00061, 1965.

Cowley, S.W.H., Morelli, J.P., Lockwood, M., Dependence of convective flows and particle precipitation in the high-latitude dayside ionosphere on the X and Y components of the interplanetary magnetic field, *J. Geophys. Res.*, 96, 5557-5564, doi:10.1029/90JA02063, 1991.

Daglis, I.A., Thorne, R.M., Baumjohann, W., Orsini, S., The terrestrial ring current: Origin, formation, and decay, *Rev. Geophys.*, 37, 407-438, doi:10.1029/1999RG900009, 1999.

Davies, J.A., Yeoman, T.K., Rae, I.J., Milan, S.E., Lester, M., Lockwood, M., McWilliams, A., Ground-based observations of the auroral zone and polar cap ionospheric responses to dayside transient reconnection, *Ann. Geophys.*, 20, 781-794, doi:10.5194/angeo-20-781-2002, 2002.

Davies, K., A nomenclature for oblique ionospheric soundings and ray tracing, *Radio Sci.*, 2, 1395-1396, 1967.

Davis, T.N., Sugiura, M., Auroral electrojet activity index AE and its universal time variations, *J. Geophys. Res.*, 71, 785-801, doi:10.1029/JZ071i003p00785, 1966.

- Demekhov, A.G., Recent progress in understanding Pc1 pearl formation, *J. Atmos. Solar-Terr. Phys.*, 69, 1609-1622, doi:10.1016/j.jastp.2007.01.014, 2007.
- Demekhov, A.G., Trakhtengerts, V.Y., Bösinger, T., Pc 1 waves and ionospheric Alfvén resonator: Generation or filtration?. *Geophys. Res. Lett.*, 27, 3805-3808, doi:10.1029/2000GL000126, 2000.
- Dessler, A.J., Parker, E.N., Hydromagnetic theory of geomagnetic storms, *J. Geophys. Res.*, 64, 2239-2252, doi:10.1029/JZ064i012p02239, 1959.
- Dowden, R.L., Micropulsation mode" propagation in the magnetosphere, *Planet. Space Sci.*, 13, 761-772, doi:10.1016/0032-0633(65)90113-3, 1965.
- Dungey, J.W., Interplanetary Magnetic Field and the Auroral Zones. *Phys. Rev. Lett.*, 6, 47-48, doi:10.1103/PhysRevLett.6.47, 1961.
- Dyrud, L.P., Engebretson, M.J., Posch, J.L., Hughes, W.J., Fukunishi, H., Arnoldy, R.L., Newell, P.T., Horne, R.B., Ground observations and possible source regions of two types of Pc 1-2 micropulsations at very high latitudes, *J. Geophys. Res.*, 102, 27011-21027, doi:10.1029/97JA02191, 1997.
- Engebretson, M.J., Peterson, W.K., Posch, J.L., Klatt, M.R., Anderson, B.J., Russell, C.T., Singer, H.J., Arnoldy, R.L., Fukunishi, H., Observations of two types of Pc 1–2 pulsations in the outer dayside magnetosphere, *J. Geophys. Res.*, 107, A20, 1451, doi:10.1029/2001JA000198, 2002.
- Engebretson, M.J., Onsager, T.G., Rowland, D.E., Denton, R.E., Posch, J.L., Russell, C.T., Chi, P.J., Arnoldy, R.L., Anderson, B.J., Fukunishi, H., On the source of Pc1-2 waves in the plasma mantle, *J. Geophys. Res.*, 110, A06201, doi:10.1029/2004JA010515, 2005.
- Engebretson, M.J., Moen, J., Posch, J.L., Lu, F., Lessard, M.R., Kim, H., Lorentzen, D.A., Searching for ULF signatures of the cusp: Observations from search coil magnetometers and auroral imagers in Svalbard, *J. Geophys. Res.*, 114, A06217, doi:10.1029/2009JA014278, 2009.
- Engebretson, M., Lessard, M., Bortnik, J., Green, J., Horne, R., Detrick, D., Weatherwax, A., Manninen, J., Petit, N., Posch, J., Pc1–Pc2 waves and energetic particle precipitation during and after magnetic storms: Superposed epoch analysis and case studies. *J. Geophys. Res.*, 113, A01211, doi:10.1029/2007JA012362, 2008.
- Erlandson, R.E., Mursula, K., Bösinger, T., Simultaneous ground-satellite observations of structured Pc 1 pulsations, *J. Geophys. Res.*, 101, 27149-27156, doi:10.1029/96JA02645, 1996.
- Erlandson, R.E., Anderson, B.J., Zanetti, L.J., Viking magnetic and electric field observations of periodic Pc 1 waves- Pearl pulsations, *J. Geophys. Res.*, 97, 14823-14832, doi:10.1029/92JA00838, 1992.

Erlandson, R.E., Anderson, B.J., Pc 1 waves in the ionosphere: A statistical study, *J. Geophys. Res.*, 101, 7843-7857, doi:10.1029/96JA00082, 1996.

Erlandson, R.E., Ukhorskiy, A.J., Observations of electromagnetic ion cyclotron waves during geomagnetic storms: Wave occurrence and pitch angle scattering, *J. Geophys. Res.*, 106, 3883-3895, doi:10.1029/2000JA000083, 2001.

Fear, R.C., Milan, S.E., Fazakerley, A.N., Fornaçon, K.H., Carr, C.M., Dandouras, I., Simultaneous observations of flux transfer events by THEMIS, Cluster, Double Star and SuperDARN: Acceleration of FTEs, *J. Geophys. Res.*, 114, A10213, doi:10.1029/2009JA014310, 2009.

Fejer, B.G., Kelley, M.C., Ionospheric irregularities, *Rev. Geophys.*, 18, 401-454, doi:10.1029/RG018i002p00401, 1980.

Feygin, F.Z., Prikner, K., Kangas, J., PC1 with a broad frequency spectrum—"Goose pulsations", *Studia Geophysica et Geodaetica*, 53, 519-536, doi: 10.1007/s11200-009-0037-3, 2009.

Frank, L.A., Ackerson, K.L., Paterson, W.R., Lee, J.A., English, M.R., Pickett, G.L., The comprehensive plasma instrumentation (CPI) for the GEOTAIL spacecraft, *J. Geomag. Geoelectr.*, 46, 23-37, 1994.

Franz, H., Sharer, P., Ogilvie, K., Desch, M., WIND nominal mission performance and extended mission design, 1998.

Fraser, B.J., Propagation of Pcl micropulsations in a proton-helium magnetosphere, *Planet. Space Sci.*, 20, 1883-1884, doi:10.1016/0032-0633(72)90121-3, 1972.

Fraser, B.J., Ionospheric duct propagation and Pc 1 pulsation sources, *J. Geophys. Res.*, 80, 2790-2796, doi:10.1029/JA080i019p02790, 1975a.

Fraser, B.J., Polarization of Pc 1 pulsations at high and middle latitudes, *J. Geophys. Res.*, 80, 2707-2807, doi:10.1029/JA080i019p02797, 1975b.

Fraser, B.J., Observations of ion cyclotron waves near synchronous orbit and on the ground, *Space Sci. Rev.*, 42, 357-374, doi: 10.1007/BF00214993, 1985.

Fraser, B.J., Singer, H.J., Hughes, W.J., Wygant, J.R., Anderson, R.R., Hu, Y.D., CRRES Poynting vector observations of electromagnetic ion cyclotron waves near the plasmapause, *J. Geophys. Res.*, 101, 15331-15343, doi:10.1029/95JA03480, 1996.

Fraser, B.J., Singer, H.J., Adrian, M.L., Gallagher, D.L., Thomsen, M.F., The relationship between plasma density structure and EMIC waves at geosynchronous orbit, *Geophysical monograph*, 159, 55-70, 2005.

Fraser, B., Webster, D., ULF Goniometer techniques for locating Pc 1 geomagnetic pulsation sources, *Ann. Telecommunic.*, 34, 237-242, doi: 10.1007/BF03004201, 1979.

- Fraser, B.J., Nguyen, T.S., Is the plasmapause a preferred source region of electromagnetic ion cyclotron waves in the magnetosphere?, *J. Atmos. Solar-Terr. Phys.*, 63, 1225-1247, doi:10.1016/S1364-6826(00)00225-X, 2001.
- Fraser-Smith, A.C., Some statistics on Pc1 geomagnetic micropulsation occurrence at middle latitudes: Inverse relation with sunspot cycle and semiannual period, *J. Geophys. Res.*, 75, 4735-4745, doi:10.1029/JA075i025p04735, 1970.
- Fraser-Smith, A.C., Chevron frequency structure in Pc 1 geomagnetic pulsations, *Geophys. Res. Lett.*, 4, 53-56, doi:10.1029/GL004i001p00053, 1977.
- Fraser-Smith, A.C., ULF/Lower ELF electromagnetic field measurements in the polar caps, *Rev. Geophys.*, 20, 497-512, doi:10.1029/RG020i003p00497, 1982.
- Fujita, S., Tamao, T., Duct propagation of hydromagnetic waves in the upper ionosphere, 1, Electromagnetic field disturbances in high latitudes associated with localized incidence of a shear Alfvén wave, *J. Geophys. Res.*, 93, 14665-14673, doi:10.1029/JA093iA12p14665, 1988.
- Fukunishi, H., TOYA, T., KOIKE, K., KUWASHIMA, M., KAWAMURA, M., Classification of hydromagnetic emissions based on frequency-time spectra, *J. Geophys. Res.*, 86, 9029-9039, doi:10.1029/JA086iA11p09029, 1981.
- Gail, W., Theory of electromagnetic cyclotron wave growth in a time-varying magnetoplasma, *J. Geophys. Res.*, 95, 19089-19097, doi:10.1029/JA095iA11p19089, 1990.
- Gary, S.P., Winske, D.A.N., Simulations of ion cyclotron anisotropy instabilities in the terrestrial magnetosheath, *J. Geophys. Res.*, 98, 9171-9179, doi:10.1029/93JA00272, 1993.
- Gary, S.P., Electromagnetic ion/ion instabilities and their consequences in space plasmas-A review, *Space Sci. Rev.*, 56, 373-415 1991.
- Goertz, C.K., Nielsen, E., Korth, A., Glassmeier, K.H., Haldoupis, C., Hoeg, P., Hayward, D., Observations of a possible ground signature of flux transfer events, *J. Geophys. Res.*, 90, 4069-4078, doi:10.1029/JA090iA05p04069, 1985.
- Gonella, J., A rotary-component method for analysing meteorological and oceanographic vector time series, *Deep Sea Research and Oceanographic Abstracts*, 19, 833-846, doi:10.1016/0011-7471(72)90002-2, 1972.
- Gonzalez, W.D., Joselyn, J.A., Kamide, Y., Kroehl, H.W., Rostoker, G., Tsurutani, B.T., Vasyliunas, V.M., What is a geomagnetic storm?, *J. Geophys. Res.*, 99, 5771-5792, doi:10.1029/93JA02867, 1994.
- Göpel, W, Boll, R., Ricolfi, T., Grandke, T., Bau, H.H., Wagner, E., Meixner, H., Sensors: a comprehensive survey. Cumulative index. VCH, 1996.

Greenwald, R.A., Weiss, W., Nielsen, E., Thomson, N.R., STARE- A new radar auroral backscatter experiment in northern Scandinavia, *Radio Sci.*, 13, 1021-1039, doi:10.1029/RS013i006p01021, 1978.

Greenwald, R.A., Baker, K.B., Dudeney, J.R., Pinnock, M., Jones, T.B., Thomas, E.C., Villain, J.P., Cerisier, J.C., Senior, C., Hanuise, C., DARN/SuperDARN A global view of the dynamics of high-latitude convection, *Space Sci. Rev.*, 71, 761-796, DOI: 10.1007/BF00751350, 1995a.

Greifinger, C., Greifinger, P.S., Theory of hydromagnetic propagation in the ionospheric waveguide, *J. Geophys. Res.*, 73, 7473-7490, doi:10.1029/JA073i023p07473, 1968.

Greifinger, P., Micropulsations from a finite source, *J. Geophys. Res.*, 77, 2392-2396, doi:10.1029/JA077i013p02392, 1972.

Guglielmi, A., Kangas, J., Potapov, A., Quasiperiodic modulation of the Pc1 geomagnetic pulsations: An unsettled problem, *J. Geophys. Res.*, 106, 25847-25855, doi:10.1029/2001JA000136, 2001.

Guglielmi, A., Kangas, J., Kultima, J., Potapov, A., Solar wind dependence of the Pc1 wave activity, *Adv. Space Res.*, 36, 2413-2416, doi:10.1016/j.asr.2003.11.024, 2005.

Guglielmi, A., Potapov, A., Matveyeva, E., Polyushkina, T., Kangas, J., Temporal and spatial characteristics of Pc1 geomagnetic pulsations, *Adv. Space Res.*, 38, 1572-1575, doi:10.1016/j.asr.2003.11.024, 2006.

Guglielmi, A., Kangas, J., Pc1 waves in the system of solar-terrestrial relations: New reflections, *J. Atmos. Solar-Terr. Phys.*, 69, 1635-1643, doi:10.1016/j.jastp.2007.01.015, 2007.

Guglielmi, A.V., Pokhotelov, O.A., Geoelectromagnetic waves, 1996.

Haaland, S., Paschmann, G., Sonnerup, B.U., O.: Comment on "A new interpretation of Weimer et al.'s solar wind propagation delay technique" by Bargatze et al., *J. Geophys. Res.*, 111, A06102, doi:10.1029/2005JA011376 2006.

Haerendel, G., Paschmann, G., Sckopke, N., Rosenbauer, H., Hedgecock, P.C., The frontside boundary layer of the magnetosphere and the problem of reconnection, *J. Geophys. Res.*, 83, 3195-3216, doi:10.1029/JA083iA07p03195, 1978.

Hale, G.E., On the Probable Existence of a Magnetic Field in Sun-Spots, *Astrophysical Journal*. 28, 315-343, 1908.

Hanuise, C., Villain, J.P., Gresillon, D., Cabrit, B., Greenwald, R.A., Baker, K.B., Interpretation of HF radar ionospheric Doppler spectra by collective wave scattering theory, 11, 29-39, 1993.

Harang, L., Oscillations and vibrations in magnetic records at high-latitude stations, *Terr. Magn. Atmos. Electr.*, 41, 329-336, doi:10.1029/TE041i004p00329, 1936.

- Hardy, D.A., Schmitt, L.K., Gussenhoven, M.S., Marshall, F.J., Yeh, H.C., Shumaker, T.L., Hube, A., Pantazis, J., Precipitating electron and ion detectors (SSJ/4) for the block 5D/flights 6-10 DMSP satellites: Calibration and data presentation, *Rep. AFGL-TR-84*. 317, 1984.
- Heacock, R.R., Hessler, V.P., Polarization characteristics of Pc 1 micropulsations at College, *Planet. Space Sci.*, 15, 1361-1364, doi:10.1016/0032-0633(67)90110-9, 1967.
- Heacock, R.R., Hessler, V.P., Pearl-type micropulsations associated with magnetic storm sudden commencements, *J. Geophys. Res.*, 70, 1103-1111, doi:10.1029/JZ070i005p01103 1965.
- Heacock, R.R., Kivinen, M., Relation of Pc 1 micropulsations to the ring current and geomagnetic storms, *J. Geophys. Res.*, 77, 6746-6760, doi:10.1029/JA077i034p06746, 1972.
- Heaviside, O., The theory of electric telegraphy, *Encyclopaedia Britannica*, 1902.
- Hedin, A.E., Extension of the MSIS thermosphere model into the middle and lower atmosphere, *J. Geophys. Res.*, 96, 1159-1172, doi:10.1029/90JA02125, 1991.
- Henderson, M.G., Reeves, G.D., Skoug, R., Thomsen, M.F., Denton, M.H., Mende, S.B., Immel, T.J., Brandt, P.C., Singer, H.J., Magnetospheric and auroral activity during the 18 April 2002 sawtooth event, *J. Geophys. Res.*, 111, A01S90, doi:10.1029/2005JA011111, 2006.
- Heppner, J.P., Maynard, N.C., Empirical high-latitude electric field models, *J. Geophys. Res.*, 92, 4467-4489, doi:10.1029/JA092iA05p04467, 1987.
- Hirasawa, T., Effects of Magnetospheric Compression and Expansion on Spectral Structure of ULF Emissions. National Institute Polar Research Memoirs. 18, 127-151, 1981.
- Hosokawa, K., Yamashita, S., Stauning, P., Sato, N., Yukimatu, A.S., Iyemori, T., Origin of the SuperDARN broad Doppler spectra: simultaneous observation with Oersted satellite magnetometer, 22, 159-168, doi:10.5194/angeo-22-159-2004, 2004.
- Huber, M., Sofko, G.J., Small-scale vortices in the high-latitude F region, *J. Geophys. Res.*, 105, 20885-20897, doi:10.1029/1999JA000417, 2000.
- Humboldt, A., *Kosmos*, 1850.
- IAGA, *IAGA News*, 20, 112, 1981.
- Jacobs, J.A., Watanabe, T., Micropulsation whistlers, *J. Atmos. Terr. Phys.*, 26, 825-829, doi:10.1016/0021-9169(64)90180-1, 1964.
- Jokipii, J.R., Thomas, B., Effects of drift on the transport of cosmic rays. IV-Modulation by a wavy interplanetary current sheet. *Astrophys. J.*, 243, 1115-1122, doi:10.1086/158675, 1981.

- Kan, J.R., Lee, L.C., Energy coupling function and solar wind-magnetosphere dynamo, *Geophys. Res. Lett.*, 6, 577-580, doi:10.1029/GL006i007p00577, 1979.
- Kangas, J., Aikio, A., Olson, J.V., Multistation Correlation of ULF Pulsation Spectra Associated with Sudden Impulses, *Planet. Space Sci.*, 34, 543-553, doi:10.1016/0032-0633(86)90092-9, 1986.
- Kangas, J., Guglielmi, A., Pokhotelov, O., Morphology and physics of short-period magnetic pulsations, *Space Sci. Rev.*, 83, 435-512, doi: 10.1023/A:1005063911643, 1998.
- Kangas, J., Kultima, J., Pikkarainen, T., Kerttula, R., Mursula, K., Solar Cycle Variation in the Occurrence Rate of Pc 1 and IPDP Type Magnetic Pulsations at Sodankylä, *Geophysica*, 35, 23–31, 1999.
- Kennelly, A.E., On the elevation of the electrically-conducting strata of the earth's atmosphere, *Electrical World and Engineer*. 39, 473, 1902.
- Kenney, J.F., Knafllich, H.B., A systematic study of structured micropulsations, *J. Geophys. Res.*, 72, 2857-2869, doi:10.1029/JZ072i011p02857, 1967.
- Kerttula, R., Mursula, K., Pikkarainen, T., Kangas, J., Storm-time Pc 1 activity at high and middle latitudes, *J. Geophys. Res.*, 106, 6213-6227, doi:10.1029/2000JA900125, 2001a.
- Kerttula, R., Mursula, K., Pikkarainen, T., Kangas, J., Effect of magnetic storm intensity on Pc1 activity at high and mid-latitudes, *J. Atmos. Solar-Terr. Phys.*, 63, 503-511, doi:10.1016/S1364-6826(00)00172-3, 2001b.
- King, J.H., IMP series report. NSSDC Documents
- King, J.H., Papitashvili, N.E., 2010. One min and 5-min solar wind data sets at the Earth's bow shock nose. <http://omniweb.gsfc.nasa.gov/html/HROdocum.html#4>, 1971.
- King, J.H., Papitashvili, N.E., Solar wind spatial scales in and comparisons of hourly Wind and ACE plasma and magnetic field data, *J. Geophys. Res.*, 110, A02104, doi:10.1029/2004JA010649, 2005.
- Kivelson, M G, Russell, C.T., Introduction to space physics. Cambridge Univ Pr, 1995.
- Kleimenova, N.G., Kozyreva, O.V., Breus, T.K., Rapoport, S.I., Pc1 geomagnetic pulsations as a potential hazard of the myocardial infarction, *J. Atmos. Solar-Terr. Phys.*, 69, 1759-1764, doi:10.1016/j.jastp.2006.10.018, 2007.
- Knetter, T., Neubauer, F.M., Horbury, T., Balogh, A., Four-point discontinuity observations using Cluster magnetic field data: A statistical survey, *J. Geophys. Res.*, 109, A06102, doi:10.1029/2003JA010099, 2004.
- Kokubun, S., Yamamoto, T., Acuña, M.H., Hayashi, K., Shiokawa, K., Kawano, H., The Geotail magnetic field experiment, *J. Geomag. Geoelectr.*, 46, 7-21, 1994.

- Krimigis, S.M., Armstrong, T.P., Axford, W.I., Bostrom, C.O., Fan, C.Y., Gloeckler, G., Lanzerotti, L.J., The low energy charged particle (LECP) experiment on the Voyager spacecraft, *Space Sci. Rev.*, 21, 329-354, doi: 10.1007/BF00211545, 1977.
- Kunt, M., Edge detection: A tutorial review, Acoustics, Speech, and Signal Processing, IEEE International Conference on ICASSP'82. 2003, IEEE, 1172, 2003.
- Labonte, B.J., The orientation of the solar rotation axis from Doppler velocity observations, *Solar Physics*, 69, 177-183, doi: 10.1007/BF00151265, 1981.
- Le, G., Blanco-Cano, X., Russell, C.T., Zhou, X.W., Mozer, F., Trattner, K.J., Fuselier, S.A., Anderson, B.J., Electromagnetic ion cyclotron waves in the high altitude cusp: Polar observations, *J. Geophys. Res.*, 106, 19067-19079, doi:10.1029/2000JA900163, 2001.
- Lester, M., Chapman, P.J., Cowley, S.W.H., Crooks, S.J., Davies, J.A., Hamadyk, P., McWilliams, K.A., Milan, S.E., Parsons, M.J., Payne, D.B., Stereo CUTLASS-A new capability for the SuperDARN HF radars, *Ann. Geophys.*, 22, 459-473, doi:10.5194/angeo-22-459-2004, 2004.
- Lijima, T., Field-aligned currents in geospace: substance and significance, Magnetospheric current systems, 107-130, 2000.
- Loto'aniu, T.M., Fraser, B.J., Waters, C.L., Propagation of electromagnetic ion cyclotron wave energy in the magnetosphere, *J. Geophys. Res.*, 110, A07214, doi:10.1029/2004JA010816, 2005.
- Lühr, H., STEP International Newsletter, 4, 4-6, 1994.
- Lühr, H., Aylward, A., Bucher, S.C., Pajunpää, A., Pajunpää, K., Holmboe, T., Zaleski, S.M., Westward moving dynamic substorm features observed with the IMAGE magnetometer network and other ground-based instruments, *Ann. Geophys.*, 16, 425-440, doi:10.1007/s00585-998-0425-y, 1998.
- Manchester, R.N., Propagation of Pc 1 micropulsations from high to low latitudes, *J. Geophys. Res.*, 71, 3749-3754, doi:10.1029/JZ071i015p03749, 1966.
- Manchester, R.N., Correlation of Pc 1 micropulsations at spaced stations, *J. Geophys. Res.*, 73, 3549-3556, doi:10.1029/JA073i011p03549, 1968.
- Mann, I.R.; Wright, A.N.; Hood, A.W., Multiple-timescales analysis of ideal poloidal Alfvén waves, *J. Geophys. Res.*, 102, 2381-2390, doi:10.1029/96JA03034, 1997.
- Manninen, J, Some aspects of ELF-VLF emissions in geophysical research; PhD Thesis, Oulun yliopisto. Oulu University Press, 2005.
- Marchaudon, A., Cerisier, J.C., Dunlop, M.W., Pitout, F., Bosqued, J.M., Fazakerley, A.N., Shape, size, velocity and field-aligned currents of dayside plasma injections: a multi-altitude study, *Ann. Geophys.*, 27, 1251-1266, doi:10.5194/angeo-27-1251-2009, 2009.

- Mauk, B.H., McPherron, R.L., An experimental test of the electromagnetic ion cyclotron instability within the earth's magnetosphere. *Phys. Fluids*, 23, 2111-2127, doi:10.1063/1.862873, 1980.
- Maxwell, J.C., A dynamical theory of the electromagnetic field, *Philosophical Transactions of the Royal Society of London*, 155, 459-512, 1865.
- McCrea, I.W., Lockwood, M., Moen, J., Pitout, F., Eglitis, P., Aylward, A.D., Cerisier, J.C., Thorolfsson, A., Milan, S.E., ESR and EISCAT observations of the response of the cusp and cleft to IMF orientation changes, *Ann. Geophys.*, 18, 1009-1026, doi:10.1007/s00585-000-1009-7, 2000.
- McIlwain, C.E., MAGNETIC COORDINATES, *Space Sci. Rev.*, 5, 585-598 doi:10.1007/BF00167327, 1966.
- McWilliams, K.A., Yeoman, T.K., Provan, G., A statistical survey of dayside pulsed ionospheric flows as seen by the CUTLASS Finland HF radar, *Ann. Geophys.*, 18, 445-453, doi:10.1007/s00585-000-0445-8, 2000.
- Means, J.D., Use of the three-dimensional covariance matrix in analyzing the polarization properties of plane waves, *J. Geophys. Res.*, 77, 5551-5559, doi:10.1029/JA077i028p05551, 1972.
- Meier, M.M., Belian, R.D., Cayton, T.E., Christensen, R.A., Garcia, B., Grace, K.M., Ingraham, J.C., Laros, J.G., Reeves, G.D., The energy spectrometer for particles (ESP): Instrument description and orbital performance. *AIP Conf. Proc.*, 383, 203-210, doi:10.1063/1.51533, 1996.
- Menk, F.W., Fraser, B.J., Hansen, H.J., Newell, P.T., Meng, C.I., Morris, R.J., Identification of the magnetospheric cusp and cleft using Pc1-2 ULF pulsations, *J. Atmos. Terr. Phys.*, 54, 1021-1042, doi:10.1016/0021-9169(92)90069-W, 1992.
- Menk, F.W., I.R. Mann, A.J. Smith, C.L. Waters, M.A. Clilverd and D.K. Milling, Monitoring the plasmopause using geomagnetic field line resonances, *J. Geophys. Res.*, 109, 53-63, doi:10.1029/2003JA010097, 2004.
- Milan, S.E., Yeoman, T.K., Lester, M., Thomas, E.C., Jones, T.B., Initial backscatter occurrence statistics from the CUTLASS HF radars, *Ann. Geophys.*, 15, 703-718, DOI: 10.1007/s00585-997-0703-0, 1997.
- Milan, S.E., Lester, M., Greenwald, R.A., Sofko, G., The ionospheric signature of transient dayside reconnection and the associated pulsed convection return flow, *Ann. Geophys.*, 17, 1166-1171, doi:10.1007/s00585-999-1166-2, 1999.
- Milan, S.E., Boakes, P.D., Hubert, B., Response of the expanding/contracting polar cap to weak and strong solar wind driving: Implications for substorm onset, *J. Geophys. Res.*, 113, A09215, doi:10.1029/2008JA013340, 2008.
- Moen, J., Sandholt, P.E., Lockwood, M., Denig, W.F., Løvhaug, U.P., Lybekk, B., Egeland, A., Opsvik, D., Friis-Christensen, E., Events of enhanced convection and

related dayside auroral activity, *J. Geophys. Res.*, 100, 23917, doi:10.1029/95JA02585, 1995.

Mooers, C N K, The interaction of an internal tide with the frontal zone of a coastal upwelling region. sn, *Ph. D. Thesis*, 1970.

Morris, R.J., Cole, K.D., High-latitude day-time Pc1-2 continuous magnetic pulsations: A ground signature of the polar cusp and cleft projection, *Planet. Space Sci.*, 39, 1473-1491, doi:10.1016/0032-0633(91)90076-M, 1991.

Mursula, K., Kangas, J., Pikkarainen, T., Kivinen, M., Pc 1 micropulsations at a high-latitude station- A study over nearly four solar cycles, *J. Geophys. Res.*, 96, 17651-17661, doi:10.1029/91JA01374, 1991.

Mursula, K., Blomberg, L.G., Lindqvist, P.A., Marklund, G.T., Bräysy, T., Rasinkangas, R., Tanskanen, P., Dispersive Pc1 bursts observed by Freja, *Geophys. Res. Lett.*, 21, 1851-1854, doi:10.1029/94GL01584, 1994a.

Mursula, K., Kangas, J., Pikkarainen, T., Properties of structured and unstructured Pc1 pulsations at high latitudes: Variation over the 21st solar cycle, *Solar Wind Sources of Magnetosph. ULF Waves, Geophys. Monogr. AGU, Washington*. 81, 409, 1994b.

Mursula, K., Anderson, B., Erlandson, R., Pikkarainen, T., Solar cycle change of Pc 1 waves observed by an equatorial satellite and on the ground, *Adv. Space Res.*, 17, 51-55, doi:10.1016/0273-1177(95)00694-A, 1996.

Mursula, K., Rasinkangas, R., Bosinger, T., Erlandson, R., Lindqvist, P., Nonbouncing Pc 1 wave bursts, *J. Geophys. Res.*, 102, 17611-17624, doi:10.1029/97JA01080, 1997.

Mursula, K., Braysy, T., Rasinkangas, R., Tanskanen, P., Mozer, F., A modulated multiband Pc1 event observed by POLAR/EFI around the plasmopause, *Adv. Space Res.*, 24, 81-84, doi:10.1016/S0273-1177(99)00429-9, 1999a.

Mursula, K., Kangas, J., Kerttula, R., Pikkarainen, T., Guglielmi, A., Pokhotelov, O., Potapov, A., New constraints on theories of Pc1 pearl formation, *J. Geophys. Res.*, 104, 12399-12406, doi:10.1029/1999JA900055, 1999b.

Mursula, K., Prikner, K., Feygin, F.Z., Bräysy, T., Kangas, J., Kerttula, R., Pollari, P., Pikkarainen, T., Pokhotelov, O.A., Non-stationary Alfvén resonator: new results on Pc1 pearls and IPDP events, *J. Atmos. Solar-Terr. Phys.*, 62, 299-309, doi:10.1016/S1364-6826(99)00124-8, 2000.

Mursula, K., Braysy, T., Niskala, K., Russell, C., Pc 1 pearls revisited- Structured electromagnetic ion cyclotron waves on Polar satellite and on ground, *J. Geophys. Res.*, 106, 29543-29553, doi:10.1029/2000JA003044, 2001.

Neubert, T., Christiansen, F., Small-scale, field-aligned currents at the top-side ionosphere. *Geophys. Res. Lett.* 30, No.19, doi:10.1029/2003GL017808, 2010.

- Newell, P.T., Meng, C.I., The cusp and the cleft/boundary layer: low-altitude identification and statistical local time variation, *J. Geophys. Res.*, 93, 14549-14556, doi:10.1029/JA093iA12p14549, 1988.
- Nishida, A., Uesugi, K., Nakatani, I., Mukai, T., Fairfield, D.H., Acuna, M.H., Geotail mission to explore earth's magnetotail, *EOS Transactions*, 73, 425, doi:10.1029/91EO00314, 1992.
- Noerdlinger, P.D., Wave Generation Near the Outer Boundary of the Magnetosphere", *J. Geophys. Res.*, 69, 369-375, doi:10.1029/JZ069i003p00369, 1964.
- Nuttall, A., Some windows with very good sidelobe behaviour, *Acoustics, Speech and Signal Processing, IEEE Transactions*, 29, 84-91, doi:10.1109/TASSP.1981.1163506, 1981.
- Nykyri, K., Cargill, P.J., Lucek, E.A., Horbury, T.S., Balogh, A., Lavraud, B., Dandouras, I., Rème, H., Ion cyclotron waves in the high altitude cusp: CLUSTER observations at varying spacecraft separations, *Geophys. Res. Lett.*, 30, 2263, doi:10.1029/2003GL018594, 2003.
- Nykyri, K., Cargill, P.J., Lucek, E., Horbury, T., Lavraud, B., Balogh, A., Dunlop, M.W., Bogdanova, Y., Fazakerley, A., Dandouras, I., Cluster observations of magnetic field fluctuations in the high-altitude cusp, *Ann. Geophys.*, 22, 2413-2429, doi:10.5194/angeo-22-2413-2004, 2004.
- Nykyri, K., Grison, B., Cargill, P.J., Lavraud, B., Lucek, E., Dandouras, I., Balogh, A., Cornilleau-Wehrlin, N., Rème, H., Origin of the turbulent spectra in the high-altitude cusp: Cluster spacecraft observations, *Ann. Geophys.*, 24, 1057-1075, doi:10.5194/angeo-24-1057-2006, 2006.
- O'Brien, T.P., Moldwin, M.B., Empirical plasmopause models from magnetic indices, *Geophys. Res. Lett.*, 30, 1152, doi:10.1029/2002GL016007, 2003.
- Obayashi, T., Hydromagnetic whistlers, *J. Geophys. Res.*, 70, 1069-1078, doi:10.1029/JZ070i005p01069, 1965.
- Olson, J.V., Lee, L.C., Pc1 wave generation by sudden impulses, *Planet. Space Sci.*, 31, 295-302, doi:10.1016/0032-0633(83)90079-X, 1983.
- Orr, D., Magnetic pulsations within the magnetosphere- A review (Geomagnetic micropulsations within magnetosphere, investigating MHD waves and particle-wave interactions). *J. Atmos. Solar-Terr. Phys.*, 35, 1-50, 1973.
- Parker, E.N., Dynamics of the Interplanetary Gas and Magnetic Fields, *Astrophys. J.*, 128, 664-676, 1958.
- Pinnock, M., Rodger, A.S., Dudeney, J.R., Baker, K.B., Newell, P.T., Greenwald, R.A., Greenspan, M.E., Observations of an enhanced convection channel in the cusp ionosphere, *J. Geophys. Res.*, 98, 3767-3776, doi:10.1029/92JA01382, 1993.

- Plyasova-Bakounina, T.A., Kangas, J., Mursula, K., Molchanov, O.A., Green, A.W., Pc 1-2 and Pc 4-5 pulsations observed at a network of high-latitude stations, *J. Geophys. Res.*, 10965-10973, doi:10.1029/95JA03770, 1996.
- Pneuman, G.W., Kopp, R.A., Gas-magnetic field interactions in the solar corona. *Solar Phys.*, 18, 258-270, doi:10.1007/BF00145940, 1971.
- Ponomarenko, P.V., Waters, C.L., The role of Pc1-2 waves in spectral broadening of SuperDARN echoes from high latitudes, *Geophys. Res. Lett.*, 30, 1122, doi:10.1029/2002GL016333, 2002.
- Prikner, K., Mursula, K., Kangas, J., Feygin, F.Z., Ionospheric Alfvén Resonator Control over the Frequency-Variable Pc1 Event in Finland on May 14, 1997, *Studia Geophysica et Geodaetica*, 45, 363-381, doi: 10.1023/A:1022025619872, 2001.
- Provan, G., Yeoman, T.K., Statistical observations of the MLT, latitude and size of pulsed ionospheric flows with the CUTLASS Finland radar, *Ann. Geophys.*, 17, 855-867, doi:10.1007/s00585-999-0855-1, 1999.
- Raita, T., Kultima, J., Discovery of the pearl waves by Eyvind Sucksdorff, *J. Atmos. Solar-Terr. Phys.* 69, 1600-1603, doi:10.1016/j.jastp.2007.01.013, 2007.
- Rankin, D., Kurtz, R., Statistical study of micropulsation polarizations, *J. Geophys. Res.*, 75, 5444-5458, doi:10.1029/JA075i028p05444, 1970.
- Rasinkangas, R., Mursula, K., Kremser, G., Singer, H.J., Fraser, B.J., Korth, A., Hughes, W.J., Simultaneous Occurrence of Pc 5 and Pc 1 Pulsations in the Dawnside Magnetosphere: CRRES Observations, *Geophysical Monograph*, 81, 417, 1994.
- Rasinkangas, R., Mursula, K., Modulation of magnetospheric EMIC waves by Pc 3 pulsations of upstream origin, *Geophys. Res. Lett.*, 25, 869-872, doi:10.1029/98GL50415, 1998.
- Rich, F.J., Hairston, M., Large-scale convection patterns observed by DMSP, *J. Geophys. Res.*, 99, 3827-3844, doi:10.1029/93JA03296, 1994.
- Rietveld, M.T., Mauelshagen, H.P., Stubbe, P., Kopka, H., Nielsen, E., The characteristics of ionospheric heating-produced ELF/VLF waves over 32 hours, *J. Geophys. Res.*, 92, 8707-8722, doi:10.1029/JA092iA08p08707, 1987.
- Rodger, A.S., Pinnock, M., The ionospheric response to flux transfer events: the first few minutes, *Ann. Geophys.*, 15, 685-691, doi:10.1007/s00585-997-0685-y, 1997.
- Rosenbauer, H., Grünwaldt, H., Montgomery, M.D., Paschmann, G., Sckopke, N., Heos 2 plasma observations in the distant polar magnetosphere- The plasma mantle, *J. Geophys. Res.*, 80, 2723-2737, doi:10.1029/JA080i019p02723, 1975.
- Roth, B., Orr, D., Locating the Pc 1 generation region by a statistical analysis of ground based observations, *Planet. Space Sci.*, 23, 993-1002, doi:10.1016/0032-0633(75)90187-7, 1975.

- Roux, A., Perraut, S., Rauch, J.L., de Villedary, C., Kremser, G., Korth, A., Young, D.T., Wave-particle interactions near Ω_{He^+} observed on board GEOS 1 and 2, 2. Generation of ion cyclotron waves and heating of He^+ ions, *J. Geophys. Res.*, 87, 8174-8190, doi:10.1029/JA087iA10p08174, 1982.
- Ruohoniemi, J.M., Greenwald, R.A., Statistical patterns of high-latitude convection obtained from Goose Bay HF radar observations, *J. Geophys. Res.*, 101, 21743-21763, doi:10.1029/96JA01584, 1996.
- Ruohoniemi, J.M., Baker, K.B., Large-scale imaging of high-latitude convection with Super Dual Auroral Radar Network HF radar observations, *J. Geophys. Res.*, 103, 20797-20811, doi:10.1029/98JA01288, 1998.
- Ruohoniemi, J.M., Greenwald, R.A., Dependencies of high-latitude plasma convection: Consideration of interplanetary magnetic field, seasonal, and universal time factors in statistical patterns, *J. Geophys. Res.*, 110, A09204, doi:10.1029/2004JA010815, 2005.
- Russell, C.T., Elphic, R.C., Initial ISEE magnetometer results: Magnetopause observations, *Space Sci. Rev.*, 22, 681-715, doi:10.1007/BF00212619, 1978.
- Russell, C.T., Elphic, R.C., ISEE observations of flux transfer events at the dayside magnetopause, *Geophys. Res. Lett.*, 6, 33-36, doi:10.1029/GL006i001p00033, 1979.
- Safargaleev, V., Serebryanskaya, A., Koustov, A., Lester, M., Pchelkina, E., Vasilyev, A., A possible origin of dayside Pc1 magnetic pulsations observed at high latitudes, *Ann. Geophys.*, 22, 2997-3008, doi:10.5194/angeo-22-2997-2004, 2004.
- Saito, T., Period analysis of geomagnetic pulsations by a sona-graph method, *General Meetings of the Society of Terrestrial Magnetism and Electricity of Japan*, 1960.
- Saito, T., Geomagnetic pulsations, *Space Sci. Rev.*, 10, 319-412, doi:10.1007/BF00203620, 1969.
- Schiffler, A., Sofko, G., Newell, P.T., Greenwald, R., Mapping the outer LLBL with SuperDARN double-peaked spectra, *Geophys. Res. Lett.*, 24, 3149-3152, doi:10.1029/97GL53304, 1997.
- Schwenn, R., Solar wind sources and their variations over the solar cycle, *Space Sci. Rev.*, *Space Sciences Series of ISSI*, 22, 51-76, doi:10.1007/978-0-387-69532-7_5, 2006.
- Shue, J.H., Chao, J.K., Fu, H.C., Russell, C.T., Song, P., Khurana, K.K., Singer, H.J., A new functional form to study the solar wind control of the magnetopause size and shape, *J. Geophys. Res.*, 102, 9497-9511, doi:10.1029/97JA00196, 1997.
- Shue, J.H., Kokubun, S., Song, P., Russell, C.T., Steinberg, J.T., Chao, J.K., Zastenker, G., Vaisberg, O.L., Singer, H.J., Detman, T.R., Magnetopause location under extreme solar wind conditions, *J. Geophys. Res.*, 103, 17691-17700, doi:10.1029/98JA01103, 1998.

Song, P., Russell, C., Time series data analyses in space physics, *Space Sci. Rev.*, 87, 387-463, doi:10.1023/A:1005035800454, 1999.

Sonnerup, B.U.Ö., Cahill Jr, L.J., Magnetopause structure and attitude from Explorer 12 observations *J. Geophys. Res.*, 72, 171-183, doi:10.1029/JZ072i001p00171, 1967.

Sonnerup, B.U.Ö., Cahill Jr, L.J., Explorer 12 observations of the magnetopause current layer, *J. Geophys. Res.*, 73, 1757-1770, doi:10.1029/JA073i005p01757, 1968.

Spasojevic, M., Frey, H., Thomsen, M., Fuselier, S., Gary, S., Sandel, B., Inan, U., The link between a detached subauroral proton arc and a plasmaspheric plume, *Geophys. Res. Lett.*, 31, 4803-4806, doi:10.1029/2003GL018389, 2004.

Southwood, D.J., The behaviour of ULF waves and particles in the magnetosphere, *Planet. Space Sci.*, 21, 53-65, doi:10.1016/0032-0633(73)90019-6, 1973.

Stix, T H, Waves in plasmas. *Amer. Inst. Phys.*, 1992.

Stone, E.C., Burlaga, L.F., Cummings, A.C., Feldman, W.C., Frain, W.E., Geiss, J., Gloeckler, G., Gold, R.E., Hovestadt, D., Krimigis, S.M., The advanced composition explorer, *AIP Conference Proceedings*, 203, 48, 1990.

Stone, E.C., Cohen, C.M.S., Cook, W.R., Cummings, A.C., Gauld, B., Kecman, B., Leske, R.A., Mewaldt, R.A., Thayer, M.R., Dougherty, B.L., The Cosmic-Ray Isotope Spectrometer for the Advanced Composition Explorer, *Space Sci. Rev.*, 86, 285-356, doi:10.1023/A:1005075813033, 1998.

Sucksdorff, E., Occurrence of rapid micropulsations at Sodankyla during 1932 to 1935, *Terr. Magn. Atmos. Electr.*, 41, 337-344, 1936.

Sugiura, M., Hourly values of equatorial Dst for the IGY, *Ann.Int.Geophys.Yr.*, 35, 1964.

Sugiura, M., Poros, D.J., Hourly values of equatorial Dst for years 1957 to 1970, *Rep. X-645-71-278*, Goddard Space Flight Center, Greenbelt, Maryland, 1971.

Summers, W.R., Fraser, B.J., Polarization properties of Pc 1 micropulsations at low latitudes. *Planet. Space Sci.*, 20, 1323-1326, doi:10.1016/0032-0633(72)90019-0, 1972.

Tamao, T., Magnetosphere-ionosphere interaction through hydromagnetic waves. *Achievements of the Intern. Magnetospheric Study*, 217, 427-435, 1984.

Tepley, L., Low-Latitude Observations of Fine-Structured Hydromagnetic Emissions, *J. Geophys. Res.*, 69, 2273-2290, doi:10.1029/JZ069i011p02273, 1964.

Tepley, L., Landshoff, R.K., Waveguide theory for ionospheric propagation of hydromagnetic emissions, *J. Geophys. Res.*, 71, 1499-1503, doi:10.1029/JZ071i005p01499, 1966.

Tepley, L.R., Observations of hydromagnetic emissions, *J. Geophys. Res.*, 66, 1651-1658, doi:10.1029/JZ066i006p01651, 1961.

Tepley, L.R., Wentworth, R.C., Hydromagnetic Emissions, X-Ray Bursts, and Electron Bunches 1. Experimental Results, *J. Geophys. Res.*, 67, 3317-3333, doi:10.1029/JZ067i009p03317, 1962.

Thorne, R.M., Horne, R.B., The contribution of ion-cyclotron waves to electron heating and SAR-arc excitation near the storm-time plasmopause, *Geophys. Res. Lett.*, 19, 417-420, doi:10.1029/92GL00089, 1992.

Thorne, R.M., Horne, R.B., Energy transfer between energetic ring current H and O by electromagnetic ion cyclotron waves, *J. Geophys. Res.*, 99, 17275-17282, doi:10.1029/94JA01007, 1994.

Trakhtengerts, V.Y., Magnetosphere cyclotron maser: Backward wave oscillator generation regime, *J. Geophys. Res.*, 100, 17205-17210, doi:10.1029/95JA00843, 1995.

Trakhtengerts, V.Y., Demekhov, A.G., Belyaev, P.P., Polyakov, S.V., Ermakova, E.N., Isaev, S.V., A mechanism of anticorrelation in the occurrence of ULF electromagnetic noise resonance structure and Pc 1 magnetic pulsations through the solar activity cycle, *J. Atmos. Solar Terr. Phys.* 62, 253-256, doi:10.1016/S1364-6826(99)00116-9, 2000.

Trakhtengerts, V.Y., Demekhov, A.G., Titova, E.E., Kozelov, B.V., Santolik, O., Gurnett, D., Parrot, M., Interpretation of Cluster data on chorus emissions using the backward wave oscillator model, *Phys. Plasmas*, 11, 1345, doi:10.1063/1.1667495, 2004.

Trakhtengerts, V.Y., Demekhov, A.G., Generation of Pc 1 pulsations in the regime of backward wave oscillator, *J. Atmos. Solar-Terr. Phys.*, 69, 1651-1656, doi:10.1016/j.jastp.2007.02.009, 2007.

Troitskaya, V.A., Pulsation of the earth's electromagnetic field with periods of 1 to 15 seconds and their connection with phenomena in the high atmosphere, *J. Geophys. Res.*, 66, 5-18, doi:10.1029/JZ066i001p00005, 1961.

Troitskaya, V.A., Gul'Elmi, A.V., Geomagnetic micropulsations and diagnostics of the magnetosphere, *Space Sci. Rev.*, 7, 689-768, doi:10.1007/BF00542894, 1967.

Tsurutani, B.T., Gonzalez, W.D., The interplanetary causes of magnetic storms: A review, *Geophysical monograph*. 98, 77-89, 1997.

Van Eyken, A.P., Rishbeth, H., Willis, D.M., Cowley, S.W.H., Initial EISCAT observations of plasma convection at invariant latitudes 70-77, *J. Atmos. Solar-Terr. Phys.*, 46, 635-641, doi:10.1016/0021-9169(84)90081-3, 1984.

Villain, J.P., André, R., Pinnock, M., Greenwald, R.A., Hanuise, C., A statistical study of the Doppler spectral width of high-latitude ionospheric F-region echoes recorded with SuperDARN coherent HF radars, *Ann. Geophys.*, 20, 1769-1781, doi:10.5194/angeo-20-1769-2002, 2002.

Walker, A.D.M., Magnetohydrodynamic waves in geospace, 2005.

Wanliss, J.A., Showalter, K.M., High-resolution global storm index: Dst versus SYM-H, *J. Geophys. Res.*, 111, A02202, doi:10.1029/2005JA011034, 2006.

Wannberg, G., Wolf, I., Vanhainen, L.G., Koskenniemi, K., Röttger, J., Postila, M., Markkanen, J., Jacobsen, R., Stenberg, A., Larsen, R., The EISCAT Svalbard radar: A case study in modern incoherent scatter radar system design, *Radio Sci.*, 32, 2283-2307, doi:10.1029/97RS01803, 1997.

Webster, D J, ULF Goniometer Studies on Pc1 Geomagnetic Pulsations, *Ph.D. Thesis*, University of Newcastle, 1982.

Webster, D.J., Fraser, B.J., Source regions of low-latitude Pc1 pulsations and their relationship to the plasmopause, *Planet. Space Sci.*, 33, 777-793, doi:10.1016/0032-0633(85)90032-7, 1985.

Wentworth, R.C., Enhancement of Hydromagnetic Emissions after Geomagnetic Storms, *J. Geophys. Res.*, 69, 2291-2298, doi:10.1029/JZ069i011p02291, 1964.

Wild, J., Cowley, S., Davies, J., Khan, H., Lester, M., Milan, S., Provan, G., Yeoman, T., Balogh, A., Dunlop, M., First simultaneous observations of flux transfer events at the high-latitude magnetopause by the Cluster spacecraft and pulsed radar signatures in the conjugate ionosphere by the CUTLASS and EISCAT radars, *Ann. Geophys.*, 19, 1491-1508, doi:10.5194/angeo-19-1491-2001, 2001.

Willson, R.C., Hudson, H.S., 1988. Solar luminosity variations in solar cycle 21, *Nature*, 332, 810-812, doi:10.1038/332810a0, 1998.

Wright, D.M., Yeoman, T.K., Baddeley, L.J., Davies, J.A., Dhillon, R.S., Lester, M., Milan, S.E., Woodfield, E.E., High resolution observations of spectral width features associated with ULF wave signatures in artificial HF radar backscatter, *Ann. Geophys.*, 22, 169-182, doi:10.5194/angeo-22-169-2004, 2004.

Xu, D., Chen, T., Zhang, X.X., Liu, Z., Statistical relationship between solar wind conditions and geomagnetic storms in 1998-2008, *Planet. Space Sci.*, 57, 1500-1513, doi:10.1016/j.pss.2009.07.015, 2009.

Yahnin, A.G., Yahnina, T.A., Frey, H.U., Subauroral proton spots visualize the Pc1 source, *J. Geophys. Res.*, 112, A10223, doi:10.1029/2007JA012501, 2007.

Yahnina, T.A., Yahnin, A.G., Kangas, J., Manninen, J., Proton precipitation related to Pc1 pulsations, *Geophys. Res. Lett.*, 27, 3575-3578, doi:10.1029/2000GL003763, 2000.

Yahnina, T.A., Yahnin, A.G., Kangas, J., Manninen, J., Evans, D.S., Demekhov, A.G., Trakhtengerts, V.Y., Thomsen, M.F., Reeves, G.D., Gvozdevsky, B.B., Energetic particle counterparts for geomagnetic pulsations of Pc1 and IPDP types, *Ann. Geophys.*, 21, 2281-2292, doi:10.5194/angeo-21-2281-2003, 2003.

Yukimatu A.S. and Tsutsumi, M., A new SuperDARN meteor wind measurement: Raw time series analysis method and its application to mesopause region dynamics, *Geophys. Res. Lett.*, 29, 1981, doi:10.1029/2002GL015210, 2002.

Ziou D. and Tabbone, S., Edge detection techniques-an overview, *International Journal of Pattern Recognition and Image Analysis*, 8, 537, 1998.